Stian Høegh Sørum

Uncertainties in the Design of Monopile Offshore Wind Turbines

Stian Høegh Sørum

Doctoral thesis

NTNU
Norwegian University of
Science and Technology

NTNU
Norwegian University of
Science and Technology

NTNU

Stian Høegh Sørum

Uncertainties in the Design of Monopile Offshore Wind Turbines

Thesis for the degree of Philosophiae Doctor

Trondheim, September 2023

Norwegian University of Science and Technology
Faculty of Engineering
Department of Marine Technology

NTNU
Norwegian University of
Science and Technology

PRINTED IN
NORWAY
NO - 1598

NORDIC SWAN ECOLABEL

Printed matter
2041 0731

As yet, the wind is an untamed, and unharnessed force;
and quite possibly one of the greatest discoveries hereafter to be made,
will be the taming, and harnessing of the wind.

- Abraham Lincoln

Abstract

If the ambitious targets for growth in installed capacity of offshore wind turbines over the next decades are to be met, more cost-efficient wind farms need to be developed. One way of achieving this can be to reduce the uncertainty in the design calculations, which will allow for reducing the conservatism in the design process. Focusing on the support structure of monopile offshore wind turbines, this thesis aims at identifying the major sources of uncertainty when performing fatigue calculations. This spans both uncertainty in the design basis parameters, productions tolerances, and operational parameters, as well as uncertainties in the engineering models and software used. Further, an efficient method for fatigue calculations has been developed. In total, the results of this thesis will: (*i*) help designers prioritize which parameters to focus on to gain more confidence in the fatigue design calculations; (*ii*) identify the engineering models that should be the focus of further research; and (*iii*) provide a computationally efficient method for performing fatigue analysis in early design stages or in screening studies.

To identify the parameters accounting for the majority of the uncertainty in the fatigue calculations, a screening study was performed. This included 16 parameters from a variety of fields, including the environmental design basis, aerodynamic loads, hydrodynamic loads, geotechnics, material properties and turbine operation. The fatigue properties of steel were found to have the largest influence on the calculated fatigue utilization. However, the uncertainties of these parameters have been unchanged for nearby 40 years (since 1984), with no promises of improvement in the near future. The second largest influence on the uncertainty was seen for a group of parameters describing the environmental conditions at the site. The uncertainty in these may be reduced by using longer time series of data when determining the design basis. As the turbine size increases, the effect of uncertainty in design turbulence intensity increases, as wind loads become more important compared to wave loads. In the monopile below seafloor, the soil conditions also have a significant effect on the total uncertainty.

When using different engineering models in the design calculations, the largest variation in predicted fatigue damage was seen when waves were modelled as short-crested rather than long-crested. The software used for performing the calculations also had a significant influence, with particularly the stiffness modelling of the blades being important. In the tower, the wind coherence model also has a significant impact on the fatigue damage. For the monopile, the difference between the two investigated soil models depends heavily on the model calibration. These topics are all suggested for further research to develop models and methods suitable for

offshore wind turbines. It is also important for the designer to be aware of the large difference in fatigue damage than can occur with the different engineering models, as it is not known a priori which models that are conservative.

Finally, a method for performing fatigue calculations was developed. This uses one lumped sea state per wind bin, as opposed to analysing the full wave scatter diagram for each wind speed class. The lumped sea state is identified by performing computationally efficient wave-only analysis. In this work, an empirical wave-to-stress transfer function has been used, but other modelling methods may also be applied. In this case study, the long-term fatigue damage was predicted with an error of <6% for aligned wind and waves, and ~10% for misaligned wind and waves, while the computational effort was reduced by >90%.

Acknowledgments

Contents

List of Acronyms

ALS	Accidental limit state
BEM	Blade elemement momentum
C.o.V.	Coefficient of variation
EE	Elementary effect
FDLM	Frequency domain lumping method
FLS	Fatigue limit state
FNV	Faltinsen-Newman-Vinje
JONSWAP	Joint North Sea Wave Project
LCOE	Levelized cost of energy
LES	Large eddy simulations
OWT	Offshore wind turbine
RNA	Rotor-nacelle-assembly
SLS	Serviceability limit state
SSI	Soil-structure interaction
TDLM	Time domain lumping method
TI	Turbulence intensity
ULS	Ultimate limit state

List of Figures

List of Tables

Part I

Thesis Overview and Background

Chapter 1

Introduction

This chapter introduces the research questions and objectives of the thesis. First, the background and motivation for the research is presented. Next, the research questions and scientific contributions are formulated. Finally, the articles prepared in the course of the thesis work are presented, and the outline of the remaining thesis is given.

1.1 Motivation and Background

In light of climate change and increasing carbon dioxide levels in the atmosphere, there is a need to shift from carbon-emitting energy sources (such as coal, oil and gas) to carbon-free alternatives. In terms of electricity production, the shift should allow for increasing both the renewable contribution to today's energy usage, as well as facilitating the expected growth in energy consumption. DNV's Energy Transition Outlook predicts that the electricity production capacity increase will be covered mainly by growth of solar photovoltaic and wind energy capacity (DNV, 2022). The forecast predicts 30% of wind energy to be produced from offshore wind farms by 2050 - a significant increase from 5% in 2020. This is in line with WindEurope's expectations of the yearly commissioning rate for offshore wind doubling from 2021 to 2026 (WindEurope, 2022).

While a large number of concepts for floating offshore wind turbines (OWTs) are being developed, the majority of the installed turbines are bottom-fixed and supported by monopiles. This is also reflected in DNV's forecast of ~1700 GW capacity installed for bottom-fixed OWTs by 2050. For floating OWTs, 300 GW are expected to be installed (DNV, 2022). Large projects being planned include multi-gigawatt farms like Dogger Bank in Europe (Dogger Bank Wind Farm, 2022) and Empire Wind outside the East Coast of the US (Empire Wind, 2022). A key enabler for planned and future projects is more cost-efficient designs. Reducing the cost might also open up for installation of OWTs in waters now considered infeasible. These waters may be either too deep for today's monopiles and too shallow for floating OWTs, or at a too large distance from shore to run maintenance in an economical matter.

A key element for allowing the expansion of offshore wind turbines is a reduc-

tion of the levelized cost of energy (LCOE), i.e. the price of producing one unit of energy. The major cost components of offshore wind turbines are the turbine itself, and operation and maintenance, both accounting for approximately 25% of the cost. A significant portion of the cost is also attributed to the substructure (20%) and installation (15%) (Smith et al., 2015). While these figures are project-dependent, the LCOE is in general expected to decrease with increasing turbine size and increase with increasing distance to shore.

One way of lowering the LCOE is to reduce the uncertainty in the design of the support structure. Design codes, such as IEC 61400-1 (IEC, 2019) and DNV ST-0126 (DNV, 2021d), require the support structures to be designed for a target reliability level where the probability of failure for the support structure is less than a target probability, p_f. Formally, this is written as

$$\mathrm{P}(S > R) \leq p_f \qquad (1.1)$$

where S is the load effect on the structure and R is the capacity of the structure. A conventional design process does not calculate the failure probability directly, but considers the structural capacity in predefined limit states and load cases. The limit states considered are the fatigue limit state (FLS), ultimate limit state (ULS), accidental limit state (ALS) and serviceability limit state (SLS) (DNV, 2021d). The ULS check evaluates the capacity against independent, extreme load events, while FLS considers the aggregated effect of all load actions over the lifetime of the structure. The ALS criteria takes into account accidental events not normally part of the structure's lifetime, such as boat collisions, and abnormal environmental actions. SLS does not relate directly to the failure of the support structure, but evaluates if the operational limitations of the turbine are met.

Within the limit state framework, the design requirement in Equation (1.1) is translated into the requirement that the characteristic capacity (R_c) must be larger than the characteristic load effect (S_c). The capacity is reduced and the load effect increased by the use of partial safety factors:

$$\gamma_S S_c \leq \frac{R_c}{\gamma_R}. \qquad (1.2)$$

Here, γ_S and γ_R are the partial safety factors on the load effect and capacity, respectively. These safety factors are calibrated so that the limit-state design check in Equation (1.2) will provide the same structural reliability as Equation (1.1). This is illustrated in Figure 1.1, where the relationship between the uncertainty in the load effects and capacity, and the design requirements are given.

Reducing the uncertainty in a design can reduce the safety factors, allowing for more economical support structures. A first step towards reducing uncertainty is identification of the parameters that contribute the most towards the total uncertainty. The following sections will review the current knowledge on uncertainties in the design of monopile OWTs, with focus on the fatigue limit state. Where relevant, other support structures and land-based turbines are also included, as well as other limit states. An overview of the the main sources of uncertainty is given in Figure 1.2.
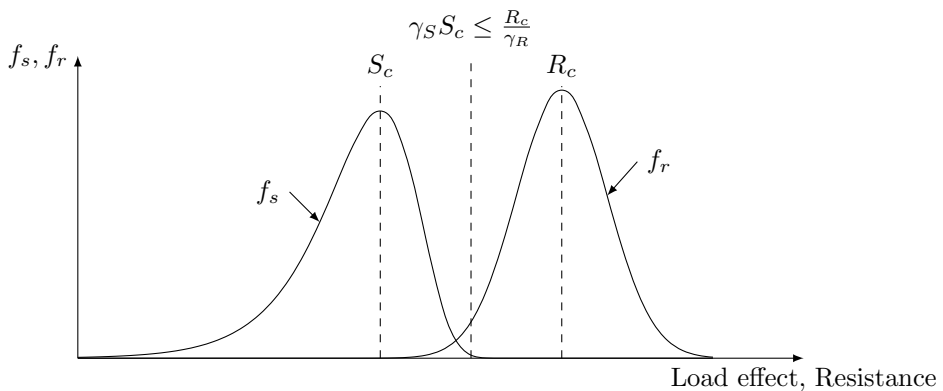
Figure 1.1: Probability density function of load effect (f_s) and capacity (f_r). Adapted from Moan (2009).

1.1.1   Design Basis Parameter Uncertainties

While numerous studies have investigated the effect of uncertainties in the design basis parameters for OWTs, only a few of these have considered multiple parameters or parameters from different engineering fields. Hübler et al. (2017) considered more than 100 parameters relevant for the design of monopiles, and used a four-step method to perform increasingly accurate sensitivity analyses of the parameters found most influential in the previous step. Robertson et al. (2019) considered a large number of parameters of the incoming wind field and the turbine itself, and investigated how they influenced the fatigue and ultimate loads on a land-based turbine. While Hübler et al. (2017) found that the parameters related to the soil-structure-interaction and pile diameter had the largest influence on the uncertainty of the design capacity, these parameters were not considered by Robertson et al. (2019). The latter found turbulence intensity (TI), wind shear, yaw error and air-foil parameter uncertainties to be most important. Teixeira et al. (2019) compared the effect of uncertainty of 13 parameters describing the environmental conditions, considering both wind and waves. They concluded that TI contributed the most to the uncertainty in the design. Further, Toft et al. (2016b) investigated the effect of uncertainties in TI, wind shear and air density, and found TI to be most important. The same authors compared the effect of the total uncertainties in the wind parameters to the uncertainties in the fatigue parameters (SN-curve and fatigue capacity) and "general uncertainties" (load model and stress concentration factor) (Toft et al., 2016a). They found that the fatigue parameters were the most important, while also the "general uncertainties" were found more important than the uncertainties in the wind parameters. Both Peeringa and Bedon (2017) and Velarde et al. (2020) support the notion that the fatigue parameters are important, finding the fatigue capacity amongst the most influential parameters. Peeringa and Bedon (2017) also found the SN-curve parameters important. In addition, Velarde et al. (2020) found both the structural dynamic model and wave load model to be

5
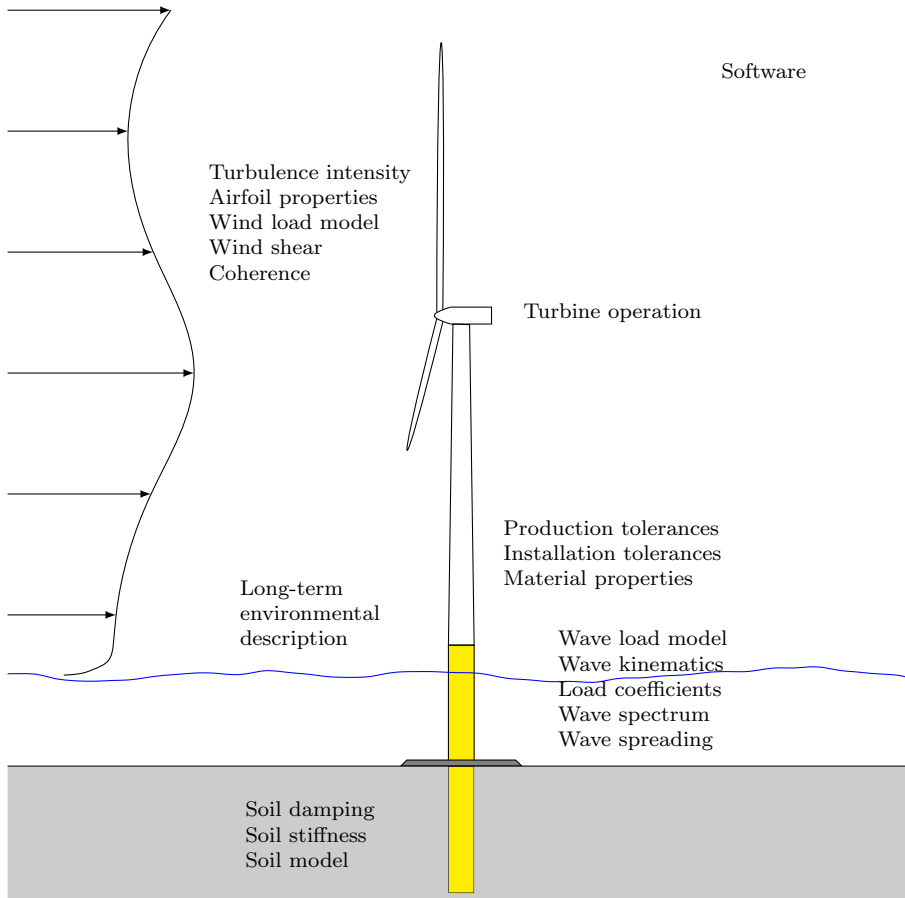
Figure 1.2: Overview of major sources of uncertainties in the design of monopile OWTs.

important when multiplying the stress ranges with random variables to account for the uncertainty of these properties.

A summary of the parameters considered in the above mentioned studies is given in Figure 1.3. The parameters are divided into three groups: "Important" denotes a parameter found to have significantly larger influence on the total uncertainty in the fatigue lifetime than the other parameters. Conversely, "Not important" denotes the parameters with less influence on the total uncertainty. Of the 38 parameters or parameter groups identified in the studies, 15 have been identified as important by one or more studies. Of these, fatigue capacity and turbulence intensity are the only parameters found of major importance by more than one study. For the parameters denoted "Variability" in Figure 1.3, the long-term variability of the
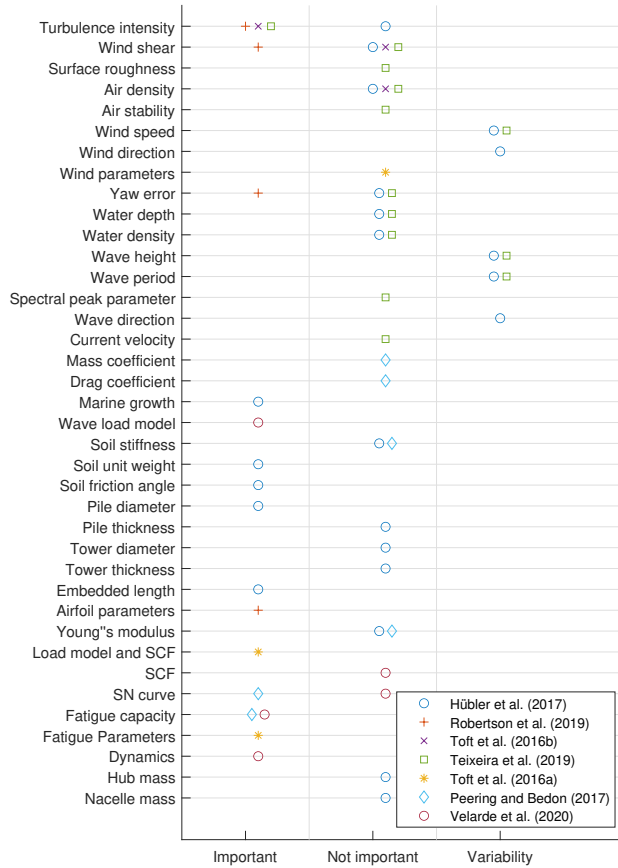
Figure 1.3: Summary of the results from previous studies categorizing the parameters as "important" or "not important" w.r.t. the overall uncertainty of the fatigue design of monopile OWTs. Parameters where the variability is considered are marked separately. Note that only the most influential parameters are included from Robertson et al. (2019).

parameters has been considered. The variability is larger than the uncertainty in
the equivalent design parameter, and will inflate the importance of the respective
parameter if included in the sensitivity analysis. This is illustrated in Figure 1.4,
where the long-term variability of TI measured over several years is given by the
blue bars. The design value of TI is the 90th percentile, measured over minimum
one year (IEC, 2019). The variation of this value over different years is given by
the red curve, showing significantly less uncertainty than the variability of the
instantaneous TI. Using the long-term variability as the measure of the parameter
uncertainty will significantly inflate the importance of the parameter. The result is
that none of the above mentioned studies consider the effect of the uncertainty in
the long-term distribution of mean wind speed, significant wave height, wave peak
period and environmental load directions.
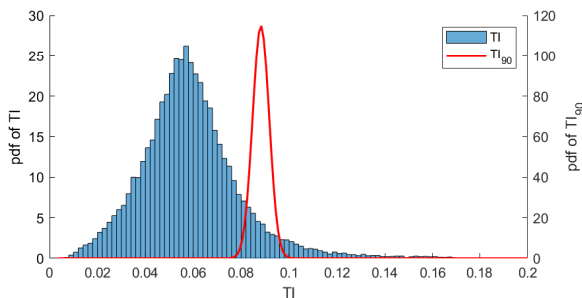
Figure 1.4: Long-term variability of turbulence intensity (TI) and uncertainty in
the 1-year design turbulence intensity (TI_{90}) (Sørum et al., 2022b).

The works mentioned above have all looked at multiple parameters and inves-
tigated how these influence the uncertainty of a design. Numerous other studies
have investigated how variations of a single or a few parameters influence the de-
sign. Türk and Emeis (2010) used measurement data from the FINO1 platform
to demonstrate how the wind speed-dependent turbulence intensity prescribed by
IEC 61400-3 differed from the 90-percentile of the measured TI. Both approaches
are allowed by the standard. The same discrepancy in the resulting design TI was
observed by Nybø et al. (2019). Ernst and Seume (2012) demonstrated that using
the TI values from the standard may lead to a very conservative design, while Toft
et al. (2016a) showed that for a land-based turbine, the blade loads were accurately
predicted if the 90th-percentile of TI was used. The 90th-percentile was found to
be conservative for the tower base. Bakhshi and Sandborn (2016) found that any
yaw error increased the fatigue damage in the support structure and reduced the
power production. Consequently, the structural reliability was increased if any yaw
error was corrected.

Little research has been performed on the sensitivity of the design to hydro-
dynamic load parameters for monopile OWTs. Ziegler et al. (2015) showed how
the fatigue loads on a 4 MW turbine were sensitive to variations in T_p and water
depth within a wind park. This becomes important to consider if designing the
foundations by clustering turbines within a farm.

Variations in the natural frequency may be caused by variations in either mass or stiffness properties. Fallais et al. (2022) compared the as-built natural frequency of monopile OWTs across a farm with the design predictions, observing differences of 1%-9% for the 1st natural frequency and 20%-50% for the 2nd natural frequency. Uncertainties in the soil stiffness, scour depth, inertia of the rotor-nacelle-assembly (RNA) and linearization effects could not fully explain the discrepancies. Zaaijer (2006) showed that uncertainty in the RNA mass may cause significant variations in the natural period. Uncertainty in the soil friction angles and scour depths gave smaller variations, with differences up to 4% and 6%, respectively. Haldar et al. (2018) demonstrated that uncertainty in the variation of soil shear strength with depth can cause weak zones in the soil that decrease the natural frequency and reduce the fatigue life. A related study was performed by Hsu et al. (2022), who showed that limiting the number of soil samples taken within a wind park introduced uncertainty in the soil layering. This again influenced the foundation designs, leading to both increased dimensions and increased probability of failure in the vertical load bearing capacity. The importance of uncertainty in the soil characteristics and the occurrence of scour was compared by Prendergast et al. (2018). They found that scour depths of both 5 m and 10 m have a larger influence on the natural frequency than the uncertainty in the soil parameters. Further, the soil parameters had a higher influence on the natural frequency when the scour depth increased. Jawalageri et al. (2022), Prendergast et al. (2015) and Li et al. (2018) all showed how the 1st natural frequency of a monopile in sand is most influenced by scouring if the sand is loose. Jawalageri et al. (2022) also showed that the mode shape of the 1st mode was influenced most by scour in loose sand, while the 2nd mode was influenced most in dense sand. Niu et al. (2022) performed model tests on a pile with different soil stratification, and found that the influence of scour was largest if the top layer was made of clay. Kallehave et al. (2015) investigated how the natural frequency varies with changes in corrosion, soil stiffness, scour protection height, wall thickness, marine growth, entrapped water and soil in the pile, total mass of the OWT, and the nacelle height. For realistic uncertainties in a design case, only the soil stiffness and height of the scour protection were found to have a significant impact on the natural frequency. Finally, Damgaard et al. (2015) showed that soil variations may give a coefficient of variation (C.o.V.) of 30% for the modal damping, corresponding to a C.o.V. of 8% of the side-side damage equivalent moment.

1.1.2 Model Uncertainty

While the previous section reviewed work performed on the effect of uncertainty in the design basis parameters for a monopile OWT, there are also significant uncertainties in the models used for analysing the response of monopile OWTs. A review of the work performed on these issues is given in the following.

Wind Model

The incoming wind field is typically modelled using medium-fidelity models like the Kaimal spectrum or Mann model, but more accurate methods based on computa-

tional fluid mechanics may also be used. Nybø et al. (2020) compared the coherence of the Kaimal model, the Mann model, large eddy simulations (LES) and measurements from FINO1. They demonstrated differences in the wind shear profiles of the engineering models, and deviations between the engineering models, the LES and, the measurements. Further, the difference in coherent structures of the wind fields was demonstrated. The difference in vertical coherence between the Kaimal and Mann models and measurements was also shown by Eliassen and Obhrai (2016). These differences had a significant impact on the predicted tower fore-aft bending moments, as well as tower torsion and blade root moments (Myrtvedt et al., 2020; Nybø et al., 2021). Nybø et al. (2021) focused on the low-frequency response ($f < 0.1$ Hz), and demonstrated how the lower coherence of the Mann model yielded a lower variation in the tower top and base moment than the Kaimal model. Still, these two models were more similar to each other than the LES predictions and the measured time series. A similar deviation in the tower fore-aft bending moments was observed by Myrtvedt et al. (2020), who compared the Kaimal and Mann models for cases for high TI.

Wave Kinematics

Wave kinematics are often described as linear or second-order, although more accurate simulations of wave kinematics may be obtained by the use of e.g. computational fluid dynamics. Bachynski and Ormberg (2015) found that there was little difference in the fatigue predictions when using 1st and 2nd-order wave kinematics in fully integrated simulations including turbulent wind loads. Horn et al. (2016) compared the extreme and fatigue response for a monopile subject to irregular waves, with constant wind loads and aerodynamic damping included. They found that the effect of including higher-order wave kinematics at low sea states was small, but had a significant effect in more severe sea states. Schløer et al. (2012) investigated the effect of fully non-linear wave excitation, i.e. non-linear wave kinematics and load models. An increase in the short-term fatigue damage was observed in severe sea states, associated with transient ringing-type response to steep waves. The same was seen by Horn et al. (2016), who used the deep-water Faltinsen-Newman-Vinje (FNV) model (Faltinsen et al., 1995; Newman, 1996). This model is known to over-predict certain load components (Krokstad et al., 1998), and a new shallow-water formulation has later been developed (Kristiansen and Faltinsen, 2017). An increase in fatigue damage was also observed by Horn et al. (2016) and Horn et al. (2019), where higher-order wave loads were modelled by a panel model. For large-volume cylinders, such as modern monopiles, wave diffraction loads are important. This was shown by e.g. Bachynski and Ormberg (2015) and Horn et al. (2016), both demonstrating how the fatigue damage reduces when near-field diffraction is taken into account. Haldar et al. (2018) showed that the choice of the Pierson-Moskowitz or JONSWAP wave spectrum had little influence on the fatigue damage prediction for a 5 MW turbine.

Directionality of Loads

The direction of environmental loads is important for OWTs in operational conditions, because the aerodynamic damping is substantial in-line with the wind and almost negligible in the cross-wind direction. Horn et al. (2019) demonstrated that the fatigue life is reduced when the directional distribution of the wind is taken into account. The same was seen when including wind-wave misalignment. Horn et al. (2018) showed that separating the total wave energy into a wind-driven and swell component may reduce the total fatigue damage. The same was seen when the waves were modelled as short-crested. Kim and Natarajan (2013) found that the effect of modelling waves as short-crested varied with the soil stiffness. Finally, Trumars et al. (2006) investigated the response of a turbine built outside Bockstigen, and found a significant increase in the wave-induced response in cases with wind-wave misalignment.

Soil-Structure Interaction

Modelling of soil-structure interaction (SSI) can be done in several ways. Early recommendations were to use the p-y curve approach from the offshore oil and gas industry where the lateral response of the soil was modelled as function of the pile displacement. This approach was developed for long, slender piles, with response characteristics that differ from OWT monopile foundations. Byrne et al. (2015) showed how the parameterised curves from oil and gas become increasingly inaccurate when the pile length-to-diameter ratio decreases. They suggested the PISA model, adding three load components to the SSI model: a distributed moment to capture the effect of shear forces on the wall of the pile, and a base moment and shear force component. For the pile designs and soil conditions that were investigated, this model showed a better fit to the response predicted by finite element simulations.

Zaaijer (2006) aimed at providing simplified SSI models to reduce the computational effort in fatigue analyses. An apparent fixity model, a model with the SSI response reduced to uncoupled rotation and translation springs, and a stiffness matrix applied at seafloor were compared. The stiffness matrix showed the best agreement with the two first natural frequencies predicted by a full finite element representation of the soil. When compared to full-scale measurements of piles with diameter 3-4 m, the first natural frequency was predicted with an error of $< 4\%$ for the majority of the cases when using the stiffness matrix model. Larger deviations were obtained for some turbines. Aasen et al. (2017) compared the fatigue lifetime of a monopile foundation when using p-y curves, a stiffness matrix, a combination of stiffness and damping matrices, and a non-linear 1D rotational model with amplitude-dependent stiffness and damping. The latter incorporates the hysteretic damping that is typical for the soil behaviour. The 1D model predicted fatigue lifetimes of 1-4 years more than the other models.

A macro-element model reducing the SSI to a load-displacement relationship at seafloor was presented by Page et al. (2018). For correctly calibrated input parameters, it reproduced the SSI with the same level of accuracy as finite element analysis, at a significantly reduced computational effort. Katsikogiannis et al.

11

(2019) compared the response predictions for a fully integrated OWT using the same macro-element model, non-linear p-y curves, and a linear SSI model. The predicted fatigue damage varied significantly, particularly in load cases with little aerodynamic damping, due to variations in both damping and natural frequency. Only the macro-element model was capable of predicting the amplitude-dependent stiffness and damping. Varelis et al. (2021) investigated the effect of scour, by comparing the water flow around the monopile and the quasi-static response of a monopile to wind and current loads. The occurrence of scour was found to change the turbulence of the flow at the base of the monopile, as well as the hydrodynamic loads on the cylinder.

Software

The capabilities and differences in computer codes used for analysing OWTs were investigated in the OC3[1], OC4[2], OC5[3] and OC6[4] projects (IEA Wind TCP, 2023). The various phases of the projects have studied different support structure concepts, including both bottom-fixed and floating OWTs. A review of the findings that are relevant for monopile OWTs is given in the following, including both extreme and normal load levels. OC3 Phase II (Jonkman et al., 2007) compared the response predictions for a monopile OWT using five different computer programs. While the overall response predictions were similar, there were deviations due to different SSI models, structural models, implementation of aerodynamic loads and discretisation of the hydrodynamic loads. OC5 Phase Ia compared the hydrodynamic loads from model tests with a rigid cylinder to those predicted by different simulation software. While all computer codes were able to predict the 1st order loads well, there were differences in the higher-order loads. This was attributed to how the wave loads were integrated up to the instantaneous free surface, and whether non-linear wave kinematics were taken into consideration (Robertson et al., 2015). OC5 Phase Ib compared the response predicted by the computer codes with a model test of a flexible monopile with a sloped seafloor. The importance of including higher-order loads in extreme sea states was shown, as this can excite the natural frequencies of the monopile. Further, the importance of taking the sloped seafloor into account when calculating the wave kinematics was shown. This is problematic if standard wave theories are used. Finally, the importance of including breaking-wave events in the simulation codes was demonstrated. These events cause impulsive loads on the structure, and may excite the natural frequencies of the foundation.

OC5 Phase III (Popko et al., 2018, 2020, 2019) compared the response predictions for a jacket mounted OWT with full-scale measurements. This phase demonstrated the challenges related to full-scale validation of software. The different codes were capable of representing the main structural response fairly similarly. However, there were differences in the dynamic response that may have a significant impact on fatigue life predictions. OC6 Phase II (Bergua et al., 2022) integrated the RED-

---

[1]Offshore Code Comparison Collaboration
[2]Offshore Code Comparison Collaboration, Continuation
[3]Offshore Code Comparison Collaboration, Continuation, with Correlation
[4]Offshore Code Comparison Collaboration, Continuation, with Correlation and unCertainty

WIN macro-element for SSI (Page et al., 2019) into a number of different software tools. The implementation was validated by comparing the response predictions in the different software, and a comparison against other SSI-models was performed. This showed reduced response amplitudes when using the REDWIN model due to the non-linear hysteretic effect, which in turn leads to lower, and more accurate, fatigue damage predictions. Following the experience from the OCX projects, a recommended practice for verification of numerical models was developed by Huhn and Popko (2020).

1.2 Research Questions and Objectives

While there are numerous studies determining the effect of uncertainties in the design of monopile OWTs, there is a lack of knowledge about which parameters have the highest influence on the total uncertainty. This is particularly true when parameters and models from different engineering fields are compared. Further, there have been no studies of how the design of the OWT influences this uncertainty, for example when the size of the turbine changes. Therefore, the aim for this thesis is to answer the following research question:

RQ What are the major sources of uncertainty in the fatigue design of monopile offshore wind turbine support structures?

The work will include turbines of different sizes, but be limited to one geographical location. Uncertainties due to both the modelling of OWTs and the uncertainty in the site and operational parameters, and production tolerances will be included. Focus will be on the uncertainty in the capacity of the monopile and tower of a given design. In other words: Once the designer has calculated the capacity of a support structure, how certain can the designer be that this number reflects the true capacity of the installed turbine? Other components of the turbine, such as the blades, hub, and drive-train are not assessed. The focus is placed on the fatigue lifetime predictions, although both ultimate strength and serviceability requirements may govern certain aspects of the design or designs at specific locations.

1.3 Scientific Contributions

To answer the research question, focus has been on three contributions:

C1 Identification of parameters responsible for the majority of the uncertainty in fatigue design of monopile offshore wind turbines

C2 Evaluation of uncertainty introduced in the global numerical modelling of monopile offshore wind turbines

C3 Development of a method for efficient fatigue analysis of monopile and tower support structures

C1 and **C2** answer directly to two separate parts of the **RQ**, while **C3** is both a prerequisite for efficient assessment of the two other contributions and answers parts of the **RQ**.

1.4 Publications

A number of journal publications have been prepared as part of the thesis work. **P1** to **P5** are listed below, which all contribute towards one or more of the scientific contributions.

P1 **Stian H. Sørum**, George Katsikogiannis, Erin E. Bachynski-Polić, Jørgen Amdahl, Ana M. Page, Rasmus T. Klinkvort (2022). Fatigue design sensitivities of large monopile offshore wind turbines. *Wind Energy*, **25**(10), 1684-1709

P2 George Katsikogiannis, **Stian H. Sørum**, Erin E. Bachynski, Jørgen Amdahl (2021). Environmental lumping for efficient fatigue assessment of large-diameter monopile wind turbines. *Marine Structures*, **77**, 102939

P3 **Stian H. Sørum**, Jan-Tore H. Horn, Jørgen Amdahl (2017). Comparison of numerical response predictions for a bottom-fixed offshore wind turbine. *Energy Procedia*, **137**, 89-99

P4 **Stian H. Sørum**, Jørgen R. Krokstad, Jørgen Amdahl (2019). Wind-wave directional effects on fatigue of bottom-fixed offshore wind turbine. *Journal of Physics: Conference Series*, **1356**, 012011

P5 **Stian H. Sørum**, Erin E. Bachynski-Polić, Jørgen Amdahl (2022). Wind and soil model influences on the uncertainty in fatigue of monopile supported wind turbines. *Journal of Physics: Conference Series*, **2362**, 012038.

The contribution from each author towards **P1**-**P5** is outlined in Table 1.1.

Contributions to the following publications have also been made in the course of the thesis, but are excluded due to scope or limited contribution:

Stian H. Sørum, Emil Smilden, Jørgen Amdahl, Asgeir J. Sørensen (2018). Active load mitigation to counter the fatigue damage contributions from unavailability in offshore wind turbines. *ASME 2018 37th International Conference on Ocean, Offshore and Arctic Engineering*, V010T09A061, ASME

Emil Smilden, **Stian H. Sørum**, Erin E. Bachynski, Asgeir J. Sørensen, Jørgen Amdahl (2020). Post-installation adaptation of offshore wind turbine controls. *Wind Energy* **23** (4) 967-985

Wojciech Popko, Amy Robertson, Jason Jonkman, Fabian Wendt, Philipp Thomas ... **Stian H. Sørum** ... Robert Harries (2021). Validation of numerical models of the offshore wind turbine from the Alpha Ventus wind farm against full-scale measurements within OC5 Phase III. *Journal of Offshore Mechanics and Arctic Engineering* **143**(1) 012002

Wojciech Popko, Matthias L. Huhn, Amy Robertson, Jason Jonkman, Fabian Wendt ... Erin E. Bachynski, **Stian H. Sørum** ... Jifeng Cai (2018). Verification of a numerical model of the offshore wind turbine from the Alpha Ventus wind farm within OC5 Phase III. *ASME 2018 37th International Conference on Ocean, Offshore and Arctic Engineering*, V010T09A056, ASME

Wojciech Popko, Amy Robertson, Jason Jonkman, Fabian Wendt, Philipp Thomas ... **Stian H. Sørum** ... Robert Harries (2019). Validation of numerical models of the offshore wind turbine from the Alpha Ventus wind farm against full-scale measurements within OC5 Phase III. *ASME 2019*

38th International Conference on Ocean, Offshore and Arctic Engineering, V010T09A065, ASME

Table 1.1: Author contributions, following the definition from Allen et al. (2019). The author initials are capitalized where the author has had a leading role towards the contribution, and lower case where the author has made a contribution.

	P1	P2	P3	P4	P5
Co	SHS,gk,ebp	GK,shs	SHS,jth	SHS,jrk	SHS
Me	SHS,gk,ebp	GK,SHS	SHS,jth	SHS,jrk	SHS,ebp
So	GK,shs	GK,shs	SHS,JTH	SHS	SHS
Va	SHS	GK,shs	SHS,jth	SHS	SHS
FoA	SHS,GK,amp,rtk	GK,SHS	SHS,jth	SHS	SHS
In	SHS,gk,ebp,ja	GK,SHS	SHS,jth	SHS,jrk	SHS
DC	SHS,gk	GK	shs,JTH	SHS	SHS
W-od	SHS,gk	GK,shs	SHS	SHS	SHS
W-re	SHS,*all*	GK,*all*	SHS,*all*	SHS,*all*	SHS,*all*
Vi	SHS,gk	GK,shs	SHS,jth	SHS	SHS
Su	EBP,JA	EBP,JA	JA	JRK,JA	EBP,JA
PA	SHS	GK	SHS	SHS	SHS
FuA	EBP,JA,AMP	EBP,JA	JA	JA	JA

Contribution abbreviations: **Co**: Conceptualization, **Me**: Methodology, **So**: Software, **Va**: Validation, **FoA**: Formal analysis, **In**: Investigation, **DC**: Data curation, **W-od**: Writing (original draft), **W-re**: Writing (review & editing), **Vi**: Visualization, **Su**: Supervision, **PA**: Project administration, **FuA**: Funding acquisition.
Author abbreviations: **SHS**: Stian Høegh Sørum, **GK**: George Katsikogiannis, **EBP**: Erin Bachynski-Polić, **JA**: Jørgen Amdahl, **JRK**: Jørgen Ranum Krokstad, **AMP**: Ana M. Page, **RTK**: Rasmus T. Klinkvort, **JTH**: Jan-Tore Horn.

1.5   Outline of Thesis

The thesis is organised into two parts, with the following content:

Part I

Part I introduces the motivation for the thesis work in Chapter 1, before Chapter 2 describes the operation and design of monopile OWTs, including the uncertain parameters and models considered in this work. The individual contributions are presented in Chapter 3, where the link between the publications and contributions is also presented. Finally, Part I is concluded and recommendations for further work are given in Chapter 4.

Part II

Part II contains papers **P1**-**P5**, presented in the same order as in Section 1.4.

Chapter 2

Design and Analysis of Offshore Wind Turbines

The design of a wind turbine support structure must also consider the other components and the operational modes of the turbine. This chapter will briefly introduce the components and operation of the OWT, as well as the design considerations, before the external conditions relevant for the design and the models used in the FLS analysis are presented.

The major components of a monopile-supported OWT are illustrated in Figure 2.1. Electrical power is produced in the RNA. The rotor consists of the blades, which transform the wind velocity into rotation of the rotor. At the root, the blades are connected to the hub. Pitching of the blades is performed by the use of the blade-pitch actuators in the hub. The rotation of the rotor is transferred via the shaft to the generator inside the nacelle, where the electrical power is produced. The RNA is kept in place by the support structure, here consisting of the tower, the transition piece, and the monopile. The support structure transfers the environmental loads to the soil, which provides the resistance that keeps the turbine in place. If scouring is likely to erode the top layer of soil, a scour protection may be installed at seafloor.

The lifetime of the support structure consists of several phases, such as production, transportation, installation, operation and decommissioning. The focus in this work is placed on the operation phase. This phase consists of the operational and non-operational conditions, where the turbine in the latter may be parked or idling due to non-operational wind speeds, faults or planned maintenance. Switching between operational and non-operational conditions introduces transient loads, but these are not considered here.

The operational regimes of a wind turbine are typically separated in four regions (Aho et al., 2012), as illustrated in Figure 2.2. Region 1 is wind speeds below cut-in, where the available power is so low that the generator is not engaged and the turbine is not producing any power. Region 2 is below rated wind speed, but above cut-in. Here, the primary aim of the controller is to maximize the power output. This is done by varying the generator torque to give the optimal tip-speed ratio. Above rated wind speed (region 3), the turbine is producing at rated capacity. The
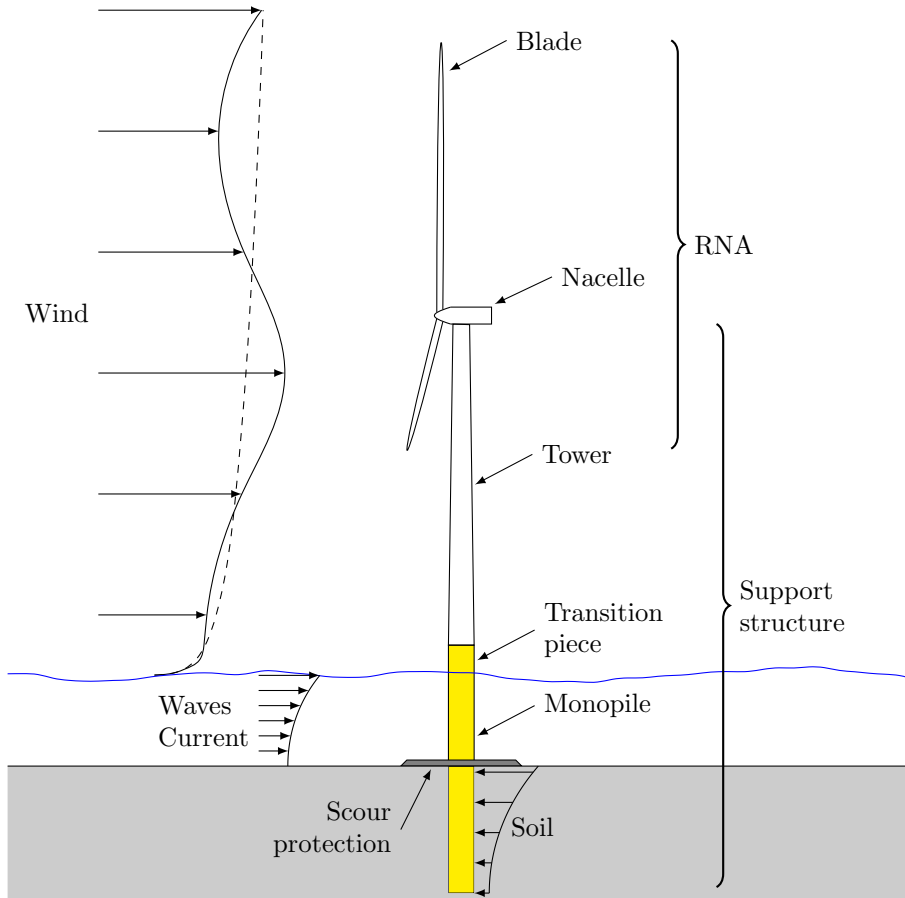
Figure 2.1: Components of the monopile OWT and external loads acting on the turbine.

aim of the controller is then to limit the power production and structural loads. The rotor speed is controlled to the rated rotor speed by pitching the blades, limiting the aerodynamic power. A constant power output, as most commonly desired for bottom-fixed turbines, is achieved by varying the generator torque with the fluctuations in the rotor and generator speed. As the wind speed increases above cut-out (region 4), the turbine is shut down.

In this thesis, the non-operational turbine is only included as the idling turbine at operational wind speeds, neglecting wind speeds below cut-in and above cut-out. Although the reason the turbine is non-operational may be e.g. failure of one of the blade-pitch actuators, it has been assumed that the blades for the parked turbine are pitched to feather in all cases. While the aerodynamic loads
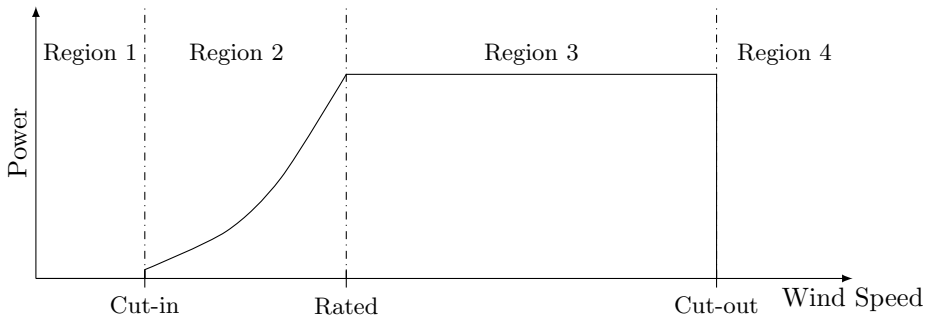
Figure 2.2: Operational regions of the wind turbine, together with the produced power.

are greatly reduced for the non-operational turbine, the aerodynamic damping is also significantly lower. This leaves the turbine more prone to resonant response to wave loads close to the natural frequency of the support structure. While the parked turbine in operational conditions only accounts for a small amount of the time - 10% is assumed in the design standards (DNV, 2021c) - this may contribute significantly to the total fatigue damage.

2.1   Design Considerations

There are several properties and possible failure modes that must be considered when designing the support structure, outlined for a monopile foundation by Arany et al. (2017). The main design parameters of the monopile are the pile diameter, wall thickness and length. For the tower, the length is governed by the hub height and the main design parameters are the diameter wall thickness, which typically reduces with height. Individually produced sections of the tower are bolted together, but the detailed design of the flanges and bolt are not considered here. All dimensions must be selected so that the limit state requirements are fulfilled. From an extreme response perspective, failure may occur through exceedance of the soil capacity, or by creation of a plastic hinge if the support structure fails first. The stability of the support structure must also be checked, as both local and global buckling may occur. In SLS, concerns are primarily on the tilt angle and acceleration of the nacelle. The former is mainly governed by the deformations at seafloor, while excitation of the natural frequencies also influences the accelerations.

While the structural dimensions govern the fatigue damage to given load cycles, the natural frequencies change the dynamic amplification of the loads. This is important when considering the FLS capacity. Multiple frequencies contribute to the loading of monopile OWTs, including wave loads, aerodynamic loads at the rotational frequency (1P loads) and at the blade passing frequency (3P loads). The low-frequent loads from the wind speed fluctuations are typically of less concern when designing the natural frequency of monopiles. Care must be taken to avoid resonance of the 1$^{\text{st}}$ structural modes of the support structure with any of these

loads. For monopiles, the most common is a "soft-stiff" design, where the 1st natural frequency is placed between the 1P and 3P frequencies.

More practical considerations also apply. The monopile dimensions must be such that pile driving is possible at the location of each turbine. Production limitations, such as maximum wall thickness for welding and rolling of steel, must also be considered.

2.1.1 Fatigue Damage Estimation

The focus in this thesis is on the fatigue limit state, where the tower and monopile accumulate damage from stress cycles. By using e.g. the rainflow counting method, the stress cycles in a time-domain simulation can be identified. From these, the short-term fatigue damage can be calculated using the Miner sum approach:

$$D_{ST} = \sum_{i=1}^{n_\sigma} \frac{(\Delta\sigma_i)^{m_i}}{a_i} \left(\frac{t}{t_{ref}}\right)^{km_i}. \qquad (2.1)$$

Here, $\Delta\sigma_i$ is the range of stress cycle i, and n_σ is the number of stress cycles identified. a_i, m_i and k are material factors, namely the intercept with the $\log(N)$-axis, slope of the SN-curve, and the thickness correction exponent. t is the wall thickness and t_{ref} is the reference wall thickness of the SN-curve (DNV, 2021b).

The lifetime fatigue damage can then be found as

$$D_{LT} = \frac{T_{LT}}{T_{ST}} \sum_{j=1}^{n_{ST}} P_j D_{ST,j} \qquad (2.2)$$

with T_{LT} being the design lifetime of the structure and T_{ST} the duration of each short-term analysis. P_j is the probability of occurrence for load case j, described by e.g. Equation (2.3) or Equation (2.4). Fatigue failure is commonly assumed to occur for $D_{LT} = 1$, but variations in the material capacity, Δ_C, may be included by assuming full utilization is reached when $D_{LT} = \Delta_C$ (Wirsching, 1984). Design rules (DNV, 2021b) do not explicitly include the uncertainty of the fatigue capacity in the design requirements, but apply a safety factor on the calculated D_{LT}.

2.2 External Conditions

The external conditions considered in this thesis are the long-term distributions of the environmental parameters, as well as the soil conditions at the site. The influence these parameters have on the design is investigated in contributions **C1** and **C3**.

2.2.1 Environmental Conditions

Multiple environmental loads act on an OWT. These include aerodynamic loads, hydrodynamic loads from waves and ocean current, and possibly ice loads. Local environmental conditions, such as wind speed and wave elevation, govern these loads, together with the design of the wind turbine and support structure. Description of

the environmental conditions is typically split into two parts: The long-term and short-term variations. Short-term variations are modelled for a time period where the wind and wave processes can be assumed to be stationary. The short-term period is assumed to be one hour in this thesis, although periods as short as 10 minutes are often applied for wind-only scenarios. For waves, a 3-hour period is often assumed.

The long-term environmental model describes the joint probability of occurrence for the parameters describing the long-term variability of the environmental conditions. In principle, this is a joint distribution of all environmental parameters:

$$P(\bar{U}, \theta_{wi}, H_{s,wi}, T_{p,wi}, \theta_{wa,wi}, H_{s,sw}, T_{p,sw}, \theta_{wa,sw}) \tag{2.3}$$

Here, $\bar{U}$ is the mean wind speed and θ_{wi} is the mean wind direction. θ_{wa} is the mean wave direction, H_s is the significant wave height and T_p is the wave peak period. For the wave parameters, subscript wi denotes wind-driven waves and subscript sw refers to swell waves. In this thesis, the environmental model has been simplified based on the work by Horn et al. (2017). Mean wind speed and wind direction have been assumed independent of the other parameters. The wave direction is implicitly modelled by the wind-wave misalignment angle, $\theta_{rel} = \theta_{wi} - \theta_{wa}$. Wave parameters (H_s, T_p) are assumed conditional on wind velocity and wind-wave misalignment. A total sea approach is taken, modelling the wind-driven and swell waves as one wave system. This gives the long-term distribution as

$$P(\bar{U}, \theta_{wi}, H_s, T_p, \theta_{wa}) \approx P(\bar{U}) \cdot P(\theta_{wi}) \cdot P(\theta_{rel}|\bar{U}) \cdot P(H_s, T_p|\bar{U}, \theta rel). \tag{2.4}$$

In practice, $P(H_s, T_p|\bar{U}, \theta rel)$ has been replaced by an equivalent sea state. Paper **P3** uses the most probable sea state in each wind bin, while paper **P4** uses the lumping method developed by Kühn (2001). Paper **P2** further develops the lumping method from Passon (2015), and the new method is applied in paper **P1** and paper **P5**.

2.2.2 Wind Conditions

Several components make up the description of the short-term wind speed fluctuations, as indicated in Figure 2.1. In the mean wind direction, the wind speed may be written as

$$U(x, y, z, t) = \bar{U}(z) + u(z, y, z, t) \tag{2.5}$$

with $U(x, y, z, t)$ being the instantaneous wind speed at a location in space at time t, while $\bar{U}(z)$ is the mean wind speed at height z and $u(x, y, z, t)$ is the turbulent wind component (Burton et al., 2011). In the transverse and vertical direction, the wind field is typically modelled as turbulent fluctuations around a zero mean wind speed.

The mean wind speed varies with the height over the sea surface, typically described by the power law formulation:

$$\bar{U}(z) = U_{ref} \left(\frac{z}{z_{ref}} \right)^{\alpha}. \tag{2.6}$$

U_{ref} is the reference wind speed given at the reference height z_{ref}. The power law exponent, α, depends on the surface roughness, and may vary with the wave conditions (Donelan et al., 1993).

The magnitude of the fluctuations in the wind speed in the mean wind direction is described by the turbulence intensity (TI). This is defined as

$$TI = \frac{\sigma_u}{\overline{U}}, \tag{2.7}$$

where σ_u is the standard deviation of the fluctuating component (Burton et al., 2011). More details on the modelling of the short-term wind conditions are given in Section 2.4.2.

2.2.3 Soil conditions

The soil composition is important for the stability and stiffness of a monopile. For the purpose of this thesis, the description of the soil is closely related to the numerical models (Section 2.4.5). Several soil models can be applied in the analysis of monopiles. This thesis has used p-y curves based on ISO 19901-4 (ISO, 2016), p-y curves based on finite-element simulations of the SSI, and a macro-element formulation.

In order to calculate the spring stiffness of the p-y curves as described by ISO 19901-4, the designer must know the undrained shear strength and unit weight of the soil for clay soil. For sand, the effective angle of internal friction must be known, in addition to the unit weight.

For the macro-element, the soil model is described by the shear stress-shear strain curve normalized with the ratio between the maximum shear modulus and undrained shear strength. The maximum undrained strength is also a required input parameter (Page et al., 2019). Calibration of the macro-element is described in Section 2.4.5.

2.3 Production and Operational Parameters

In addition to the uncertainty of the conditions at the site, there are also uncertainties caused by the production and operation of the turbine. The parameters discussed in the following sections have been considered in contribution **C1**.

2.3.1 Pile Diameter

Due to production tolerances, the actual diameter of the pile may vary from the specified diameter (Zaaijer, 2006). This may be due to both ovalization of the pile and deviations in the mean diameter. Only the latter has been considered here.

2.3.2 Availability

During the lifetime of a turbine, there will be periods where the turbine is not available for power production despite the environmental conditions being favourable. This can be due to both planned stops for maintenance and unforeseen events

forcing the turbine to be shut down. As the majority of the damping of monopile supported wind turbines come from the aerodynamic damping, resonant responses from the low-damped, non-operational condition contribute significantly to the fatigue damage.

2.3.3 Marine Growth and Drag Coefficient

As the foundation is placed in the ocean, marine organisms will start growing on it. The growth will influence both the diameter and weight of the monopile, and the type and thickness of growth depends on the water depth and location of the turbine (Wolfram and Theophanatos, 1985). Further, uneven marine growth will change the surface roughness of the monopile, changing the drag coefficient used in the load calculations described in Section 2.4.3 (Jusoh and Wolfram, 1996).

2.4 Modelling

Engineering models are applied for calculating the response of the wind turbine when subjected to the external, production and operation parameters described in Sections 2.2 and 2.3. The effects of these models are evaluated in contribution **C2**, and an overview of the different models used in this thesis is provided in the following.

2.4.1 Wave Spectrum

The wave climate is described by the long-term distribution of H_s and T_p, and the short-term wave conditions are described by a wave spectrum, $S_{\zeta\zeta}(\omega)$. This describes how the total energy of the waves is distributed across the different frequencies. If the wave spectrum is discretized into N components, the amplitude of each wave component, $\zeta_{a,i}$, can be found as

$$\zeta_{a,i} = \sqrt{2S_{\zeta\zeta}(\omega_i)\Delta\omega_i}. \tag{2.8}$$

Here, ω_i is the mean angular frequency of each wave component, while $\Delta\omega_i$ is width of the frequency range that contributes to component i.

According to linear wave theory, the elevation of long-crested waves is described by

$$\zeta(x,y,t) = \sum_{i=1}^{N} \zeta_{a,i} \cos(\omega_i t + k_i(\cos(\theta_{wa})x + \sin(\theta_{wa})y) + \epsilon_i). \tag{2.9}$$

The summation is conducted for the N components of the wave spectrum, with k_i being the wave number. The relationship between ω_i and k_i is given by the dispersion relation (Faltinsen, 1990). The wave realization is made stochastic by drawing a random number for the phase, ϵ_i, from a uniform distribution between 0 and 2π.

While the wave spectrum can be found from measurements of the wave elevation at a site, parameterized spectra are available for the design. The most common ones are the Pierson-Moskowitz spectrum for fully developed seas and the

JONSWAP spectrum for fetch-limited seas. Alternative wave spectra include the TMA spectrum (an adaption of the JONSWAP spectrum to shallow water) and the Torsethaugen spectrum (a two-peaked spectrum including both wind-generated waves and swell). All the spectra contain the same wave energy (for the same H_s), but the frequency-distribution of the waves varies.

The above wave spectrum models all describe the waves as long-crested. A short-crested wave pattern may be described by different spectra over varying wave directions. This is typically modelled by multiplying the long-crested wave spectrum with a spreading function, $D(\omega, \theta; \theta_{wa})$. The total spectrum is then given as

$$S_{\zeta\zeta}(\omega, \theta; \theta_{wa}) = S_{\zeta\zeta}(\omega) D(\omega, \theta; \theta_{wa}). \tag{2.10}$$

Here, $S_{\zeta\zeta}(\omega, \theta; \theta_{wa})$ is the short-crested wave spectrum, with angular frequencies ω, wave component directions θ and mean wave direction θ_{wa}. $S_{\zeta\zeta}(\omega)$ is the long-crested wave spectrum. $D(\omega, \theta; \theta_{wa})$ can be modelled in several ways, but is typically taken as dependent on direction only (DNV, 2021a). The following formulation is adopted here:

$$D(\theta; \theta_{wa}) = \frac{\Gamma(1 + n/2)}{\sqrt{\pi}\Gamma(1/2 + n/2)} \cos^n(\theta - \theta_{wa}), \quad |\theta - \theta_{wa}| \leq \pi/2 \tag{2.11}$$

The spreading exponent, n, is assumed to be 2. To generate the wave time series, the summation in Equation (2.9) will then be a double summation over both frequencies and directions.

2.4.2 Wind Spectrum and Coherence

The time series of the wind speed at a point in space may be generated from a wind spectrum, e.g., the Kaimal wind spectrum. This represents the energy distribution of the wind fluctuations at each grid point in a wind field (Burton et al., 2011). Different spectra are applied for the three components of the wind. Correlation of the wind speed at two different spatial locations can be described by the coherence function, defined as

$$\gamma_{xy}(f) = \frac{S_{xy}(f)}{\sqrt{S_{xx}(f)S_{yy}(f)}} = C_{xy}(f) + iQ_{xy}(f). \tag{2.12}$$

γ_{xy} is the coherence between two points x and y, S_{xy} is the cross-spectrum of the wind speed at the two points, and S_{xx} and S_{yy} are the auto spectra. C_{xy} and Q_{xy} are the real and imaginary part of the coherence. In this work, an exponential coherence has been assumed (IEC, 2019), and the TurbSim turbulence generator was used to make the wind boxes. The coherence modelling can be performed for the longitudinal wind components only, or to all wind components.

Alternatively, the Mann uniform shear turbulence model may be used. Unlike the model described above, the Mann model does not use a spectral description and coherence function to generate the time series of the wind. Instead, the Mann model derives the turbulence time series directly from the velocity spectral tensor based on the distortion of isotropic turbulence under a vertical shear profile (Burton et al., 2011).

2.4.3 Wave Load Models

Wave loads on a cylindrical monopile structure are typically modelled as a drag term dependent on the wave particle velocity, and an inertia term dependent on the wave particle acceleration. For small-volume cylinders, the inertia term may be assumed independent of the wave frequency and Morison's equation is applied to calculate the load (Faltinsen, 1990). A frequency-dependent inertia term (MacCamy and Fuchs, 1954) should be applied to large-volume cylinders. For a vertical cylinder, both load models may be formulated as

$$dF = \frac{1}{2}\rho D C_d (u - \dot{x})|u - \dot{x}|dz + \rho A \left[1 + C_a^*(\omega)\right] \dot{u}dz - \rho A C_a^*(\omega)\ddot{x}dz \qquad (2.13)$$

Here, dF is the force on a cylinder strip with length dz, diameter D and cross-sectional area A. u is the horizontal wave particle velocity, while $\dot{u}$ is the corresponding acceleration. $\dot{x}$ and $\ddot{x}$ are the velocity and acceleration of the cylinder in the direction parallel to the flow. C_d is the drag coefficient, while $C_a^*(\omega)$ is the added mass coefficient. Using Morison's equation, $C_a^*(\omega) = C_a$ is constant, while it is frequency dependent when using MacCamy and Fuchs' load model. The difference between the two load models is illustrated in Figure 2.3, where the reduced inertia load at high frequencies when using MacCamy & Fuchs' load model is observed.
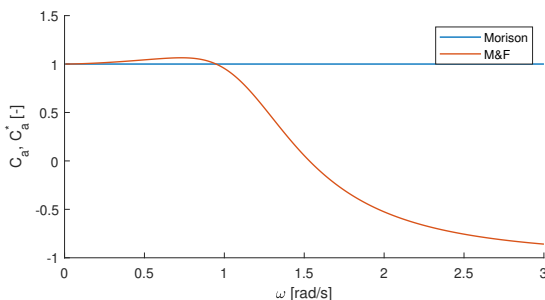
Figure 2.3: Added mass coefficient using Morisons equation (C_a) and MacCamy & Fuchs' load model (C_a^*) for a pile diameter of 11 m. A reduced load coefficient is seen for angular frequencies above ~1 rad/s.

2.4.4 Wind Load Models

The aerodynamic properties of the blades are described by the lift, drag and moment coefficients at discrete sections of the blades. From this, aerodynamic forces are calculated using the unsteady blade element momentum (BEM) theory (Burton et al., 2011; Hansen, 2008). As the aerodynamic loads on the blades will cause a reaction force on the wind, the aerodynamic forces on the blades will cause a change in the linear and angular momentum of the passing wind field. By equating the loads on the blades and the change in momentum of the air, the aerodynamic loads can be calculated taking the disturbance of the wind field into consideration.

However, the BEM method assumes that there is no interaction between blade elements at different radial positions of the blades and that the changes in momentum and loads are instantaneous. Further, the theory is not valid for highly loaded blades. To account for this, corrections must be applied. In the RIFLEX models, Prandtl tip-loss and Glauert induction corrections are applied, together with Øye's dynamic stall and wake corrections (SINTEF Ocean, 2017). For the other simulation programs used in this thesis, reference is made to paper **P3**.

2.4.5 Soil Models

Two soil models have been utilized in this thesis: the p-y curve approach (with two calibration methods, see 2.2.3) and the macro-element. The p-y-curve model uses non-linear elastic springs to distribute the resistance of the soil along the pile. The properties of the springs may be determined from design codes (ISO, 2016) or calibrated from numerical simulations of the SSI. Soil damping has been included by increasing the structural damping below seafloor to provide the desired total damping level.

The macro-element condenses the SSI to a force-displacement relationship at the seafloor. By using elasto-plastic theory, the macro-element is able to model the different loading and unloading paths, thereby including hysteretic soil damping. The macro-element accounts for multi-directional loading, which influences both the stiffness and hysteretic damping (Page et al., 2018, 2019). To calibrate the macro-element, the monopile response at the seafloor from two push-over analyses is needed: One where only horizontal shear force is applied and one where only bending moment is applied. The load-displacement-rotation and moment-displacement-rotation are then used as input to the macro-element. These analyses can, for example, be performed using a 3D finite element model with an appropriate soil model (Page et al., 2019). As the macro-element is connected to the structural model at seafloor, the response below the seafloor must be calculated after the simulations have been performed. This is done with the method developed by Klinkvort et al. (2022), using a beam model with springs calibrated to the finite element analysis.

2.4.6 Structural Model

Several methods may be applied for modelling the structure, including finite element models and modal models. This section describes the finite element approach adopted by RIFLEX. Reference is made to paper **P3** for the other programs used in the thesis. The blades, tower and monopile are all modelled as non-linear beam elements with linear-elastic material behaviour. Structural damping is accounted for by the use of stiffness-proportional Rayleigh damping. The damping coefficients of the blades are tuned to provide the predefined damping at the first mode of an individual blade. In the tower and monopile, the damping coefficient is tuned to provide the desired damping level at the first fore-aft global bending mode.

Chapter 3

Contributions

Chapter 3 will present the main scientific contributions of the thesis, using the contributions identified in Section 1.3. The links between the research question, each contribution and the individual papers are presented in Figure 3.1 (**C1**), Figure 3.5 (**C2**) and Figure 3.12 (**C3**).

3.1 Contribution 1

Identification of parameters responsible for the majority of the uncertainty in fatigue design of monopile offshore wind turbines
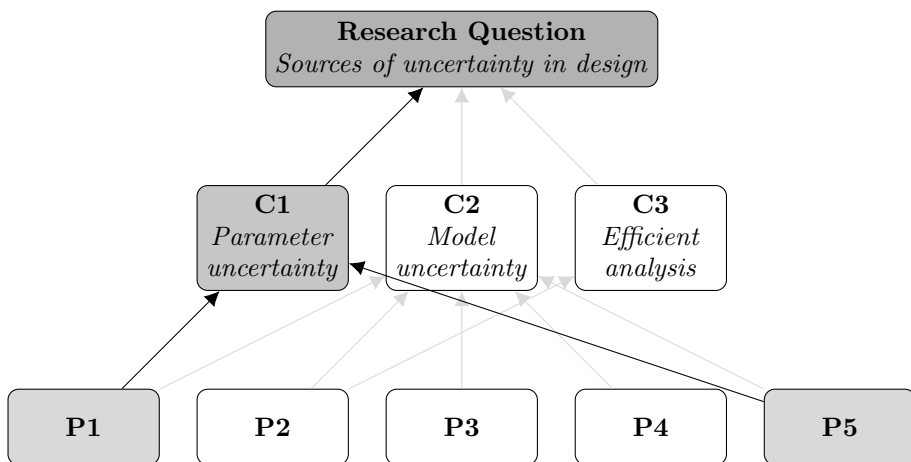
Figure 3.1: Link between research papers, contribution 1 and research question.

In principle, all parameters in a design basis are associated with uncertainty, leading to the total uncertainty of a specific design. However, typically only a small number of parameters contribute to the majority of the design uncertainty. Identifying these parameters can be challenging, as results for one design may not be valid

for other designs. Additionally, the lack of data for the probability distributions of the uncertain parameters introduces uncertainty in the validity of any performed sensitivity analysis. The multi-disciplinarity of offshore wind turbines poses challenges in finding suitable software and methods for analysing the complete range of input parameters.

The challenge of consistently identifying the most influential uncertainties is demonstrated in **P1**. Across six papers, 13 parameters were identified as contributing significantly to the fatigue design uncertainty with only two parameters found important by more than one paper.

Contribution **C1** seeks to identify the parameters from the design basis, production and operational parameters that contribute the most to the uncertainty in the fatigue damage calculated during the design process. This is evaluated in **P1** where the uncertainty in the fatigue damage of the monopile and tower is considered using input parameters from all relevant engineering disciplines. Partially based on the results from previous studies (Hübler et al., 2017; Peeringa and Bedon, 2017; Robertson et al., 2019; Teixeira et al., 2019; Toft et al., 2016b; Velarde et al., 2020), the 16 parameters listed in Table 3.1 were selected for a screening study. Three turbines (5, 10 and 15 MW) were included, to capture the effects of different turbine sizes. The long-term fatigue damage calculations were performed using the method developed in **P2**.

Table 3.1: Design parameters considered in **P1**.

Parameter	Symbol
Wind speed	U
Wind direction	θ_{wi}
Turbulence intensity	TI
Wind shear	α
Yaw error	γ_Y
Significant wave height	H_s
Wave peak period	T_p
Wind-wave misalignment	θ_{rel}
Marine growth	t_{mg}
Drag coefficient	C_d
Undrained shear strength	s_u/σ'_{v0}
Void ratio	e
Monopile diameter	D_p
SN parameters	$\log(a_1, a_2)$
Fatigue capacity	Δ_C
Turbine availability	A

The results of the screening study are expressed in terms of the statistics of the elementary effect (EE) (Saltelli et al., 2008), defined as

$$EE_i = \frac{D_{LT}(X_1, ..., X_i \pm \Delta_i, ..., X_l) - D_{LT}(X_1, ..., X_i, ..., X_l)}{\pm \Delta_F}. \quad (3.1)$$

Here, EE_i is the elementary effect when varying the numerical value of input parameter i, with $X_1, ..., X_i, ..., X_l$ being the l input parameters considered. D_{LT} is the long-term fatigue damage, and Δ_i and Δ_F are the variations of the parameters in physical and probability space, respectively. 30 realizations of the EE were calculated for each parameter, and a large mean EE indicates a parameter with a large influence on the total uncertainty in the design. Figure 3.2 illustrates the typical screening results for the support structure. All across the monopile and tower, on all three turbines, the uncertainty in the SN curve and fatigue capacity cause the majority of the design uncertainty.
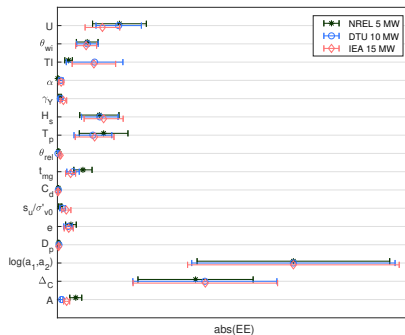
Figure 3.2: Elementary effects (EE) of considered design parameters at seafloor. A high value indicates a parameter important for the total uncertainty in the design calculations. The mean value is given by the markers and the standard deviation given by the bars. Reproduced from **P1**, with symbols defined in Table 3.1.

From the perspective of a designer seeking to reduce the uncertainty in a design, this knowledge may be of limited use. The probability distributions used to describe the uncertainties of the fatigue parameters were used already in 1984 (Wirsching, 1984) and are unlikely to be modified. With this in mind, it is also interesting to consider the uncertainty when the fatigue parameters are disregarded. **P1** shows which of the parameters a designer should focus on in order to reduce the uncertainty in a design, and how different parameters are important in different parts of the support structure - from the tower top to the monopile below seafloor.

In general, the uncertainties of the environmental parameters are the largest contributors to the uncertainty of the lifetime fatigue damage. Reducing the uncertainty in these parameters is then considered the most efficient method to reduce the total uncertainty in a design. This holds true for the case where one year of environmental data is utilized in the design, as required by the design standards (IEC, 2019). The uncertainty in the environmental parameters may easily be reduced by using longer time series - by ∼30% if two years of measurements are used and ∼55% if five years of data is available.

More details about the importance of the parameters are provided in Figure 3.3, which shows the elementary effects at the tower top (Figure 3.3(a)) and approximately 5 m below seafloor, where the fatigue damage in the monopile is highest

(Figure 3.3(b)). Results at intermediate locations can be found in **P1**, but are in general a combination of the tower top and monopile results. In the tower top, the design uncertainty is dominated by the uncertainty in the turbulence intensity, wind speed and wind direction.

(a) Tower top. (b) Monopile maximum fatigue utilization.
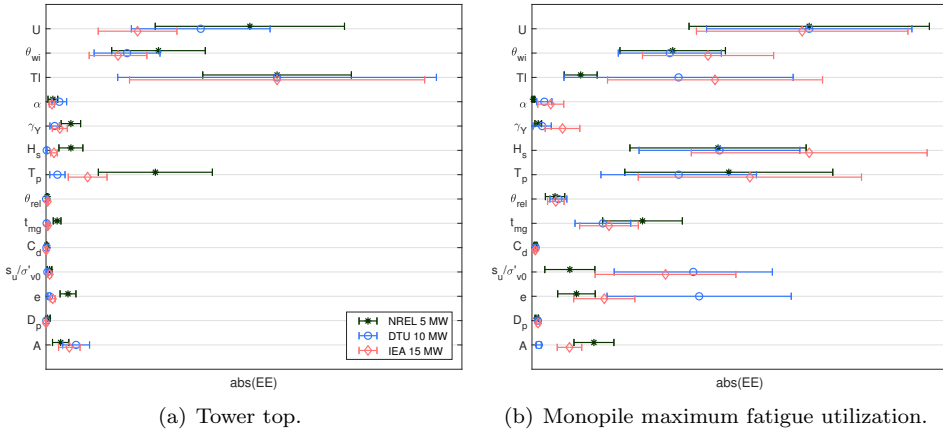
Figure 3.3: Elementary effects (EE) when excluding the fatigue parameters. A high value indicates a parameter important for the total uncertainty in the design calculations. The mean value is given by the markers and the standard deviation given by the bars. Reproduced from **P1**, with symbols defined in Table 3.1.

Wave loads become increasingly important at locations lower in the support structure, here illustrated by the location of the monopile with the highest fatigue damage. With the applied formulation for the distribution of the environmental parameters, the conditioning of significant wave height (H_s) and wave peak period (T_p) on wind speed (U) makes the wind speed distribution a measure of the overall severity of the environmental conditions. The uncertainty in H_s and T_p represent the uncertainty in the equivalent sea state within a wind bin. The high elementary effect of both U, H_s, and T_p in the monopile indicates that H_s and T_p are important for the overall uncertainty in the fatigue calculations. From the seafloor and down, the soil parameters have an increased influence on the uncertainty of the fatigue damage predictions.

When the turbine size is changed, one clear trend is seen. Turbulence intensity becomes increasingly important for the overall uncertainty as the turbine size increases, seen as the increased EE in Figure 3.3. This is due to wind loads increasing in importance compared to wave loads for larger turbines, increasing the influence of parameters related to the wind conditions. With even larger turbines being designed, the uncertainty in the turbulence intensity can be expected to contribute to an even larger portion of the design uncertainty in future turbines.

The work presented in **P1** neglects the effects of model choices (see contribution **C2**) have on the results. However, it is not given that the results in **P1** would be the same if other engineering models were used. **P5** investigates the validity of results from **P1** when different soil and wind coherence models are used. When varying

the soil model, the fatigue damage predicted by the macro-element increases faster with undrained shear strength than if p-y curves are used. This is illustrated in Figure 3.4, where a lower ratio $(D_{py} - D_{macro})/D_{macro}$ corresponds to a higher fatigue prediction using the macro-element model. The consequence of a non-zero slope of this relationship is that the sensitivities calculated in **P1** are dependent on the model choice. As a result, the uncertainty in the undrained shear strength will show different influence on the total uncertainty based on the soil model used. For the remaining parameters investigated in **P1** and the variations in the wind coherence models, there was no evidence of the modelling choices influencing the calculated design sensitivities.
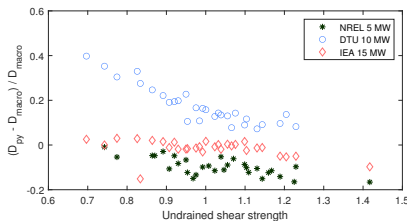
Figure 3.4: Normalized difference in fatigue damage versus normalized undrained shear strength. As the undrained shear strength increases, the macro-element model (D_{macro}) tends to predict a higher fatigue damage compared to the p-y-curve model (D_{py}). Reproduced from **P5**.

3.2 Contribution 2

Evaluation of uncertainty introduced by the modelling of monopile offshore wind turbines

While contribution **C1** deals with the uncertainty in a design introduced by limited knowledge about the site, production and operational parameters, a different type of uncertainty is introduced when considering the engineering tools and models utilized to perform design calculations. These uncertainties are evaluated in contribution **C2**, where papers **P1** through **P5** (Figure 3.5) investigate the influence of choosing different engineering models and software in the fatigue analysis. The model variations used are given in Table 3.2, while a summary of the influences are provided in Table 3.3. Here, the upper bounds of the observed changes in fatigue damage are listed. With the exception of software influence, the figures in the table are normalized using the baseline models in **P1** as the reference. As the results from the articles are case-dependent and only indicative of the uncertainty level, the results in the table are discretized into levels of $<10\%$, $<25\%$, $<50\%$, $<75\%$ and $<100\%$. The sensitivities are calculated as

$$Model\ uncertainty = \frac{|D_{baseline\ model} - D_{alternative\ model}|}{D_{baseline\ model}} \quad (3.2)$$

The largest model uncertainty is associated with modelling the waves as short-crested or long-crested ("wave spreading"). Significant uncertainties are also intro-
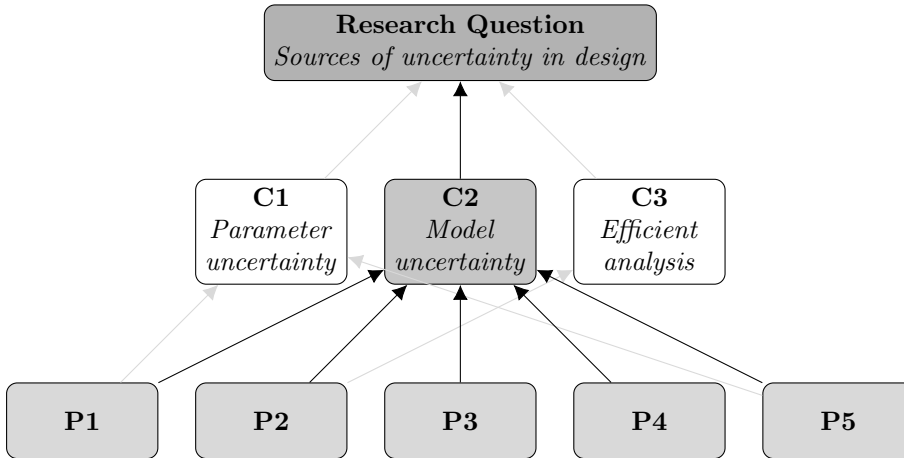
Figure 3.5: Link between research papers, contribution 2 and research question.

duced by the wind coherence modelling and by the software used in the analysis. The smallest uncertainty is introduced by replacing a full fatigue analysis by the lumping method presented in contribution **C3** and by alternative wave spectra formulations. The following sections will summarize the effects of selected model variations.

Table 3.2: Model variations considered.

Parameter	Baseline	Variations	
Wind coherence	Exponential in x	Exponential in x,y,z	Mann model
Wave spreading	Long-crested	Short-crested	
Wave spectrum	PM/JONSWAP	TMA	Torsethaugen
Wave lumping	Full scatter diagram	Lumped load cases	
Soil model	Macro-element	$p - y$ curves	
Scour protection	No	Yes	
Software[a]	SIMO-RIFLEX	FAST	vpOne

[a] Mean of all three programs is used as baseline value for calculating effect of model variations

3.2.1 Wave Spreading

The difference between modelling waves as long or short-crested is investigated in **P4**. For three different soil stiffness models, the tower design of the DTU 10 MW turbine is varied to achieve a target natural period of 4.8 seconds for the first fore-aft mode. This modifies the mode shape of the support structure to be more sensitive to wave loads (soft soil, stiff tower) or wind loads (stiff soil, soft tower). The stiff soil model shows little sensitivity to the wave modelling. On the other hand, the

Table 3.3: Upper bounds on model uncertainty. The difference in calculated lifetime fatigue damage between an alternative model and the reference model is shown. As all studies are specific case studies, the figures must be considered indicative. The values are discretized into levels of $<10\%$, $<25\%$, $<50\%$, $< 75\%$ and $<100\%$.

Parameter	Tower	Monopile	Papers
Wind coherence	$<75\%$	$<25\%$	P1, P5
Wave spreading	$<100\%$	$<100\%$	P1, P4
Wave spectrum	$<50\%$	$<25\%$	P1
Wave lumping	$<10\%$	$<10\%$	P2
Soil model	$<50\%$	$<50\%$	P1, P5
Scour protection	$<50\%$	$<50\%$	P1
Software[a]	-	$<75\%$	P3

[a] Calculated value depends heavily on the normalization

baseline model observes an increase of 60% for the maximum fatigue damage in the tower when short-crested waves are assumed, while the fatigue damage in the monopile increases by $\sim$85% with soft soil.

While the foundations were varied to accommodate the same turbine in **P4**, the NREL 5 MW, DTU 10 MW and IEA 15 MW turbines were considered in **P1**. The largest sensitivity to the wave spreading model was observed for the 5 MW turbine, and the lowest sensitivity observed for the 15 MW turbine. This is a consequence of the wave loads being more dominant for the smaller turbines, increasing the sensitivity to the wave modelling. Further, the sensitivities observed in **P1** are lower than those in **P4**, with the wave spreading model increasing the lifetime fatigue damage by no more than 35%. This is due to the lower natural frequencies of the 5 MW and 10 MW turbines in **P1** and the lower sensitivity to wave loads for the 15 MW turbine.

Based on the combined results from **P1** and **P4** it follows that modelling the waves as long-crested will be non-conservative in most cases. The extent of non-conservatism is dependent on how sensitive the design is to wave loads. The sensitivity depends on the support structure natural period relative to the wave period, the mode shape of the foundation, and the amplitude of the wave load effects and wind load effects.

3.2.2 Wind Coherence

Several wind coherence models are available for analysis of OWTs. The Kaimal turbulence model with exponential coherence and the Mann uniform shear model are recommended by design standards (IEC, 2019). **P1** demonstrates how the coherence model plays a major role in the model uncertainty at the tower top. The predicted fatigue damage differs up to 60% between the Mann model and the Kaimal model. At locations lower in the support structure, the difference is smaller; up to 25% in the tower base and 15% in the monopile at or below seafloor.

In **P1** there is no apparent logic regarding which of the turbines appears more sensitive to the changes in wind coherence models. **P5** demonstrates two differences

in the response to the Kaimal and Mann models. These have opposite effect on the fatigue damage. At low frequencies ($<\sim 0.1$ Hz) the spatial coherence of the Kaimal model is higher, shown in Figure 3.6(a). This results in higher thrust variations and higher fatigue damage contributions at low frequencies (Figure 3.6(b)). This is in line with the findings of Nybø et al. (2020), who investigated the low-frequency response of monopiles under different coherence models. At higher frequencies, the spatial coherence of the exponential coherence model is smaller, with a smaller influence on the results. Here, the Mann model predicts higher thrust variations and thereby larger fatigue damage. This is particularly true for responses at the blade passing frequencies. In total, this means that the relative importance of the low-frequency and high-frequency aerodynamic loads governs which wind model yields the highest fatigue damage. Finally, the location of the support structure's natural frequency also influences whether the Kaimal or Mann model yields the highest fatigue damage. For a low natural frequency, the low-frequency response is amplified which increases the tendency of highest fatigue damage estimations from the Kaimal model. Similarly, a high natural frequency increases the tendency of a higher estimation from the Mann model.

At the tower top, the difference at the higher frequencies is most dominant, which in general gives higher fatigue damage predictions when using the Mann model. Lower in the support structure, the low-frequency response becomes more dominant, with the Kaimal model yielding the highest fatigue damage estimate. **P5** also demonstrates how the fatigue damage predictions provided by the Mann model increase faster for high wind speed, increasing the predicted importance of high wind speeds.
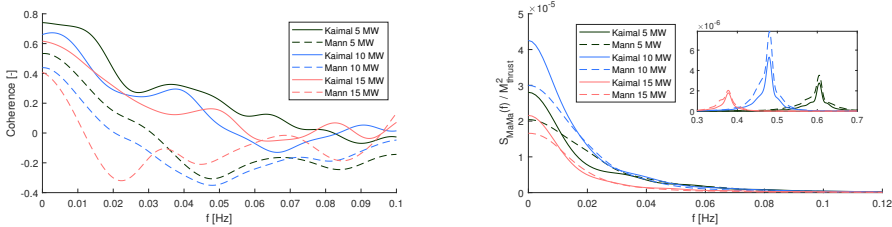
(a) Wind speed coherence at hub and outer rotor disk at hub height.

(b) Thrust force spectrum for the rotors, with the position of the nacelle fixed.

Figure 3.6: Coherence and rotor thrust force using the Kaimal and Mann models. The Kaimal model shows a higher coherence at low frequencies, which gives larger fluctuations in rotor thrust force. At higher frequencies, the Mann model yields the highest variations in thrust force. Reproduced from **P5**.

3.2.3 Software

Fatigue analysis of OWTs is typically performed using a designated software, but different software packages utilize different methods and have different capabilities. This will result in different response predictions. The fatigue damage estimates at

seafloor from three different software packages are compared in **P3** using the DTU 10 MW turbine. Simplified load cases demonstrate how the blade structural models and the definition of the aerodynamic properties yield different aerodynamic forces. While this influences the loads at all wind speeds, the differences are most significant at wind speeds close to rated. It has later been shown that in particular the blade torsional stiffness model is important for the aerodynamic load predictions (Rinker et al., 2020).

The difference in turbine operation and aerodynamic force is shown in Figure 3.7(a) for the three programs used in **P3**: SIMA (RIFLEX), vpOne and FAST. Due to the increased rotor speed at low wind speeds, the controller in SIMA initiates the blade pitching at lower wind speeds. This reduces the thrust force, and thereby the fatigue damage compared to FAST. At higher wind speeds, the fatigue damage per hour of these two programs converges to similar values, as shown in Figure 3.7(b). For vpOne, the difference compared to the other programs is more consistent, with a lower fatigue damage predicted at all wind speeds.
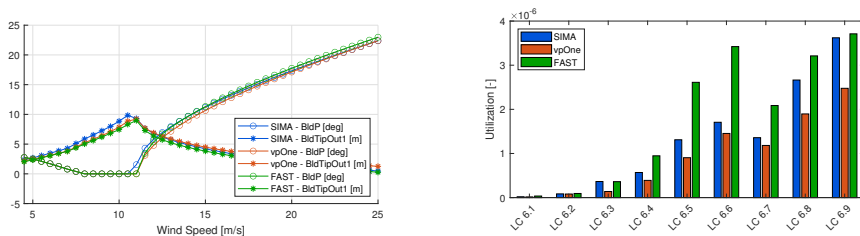
(a) Steady-state blade pitch and blade tip deflection in uniform wind.

(b) 1-hour fatigue damage at seafloor. Higher LC corresponds to higher wind speed.

Figure 3.7: Comparison of steady-state turbine performance and 1-hour fatigue damage in SIMA, vpOne and FAST. Reproduced from **P3**.

This study also demonstrates the importance of the coupling between the aerodynamic loads and the control system for OWTs. While the difference between the two programs SIMA and FAST is small for a majority of the wind speeds considered, the effect is significant due to the influence of the control system and the switching between below and above rated operations. This demonstrates the importance of the analyst having a holistic approach to the modeling and model verification, and how small differences in various parts of the model may accumulate to large differences in the lifetime fatigue estimates.

3.2.4 Soil Model

Differences up to 50% in the fatigue damage predictions with the p-y-curve soil model and macro-element model were observed in **P1**. **P5** shows how both the macro-element and the p-y-curve models may predict the highest fatigue damage, depending on model calibration. This is illustrated in Figure 3.8, where the p-y-curve model predicts the highest lifetime fatigue damage for the 10 MW turbine, while the macro-element yields the highest damage for the 5 MW and 15

MW turbines. It is the calibration of the two models that determines whether the macro-element or p-y curves predicts the highest fatigue damage. This is shown in Figure 3.9, where the two models predict the same natural frequency for small response amplitudes for the 5 MW turbine. For the 10 MW turbine the natural frequency is similar for response amplitudes of ∼70% of the rated moment. The 15 MW turbine yields similar estimates for all response amplitudes. Figure 3.10 illustrates how these differences influence the short-term response. The change in natural frequency is due to differences in stiffness, which both changes the wave frequency response and alters the natural period. Differences in damping alter the response amplitude at the natural frequency. The combined effect of these two mechanisms govern which soil model yields the highest fatigue damage.
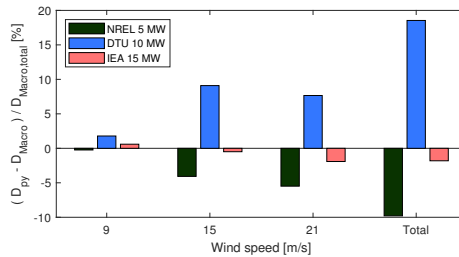
Figure 3.8: Difference in fatigue damage between the soil models. Both models may predict the highest fatigue damage, and as shown for the 15 MW turbine this may be wind-speed dependent. Reproduced from **P5**.
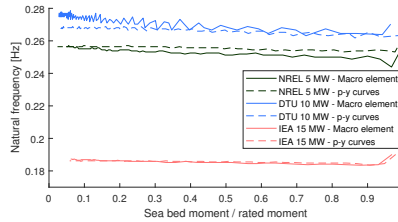
Figure 3.9: Natural frequency as function of seafloor bending moment for the two soil models. Only the macro-element shows an amplitude-dependent natural frequency. Reproduced from **P5**.

3.2.5   Scour Protection

Including the scour protection in the simulation model reduces the fatigue damage predictions. This effect is largest close to the seafloor. Still, an influence may be seen also in the remaining parts of the support structure if resonant responses are particularly important. This is the case for the 5 MW turbine in **P1**, where the increased stiffness shifts the natural frequency away from the majority of the

(a) Operational turbine.

(b) Parked turbine.
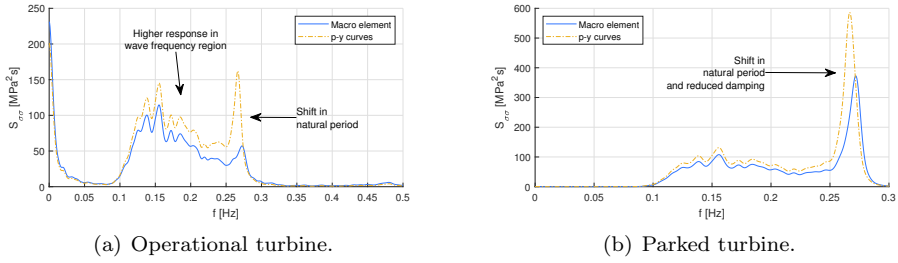
Figure 3.10: Effects of soil model on the response, illustrated for the 10 MW turbine. The spectra show how the stiffness differences change both the wave-frequency response and natural frequency, while the damping model influences the resonant response. Figures are reproduced from **P1**

wave excitation. The same stiffness increase also reduces the response in the wave-frequency region. Both these effects are illustrated in Figure 3.11.

(a) Operational turbine.

(b) Parked turbine.
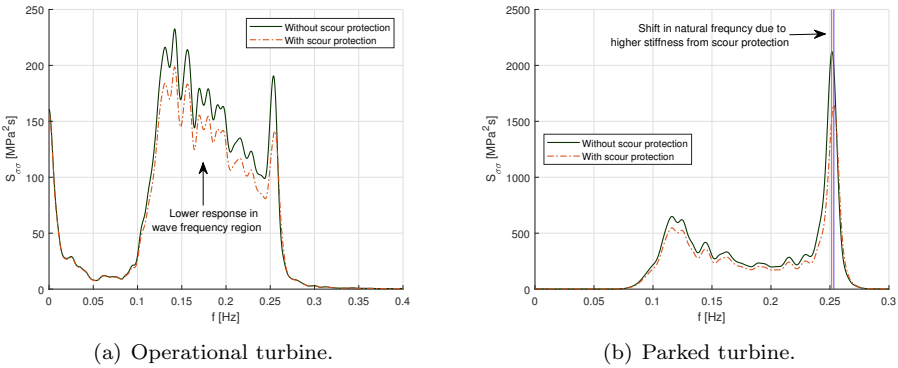
Figure 3.11: Effects of including the scour protection in the soil model for the NREL 5 MW turbine. This increases the soil stiffness, giving a lower response in the wave-frequency region and a higher natural frequency. Figures are reproduced from **P1**.

3.3 Contribution 3

Development of a method for efficient fatigue analysis of monopile and tower support structures

A full fatigue evaluation is computationally demanding, with many hundreds or thousands of environmental conditions to be analysed. A method for reducing the computational effort was developed within contribution **C3** and demonstrated in **P2**. The method is capable of reducing the computational effort by ∼93% while
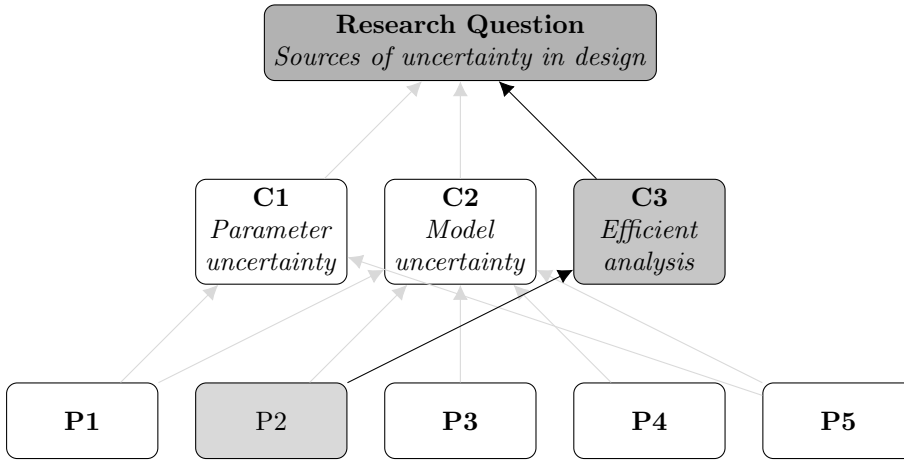
Figure 3.12: Link between research papers, contribution 3 and research question.

predicting the fatigue damage with an error of ~6% for the support structure used in the case study. For individual wind speed classes, the error is larger, up to ~15%. The basis of the method is the assumption that an equivalent sea state can be found for a given wind speed class by considering the fatigue damage from wave loads only. This equivalent sea state can then be used in a fully integrated analysis with both aerodynamic and hydrodynamic loads to predict the total fatigue damage. The reduction in computational requirements is achieved by applying simplified analysis methods when identifying the equivalent sea state.

When employing the lumping method, the 1-hour fatigue damage must be computed for all sea states within a wind speed class. Scaled by the probability of occurrence for wind bin i, this damage $d^*_{Si,j,k}$ represents the fatigue damage that will be predicted if sea state j, k is selected as the lumped sea state. The target fatigue damage, d_{t_k}, is calculated as the sum of the one-hour fatigue damage and probability of occurrence for all sea states. All combinations of H_s, T_p on the intersection of $d^*_{Si,j,k}$ and d_{t_k} represent lumped load cases for the location where the fatigue damage is calculated. This intersection is given for the seafloor in the wind speed bin 16-18 m/s in Figure 3.13, together with d^*_{Sk} and d_{t_k}.

Contour lines similar to the intersection in Figure 3.13 can be extracted for all desired locations in the support structure. In **P2**, this is done for the up-wind location of the support structure at different elevations. Combining these contour lines reveals if a single sea state can be used to represent the scatter diagram at all locations. Figure 3.14 shows the contour lines for the monopile and tower of the DTU 10 MW turbine, with the red dot identifying a sea state that will predict the correct fatigue damage across the full support structure.

Three fatigue damage calculation methods are utilized in **P2**. These are shown in Figure 3.15. The full scatter analysis serves as the ground truth for the lifetime fatigue damage when assessing the lumping procedure. The time-domain lumping method (TDLM) includes both turbulent wind and irregular wave excitation. How-
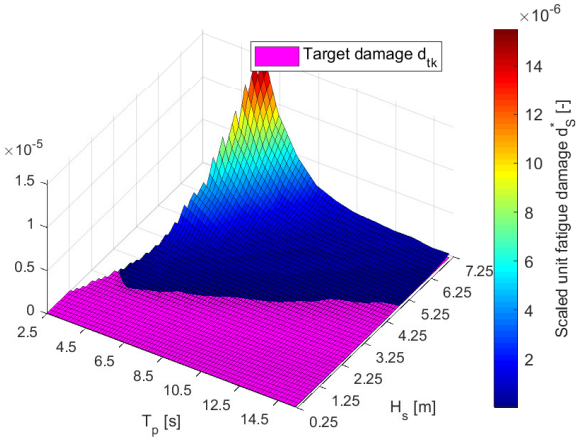
Figure 3.13: Target fatigue damage, d_{t_k}, and scaled unit fatigue damage, $d^*_{Si,j,k}$, at seafloor for wind bin 16-18 m/s. The plane shows d_{t_k}, while the surface is $d^*_{Si,j,k}$. The intersection between these gives possible equivalent sea states. Adapted from **P2**.
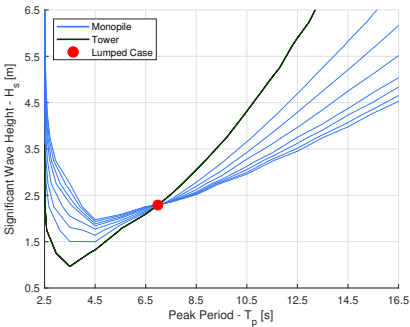
Figure 3.14: Contour lines for the tower and monopile in wind bin 14-16 m/s. Each contour represents sea states that will reproduce the fatigue damage the full scatter diagram for the given wind speed. Reproduced from **P2**.

ever, the computational effort of this method is larger than the full scatter analysis, and statistical uncertainty can be expected due to the stochastic nature of each realization. The TDLM is, therefore, only a benchmark for the sea states provided by the frequency-domain lumping method (FDLM). The FDLM represents the computationally efficient lumping method. In **P2** a frequency-domain model based on the extracted wave-to-stress transfer function is utilized. In principle, any model capable of predicting the wave-induced response in a computationally efficient manner can be utilized.
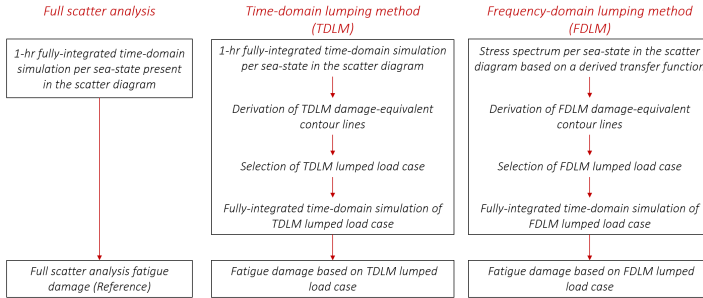
Figure 3.15: Fatigue damage calculation methods applied in **P2**. Reproduced from **P2**.

Figure 3.16 compares the sea states predicted by the FDLM to those given by the TDLM, as well as the most probable H_s and T_p class. The class contributing the most to the fatigue damage is also shown. The agreement with the TDLM and FDLM is good in the majority of the wind speed bins for H_s, with differences typically less than 0.1 m. For the wave peak period, the deviations are typically 0.1-0.5 s. The selected H_s typically lies within the most probable bin, while deviations are seen for T_p. This highlights the importance of considering the turbine dynamics when selecting equivalent sea states.

The lifetime fatigue damage from the lumped load cases is compared to that from the full scatter diagram in Figure 3.17. A good agreement between the two methods is seen, with differences less than 6% for all four realizations of the lumped load cases. When including wind-wave misalignment, the performance decreases to errors of ∼10-12% for the three wind speeds considered in **P2**. The performance decrease is caused by the error in estimating the angular position of the location with the highest fatigue damage in the FDLM. The low side-side damping leads to high fatigue damage at a position towards the cross-wind direction, due to the significant resonant response to the cross-wind wave loading in the white-noise test. In the case with turbulent wind loads, a majority of the loading is aligned with the mean wind direction. Thus, the highest fatigue damage is more aligned with the wind direction. An example is given in Figure 3.18, where the FDLM predicts the highest fatigue damage ∼60°from the mean wind direction, while the analysis with turbulent wind predicts the largest fatigue damage ∼15°from the wind direction.

(a) H_s.

(b) T_p.
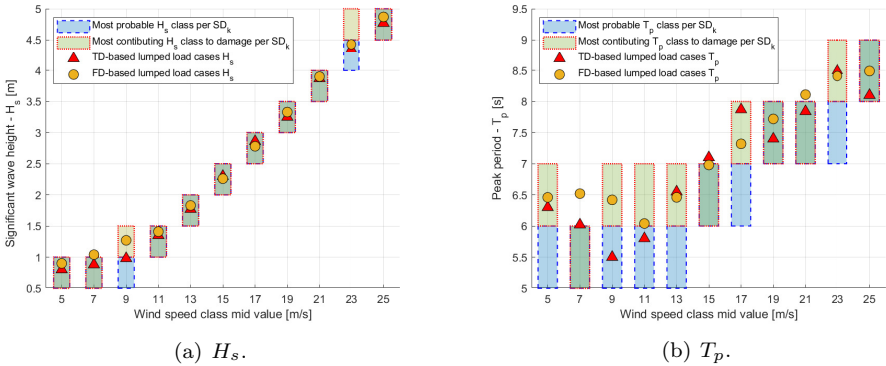
Figure 3.16: Comparison of the lumped sea states selected by the time-domain lumping method, the frequency-domain lumping method, the most probably sea state and the sea state with the highest fatigue damage. Reproduced from **P2**.

(a) Tower base.

(b) 15 m above seafloor.

(c) 8.25 m below seafloor.
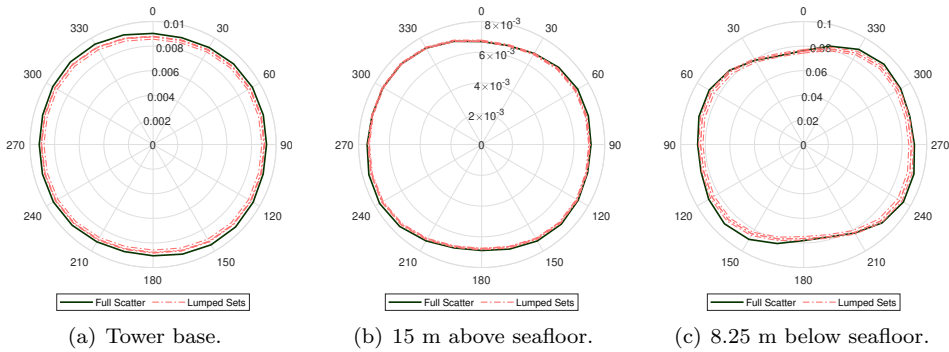
Figure 3.17: Comparison of the lifetime fatigue damage predictions using the full scatter diagram and 4 realization of the lumped load cases. Reproduced from **P2**.

(a) Seafloor.

(b) Tower base.
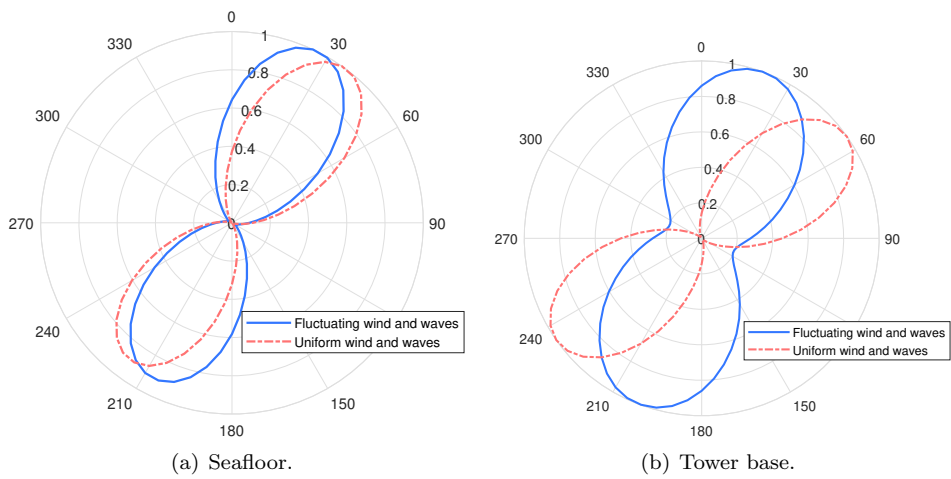
Figure 3.18: Normalized 1-hour fatigue damage with wind arriving from 0° and waves arriving from 30°. A difference in the angular position of highest fatigue damage is seen due to the wind and waves arriving from different directions. This introduces additional errors in the lumped load cases. Reproduced from **P1**.

Chapter 4

Conclusions and Recommendations for Further Work

This thesis investigates the uncertainty in the fatigue analysis of monopile offshore wind turbines, with focus on three reference turbines: The NREL 5 MW, DTU 10 MW and IEA 15 MW turbines. These have all been located at the Dogger Bank area.

Using these three turbines as a case study, the design basis, operational, and production parameters responsible for the majority of the uncertainty in the fatigue design have been identified. The largest uncertainty was found to be due to the variations in the fatigue properties of steel. The group of parameters describing the environmental conditions at the site have the second-largest influence on the uncertainty, with wind-related parameters influencing the tower design. Both wind- and wave-related parameters influence the monopile, but the importance of the wind-related parameters (in particular turbulence intensity) increases as the turbine size increases. In the monopile below the seafloor, the uncertainty in the soil parameters also plays a significant role.

Considering the engineering models used in the design calculations, the largest uncertainty is introduced when selecting whether the waves should be modelled as long or short-crested. The wind coherence model also has a significant influence on the calculated fatigue damage in the tower. For both of these, the selection of a conservative model depends on the first natural period of the support structure. Significant uncertainty is also introduced by the capabilities of the software used and the modelling approach taken by the analyst. These cannot easily be separated. Finally, the p-y curve and macro element soil models show differences in both damping and stiffness properties. In the present work, these differences have opposite effects on the calculated fatigue damage, reducing difference in the predicted fatigue damage. For other designs or soil model calibrations, the difference may very well be larger.

Finally, a method for efficient fatigue analysis of monopile OWTs was developed. This method uses simplified models to determine equivalent sea states, capable of

replicating the fatigue damage along the full support structure. For the considered case study, the equivalent sea states can predict the fatigue damage with an error less than 6%, while reducing the computational effort by more than 90% if aligned wind and waves is assumed. For misaligned wind and waves, the error is ∼10% compared to the full fatigue analysis.

4.1   Limitations

While the work performed has aimed at producing as general results as possible, some limitations had to be applied. The most important are presented in the following.

The studies have all been limited to single turbines located at Dogger Bank. Results may be different if other locations are considered, with e.g., less or more severe weather conditions or different types of soil. Other turbine and foundation designs may also show different sensitivity to variations in the parameters, due to e.g., changes in the relative importance of wind and wave loads or changes in the natural period. No variations to the controller have been considered, although different control regimes may give different behaviour of the turbine and thereby different results. Focus has been on the fatigue limit state, which historically has been governing the foundation designs. For certain areas and designs, this may not be the design driving limit state. Only contributions to fatigue damage from the operational and idling turbine have been considered. Fatigue damage accumulation during transport, installation, decommissioning, fault conditions, start-up and shutdown has not been included.

When investigating the design basis, production and operational parameters, a screening method was applied. This does not quantify the contribution from each parameter to the total uncertainty, but allows for ranking the parameters in accordance to their importance. The method can indicate if there is coupling of the sensitivity for the parameters, but is unable to identify which parameters are coupled.

The effect of changing the models used in the fatigue calculations was assessed by comparing the results using different models. Comparisons with full-scale measurements were not performed, and no evaluation has been performed as to which of the models are most correct. Models recommended by design standards, models frequently used, and models offering a more detailed representation of the physical phenomena they should represent have been chosen. Other alternative models not investigated here do exist.

4.2   Recommendations for Further Work

Based on the findings of the thesis and the limitations to the work, the following further work is recommended:

- The effect on the design and related cost savings when reducing the uncertainty in the design basis, production and operational parameters should be quantified. This may be done for only the most influential parameters identi-

fied in **C1**, allowing for assessment of the benefit of reducing the uncertainty for the designers.

- Accurate and sufficient metocean data is important for reducing the design uncertainty. While long time series exist for many areas, research is needed for assessing how reliable this data is in light of the ongoing climate changes. A further extension of this would be to develop models for using old metocean data and climate models to predict the future environmental conditions of a site.

- Identification of the most influential parameters and models for ULS, ALS, and SLS should be performed. This will allow for a more complete understanding of the design driving uncertainties. Further, the parameter and model sensitivities should be derived for other concepts, including both bottom-fixed and floating wind turbines, and locations with different environmental conditions than Dogger Bank.

- Based on the findings in **C2**, further research should be performed on most aspects related to the modelling of OWTs. This includes, but is not limited to, development and validation of wind spectra and coherence models suitable for offshore conditions, more detailed guidelines for how short-crested waves should be modelled, and further development and validation of computer codes and training of analysts.

- Efficient fatigue analysis is of importance also for other types of support structures. The suitability of existing lumping methods (including the one developed in **C3**) should be assessed, and new methods developed if needed. Both jacket structures and floating support structures have different response characteristics that may require other considerations for the lumping methods. This includes, amongst others, the combined local and global wave load effect on jackets, and the combination of linear and 2nd order wave loads and low-frequency motion induced gravity loads on floating wind turbines.

References

Aasen, S., Page, A.M., Skjolden Skau, K., and Nygaard, T.A. (2017). Effect of foundation modelling on the fatigue lifetime of a monopile-based offshore wind turbine. *Wind Energy Science*, 2(2), 361–376. doi:10.5194/wes-2-361-2017.

Aho, J., Buckspan, A., Laks, J., Fleming, P., Jeong, Y., Dunne, F., Churchfield, M., Pao, L., and Johnson, K. (2012). A tutorial of wind turbine control for supporting grid frequency through active power control. In *2012 American Control Conference*, 3120–3131. IEEE, Montreal, Canada. doi:10.1109/ACC.2012.6315180.

Allen, L., O'Connell, A., and Kiermer, V. (2019). How can we ensure visibility and diversity in research contributions? How the Contributor Role Taxonomy (CRediT) is helping the shift from authorship to contributorship. *Learned Publishing*, 32(1), 71–74. doi:10.1002/leap.1210.

Arany, L., Bhattacharya, S., Macdonald, J., and Hogan, S.J. (2017). Design of monopiles for offshore wind turbines in 10 steps. *Soil Dynamics and Earthquake Engineering*, 92, 126–152. doi:10.1016/j.soildyn.2016.09.024.

Bachynski, E.E. and Ormberg, H. (2015). Hydrodynamic modeling of large-diameter bottom-fixed offshore wind turbines. In *ASME 2015 34th International Conference on Ocean, Offshore and Arctic Engineering*, V009T09A051. ASME, St. John's, Canada. doi:10.1115/OMAE2015-42028.

Bakhshi, R. and Sandborn, P. (2016). The effect of yaw error on the reliability of wind turbine blades. In *ASME 2016 10th International Conference on Energy Sustainability collocated with the ASME 2016 Power Conference and the ASME 2016 14th International Conference on Fuel Cell Science, Engineering and Technology*, V001T14A001. ASME, Charlotte, USA. doi:10.1115/es2016-59151.

Bergua, R., Robertson, A., Jonkman, J., Platt, A., Page, A., Qvist, J., Amet, E., Cai, Z., Han, H., Beardsell, A., Shi, W., Galván, J., Bachynski-Polić, E., McKinnon, G., Harnois, V., Bonnet, P., Suja-Thauvin, L., Hansen, A.M., Mendikoa Alonso, I., Aristondo, A., Battistella, T., Guanche, R., Schünemann, P., Pham, T.D., Trubat, P., Alarcón, D., Haudin, F., Nguyen, M.Q., and Goveas, A. (2022). OC6 Phase II: Integration and verification of a new soil–structure interaction model for offshore wind design. *Wind Energy*, 25(5), 793–810. doi:10.1002/we.2698.

References

Burton, T., Jenkins, N., Sharpe, D., and Bossanyi, E. (2011). *Wind Energy Handbook*. Wiley, Hoboken, 2nd edition.

Byrne, B.W., McAdam, R., Burd, H.J., Houlsby, G.T., Martin, C.M., Zdravkovi, L., Taborda, D.M.G., Potts, D.M., Jardine, R.J., Sideri, M., Schroeder, F.C., Gavin, K., Doherty, P., Igoe, D., Muirwood, A., Kallehave, D., and Skov Gretlund, J. (2015). New design methods for large diameter piles under lateral loading for offshore wind applications. In *Proceedings of the 3rd International Symposium on Frontiers in Offshore Geotechnics, ISFOG 2015*, 705–710. CRC Press/Balkema, Oslo, Norway. doi:10.1201/b18442.

Damgaard, M., Andersen, L.V., Ibsen, L.B., Toft, H.S., and Sørensen, J.D. (2015). A probabilistic analysis of the dynamic response of monopile foundations: Soil variability and its consequences. *Probabilistic Engineering Mechanics*, 41, 46–59. doi:10.1016/j.probengmech.2015.05.001.

DNV (2021a). Environmental conditions and environmental loads (DNV-RP-C205). Høvik, Norway.

DNV (2021b). Fatigue design of offshore steel structures (DNV-RP-C203). Høvik, Norway.

DNV (2021c). Loads and site conditions for wind turbines (DNV-ST-0437). Høvik, Norway.

DNV (2021d). Support structures for wind turbines (DNV-ST-0126). Høvik, Norway.

DNV (2022). Energy transition outlook 2022. Høvik, Norway.

Dogger Bank Wind Farm (2022). Building the world's largest offshore wind farm. URL `https://doggerbank.com/`. Accessed: 20. June 2022.

Donelan, M.A., Dobson, F.W., Smith, S.D., and Anderson, R.J. (1993). On the dependence of sea surface roughness on wave development. *Journal of Physical Oceanography*, 23(9), 2143–2149. doi:10.1175/1520-0485(1993)023<2143:Otdoss>2.0.Co;2.

Eliassen, L. and Obhrai, C. (2016). Coherence of Turbulent Wind Under Neutral Wind Conditions at FINO1. *Energy Procedia*, 94, 388–398. doi:10.1016/j.egypro.2016.09.199.

Empire Wind (2022). Empire Wind - Powering New York Together. URL `https://www.empirewind.com/`. Accessed: 17. December 2022.

Ernst, B. and Seume, J.R. (2012). Investigation of site-specific wind field parameters and their effect on loads of offshore wind turbines. *Energies*, 5(10), 3835–3855. doi:10.3390/en5103835.

Fallais, D.J.M., Winkler, K., Sastre Jurado, C., Weijtjens, W., Stuyts, B., and Devriendt, C. (2022). Farm wide sensitivity assessments of resonant frequencies of integrated offshore wind turbine finite element models. *Journal of Physics: Conference Series*, 2265(4), 042053. doi:10.1088/1742-6596/2265/4/042053.

Faltinsen, O.M., Newman, J.N., and Vinje, T. (1995). Nonlinear wave loads on a slender vertical cylinder. *Journal of Fluid Mechanics*, 289, 179–198. doi:10.1017/S0022112095001297.

Faltinsen, O.M. (1990). *Sea loads on ships and offshore structures*. Cambridge University Press, Cambridge.

Haldar, S., Sharma, J., and Basu, D. (2018). Probabilistic analysis of monopile-supported offshore wind turbine in clay. *Soil Dynamics and Earthquake Engineering*, 105, 171–183. doi:10.1016/j.soildyn.2017.11.028.

Hansen, M.O.L. (2008). *Aerodynamics of Wind Turbines*. Earthscan, London, 2nd edition.

Horn, J.T., Krokstad, J.R., and Amdahl, J. (2018). Long-term fatigue damage sensitivity to wave directionality in extra-large monopile foundations. *Proceedings of the Institution of Mechanical Engineers, Part M: Journal of Engineering for the Maritime Environment*, 232(1), 37–49. doi:10.1177/1475090217727136.

Horn, J.T., Krokstad, J.R., and Leira, B.J. (2019). Impact of model uncertainties on the fatigue reliability of offshore wind turbines. *Marine Structures*, 64, 174–185. doi:10.1016/j.marstruc.2018.11.004.

Horn, J.T.H., Krokstad, J.R., and Amdahl, J. (2016). Hydro-elastic contributions to fatigue damage on a large monopile. *Energy Procedia*, 94, 102–114. doi:10.1016/j.egypro.2016.09.203.

Horn, J.T.H., Krokstad, J.R., and Amdahl, J. (2017). Joint probability distribution of environmental conditions for design of offshore wind turbines. In *Proceedings of the ASME 2017 36th International Conference on Ocean, Offshore and Arctic Engineering*, V010T09A068. ASME, Trondheim, Norway. doi:10.1115/OMAE2017-61451.

Hsu, Y.H., Lu, Y.C., Khoshnevisan, S., Juang, H., and hung Hwang, J. (2022). Influence of geological uncertainty on the design of OWTF monopiles. *Engineering Geology*, 303, 106621. doi:10.1016/j.enggeo.2022.106621.

Huhn, M.L. and Popko, W. (2020). Best practice for verification of wind turbine numerical models. *Journal of Physics: Conference Series*, 1618(5), 052026. doi:10.1088/1742-6596/1618/5/052026.

Hübler, C., Gebhardt, C.G., and Rolfes, R. (2017). Hierarchical four-step global sensitivity analysis of offshore wind turbines based on aeroelastic time domain simulations. *Renewable Energy*, 111, 878–891. doi:10.1016/j.renene.2017.05.013.

IEA Wind TCP (2023). Global Wind Energy Research Collaboration. URL `https://iea-wind.org/`. Accessed: 16. August 2023.

IEC (2019). International Electrotechnical Commission, Wind turbine generator systems-Part 1: Safety requirements. 4th edition (IEC 61400-1).

ISO (2016). ISO 19901-4 Geotechnical and foundation design considerations.

Jawalageri, S., Prendergast, L.J., Jalilvand, S., and Malekjafarian, A. (2022). Effect of scour erosion on mode shapes of a 5 MW monopile-supported offshore wind turbine. *Ocean Engineering*, 266, 113131. doi:10.1016/j.oceaneng.2022.113131.

Jonkman, J., Butterfield, S., Passon, P., and Larsen, T. (2007). Offshore Code Comparison Collaboration within IEA Wind Annex XXIII: Phase II Results Regarding Monopile Foundation Modeling. In *IEA European Offshore Wind Conference*. IEA, Berlin, Germany.

Jusoh, I. and Wolfram, J. (1996). Effects of marine growth and hydrodynamic loading on offshore structures. *Jurnal Mekanikal*, 1(1).

Kallehave, D., Byrne, B.W., LeBlanc Thilsted, C., and Mikkelsen, K.K. (2015). Optimization of monopiles for offshore wind turbines. *Philosophical Transactions of the Royal Society A: Mathematical, Physical and Engineering Sciences*, 373(2035), 20140100. doi:10.1098/rsta.2014.0100.

Katsikogiannis, G., Bachynski, E.E., and Page, A.M. (2019). Fatigue sensitivity to foundation modelling in different operational states for the DTU 10MW monopile-based offshore wind turbine. *Journal of Physics: Conference Series*, 1356(1), 012019. doi:10.1088/1742-6596/1356/1/012019.

Katsikogiannis, G., Sørum, S.H., Bachynski, E.E., and Amdahl, J. (2021). Environmental lumping for efficient fatigue assessment of large-diameter monopile wind turbines. *Marine Structures*, 77, 102939. doi:10.1016/j.marstruc.2021.102939.

Kim, T. and Natarajan, A. (2013). Effect of coupled non linear wave kinematics and soil flexibility on the design loads of offshore wind turbines. In *51st AIAA Aerospace Sciences Meeting including the New Horizons Forum and Aerospace Exposition 2013*. AIAA, Dallas, USA. doi:10.2514/6.2013-196.

Klinkvort, R.T., Sturm, H., Page, A.M., Zhang, Y., and Jostad, H.P. (2022). A consistent, rigorous and super-fast monopile design approach. In *Proceedings of the 4th International Symposium on Frontiers in Offshore Geotechnics*. American Society of Civil Engineers, Austin, Texas, US.

Kristiansen, T. and Faltinsen, O.M. (2017). Higher harmonic wave loads on a vertical cylinder in finite water depth. *Journal of Fluid Mechanics*, 833, 773–805. doi:10.1017/jfm.2017.702.

Krokstad, J.R., Stansberg, C.T., Nestegård, A., and Marthinsen, T. (1998). A new nonslender ringing load approach verified against experiments. *Journal of Offshore Mechanics and Arctic Engineering*, 120(1), 20–29. doi:10.1115/1.2829515.

Kühn, M.J. (2001). *Dynamics and design optimisation of offshore wind energy conversion systems*. Phd thesis, TU Delft, Delft, the Netherlands.

Li, H., Ong, M.C., Leira, B.J., and Myrhaug, D. (2018). Effects of soil profile variation and scour on structural response of an offshore monopile wind turbine. *Journal of Offshore Mechanics and Arctic Engineering*, 140(4), 042001. doi:10.1115/1.4039297.

MacCamy, R. and Fuchs, R.A. (1954). Wave Forces on Piles: A Diffraction Theory. Office of Naval Research, U. S. Department of the Navy, Washington, D.C., US.

Moan, T. (2009). *Structural Risk and Reliability Analysis*. Department of Marine Technology, Norwegian University of Science and Technology, Trondheim.

Myrtvedt, M.H., Nybø, A., and Nielsen, F.G. (2020). The dynamic response of offshore wind turbines and their sensitivity to wind field models. *Journal of Physics: Conference Series*, 1669. doi:10.1088/1742-6596/1669/1/012013.

Newman, J.N. (1996). *Nonlinear Scattering of Long Waves by a Vertical Cylinder*, volume 34 of *Fluid Mechanics and Its Applications*, book section 8, 91–102. Springer, the Netherlands. doi:10.1007/978-94-009-0253-4_8.

Niu, X., Chen, X., Qiu, Z., Wang, H., and Xie, A. (2022). Effects of scour on the first natural frequency of monopile in different layered foundations. *Ocean Engineering*, 265, 112580. doi:10.1016/j.oceaneng.2022.112580.

Nybø, A., Nielsen, F.G., and Reuder, J. (2019). Processing of sonic anemometer measurements for offshore wind turbine applications. *Journal of Physics: Conference Series*, 1356. doi:10.1088/1742-6596/1356/1/012006.

Nybø, A., Nielsen, F.G., and Godvik, M. (2021). Quasi-static response of a bottom-fixed wind turbine subject to various incident wind fields. *Wind Energy*, 24, 1482–1500. doi:10.1002/we.2642.

Nybø, A., Nielsen, F.G., Reuder, J., Churchfield, M.J., and Godvik, M. (2020). Evaluation of different wind fields for the investigation of the dynamic response of offshore wind turbines. *Wind Energy*, 23(9), 1810–1830. doi:10.1002/we.2518.

Page, A., Grimstad, G., Eiksund, G., and Jostad, H.P. (2018). A macro-element pile foundation model for integrated analyses of monopile based offshore wind turbines. *Ocean Engineering*, 167, 23–35. doi:10.1016/j.oceaneng.2018.08.019.

Page, A., Grimstad, G., Eiksund, G., and Jostad, H.P. (2019). A macro-element model for multidirectional cyclic lateral loading of monopiles in clay. *Computers and Geotechnics*, 106, 314–326. doi:10.1016/j.compgeo.2018.11.007.

Passon, P. (2015). Damage equivalent wind–wave correlations on basis of damage contour lines for the fatigue design of offshore wind turbines. *Renewable Energy*, 81, 723–736. doi:10.1016/j.renene.2015.03.070.

Peeringa, J. and Bedon, G. (2017). Fully integrated load analysis included in the structural reliability assessment of a monopile supported offshore wind turbine. *Energy Procedia*, 137, 255–260. doi:10.1016/j.egypro.2017.10.348.

Popko, W., Huhn, M.L., Robertson, A., Jonkman, J., Wendt, F., Müller, K., Kretschmer, M., Vorpahl, F., Hagen, T.R., Galinos, C., Le Dreff, J.B., Gilbert, P., Auriac, B., Víllora, F.N., Schünemann, P., Bayati, I., Belloli, M., Oh, S., Totsuka, Y., Qvist, J., Bachynski, E., Sørum, S.H., Thomassen, P.E., Shin, H., Vittori, F., Galván, J., Molins, C., Bonnet, P., van der Zee, T., Bergua, R., Wang, K., Fu, P., and Cai, J. (2018). Verification of a Numerical Model of the Offshore Wind Turbine From the Alpha Ventus Wind Farm Within OC5 Phase III. In *ASME 2018 37th International Conference on Ocean, Offshore and Arctic Engineering*, V010T09A056. ASME, Madrid, Spain. doi:10.1115/omae2018-77589.

Popko, W., Robertson, A., Jonkman, J., Wendt, F., Thomas, P., Müller, K., Kretschmer, M., Hagen, T.R., Galinos, C., Le Dreff, J.B., Gilbert, P., Auriac, B., Oh, S., Qvist, J., Sørum, S.H., Suja-Thauvin, L., Shin, H., Molins, C., Trubat, P., Bonnet, P., Bergua, R., Wang, K., Fu, P., Cai, J., Cai, Z., Alexandre, A., and Harries, R. (2020). Validation of Numerical Models of the Offshore Wind Turbine From the Alpha Ventus Wind Farm Against Full-Scale Measurements Within OC5 Phase III. *Journal of Offshore Mechanics and Arctic Engineering*, 143(1). doi:10.1115/1.4047378.

Popko, W., Robertson, A., Jonkman, J., Wendt, F., Thomas, P., Müller, K., Kretschmer, M., Ruud Hagen, T., Galinos, C., Le Dreff, J.B., Gilbert, P., Auriac, B., Oh, S., Qvist, J., Sørum, S.H., Suja-Thauvin, L., Shin, H., Molins, C., Trubat, P., Bonnet, P., Bergua, R., Wang, K., Fu, P., Cai, J., Cai, Z., Alexandre, A., and Harries, R. (2019). Validation of Numerical Models of the Offshore Wind Turbine From the Alpha Ventus Wind Farm Against Full-Scale Measurements Within OC5 Phase III. In *ASME 2019 38th International Conference on Ocean, Offshore and Arctic Engineering*, V010T09A065. ASME, Glasgow, Scotland. doi:10.1115/omae2019-95429.

Prendergast, L.J., Gavin, K., and Doherty, P. (2015). An investigation into the effect of scour on the natural frequency of an offshore wind turbine. *Ocean Engineering*, 101, 1–11. doi:10.1016/j.oceaneng.2015.04.017.

Prendergast, L.J., Reale, C., and Gavin, K. (2018). Probabilistic examination of the change in eigenfrequencies of an offshore wind turbine under progressive scour incorporating soil spatial variability. *Marine Structures*, 57, 87–104. doi:10.1016/j.marstruc.2017.09.009.

Rinker, J., Gaertner, E., Zahle, F., Skrzypiński, W., Abbas, N., Bredmose, H., Barter, G., and Dykes, K. (2020). Comparison of loads from HAWC2 and Open-FAST for the IEA Wind 15 MW Reference Wind Turbine. *Journal of Physics: Conference Series*, 1618(5). doi:10.1088/1742-6596/1618/5/052052.

Robertson, A.N., Shaler, K., Sethuraman, L., and Jonkman, J. (2019). Sensitivity analysis of the effect of wind characteristics and turbine properties on wind turbine loads. *Wind Energy Science*, 4(3), 479–513. doi:10.5194/wes-4-479-2019.

Robertson, A.N., Wendt, F.F., Jonkman, J.M., Popko, W., Vorpahl, F., Stansberg, C.T., Bachynski, E.E., Bayati, I., Beyer, F., de Vaal, J.B., Harries, R., Yamaguchi, A., Shin, H., Kim, B., van der Zee, T., Bozonnet, P., Aguilo, B., Bergua, R., Qvist, J., Qijun, W., Chen, X., Guerinel, M., Tu, Y., Yutong, H., Li, R., and Bouy, L. (2015). OC5 Project Phase I: Validation of Hydrodynamic Loading on a Fixed Cylinder. In *International Offshore and Polar Engineering Conference*. ISOPE, Kona, USA.

Saltelli, A., Ratto, M., Andres, T., Campolongo, F., Cariboni, J., Gatelli, D., Saisana, M., and Tarantola, S. (2008). *Global Sensitivity Analysis. The Primer*. John Wiley & Sons, Ltd, Chichester, UK. doi:10.1002/9780470725184.

Schløer, S., Bredmose, H., Bingham, H.B., and Larsen, T.J. (2012). Effects from fully nonlinear irregular wave forcing on the fatigue life of an offshore wind turbine and its monopile foundation. In *Proceedings of the ASME 2012 31st International Conference on Ocean, Offshore and Arctic Engineering*, volume 7, 393–402. ASME, Rio de Janeiro, Brazil. doi:10.1115/OMAE2012-83477.

SINTEF Ocean (2017). RIFLEX 4.10.3 User Guide. SINTEF Ocean, Trondheim, Norway.

Smilden, E., Sørum, S.H., Bachynski, E.E., Sørensen, A.J., and Amdahl, J. (2020). Post-installation adaptation of offshore wind turbine controls. *Wind Energy*, 23(4), 967–985. doi:10.1002/we.2467.

Smith, A., Stehly, T., and Musial, W. (2015). 2014-2015 Offshore Wind Technologies Market Report. National Renewable Energy Laboratory.

Sørum, S.H., Bachynski-Polić, E.E., and Amdahl, J. (2022a). Wind and soil model influences on the uncertainty in fatigue of monopile supported wind turbines. *Journal of Physics: Conference Series*, 2362, 012038. doi:10.1088/1742-6596/2362/1/012038.

Sørum, S.H., Krokstad, J.R., and Amdahl, J. (2019). Wind-wave directional effects on fatigue of bottom-fixed offshore wind turbine. *Journal of Physics: Conference Series*, 1356, 012011. doi:10.1088/1742-6596/1356/1/012011.

Sørum, S.H., Katsikogiannis, G., Bachynski-Polić, E.E., Amdahl, J., Page, A.M., and Klinkvort, R.T. (2022b). Fatigue design sensitivities of large monopile offshore wind turbines. *Wind Energy*, 25(10), 1684–1709. doi:10.1002/we.2755.

Sørum, S.H., Smilden, E., Amdahl, J., and Sørensen, A.J. (2018). Active Load Mitigation to Counter the Fatigue Damage Contributions From Unavailability in Offshore Wind Turbines. In *ASME 2018 37th International Conference on Ocean, Offshore and Arctic Engineering*, V010T09A061. ASME, Madrid, Spain. doi:10.1115/omae2018-77962.

Sørum, S.H., Horn, J.T.H., and Amdahl, J. (2017). Comparison of numerical response predictions for a bottom-fixed offshore wind turbine. *Energy Procedia*, 137, 89–99. doi:10.1016/j.egypro.2017.10.336.

Teixeira, R., O'Connor, A., and Nogal, M. (2019). Probabilistic sensitivity analysis of offshore wind turbines using a transformed kullback-leibler divergence. *Structural Safety*, 81. doi:10.1016/j.strusafe.2019.03.007.

Toft, H.S., Svenningsen, L., Moser, W., Sørensen, J.D., and Thøgersen, M.L. (2016a). Wind climate parameters for wind turbine fatigue load assessment. *Journal of Solar Energy Engineering*, 138(3), 031010. doi:10.1115/1.4033111.

Toft, H.S., Svenningsen, L., Sørensen, J.D., Moser, W., and Thøgersen, M.L. (2016b). Uncertainty in wind climate parameters and their influence on wind turbine fatigue loads. *Renewable Energy*, 90, 352–361. doi:10.1016/j.renene.2016.01.010.

Trumars, J.M.V., Jonsson, J.O., and Bergdahl, L. (2006). The effect of wind and wave misalignment on the response of a wind turbine at bockstigen. In *25th International Conference on Offshore Mechanics and Arctic Engineering*, volume 1, 635–641. ASME, Hamburg, Germany. doi:10.1115/OMAE2006-92075.

Türk, M. and Emeis, S. (2010). The dependence of offshore turbulence intensity on wind speed. *Journal of Wind Engineering and Industrial Aerodynamics*, 98(8), 466–471. doi:10.1016/j.jweia.2010.02.005.

Varelis, G.E., Ai, J., Kane, P., Ragheb, H., and Dib, E. (2021). Scour Effects on the Structural Integrity of Offshore Wind Turbine Monopiles. In *ASME 2021 3rd International Offshore Wind Technical Conference*, V001T01A022. ASME, Online. doi:10.1115/IOWTC2021-3554.

Velarde, J., Kramhøft, C., Sørensen, J.D., and Zorzi, G. (2020). Fatigue reliability of large monopiles for offshore wind turbines. *International Journal of Fatigue*, 134, 105487. doi:10.1016/j.ijfatigue.2020.105487.

WindEurope (2022). *Wind energy in Europe - 2021 Statistics and the outlook for 2022-2026*. WindEurope.

Wirsching, P.H. (1984). Fatigue reliability for offshore structures. *Journal of Structural Engineering*, 110(10), 2340–2356. doi:https://doi.org/10.1061/(ASCE)0733-9445(1984)110:10(2340).

Wolfram, J. and Theophanatos, A. (1985). The effects of marine fouling on the fluid loading of cylinders: Some experimental results. In *17th Annual Offshore Technology Conference*. OTC, Houston, Texas. doi:10.4043/4954-MS.

Zaaijer, M.B. (2006). Foundation modelling to assess dynamic behaviour of offshore wind turbines. *Applied Ocean Research*, 28(1), 45–57. doi:10.1016/j.apor.2006.03.004.

Ziegler, L., Voormeeren, S., Schafhirt, S., and Muskulus, M. (2015). Sensitivity of wave fatigue loads on offshore wind turbines under varying site conditions. *Energy Procedia*, 80, 193–200. doi:10.1016/j.egypro.2015.11.422.

Part II

Selected Publications

Paper 1:

Fatigue design sensitivities of large monopile
offshore wind turbines

**Stian H. Sørum, George Katsikogiannis, Erin E. Bachynski-Polić,
Jørgen Amdahl, Ana M. Page, Rasmus T. Klinkvort**

RESEARCH ARTICLE

Fatigue design sensitivities of large monopile offshore wind turbines

Stian H. Sørum[1,2] | George Katsikogiannis[2] | Erin E. Bachynski-Polić[1,2] |
Jørgen Amdahl[1,2] | Ana M. Page[3] | Rasmus T. Klinkvort[3]

[1]Centre for Autonomous Marine Operations and Systems, Department of Marine Technology, NTNU, Trondheim, Norway

[2]Department of Marine Technology, NTNU, Trondheim, Norway

[3]Norwegian Geotechnical Institute, Oslo, Norway

Correspondence
Stian H. Sørum, NTNU, NO-7491 Trondheim, Norway.
Email: stian.h.sorum@ntnu.no

Funding information
Research Council of Norway, Grant/Award Number: 223254; Extra Large Monopiles (WAS-XL), Grant/Award Number: 268182

Abstract

The input for fatigue analyses of offshore wind turbines is typically chosen based on design values provided by design standards. While this provides a straightforward design methodology, the contribution of different input parameters to the uncertainty in the fatigue damage estimates is usually unknown. This knowledge is important to have when improving current designs and methodologies, and the parameters governing the uncertainty is typically found through a sensitivity analysis. Several sensitivity studies have been performed for monopile-based offshore wind turbines, typically focusing on specific turbines and engineering disciplines. This paper performs a sensitivity study for three monopile-based offshore wind turbines (5 MW, 10 MW, 15 MW) using parameters from several engineering disciplines. The results show that the fatigue utilization is primarily governed by the uncertainty in the SN curves and fatigue capacity. Following this, the uncertainty in the environmental conditions is the dominating uncertainty, with wind loads becoming increasingly important as turbine size increases. Additionally, the effect of modelling uncertainties is investigated. The wind-related model uncertainties dominate in the tower top, while uncertainties in the wave and soil models dominate in the tower base and monopile. Designers wanting to reduce the uncertainty in a design are recommended to focus on the environmental conditions, and using as accurate models as possible. All modelling uncertainties are significant, but research should particularly be focused on wave directionality and soil models.

KEYWORDS
design uncertainty, fatigue design, model uncertainty, offshore wind turbine, sensitivity analysis

1 | INTRODUCTION

Fatigue limit state (FLS) design of offshore wind turbines (OWTs) is based on design load cases according to relevant design standards.[1,2] These standards account for the uncertainty in resistance and loads by applying safety factors to achieve a specified reliability level. The procedure is straightforward for designers, but safety factors give no information on how the uncertainty in specific variables influences the overall reliability

of an OWT. Such knowledge is essential for improving current design standards, reducing investment costs, evaluating novel design concepts, and guiding further research.

Although all design parameters may in principle be considered uncertain, typically only a few parameters significantly affect the total uncertainty.[3] These parameters should be given particular focus during the design process, and they can be identified through a sensitivity analysis (SA). Numerous SAs and reliability studies have been performed on individual OWTs,[4–14] with size varying from 4 to 10 MW. The results from selected studies considering several uncertain parameters are summarised in Table 1. None of the studies have directly compared different turbine sizes. Many of these have considered a limited number of design parameters, while others are more extensive.[4–6,8,10,11] Others again have focused on uncertainties from selected engineering disciplines, for example, aerodynamics.[9,11] However, there is no clear consensus between the

TABLE 1 Selected previous sensitivity analyses for monopile OWTs

Reference Turbine size (MW)	Hübler et al.[5] 5	Robertson et al.[9] 5	Toft et al.[11] -	Teixeira et al.[8] 5	Peeringa &Bedon[4] 4	Velarde et al.[6] 10
Turbulence intensity	NI	I	I	I		
Wind shear	NI	I	NI	NI		
Surface roughness				NI		
Air density	NI		NI	NI		
Air stability				NI		
Wind speed	V			V		
Wind direction	V					
Yaw error	NI	I		NI		
Water depth	NI			NI		
Water density	NI			NI		
Wave height	V			V		
Wave period	V			V		
Spectral parameter, γ				NI		
Wave direction	V					
Current velocity				NI		
Mass coefficient					NI	
Drag coefficient					NI	
Marine growth	I					
Wave load model						I
Soil stiffness	NI				NI	
Soil unit weight	I					
Soil friction angle	I					
Pile diameter	I					
Pile thickness	NI					
Tower diameter	NI					
Tower thickness	NI					
Embedded length	I					
Airfoil parameters		I				
Young's modulus	NI				NI	
SCF						NI
SN-curve					I	NI
Fatigue capacity					I	I
Dynamics						I
Hub mass	NI					
Nacelle mass	NI					

Note: "I"/green and "NI"/yellow denote parameters found influential and not influential, respectively. "V"/grey denotes parameters where the long-term variability is considered, as discussed in Section 4.1.3. Only important parameters from Robertson et al. are included.

studies regarding either the parameters considered, or the parameters identified as important. This may be caused both by different sensitivities for different turbines and foundations, as well as by the level of uncertainty assumed in the studies. Further, several studies overestimate the uncertainty in environmental conditions by considering the long-term variation in, for example, significant wave height rather than the uncertainty in the design value. An example of how this artificially increases the uncertainty is given in Section 4.1.3. Finally, some studies suggest further research topics without quantifying the uncertainty.[15,16]

The approaches followed by the studies in Table 1 differ. Hübler et al[5] focused on parameters from several engineering disciplines, looking at a large number of variables (>100). Robertson et al[9] performed a sensitivity analysis for 57 parameters, all related to wind characteristics and aerodynamic loads. For brevity, only the influential parameters from this study are included in Table 1. Toft et al[11] presented a probabilistic framework for assessment of the structural reliability level of wind turbines in fatigue loading, focusing on aerodynamic loads. Teixeira et al[8] performed a probabilistic sensitivity analysis including aerodynamic loads, wave conditions, and current velocity. Peeringa et al[4] presented a probabilistic design tool, coupling reliability analysis and wind turbine simulation tools, focusing on structural properties and fatigue capacity. Finally, Velarde et al[6] demonstrated a fatigue reliability analysis of a monopile supporting a 10-MW offshore wind turbine, focusing more on the system properties than the fundamental parameters. Three of the six studies in Table 1 found turbulence intensity to be important. Besides this, the SN curve was the only parameter found important by more than one study.

Beyond the uncertainty in design parameters, the modelling choices made in the analysis of an OWT introduce additional, different uncertainties. Several studies have been performed looking at individual parameters; some are given here to illustrate the range of model uncertainties. Kim et al[17] showed how wake effects increase the fatigue damage. Nybø et al[18] investigated the fatigue response using different wind fields and stability conditions, also comparing the engineering models with wind measurements and high-fidelity models of the wind field. Horn et al[19] and Schløer et al[20] found that higher order wave loads increase the fatigue damage in severe sea states. Horn et al[21] looked at the importance of considering multiple wave directions. They found that separation between wind generated waves and swell increased the monopile fatigue damage and reduced the tower fatigue damage. Including short-crested waves was found to reduce the fatigue damage. Sørum et al[22] showed that short-crested waves may result in both a higher and lower fatigue damage than long-crested waves, depending on the monopile design. Bachynski and Ormberg[23] showed that wave diffraction becomes more important as monopile diameters increase. Finally, Aasen et al[24] and Katsikogiannis et al[25] both demonstrated how the soil model influences the fatigue response predictions, with both nonlinear stiffness and damping being important. To the authors' knowledge, no studies compare the uncertainty caused by modelling choices to other types of uncertainty.

This paper aims to improve the understanding obtained from previous studies, focusing on fatigue design for three monopile-based OWTs with capacity 5, 10, and 15 MW. A sensitivity analysis study is first performed considering the input parameters whose uncertainty can be described by a continuous probability density function, hereafter denoted continuous parameters. The uncertainty in fatigue damage estimates due to modelling choices, hereafter denoted discrete parameters, is then calculated. The studied parameters range across various engineering disciplines, including but not limited to aerodynamics, hydrodynamics, geotechnics, and structural dynamics. The present work aims to determine which uncertainties contribute most to the uncertainty in fatigue damage for different locations along the support structure and operational states for monopile-based OWTs, and how this uncertainty varies with turbine size. The results can help designers prioritise which parameters to investigate during the design of turbines and give guidance for the focus of further research.

The paper is organized as follows: Section 2 presents the sensitivity analysis method used in the study; Section 3 describes the environmental model, simulation models and fatigue estimation method. Following this, Section 4 presents the parameters investigated in the SA. Finally, the results are presented in Section 5 and discussed in Section 6, before the paper is concluded in Section 7.

2 | SENSITIVITY ANALYSIS METHODS

Different methods can be used for a sensitivity analysis,[3] depending on the system properties and the computational effort required. The design of monopile OWTs relies on dynamic analyses, coupling aerodynamics, hydrodynamics, soil–structure interaction and the turbine control system. The system is nonlinear, and the computational effort required for analysis is significant with simulations running at approximately real-time. Local analyses, such as one-at-the-time (OAT) variation of the input parameters, are computationally efficient but not capable of capturing system nonlinearities and interactions between input parameters. Variance-based methods provide more accurate results, allowing quantification of each parameter's influence on the system's total uncertainty. However, the large computational effort of variance-based methods makes them infeasible to apply here. Screening methods can partly overcome the challenges mentioned above, capture system nonlinearities, interaction effects, and qualitatively rank the input parameters according to their importance, with acceptable computational requirements. In this study, the screening method of elementary effects is used for evaluating the continuous parameters (see Section 2.1). The method is generally considered a good alternative for highly nonlinear systems with a moderate (<100) number of input parameters.[3] The discrete parameters are evaluated based on the change relative to a baseline model, as described in Section 2.2.

2.1 | Elementary effects method

The elementary effects method is an expansion of the OAT approach, as illustrated in Figure 1. The quantity of interest (i.e. long term fatigue damage) is calculated at a base point j that represents a set of input values for the uncertain analysis parameters (e.g., turbulence intensity and yaw error). A single parameter is then changed, and the quantity of interest is calculated again. The local derivative, denoted the elementary effect (EE), can then be found. The procedure is repeated for several sets of base points distributed across the parameter space. The output quantity, Y, is a function of all input parameters, $\mathbf{X} = [X_1, X_2, ..., X_I]^T$. The EE of an input parameter X_i, at a base point $j = 1, ..., J$, is given by Equation (1).

$$EE_i^j = \frac{Y(X_1^j, ..., X_i^j \pm \Delta_i, ..., X_I^j) - Y(X_1^j, ..., X_i^j, ..., X_I^j)}{\pm \Delta_F} = \frac{Y_{pp}^j - Y_{bp}^j}{\pm \Delta_F}. \tag{1}$$

$Y(X_1^j, ..., X_i^j, ..., X_I^j) = Y_{bp}^j$ is the output quantity calculated at the base point j, while $Y(X_1^j, ..., X_i^j \pm \Delta_i, ..., X_I^j) = Y_{pp}^j$ is the output quantity calculated for a specified perturbation Δ_i of input parameter X_i in the physical space. Δ_F is the normalised step size (Section 2.1.1). The sign of the perturbation is randomly selected. The importance of a parameter X_i is determined based on the statistics of all elementary effects across the J base points.

2.1.1 | Sampling strategy

The parameter space of each input variable should be sufficiently covered to achieve reliable results. It has been found that a radial elementary effect is more efficient than the original approach[26] if the sampled sets $\mathbf{X}^j$ are sufficiently distributed. Three main sampling approaches have been identified in the literature.[27–29] The first is Crude Monte Carlo methods, which show inadequate coverage of the parameter space.[28,29] Stratified approaches (e.g., Latin Hypercube) are more efficient but do not provide sufficient multidimensional coverage.[29] Finally, quasi-random sequences (e.g., Sobol and Hammersley) show better multidimensional properties.[27,28] A method for combining Hammersley sequences and Latin Hypercube sampling has also been developed.[29] The drawback of Latin Hypercube sampling is that the number of sampling points cannot be easily expanded if convergence is not met. Therefore, the quasi-random Sobol sequences were used in this study.

It is recommended to perform the input parameter sampling for EE analyses from a uniformly distributed sampling space,[3] denoted the **U**-space. This is achieved by mapping the set of input parameters, **X**, from the physical space (X-space), to uncorrelated uniformly distributed variables, **U**, based on Equation (2).

$$X_i = F_i^{-1}(U_i). \tag{2}$$

Here, F_i^{-1} is the inverse cumulative distribution function (CDF) of X_i, and U_i is an independent stochastic variable uniformly distributed in the range [0,1]. This sampling method ensures an appropriate concentration of base points at the most probable regions of the parameter space for each variable.

Finally, the step sizes in the physical and uniformly distributed space, Δ_i and Δ_F, are defined. The step size in the physical space is given implicitly by the transformation in Equation (2) and is expressed by Equation (3)
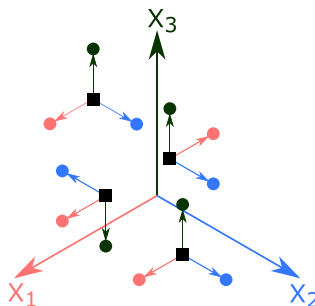

FIGURE 1 Illustration of the radial elementary effects method for three parameters ($I = 3$) and four base points ($J = 4$). The squares correspond to the base points, while the circles are the perturbed points. Adopted from Campolongo et al[26] and Robertson et al.[9]

$$X_i \pm \Delta_i = F_i^{-1}(U_i \pm \Delta_F). \tag{3}$$

In some studies,[26] the step size is treated as a random variable while other studies[9] use a fixed Δ_F with a random sign. The latter approach is adopted in the present work. To select the step size, it shall be ensured that Δ_F is sufficiently large to give a measurable change in the quantity of interest between the base point realisation $Y_{bp}^j(\mathbf{X})$ and the perturbed realisation $Y_{pp}^j(\mathbf{X})$. Additionally, it is desirable that the resultant step size Δ_i ensures an approximately linear variation between $Y_{bp}^j(\mathbf{X})$ and $Y_{pp}^j(\mathbf{X})$. $\Delta_F = 0.1$ was used here, as it gives measurable changes in $Y(\mathbf{X})$, while it is assumed to be small enough to ensure approximate linearity.

2.1.2 | Identification of important parameters

The quantity of interest for the sensitivity analysis in the present study is the long-term fatigue damage, denoted as D_{LT}. Therefore, the *EE* formulation from Equation (1) is now expressed as

$$EE_i^j = \frac{D_{LT}(X_1^j, ..., X_i^j \pm \Delta_i, ..., X_I^j) - D_{LT}(X_1^j, ..., X_i^j, ..., X_I^j)}{\pm \Delta_F}. \tag{4}$$

Several locations along the OWT support structure are considered, as different parameters may be important at different locations. The locations used are the tower top, tower base and seafloor, in addition to the location corresponding to the maximum monopile fatigue damage in each turbine. Identification of important parameters is done via evaluation of the absolute mean, $\mu_{EE,i}^*$, and variance, $\sigma_{EE,i}^2$, of the EE related to each input parameter:

$$\mu_{EE,i}^* = \frac{1}{J} \sum_{j=1}^{J} |EE_i^j|, \tag{5}$$

$$\sigma_{EE,i}^2 = \frac{1}{J-1} \sum_{j=1}^{J} \left(EE_i^j - \mu_i\right)^2. \tag{6}$$

High $\mu_{EE,i}^*$ indicates an important parameter, while a large $\sigma_{EE,i}$ indicates coupling with other parameters. The mean, μ_i, in Equation (6) is defined as

$$\mu_i = \frac{1}{J} \sum_{j=1}^{J} EE_i^j. \tag{7}$$

2.2 | Discrete analysis method

The discrete parameters varied in this study are the wind coherence model, inclusion/exclusion of wave spreading, variation of wave spectral models and soil models, as well as inclusion/exclusion of scour protection in the structural model. These variations cannot be described by a probability density function (PDF), and the effect of discrete parameter variations are evaluated based on the change in fatigue damage compared to the baseline case (see Section 4.2). Only one discrete parameter is varied at a time, meaning that interactions between discrete parameters are not captured. However, the discrete analyses are repeated for all J base points from the continuous simulations. Interactions with the continuous parameters can therefore be captured. The relative change in fatigue damage is calculated as

$$\delta D_i^j = \frac{|D_{LT}^{BL}(\mathbf{X^j}) - D_{LT}^{Var\,i}(\mathbf{X^j})|}{D_{LT}^{BL}(\mathbf{X^j})}. \tag{8}$$

$D_{LT}^{BL}(\mathbf{X^j})$ is the long-term fatigue damage using the baseline model at realization j of the continuous parameters. $D_{LT}^{Var\,i}(\mathbf{X^j})$ is the long-term fatigue damage when using alternative model i.

The effect of changing each model is evaluated based on the absolute mean, $\mu_{\delta D,i}^*$, and variance, $\sigma_{\delta D,i}^2$, of the relative change in fatigue damage:

$$\mu_{\delta D,i}^* = \frac{1}{J} \sum_{j=1}^{J} |\delta D_i^j|, \tag{9}$$

$$\sigma^2_{\delta D, i} = \frac{1}{J-1} \sum_{j=1}^{J} (\delta D_i^j - \mu_{LT,i})^2. \tag{10}$$

As for the continuous parameters, a high $\mu^*_{\delta D, i}$ indicates an important parameter. A high $\sigma_{\delta D, i}$ means there is a significant coupling between discrete model i and the continuous parameters. The mean, μ_i, in Equation (10) is defined as

$$\mu_{\delta D, i} = \frac{1}{J} \sum_{j=1}^{J} \delta D_i^j. \tag{11}$$

3 | MODEL DESCRIPTION

This section summarises the simulation models, turbine and foundation properties, load models and all relevant information for fatigue damage calculation.

3.1 | Turbine models

Three turbine models have been used in the study; the NREL 5 MW,[30] the DTU 10 MW[31] and the IEA 15 MW[32] reference wind turbines. The simulation models are based on the reference wind turbines, supported by different monopile foundations. The 5-MW foundation is based on the OC3 monopile[33] and the 10-MW foundation is based on Velarde and Bachynski.[34] The 15-MW tower is based on the original design,[32] while the monopile is designed for a target natural period below 5.5 s and verified using the method in Katsikogiannis et al.[35] Each of the three turbines applies its corresponding controller: the NREL Baseline Wind Turbine Controller,[30] the Basic DTU Wind Energy Controller[36] and NREL's Reference OpenSource Controller,[37] respectively. The turbines are assumed located at 30 m water depth on the Norwegian Continental Shelf, at (55.11°N, 3.47°E). Soil conditions at the site are assumed to consist of an idealized clay profile with linearly increasing undrained shear strength and parabolic variation of shear modulus with depth. Both operational and parked conditions are considered, using the same environmental conditions. Details of the key parameters of the different turbines are given in Table 2, while an illustration of the models is shown in Figure 2.

TABLE 2 Key parameters of the NREL 5 MW, DTU 10 MW and IEA 15 MW reference wind turbines including foundation

Parameter	Unit	NREL	DTU	IEA
Rated power	MW	5	10	15
Rated wind speed	m/s	11.4	11.4	10.59
Rated rotor speed	rpm	12.1	9.6	7.56
Hub height	m	90	119	150
Rotor diameter	m	126	178.3	240
RNA mass	tonnes	350	674	1017
Tower top diameter	m	3.87	6.25	6.54
Tower base diameter	m	6.00	9.18	9.96
Tower top wall thickness	m	0.025	0.035	0.024
Tower base wall thickness	m	0.035	0.063	0.036
Monopile diameter	m	7	9	11
Monopile wall thickness	m	0.07	0.11	0.11
Embedded length	m	28	36	44
1st fore-aft natural period[a]	s	3.9	3.6	5.3

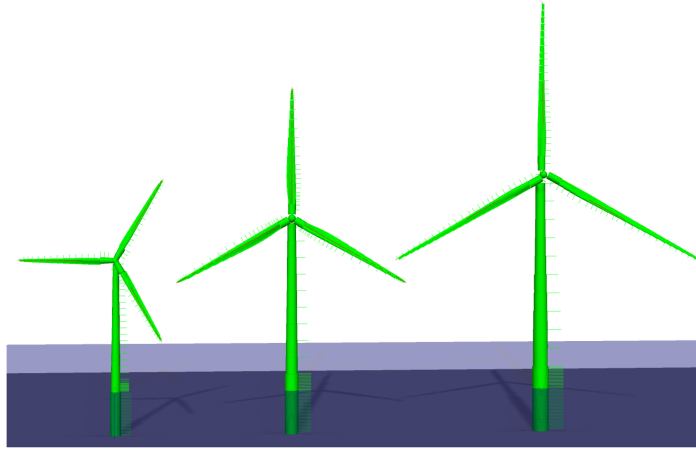[a]Using mean value of uncertain parameters, see Table 3.

FIGURE 2 Illustration of the three SIMO-RIFLEX models in SIMA. From left to rigth: NREL 5 MW, DTU 10 MW and IEA 15 MW. The models are to scale, illustrating the size differences between the turbines

3.2 | Environmental model

Several numerical hindcast models are available for the northeast Atlantic Ocean. For the present study, the Norwegian Reanalysis Archive (NORA10)[38] hindcast data have been used. The database has 3-h resolution for the years 1957 to 2017 at the site, and provides information about met-ocean parameters such as mean wind speed 10 m above sea level, significant wave height (H_s), wave peak period (T_p) and wind-wave directionality.

To limit computational requirements, only three wind bins ($N_U = 3$) were considered: Close to the rated speed (8–10 m/s), intermediate (14–16 m/s) and high (20–22 m/s) wind speeds. The wave climate is assumed dependent on wind speed through the use of representative sea-state parameters (H_s - T_p) for each wind bin, based on the lumping method described by Katsikogiannis et al.[35] A Pierson–Moskowitz wave spectrum is used at the lowest wind speed, and a JONSWAP spectrum is used for the two higher wind speeds. The wind direction is assumed independent of other environmental parameters, while the wind-wave misalignment is assumed conditional on the wind speed.[48] The probability of an environmental condition at a base point j is given by Equation (12).

$$P^j(U_k, \theta_{wi}, \theta_{rel,m}) = P^j_n(U_k) \cdot P^j(\theta_{wi}) \cdot P^j_n(\theta_{rel,m}|U_k). \tag{12}$$

$P^j_n(U_k)$ is the frequency of occurrence of wind bin k, normalised to a total value of 1 based on Equation (13).

$$P^j_n(U_k) = \frac{P^j(U_k)}{\sum_{k=1}^{N_U} P^j(U_k)}. \tag{13}$$

$P^j(\theta_{wi})$ is the probability of occurrence of the wind direction, and $P^j_n(\theta_{rel,m}|U_k)$ is the conditional probability of the wind-wave misalignment. Two misalignment angles ($N_{\theta_{rel}} = 2$) were considered for each wind bin, 0° (aligned wind-waves) and 30°. Similarly to wind speed, the probability of the wind-wave misalignment angle for each wind bin is normalised to a sum of 1 as follows:

$$P^j_n(\theta_{rel,m}|U_k) = \frac{P^j(\theta_{rel,m}|U_k)}{\sum_{m=1}^{N_{\theta_{rel}}} P^j(\theta_{rel,m}|U_k)}. \tag{14}$$

The values of $P^j(U_k), P^j(\theta_{wi})$ and $P^j(\theta_{rel,m}|U_k)$ are found by integrating the probability distributions given in Section 4.1 between the lower and upper limits for each bin considered. Two seed variations have been used for each environmental condition, to capture stochastic variations in the wind and wave loads.

3.3 | Simulation models

The rotor-nacelle assembly, tower and monopile above seabed were modelled in the aero-hydro-servo-elastic simulation tool SIMO-RIFLEX developed by SINTEF Ocean.[49,50] Structural components above seafloor are modelled as linear-elastic beam elements. The monopile part below seabed (foundation model) is described in detail in Section 3.4. The incoming wind field is generated using the program TurbSim from NREL[51] for the Kaimal spectrum and exponential coherence model, and IEC Turbulence Simulator from DTU for the Mann turbulence model.[52]

3.4 | Foundation model

The foundation model is a nonlinear macroelement model formulated within elastoplasticity theory. Macroelement models condense the response of the foundation and surrounding soil to a force-displacement relation at seafloor, separating the foundation and the rest of the structure.[53] The macroelement model has been developed to reproduce the nonlinear load-displacement response and the hysteretic damping of monopile-based OWTs in integrated time-domain analyses.[54–56] The basic features and limitations of the model are presented by Page et al.[55]

The macroelement model used in this study accounts for the change of the foundation stiffness due to nonlinear hysteretic soil behaviour, and as a consequence reproduces hysteretic damping. The model also accounts for the effect of multi-directional loading, which has been found to affect the foundation stiffness and hysteretic damping.[56] The model is calibrated to results of full 3D continuum modelling of the soil volume and the foundation by FEA. Even though the model have been calibrated to an idealized clay profile the results are equally valid for monopiles installed in sand. The importance here is the effect of the monopile head stiffness and how this influences the integrated analysis. The model communicates with SIMO-RIFLEX through a dynamic link library (DLL). The macroelement model does not directly compute the forces along the monopile below seabed, and a separate postprocessing numerical tool has been employed for that purpose. The tool is based on beam on spring model where the springs are calibrated to the results of the FEA using the methodology presented in Klinkvort et al.[57]

3.5 | Load models

Aerodynamic loads on the blades are calculated using blade element momentum theory with the Glauert induction and Prandtl tip loss corrections,[58] as well as dynamic stall and dynamic wake corrections. Hydrodynamic excitation loads are calculated using linear wave kinematics and MacCamy and Fuchs formulation[59] with Morison type drag. The hydrodynamic added mass is assumed to be constant, corresponding to an added mass coefficient $C_A = 1.0$.

3.6 | Fatigue damage estimation

Fatigue damage is estimated based on the axial stress in the monopile and tower. Individual stress cycles are identified using the rainflow counting technique implemented in the WAFO toolbox,[60] modified to allow for bi-linear S-N curves. The fatigue damage is calculated using Miner's sum[43] with thickness effects included. DNV GLs fatigue curve "D" for steel in sea water with cathodic protection was used for the monopile, while curve "D" for steel in air was selected for the tower.[43] The short-term fatigue utilization is calculated according to Equation (15).

$$D_{ST} = \frac{1}{\Delta_C} \sum_{i=1}^{n_\sigma} \frac{(\Delta\sigma_i)^{m_i}}{a_i} \left(\frac{t}{t_{ref}}\right)^{km_i}.$$

(15)

D_{ST} is the fatigue damage obtained from 1-h time-domain realisation for each environmental condition, Δ_C is the fatigue capacity and $\Delta\sigma_i$ are the individual stress ranges. m_i and a_i are the fatigue exponent and SN localisation parameters associated with each stress range. Finally, t is the wall thickness, t_{ref} is the reference wall thickness, and k is the thickness exponent on fatigue strength. A reference thickness equal to 25 mm and a thickness exponent of 0.2 were used.[43] The long-term fatigue damage, D_{LT}, is found by combining the short-term fatigue damage with the probability of occurrence for the associated environmental conditions.

4 | PARAMETERS FOR SENSITIVITY ANALYSIS

The selection of parameters for the sensitivity analysis is partly based on previously performed studies. In addition, some parameters have been added at the authors' discretion, while a limited number of parameters have been excluded due to the capabilities of the utilized simulation

software. For the continuous parameters, this selection is based on the studies in Table 1. Discrete parameters are selected based on studies on individual parameters.

4.1 | Continuous parameters

16 continuous parameters are considered in the SA, shown in Table 3. Details for the selected parameters are given in the following sections. A distinction from the distributions used in many previous studies is that the uncertainty in the design values for environmental conditions has been used. This approach is expected to give a more accurate prediction of the sensitivities than considering the short-term variability ("V" in Table 1, illustrated in Section 4.1.3). Where appropriate, the distributions are truncated 3 standard deviations above/below the mean to avoid nonphysical realizations.

4.1.1 | Wind speed

The uncertainty in the design wind speed is modelled as uncertainty in the parameters of a two-parameter Weibull distribution. Using 60 years of hindcast data from the NORA10 database,[38] a two-parameter Weibull distribution was fitted to the yearly data. This corresponds to assuming one year of measurements is available for the design, as required by design guidelines.[45] The uncertainty in the shape (α) and scale (β) parameters was assessed, and the scale parameter was found to be most important for variations in the fitted distribution. Only the scale parameter was treated as a stochastic variable, as it is desirable to limit the number of input parameters for the SA. A normal distribution was fitted to the scale parameter, while the shape parameter was taken as the value found from the fitted distribution to the full 60 years of data. The probability of occurrence for each wind speed bin is found based on Equation (16), while Table 4 summarises the wind speed distribution parameters used for the 10-MW turbine in the study. Values for the 5- and 15-MW turbines are extrapolated assuming the mean wind shear profile (Section 4.1.3).

TABLE 3 Distribution of continuous parameters considered for the sensitivity analysis

Parameter (X_i)	Symbol	Distribution	Section	Reference
Wind speed	U	-	Section 4.1.1	NORA10[38]
Wind direction	θ_{wi}	-	Section 4.1.2	NORA10[38]
Turbulence intensity	TI	-	Section 4.1.3	FINO1[39]
Wind shear	α	N(0.14,0.01)	Section 4.1.3	FINO1[39]
Yaw error	γ_Y	N(0°, 1°)	Section 4.1.4	Veldkamp[13]
Significant wave height	H_s	-	Section 4.1.5	NORA10[38]
Peak period	T_p	-	Section 4.1.5	NORA10[38]
Wind-wave misalignment	θ_{rel}	-	Section 4.1.6	NORA10[38]
Marine growth	t_{mg}	N(100 mm, 35 mm)	Section 4.1.7	Jusoh & Wolfram[40]
Drag coefficient	C_d	N(0.7,0.1)	Section 4.1.7	Peeringa & Bedon,[4] Veldkamp[13]
Undrained shear strength	s_u/σ'_{v0}	N(1,0.15)	Section 4.1.8	Lacasse & Nadim[41]
Void ratio	e	N(0.7,0.058)	Section 4.1.8	Lacasse & Nadim[41]
Monopile diameter	D_p	U(0.999μ, 1.001μ)	Section 4.1.9	Zaaijer,[42] Hübler et al.[5]
SN parameters	$\log(a_{1,2})$	-	Section 4.1.10	DNV GL[43]
Fatigue capacity	Δ_C	LN(1,0.3)	Section 4.1.10	Folsø et al.,[44] Peeringa&Bedon[4]
Unavailability	A	LN(0.1,0.025)	Section 4.1.11	DNV GL,[45] Pfaffel et al.,[46] Larsen et al.[47]

Note: -: Not described by a single distribution. N(μ,σ): Normal distribution mean μ and standard deviation σ. LN(μ,σ): Log-normal distribution mean μ and standard deviation σ. U(X_l,X_u): Uniform distribution with lower and upper limits X_l, X_u.

TABLE 4 Wind speed distribution parameters at 119 m above sea level

Parameter	Type	Distribution/value
Scale parameter, β	Stochastic	N(12.62,0.51)
Shape parameter, α	Deterministic	2.32

$$P^j(U_k;\alpha,\beta^j) = F_{wi}(U_{k,u};\alpha,\beta^j) - F_{wi}(U_{k,l};\alpha,\beta^j). \tag{16}$$

$F_{wi}(x;\alpha,\beta)$ is the Weibull CDF, U_k is the mean wind speed of bin k, while $U_{k,l}$, and $U_{k,u}$ are the lower and upper limits of the wind bin k. Superscript j represents the value of the stochastic variables at a base point j.

4.1.2 | Wind direction

Wind direction is treated similarly as the wind speed, with the uncertainty of the long-term distribution being modelled as variations in the distribution parameters. An individual distribution is fitted to each year in the NORA10 dataset. The probability of occurrence of a wind direction is found in Equation (17).

$$P^j(\theta_{wi}) = \int_{\theta_l}^{\theta_u} f(\theta_{wi};\mu,\kappa,\omega)d\theta_{wi}. \tag{17}$$

$f(\theta_{wi};\mu,\kappa,\omega)$ is the PDF of the wind direction, with θ_l, θ_u the lower and upper limits of the directionality bins. A three-mode von Mises mixture distribution is fitted to the yearly data.[61] Adopting the notation from Masseran et al,[61] the PDF of the distribution is expressed by Equation (18).

$$f(\theta_{wi};\boldsymbol{\mu},\boldsymbol{\kappa},\boldsymbol{\omega}) = \sum_{h=1}^{H} \omega_h \frac{1}{2\pi I_0(\kappa_h)} e^{\kappa_h \cos(\theta_{wi}-\mu_h)}. \tag{18}$$

Here, θ_{wi} is the wind direction in radians, while μ_h, κ_h and ω_h denote the mean direction, the concentration factor, and the weighting factor of each mode h, respectively.[61] The fitted PDF accounting for all years in the NORA 10 database is shown in Figure 3.

The variation in the fitted parameters was evaluated, and no correlation was observed. To limit the number of variables, only the mean values of the second and third modes were considered as stochastic variables. Both follow a normal distribution, as given in Table 5. The variation of the mean values is thus assumed to be representative of the uncertainty in the wind direction model.

With mode 1 being fixed, it is assumed that changing the mean of mode 2 and 3 towards a direction aligned with mode 1 (towards 58°) will increase the lifetime fatigue damage. Assuming mode 2 and 3 are related by

$$F_{\mu_3} = 1 - F_{\mu_2} \tag{19}$$

will ensure that mode 2 and 3 are either both more aligned with or more perpendicular to mode 1. This allows for representing the uncertainty in wind direction as one uncertainty in the two coupled parameters. However, the coupling is also likely to introduce overestimation of the
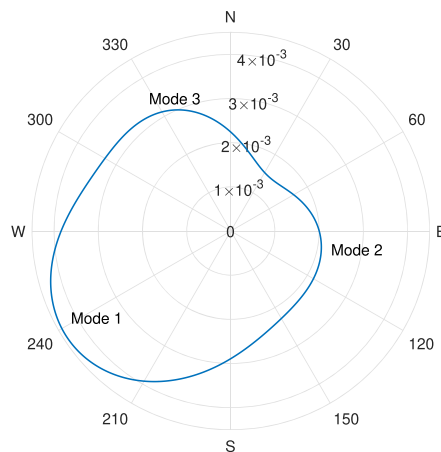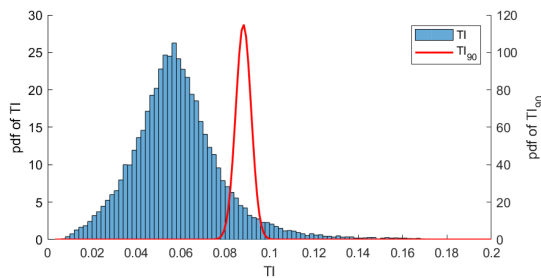

FIGURE 3 Fitted wind direction distribution for all years in NORA10 database

TABLE 5 Wind direction distribution parameters

Parameter	Type	Distribution/Value
μ_1	Deterministic	238°
μ_2	Stochastic	N(100°, 28.4°)
μ_3	Stochastic	N(333°, 43.3°)
κ_1	Deterministic	1.29
κ_2	Deterministic	1.10
κ_3	Deterministic	3.47
ω_1	Deterministic	0.598
ω_2	Deterministic	0.261
ω_3	Deterministic	0.142

Note: The uncertainty in the wind direction is modelled by the variations in μ_2 and μ_3.

FIGURE 4 Distribution of 10-min turbulence intensity (TI) and design turbulence intensity (TI_{90})

importance of wind direction, as the fatigue damage may change more than if μ_2 and μ_3 were uncoupled. It should also be noted that the wind direction distribution also influences the wave direction, as the wave direction is modelled implicitly by the relative wind-wave direction in Section 3.2. The uncertainty in the wind-wave misalignment is treated separately in Section 4.1.6.

4.1.3 | Turbulence intensity and wind shear

The turbulence intensity and wind shear are assessed using 15 years of measurements from the FINO1 platform.[39] For turbulence intensity, the data from the topmost anemometer, 100 m above mean sea level (MSL), are used. To avoid wake effects from the nearby alpha ventus wind farm, only measurements from the westerly direction (180–360°) are used. Only data that have passed the FINO 1 quality check are considered.[39] A log-normal distribution is fitted to the wind speed dependent turbulence intensity distribution for each year.[62] The 90th percentile value for the turbulence intensity is taken as the design value for each wind speed.[45] A normal distribution is fitted to the yearly design turbulence intensity and taken as input for the sensitivity analysis.

Turbulence intensity clearly demonstrates the difference between considering the short-term variability in an environmental parameter (as marked with "V" in Table 1) and the uncertainty in the design parameter. Figure 4 shows the probability distribution of the 10 min turbulence intensity measurements from FINO1 and the distribution of the 1-year design values. A significant reduction in the uncertainty is seen when considering the latter.

To limit the number of independent variables in the SA, the same percentile is used for the TI in the different wind bins (refer Section 2.1.1). Table 6 gives the distribution parameters for the turbulence intensity.

A power law wind profile is fitted to the measurements using the mean 10-min wind speed at the eight anemometers located from 33 to 100 m above MSL.[63] In addition to the exclusion zone of 0–180° mentioned for the turbulence intensity, data from wind directions between 270° and 360° are excluded from the fitting to avoid shadow effects from the met-mast.[64] Furthermore, data samples with goodness-of-fit (R^2-value) less than 0.75 are excluded. The 1-year mean is taken as the design value for the wind shear.[45] Equation (20) shows the applied power law

TABLE 6 Distribution of design turbulence intensity for each wind bin

Wind speed class (m/s)	Distribution
8–10	N(9.20%, 0.62%)
14–16	N(8.82%, 0.35%)
20–22	N(8.82%, 0.42%)
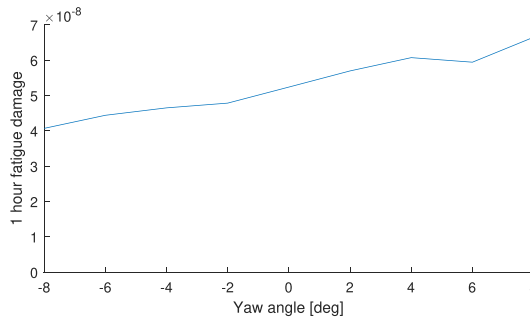
FIGURE 5 Average 1-h fatigue damage in tower base for various yaw angles

formulation, where U is the wind speed at height z and α is the power law exponent. A normal distribution with mean 0.14 and standard deviation 0.01 was fitted to the 1-year mean values of α (Table 3).

$$U(z) = U_{ref} \left(\frac{z}{z_{ref}} \right)^{\alpha}.$$ (20)

4.1.4 | Yaw error

Veldkamp[13] assigns a normal distribution with mean 0° and standard deviation 1° to the yaw error. On the other hand, the design codes[1,45] require fatigue analysis to be carried out for yaw misalignments of −8°, 0° and 8°. To avoid increasing the already large computational effort, it was desirable to use only one yaw angle in the simulations. A screening study showed that no single yaw error could predict the correct fatigue damage across the whole support structure. However, the elementary effects method is based on the derivatives of fatigue damage w.r.t. to input parameters. Figure 5 shows the fatigue damage in the tower base of the DTU 10-MW turbine as function of yaw angle, averaged over the wind speeds being used in this study. Although there is a noticeable difference in the fatigue damage at the different yaw angles, the gradient is approximately constant. It was concluded that a single yaw error could be used for the SA. The yaw error was, therefore, modelled using the distribution from Veldkamp.[13]

4.1.5 | Significant wave height and peak period

The wind speed-dependent scatter diagrams of the wave climate are represented by a single lumped sea-state for each wind speed bin. Following the frequency-domain lumping method described by Katsikogiannis et al,[35] one damage-equivalent lumped load case is found for each year of the 60-year NORA10 database.[38] Therefore, for each wind bin, 60 $H_s - T_p$ combinations are found, as shown in Figure 6 for the 14–16 m/s bin. A normal distribution was fitted to the H_s, T_p parameters of the sea-state parameters of the lumped load cases, shown in Table 7. Although Figure 6 strongly suggests there is a correlation between H_s, T_p, this correlation is disregarded to allow assessing the sensitivity of H_s and T_p individually.
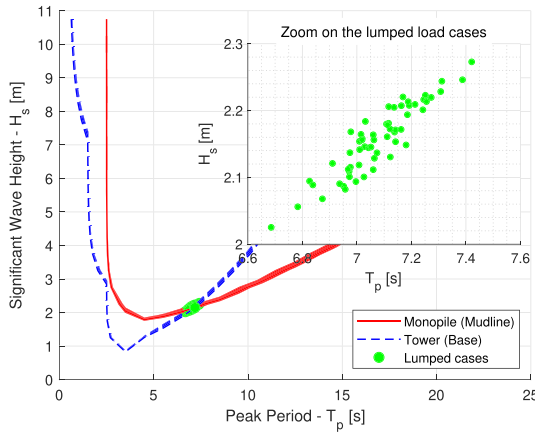
FIGURE 6 Lumped load cases for wind bin 14–16 m/s. Lines represents damage-equivalent sea states for the tower and monopile. The dots give sea states that will reproduce the lifetime fatigue damage in both the tower and monopile. One dot is seen for each year in the NORA10 data set

TABLE 7 Distribution of lumped sea-state parameters H_s, T_p for each wind bin

Wind speed bin (m/s)	5 MW		10 MW		15 MW	
	H_s (m)	T_p (s)	H_s (m)	T_p (s)	H_s (m)	T_p (s)
8–10	N(1.27, 0.03)	N(6.42, 0.11)	N(1.24, 0.05)	N(6.37, 0.15)	N(1.28, 0.03)	N(7.29, 0.15)
14–16	N(2.29, 0.03)	N(7.27, 0.12)	N(2.16, 0.05)	N(7.08, 0.14)	N(2.08, 0.06)	N(7.04, 0.22)
20–22	N(3.73, 0.09)	N(8.48, 0.21)	N(3.49, 0.07)	N(8.24, 0.18)	N(3.36, 0.07)	N(8.13, 0.21)

TABLE 8 Distribution parameters for wind-wave misalignment per wind bin

Wind speed bin (m/s)	Distribution	
	Mean	$\sigma_{\theta_{rel,m}|U_k}$
8–10	0°	N(47.9°, 2.5°)
14–16	0°	N(24.6°, 3.0°)
20–22	0°	N(15.7°, 2.0°)

4.1.6 | Wind-wave misalignment

The wave directional properties are assumed described by the wind direction and wind-wave misalignment conditional on the wind speed, similar to Horn et al.[48] The misalignment was found to follow a normal distribution, with a mean of 0° for all wind speeds. This gives the standard deviation of the misalignment, $\sigma_{\theta_{rel,m}|U_k}$, as the uncertain parameter. By analysing the NORA10 data, a normal distribution was found to be a reasonable fit for $\sigma_{\theta_{rel,m}|U_k}$. The probability of being in misalignment bin m is given as

$$P^i(\theta_{rel,m}|U_k) = 2\left(F(\theta_{m,u}; 0, \sigma^j_{\theta_{rel,m}|U_k}) - F(\theta_{m,l}; 0, \sigma^j_{\theta_{rel,m}|U_k}) \right). \quad (21)$$

Here, $F(x; \mu, \sigma)$ denotes the cumulative normal distribution with mean μ and standard deviation σ. $\theta_{m,u}$ and $\theta_{m,l}$ denote the upper and lower limits of the misalignment bin, respectively. $\sigma_{\theta_{rel,m}|U_k}$ is the wind speed dependent standard deviation of the misalignment. The multiplication with 2 assumes that positive and negative misalignment angles can be treated as equal. The properties of the misalignment model are given in Table 8.

4.1.7 | Marine growth and drag coefficient

Marine growth is modelled using the depth varying thickness profile found in GL's standards for offshore wind turbines.[65] The uncertainty is modelled by scaling the marine growth at all depths equally, where the mean value at mean sea level is set to 100 mm.[45] The standard deviation is taken from Jusoh and Wolfram[40] using the coefficient of variation (C.o.V.) for mussels in the Southern North Sea, as mussels are the most prominent growth in shallow waters.[66] A normal distribution is assumed, and the shape of the depth-dependent thickness profile is assumed constant.

The drag coefficient is assumed normally distributed with a mean of 0.7 and a standard deviation of 0.1.[4,13] In principle, there is a relationship between the marine growth and the drag coefficient. However, the drag coefficient depends on the surface roughness of the marine growth, not the thickness.[40] Therefore, the marine growth and drag coefficient are assumed independent of each other in the present study.

4.1.8 | Undrained shear strength and void ratio

The undrained shear strength, s_u, and shear modulus, G_{max}, at small strains are considered the most important uncertainties for the present soil profile. These are included in the study as s_u/σ'_{v0} and void ratio, e, respectively. σ'_{v0} is the vertical effective stress. Laccasse and Nadim[41] assign a normal distribution to s_u/σ'_{v0}, with mean value 1 and a standard deviation in the range 5–15%. The upper limit of 15% has been used here.

The void ratio, e, typically has a coefficient of variation of 7–30%.[41] However, physical bounds linked to e_{min} and e_{max} dictate a coefficient of variation of maximum 8.3% for the assumed soil profile. Therefore, a normal distribution with mean 0.7 and standard deviation 0.058 is assumed.

4.1.9 | Monopile diameter

Zaaijer[42] assumes a variation of $\pm$ 0.1% in the diameter of monopile foundations. Hübler et al[5] translated this to a uniform distribution with upper and lower bound 0.1% from the nominal diameter. The same uncertainty model is used in the present study.

4.1.10 | Fatigue parameters

Consistent with other studies,[4,6] uncertainty in the SN curve (Equation 15) is modelled as uncertainty in the intercept parameter, a, while the negative inverse slope, m, is modelled as deterministic. DNV GL gives the standard deviation in $\log(a_{1,2})$ as 0.2, and states that the design curves are given as the mean minus two standard deviations.[43] This gives the SN-parameters in Table 9 when using suitable design SN curves. In addition to the SN curve parameters, the fatigue capacity Δ_C is modelled as uncertain. This is assumed to follow a lognormal distribution with mean value 1 and standard deviation 0.3.[4,44]

4.1.11 | Availability

Little information is available concerning the availability of individual OWTs over the full lifetime. Design standards[45] consider an availability of 90%,[45] while various sources state average availability of wind farms in the range 85–96%.[46,47] Availability as low as 80.3% for the first three operational years has been reported as an extreme case.[67] Here, a lognormal distribution is assumed for the unavailability (100% - availability). This is done to avoid sampling availability above 100%, corresponding to unavailability below 0%. A mean value of 10% is assumed as indicated by design standards,[45] while the standard deviation is set to 2.5%. The latter corresponds to experience from two wind farms.[46]

TABLE 9 SN curve parameters

Parameter	Type	Tower	Monopile
$\log(a_1)$	Stochastic	N(12.564, 0.2)	N(12.164, 0.2)
$\log(a_2)$	Stochastic	N(16.006, 0.2)	N(16.006, 0.2)
m_1	Deterministic	3	3
m_2	Deterministic	5	5

4.2 | Discrete parameters

Five discrete parameters are considered in the study. The discrete parameters differ from the continuous, as a probability density function cannot be assigned to them. One discrete parameter is changed at a time, with the remaining parameters being kept at the baseline value. The calculations are repeated for all base points in the continuous analysis. A summary of the parameters is given in Table 10, with details given in the following sections. The baseline case corresponds to the modelling choices that were used for analysing the continuous parameters.

4.2.1 | Turbulence and coherence model

The Kaimal turbulence model with exponential coherence and Mann uniform shear turbulence model are compared in the study. These are recommended for design load calculations by IEC 61400-1 4th Ed.[68] In the present study, three models are compared: the Kaimal model with spatial coherence only in longitudinal direction (baseline case), the Kaimal model with spatial coherence in three directions, and the Mann model. The design standard does not provide values of the decrement ($\alpha_{u,v,w}$) and offset ($b_{u,v,w}$) coherence parameters for the lateral (v) and vertical (w) components for the exponential coherence. These are defined similarly as in Wise et al,[69] and variability in these parameters is not considered. Spatial coherence is inherently implemented in the Mann model, and the model parameters are determined based on IEC 61400-1.[68]

4.2.2 | Wave spreading

Traditionally, waves have been modelled as long-crested when performing fatigue analysis on OWTs. This is applied as the baseline model in this study, with the variation being short-crested waves. Short-crested waves are included by multiplying the unidirectional wave spectrum with a spreading function, as recommended by, for example, DNV[70]:

$$S(\omega,\theta;\theta_0) = S(\omega)D(\theta;\theta_p). \tag{22}$$

Here, $S(\omega)$ is the wave spectrum, while $D(\theta;\theta_p)$ is the spreading function with directional components θ and mean wave direction θ_p. The spreading function is modelled as

$$D(\theta;\theta_p) = \frac{\Gamma(1+n/2)}{\sqrt{\pi}\Gamma(1/2+n/2)}\cos^n(\theta-\theta_p), \tag{23}$$

with the spreading exponent n assumed equal to 2 for all sea states.

4.2.3 | Wave spectrum

To evaluate the effect of the wave spectrum, two alternative formulations are compared to the baseline wave spectra (Section 3.5). The first variation is the TMA wave spectrum,[70] which modifies the JONSWAP spectrum to account for finite water depth. This is done by multiplying the original spectrum by a depth function (Equation 24) based on the wave number $k = \omega^2/g \cdot \tanh kd$ and water depth d as shown in Equation (25).[70]

$$S_{TMA}(\omega) = S(\omega) \cdot \phi_{TMA}(\omega). \tag{24}$$

TABLE 10 Discrete parameter variations

Parameter	Baseline	Variations	
Coherence model	Coherence in x-direction	Coherence in x,y,z-directions	Mann model
Wave spreading	Long-crested	Short-crested	
Wave Spectrum	PM/JONSWAP	TMA	Torsethaugen
Soil Model	Macro element	$p-y$ curves	
Scour protection	No	Yes	

$$\phi_{TMA}(\omega) = \frac{\sinh^2(kd)}{\sinh^2(kd) + kd\coth(kd)}$$

(25)

The second variation is the Torsethaugen spectrum.[71] This is a two-peaked spectrum applicable in areas where there is an important swell component in addition to wind generated sea. The spectrum was established primarily for one location at the Norwegian Continental Shelf and is completely defined given the total significant wave height and spectral peak period. The model splits the energy into a swell component and wind-sea component, using a modified JONSWAP spectrum for both peaks.

4.2.4 | Soil-structure interaction model

The macro-element model described in Section 3.4 is the baseline soil-structure interaction model. The effect of the soil-structure interaction model has been evaluated by comparing the macro-element model, which incorporates hysteretic damping, against a $p - y$ curve-based beam on spring model. The latter is a more common approach, as these can easily be incorporated in simulation tools for OWTs. In the $p - y$ curves model, the monopile is modelled as a beam below seafloor, and the soil is represented by as a series of discrete, uncoupled elastic springs attached to nodal positions along the pile. Both models are calibrated to the same FEA results. In addition, soil damping is implemented in the monopile of the model using p-y curves as stiffness-proportional Rayleigh damping, tuned by a decay test to give the same damping ratio as the macro element (Section 5.3.2).

4.2.5 | Scour protection

Design calculations on monopile OWTs are typically performed without considering scour protection. To assess how the scour protection influences the response prediction, a 1.5-m-thick protection layer consisting of gravel and rocks was added to the foundation model (Section 3.4). The layer was assumed to be completely drained with a maximum mobilized angle of friction of 50° and an effective unit weight of 12 kN/m^3. For consistency in the results presentation, the seafloor is defined as the top of the original soil layer, i.e. below the scour protection.

5 | RESULTS

This section will present the results of the sensitivity analysis. First, the fatigue utilization from the 30 base points is presented in Section 5.1, before the results of the continuous parameters are given and discussed in Section 5.2. Finally, the results from the discrete parameters are presented in Section 5.3.

5.1 | Fatigue utilization

The fatigue utilization from the variations of the continuous parameters is shown in Figure 7. Grey lines show the results from the 30 different base points, while the black lines show the mean utilization. In the monopile, the fatigue utilization follows the same pattern in all turbines, with maximum fatigue damage 4–6 m below seafloor. The 5- and 10-MW towers both see the highest fatigue utilization in the base. A larger utilization is also seen towards the tower top, due to the rotor tilting moment. The 15-MW tower is optimized for the ultimate limit state.[32] As a result, the tower dimensions are more irregular, giving highest fatigue utilization ∼ 20 m below the tower top.

The variation in fatigue utilization among the base points is described by the coefficient of variation (C.o.V.) in Figure 7. This is fairly similar in all turbines, varying between 55% and 67%. All turbines show a slight increase in variability towards the tower top.

The contribution of individual wind speeds to the lifetime fatigue damage is determined by the short-term fatigue damage of each environmental condition and the probability of occurrence for that condition. Figure 8 shows this distribution for tower base and seafloor. The lower wind speeds contribute more to the fatigue damage as the turbine size increases, which is indicative of the wind loads becoming more important.[72] This is verified by considering the ratio between wind loads and wave loads in the three turbines. Assuming the aerodynamic moment at seafloor is given by quasi-static thrust force, F_a, and distance to the hub, z_{hub}, the aerodynamic moment can be written as
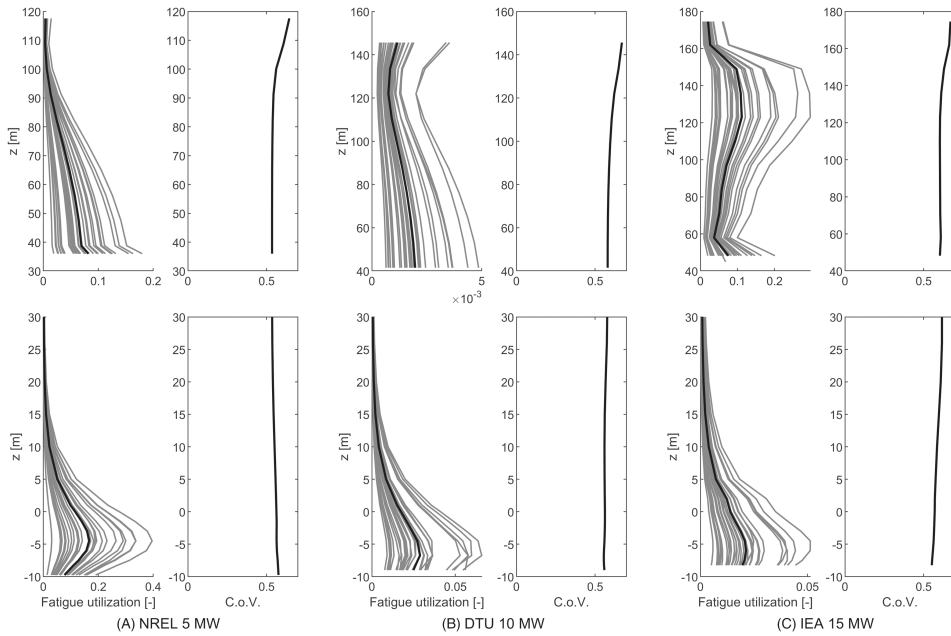
$$M_a = F_a z_{hub}.$$

(26)

FIGURE 7 Distribution of fatigue utilization and C.o.V. along the monopile and tower. The black line represents the mean of all base points, while grey lines are individual base points. Results in the lower part of the monopile are not shown. Seafloor is at $z = 0$
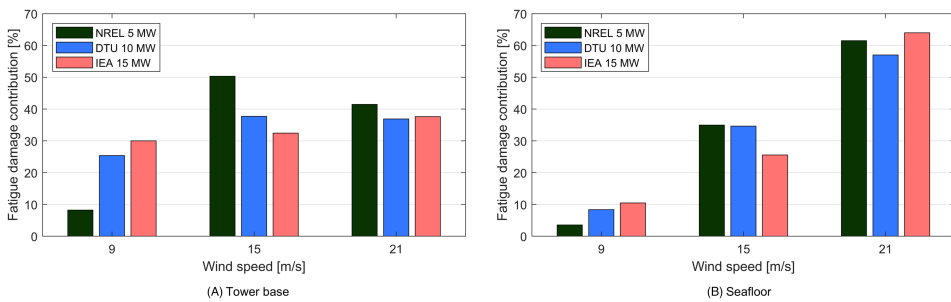

FIGURE 8 Contribution to fatigue utilization from wind speed classes

Similarly, the hydrodynamic moment is proportional to M_h if Morison's equation[73] is applied:

$$M_h = \rho C_m D_p^2 H_s T_p^{-2} h^2. \tag{27}$$

Here, ρ is the density of water, C_m is the mass coefficient equal to 2, D_p is the pile diameter and h is the water depth. Using the mean thrust, H_s and T_p from the wind bin 14–16 m/s in Table 7, the ratio M_a/M_h is approximately 25 for the 5-MW turbine, 35 for the 10-MW turbine and 43 for the 15-MW turbine. This shows that wind loads become more important as the turbine size increases.

Figure 9 shows the contribution from parked and operational conditions to the fatigue damage. It is known that parked conditions contribute significantly to the fatigue damage in monopile-supported OWTs due to the lack of aerodynamic damping and resonant response of the first global mode.[14] This is particularly true in the tower base, where the parked conditions of the 5-MW turbine account for $\sim 60\%$ of the fatigue
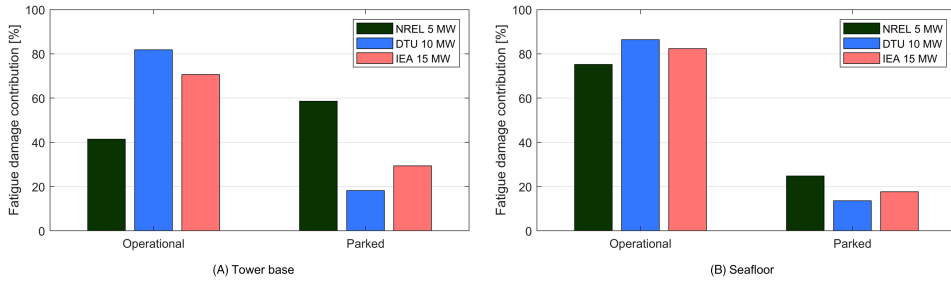
FIGURE 9 Contribution to fatigue utilization from operational and parked conditions
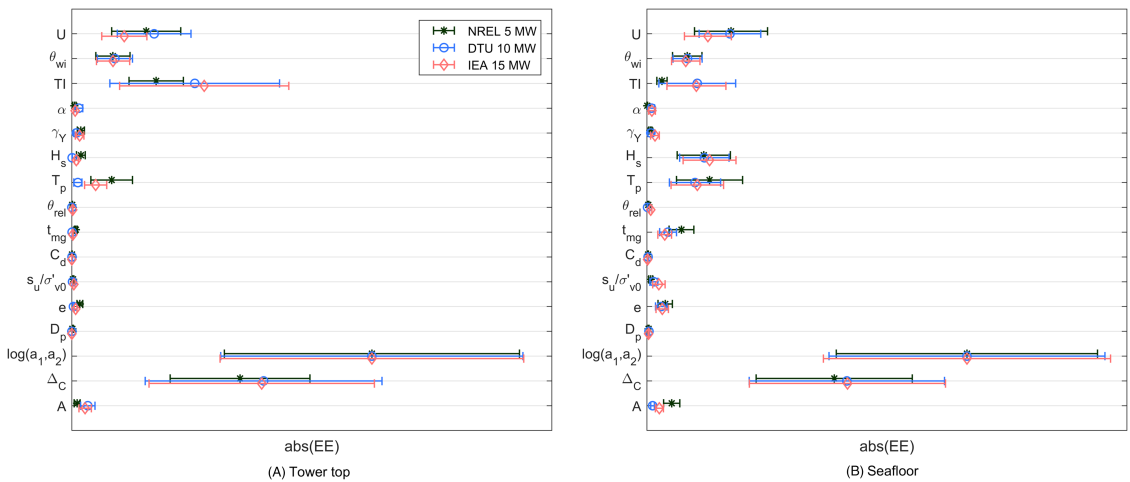

FIGURE 10 Statistics of the elementary effects at tower top and seafloor. The markers represent $\mu_{EE,i}^*$, while the bars show $\pm\sigma_{EE,i}$. All plots are scaled based on the largest mean value for each turbine and location. Confer Table 3 for definition of symbols

damage (Figure 9A). The effect is less pronounced in the larger turbines, where wave loads are less dominating for the response. Parked conditions are also significant in the fatigue utilization of the monopile (seafloor shown in Figure 9B). Only operational conditions contribute significantly to the fatigue damage in the tower top (not shown), as this is dominated by the rotor tilting moment and the generator induced side-side moment.

5.2 | Continuous parameter results

The uncertainty caused by the continuous parameters is evaluated using the absolute mean (μ_i^*) and standard deviation ($\sigma_{EE,i}$) of the elementary effects (Section 2.1). Figure 10 shows the results at the tower top and seafloor, with the tower base and monopile max fatigue showing similar results. The markers represent μ_i^* and the bar widths represent $\sigma_{EE,i}$. For each turbine and location, the values are normalized by the highest μ_i^* for that turbine and location. For all turbines and locations, the SN curve parameters $\log(a_1, a_2)$ have the largest influence on the uncertainty in fatigue utilization. The second-most influential parameter is the fatigue capacity, Δ_C. This is in accordance with the results by Peeringa and Bedon[4] and Velarde et al.[34] However, Velarde et al[6] found fatigue capacity to be the more important of the two. Both Peeringa and Bedon[4] and Velarde et al[6] have found the uncertainty in $\log(a_2)$ to be of far greater importance than $\log(a_1)$. This is due to the fatigue damage mainly being caused by stress cycles in the low-stress range of the SN curves. However, there has been little progress in reducing the uncertainty in fatigue parameters. Already in 1984, Wirsching[74] suggested distributions similar to those used today for both $\log(a_1, a_2)$ and Δ_C. One of the main goals of this paper is to suggest how to reduce uncertainty in the design process. As it is not expected that the uncertainty in the fatigue parameters

can be reduced within a design project, the fatigue parameters are omitted from the remaining results. The variation in $\log(a_1, a_2)$ and Δ_C are still included in the calculations, to capture potential interactions with the remaining parameters. When disregarding the fatigue parameters, the results are shown in Figure 11.

5.2.1 | Tower top

In the tower top, the most influential parameter is the turbulence intensity (TI), followed by wind speed distribution and wind direction distribution. For the 10- and 15-MW turbines the turbulence intensity is the parameter with the highest standard deviation in EE, indicating a significant coupling with other parameters. It should also be noted that with the current environmental model (Section 3.2) the wind speed distribution is not only a measure of the wind speed itself, but rather the severity of the environment at the site. This is caused by the environmental model used, where the H_s and T_p distributions are conditional on the wind class.
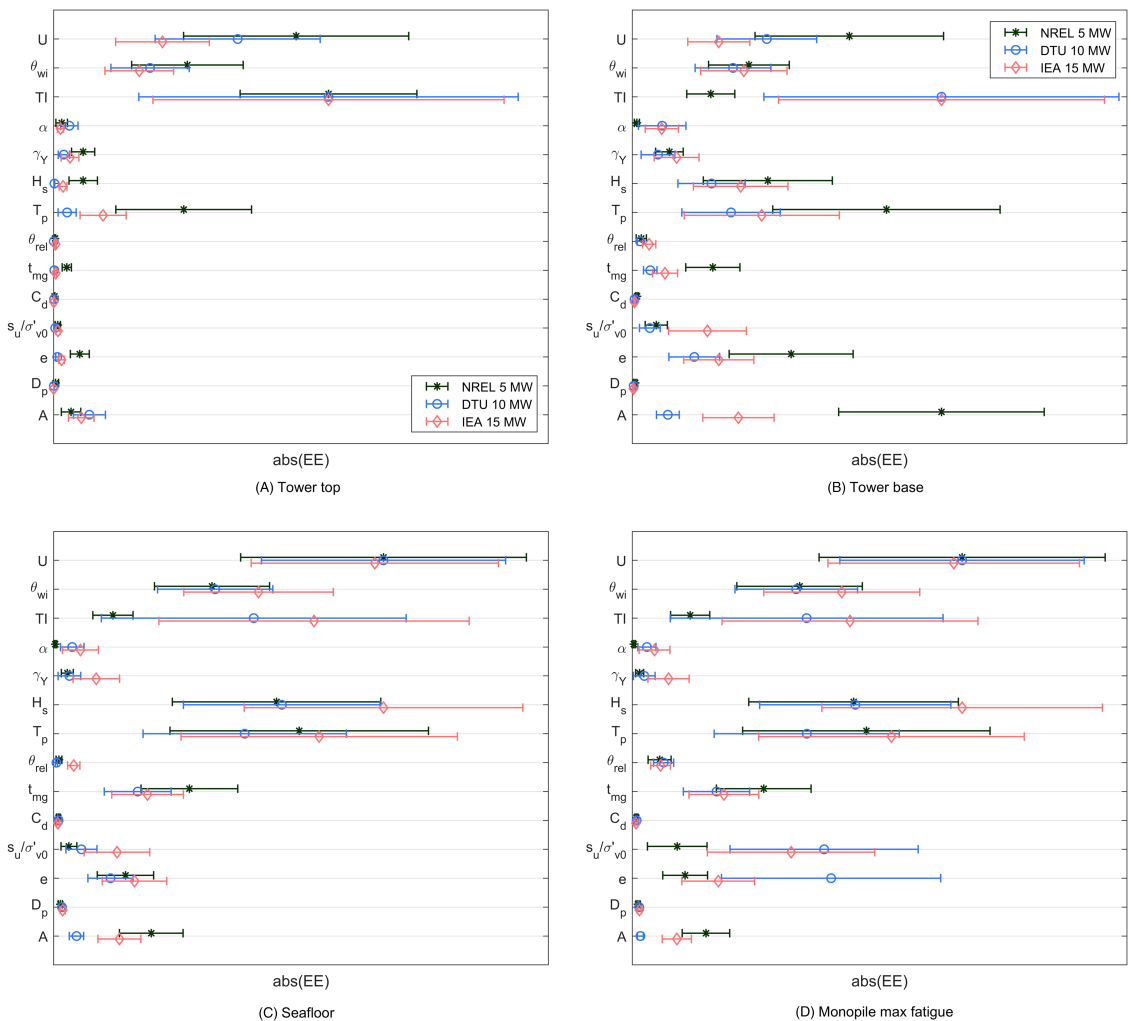

FIGURE 11 Statistics of the elementary effects excluding SN parameters and fatigue capacity. The markers represent $\mu_{EE,j}^*$, while the bars show $\pm\sigma_{EE,j}$. All plots are scaled based on the largest mean value for each turbine and location. Confer Table 3 for definition of symbols
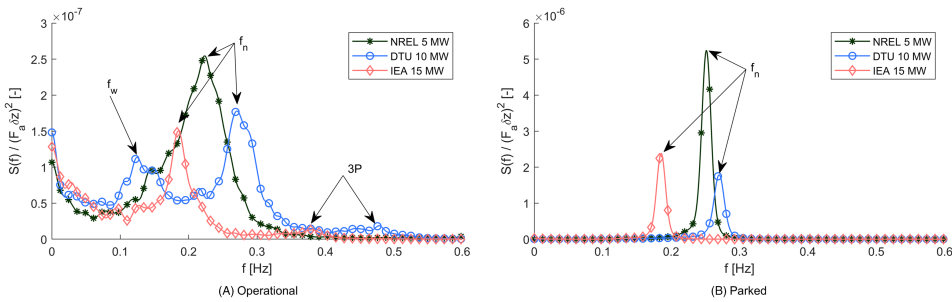
FIGURE 12 Tower base fore-aft bending moment at wind speed 21 m/s, aligned wind and waves. f_n denotes the first fore-aft natural frequency, 3P denotes the blade passing frequency and f_w indicates the wave frequency region

5.2.2 | Tower base

Turbulence intensity dominates the uncertainty also in the tower base for the 10- and 15-MW turbines. For the NREL 5-MW turbine, availability is the dominating parameter followed by wave peak period and wind speed distribution. The difference between the turbines can be explained by how the different turbine states contribute to the fatigue damage (Figure 9). The parked state contributes with about 60% of the fatigue damage in the tower base of the 5-MW turbine, which is two to three times larger than the contribution for the other turbines. Figure 12 shows the fore-aft bending moment at tower base for wind speed 21 m/s in operational and parked conditions, normalized by the steady-state bending moment caused by the thrust at the mean wind speed. In operational conditions, the wave-induced loads show a significantly higher contribution to the response in the 5-MW turbine than for the larger turbines. The higher wave loads are also seen in the increased resonant response in parked conditions, making parked conditions more important for the 5-MW turbine. The dominance of parked response explains the importance of availability for the 5-MW turbine. Further, T_p variation is more important in parked conditions due to the resonant response characteristics, and the wind speed distribution becomes important through the variation of T_p between the wind classes.

Robertson et al.,[9] Teixeira et al[8] and Toft et al[11] focused on the tower response in their studies. They found that turbulence intensity has the highest impact on the fatigue utilization uncertainty, agreeing with the overall results in this study.

5.2.3 | Monopile

The severity of the environmental conditions (represented by wind speed distribution in the used environmental model) is the most influential uncertainty in the monopile, with the uncertainty in H_s within each wind bin being equally important for the 15-MW turbine. The remaining significant parameters illustrate some of the differences between the three turbines. H_s and T_p variations both resulted in significant elementary effects for all turbines, while the importance of the turbulence intensity decreases with decreasing turbine size. The latter is caused by the higher importance of wind loads in the larger turbines.

Hübler et al.,[5] Peeringa and Bedon[4] and Velarde et al[6] have all looked at the monopile in their studies. Of these, only Hübler et al. can be directly compared with the results in this study. They found soil parameters, marine growth thickness, and pile diameter to be the most influential parameters at seafloor for the NREL 5-MW turbine. When considering only the parameters included both by Hübler et al. and the present study, the results seem consistent. Marine growth and soil parameters (void ratio in this study) are the the two most important parameters present in both studies. Structural pile diameter is not found to influence the fatigue utilization in the present study, while turbulence intensity is found more important here. The latter is particularly the case for the larger turbines.

5.3 | Discrete parameter results

The overall results from the analysis of the discrete parameters are shown in Figure 13. The wind coherence model is the most influential parameter in the tower top, with particularly the Mann model giving different results for the 5- and 10-MW turbines when compared to the baseline model. The choice of soil model and wave spectrum has the largest influence on the fatigue damage estimation in the tower base for 5- and 10-MW turbines, together with the inclusion of scour protection for the 5-MW turbine. For the IEA 15-MW turbine, the Mann coherence model also shows a significant difference compared to the baseline model. Scour protection has the highest influence on the fatigue damage estimation
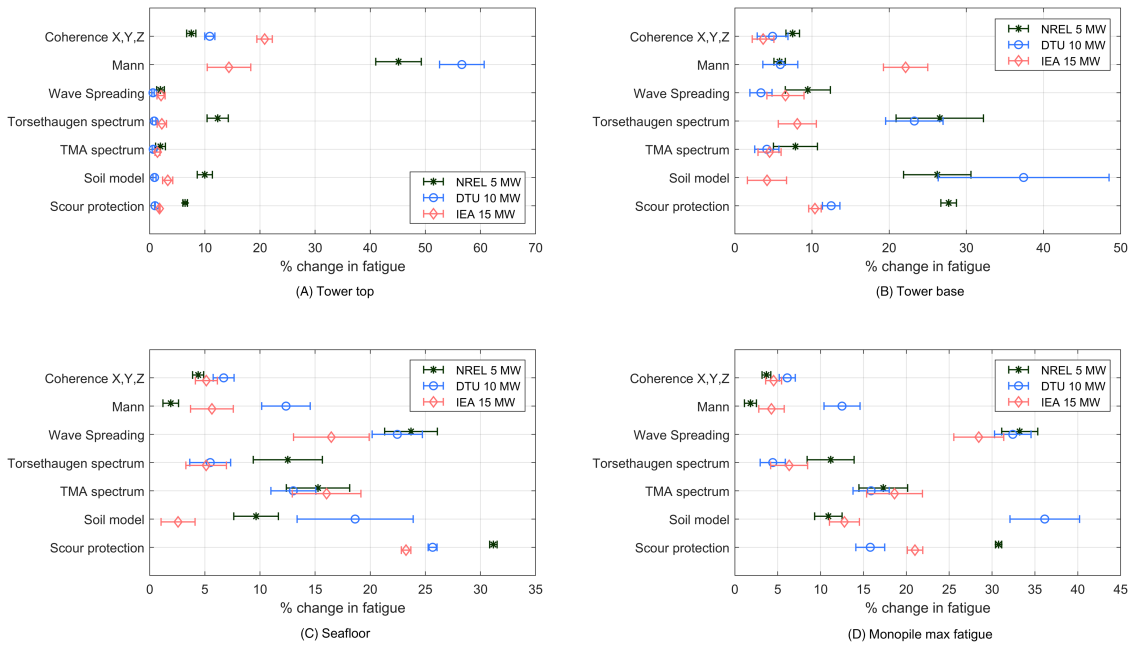
FIGURE 13 Change in fatigue damage when considering alternative models. The markers represent $\mu^*_{\delta D,i}$ while the bars show $\pm \sigma_{\delta D,i}$
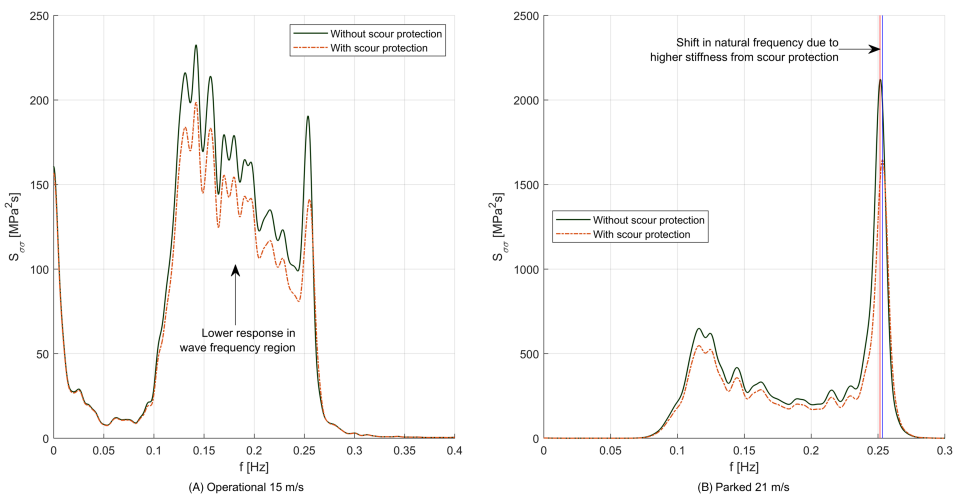

FIGURE 14 Stress spectra for location facing wave direction at seafloor with 30° wind-wave misalignment with and without scour protection modelled for NREL 5-MW turbine

at seafloor, which for consistency is defined as being the intersection between the soil and the scour protection layer. A significant difference is also seen when changing the wave spectral model and soil model, as well as when modelling the waves as short-crested. Finally, wave spreading and the soil model seems to cause the largest changes to the maximum fatigue damage prediction in the monopile. The following sections will present some of the results in more detail.

5.3.1 | Scour protection

The presence of scour protection at seafloor increases the foundation stiffness. This results in lower responses in the wave frequency region, and slightly increases the natural frequency. The latter is evident for conditions with low or negligible aerodynamic damping, e.g. conditions with wind-wave misalignment and when the OWT is parked. Figure 14 shows the stress spectra at seafloor for the 5 MW model. Both cases are with 30° misalignment, in operational and parked conditions. The change in the natural frequency is about 1.5%, 0.5% and 0.3% for the 5, 10 and 15 MW turbines, respectively. This explains the larger change in fatigue damage shown for the 5-MW turbine in Figure 13. Generally, larger variations were found for the parked conditions compared to the operational. Small changes were seen in conditions with wind-wave misalignment.

5.3.2 | Soil modelling

Figure 13 shows a significant difference between the turbines when changing soil model from the macro element formulation to p-y curves. Using the p-y curves leads to three distinct changes in the response, all illustrated in Figure 15 for the DTU 10 MW and IEA 15-MW turbines. First, the soil stiffness is reduced, leading to higher response amplitudes in the wave frequency range. This is because the p-y springs only models the virgin

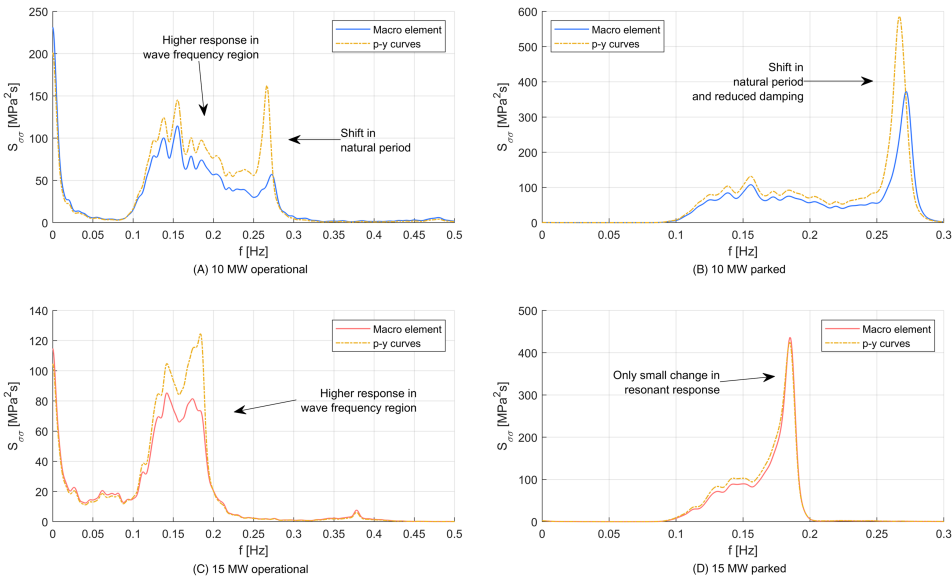**FIGURE 15** Stress spectra in monopile for DTU 10 MW and IEA 15-MW turbines in operational and parked conditions with wind speed 15 m/s
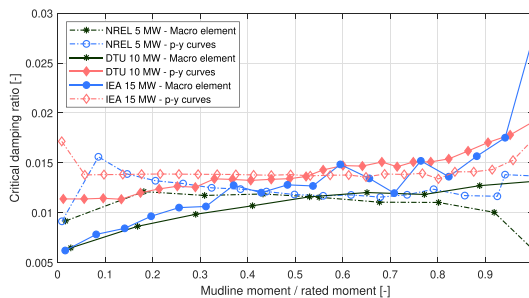

FIGURE 16 Damping ratios when using the macro element and p-y curves as function of seafloor bending moment

stiffness curve, while the macro element captures the unloading reloading stiffness better. Second, the lower soil stiffness gives a lower natural frequency. This effect is larger for the smaller turbines, consistent with what is seen in Section 5.3.1. Finally, the damping level is different when varying the soil models. In Figure 15B and D, it seems like the damping is too low for the 10-MW model with p-y curves, while the damping is more consistent in the 15-MW turbine.

However, the damping level of friction materials as soil is amplitude-dependent. This effect is captured by the macro element approach, as shown in Figure 16. Here, the global damping level is given as function of seafloor bending moment, with the latter normalized by M_a in Equation (26). The effect of the amplitude-dependent damping is that the p-y curves predict a higher resonant response in some wind classes and a lower response in other wind classes when compared to the macro element. For the 15-MW turbine these overpredictions and under-predictions cancel each other for the wind speeds considered in this study. This leads to small differences in the lifetime fatigue damage when considering the different soil models. This is particularly the case in the tower base and at seafloor, where the resonant response is significant. Below seafloor, the response is dominated by the wave-frequencies and the difference between the models is smaller. It is also worth noticing that there is still a significant difference in the short-term response characteristics of the 15-MW turbine when varying the soil model, which here happens to add up to small changes in the lifetime fatigue damage at seafloor and tower base.

6 | DISCUSSION

The results show that the uncertainty in both the continuous and discrete parameters are important for the fatigue damages estimation in mono-pile OWTs. However, designers and researchers should focus on different parameters.

The following general advice can be given to a designer who wants to reduce the uncertainty in a fatigue analysis: (i) Reduce the uncertainty in the SN curve and fatigue capacity if possible. (ii) Reduce the uncertainty in the environmental design basis, including both wind and wave parameters. Here, the design requirement of 1 year of available data has been used as the design basis. Increasing to two years of data will reduce the standard deviation of the assumed distributions by $\sim 30\%$ if the standard deviations are proportional to $1/\sqrt{n}$. Using 5 years of measurement data will reduce the standard deviations by $\sim 55\%$. (iii) Consider carefully which models are appropriate for the discrete parameters. All discrete variations have an influence on some parts of the support structure. However, the soil model seems to be particularly important at both the tower base and for the maximum fatigue damage in the monopile.

It is the discrete parameters (wind coherence model, wave spectral and spreading model, and soil models) that are of highest interest for future research, as the uncertainty in the most important continuous parameters can be reduced by increasing the amount of data available in the design basis. While all variations show importance in some part of the structure, it is worth noticing that most influential parameter for the 15-MW turbine is the wave spreading model. Together with the soil model, this is also the most influential parameter in the monopile for the other turbines. There may also be a coupling between the choice of soil model and the effect of wave spreading, which has not been investigated further here. The cross-wind and parked response of the turbines are sensitive to the soil damping level, as aerodynamic damping is mainly present in the fore-aft direction of an operational turbine. Any cross-wind loading will give a significant response level, which motivates the need to look at either the response at several locations around the circumference of the structure or the long-term response. Despite this, wave spreading has received little attention in the research community, with the authors knowing only three studies.[21,22,75] The effect of the soil model is also significant, demonstrating the need for accurate modelling of soil damping and stiffness. In terms of the coherence model, most models used today are developed for small diameter rotors with onshore wind conditions. Comparisons with measured time series and high-fidelity simulations show the need for further research also in this field.[18]

While this paper investigates both parameter uncertainty (the continuous variables) and model uncertainty (the discrete variables), no direct comparison between the two types of uncertainty has been performed. Both uncertainties contribute to the uncertainty in the design. Future studies could therefore focus on determining the relative importance of these distinctively different sources of uncertainty.

7 | CONCLUSION

This paper has investigated the uncertainty in the fatigue utilization caused by input parameters using fully coupled time-domain analyses. Continuous parameters, which are described by probability density functions, and discrete parameters, describing different engineering models, have been considered. The SN-curve parameters and fatigue capacity were found to be the continuous parameters with the highest influence in the uncertainty. Furthermore, parameters related to the description of the environmental conditions were found important. Generally, wind related parameters were found to be the most important in the tower, while wave related parameters were most important in the monopile. The importance of the wind parameters for the monopile increased with increasing turbine size, suggesting that uncertainties in the wind parameters become more important for the emerging large turbines. All the evaluated discrete parameters had an influence on the uncertainty of fatigue

damage estimates. The most important were found to be the coherence model in the tower top, and the soil model for the monopile at seafloor and tower base. Wave spreading had the highest influence on the maximum fatigue damage in the monopile.

PEER REVIEW

The peer review history for this article is available at https://publons.com/publon/10.1002/we.2755.

ORCID

Stian H. Sørum https://orcid.org/0000-0003-1131-5078

George Katsikogiannis https://orcid.org/0000-0002-1137-3764

Erin E. Bachynski-Polić https://orcid.org/0000-0002-1471-8254

Jørgen Amdahl https://orcid.org/0000-0002-3668-9896

Ana M. Page https://orcid.org/0000-0001-9197-0181

REFERENCES

1. IEC. International Electrotechnical Commission, Design Requirements for fixed offshore wind turbines (IEC 61400-3); 2019.
2. DNV GL. DNVGL-ST-0126. Support structures for wind turbines; 2018.
3. Saltelli A, Ratto M, Andres T, et al. Global sensitivity analysis. *The Primer*. Chichester, UK: John Wiley & Sons, Ltd; 2008.
4. Peeringa J, Bedon G. Fully integrated load analysis included in the structural reliability assessment of a monopile supported offshore wind turbine. *Energy Procedia*. 2017;137:255-260. https://doi.org/10.1016/j.egypro.2017.10.348
5. Hübler C, Gebhardt CG, Rolfes R. Hierarchical four-step global sensitivity analysis of offshore wind turbines based on aeroelastic time domain simulations. *Renew Energy*. 2017;111:878-891. https://doi.org/10.1016/j.renene.2017.05.013
6. Velarde J, Kramhøft C, Sørensen JD, Zorzi G. Fatigue reliability of large monopiles for offshore wind turbines. *Int J Fatigue*. 2020;134:105487. https://doi.org/10.1016/j.ijfatigue.2020.105487
7. Haldar S, Sharma J, Basu D. Probabilistic analysis of monopile-supported offshore wind turbine in clay. *Soil Dyn Earthq Eng*. 2018;105:171-183. https://doi.org/10.1016/j.soildyn.2017.11.028
8. Teixeira R, O'Connor A, Nogal M. Probabilistic sensitivity analysis of offshore wind turbines using a transformed Kullback-Leibler divergence. *Struct Saf*. 2019;81:101860. https://doi.org/10.1016/j.strusafe.2019.03.007
9. Robertson AN, Shaler K, Sethuraman L, Jonkman J. Sensitivity analysis of the effect of wind characteristics and turbine properties on wind turbine loads. *Wind Energ Sci*. 2019;4(3):479-513. https://doi.org/10.5194/wes-4-479-2019
10. Ziegler L, Muskulus M. Fatigue reassessment for lifetime extension of offshore wind monopile substructures. *J Phys Conf Ser*. 2016;753(9):092010.
11. Toft HS, Svenningsen L, Sørensen JD, Moser W, Thøgersen ML. Uncertainty in wind climate parameters and their influence on wind turbine fatigue loads. *Renew Energy*. 2016;90:352-361. https://doi.org/10.1016/j.renene.2016.01.010
12. Kallehave D, Byrne BW, LeBlanc Thilsted C, Mikkelsen KK. Optimization of monopiles for offshore wind turbines. *Philos Trans R Soc A Math Phys Eng Sci*. 2015;373(2035):20140100.
13. Veldkamp HF. Chances in wind energy: a probalistic approach to wind turbine fatigue design. *Thesis*. Delft, NL; 2006.
14. Damgaard M, Andersen LV, Ibsen LB, Toft HS, Sørensen JD. A probabilistic analysis of the dynamic response of monopile foundations: soil variability and its consequences. *Probabilistic Eng Mech*. 2015;41:46-59. https://doi.org/10.1016/j.probengmech.2015.05.001
15. Negro V, López-Gutiérrez J-S, Esteban MD, Matutano C. Uncertainties in the design of support structures and foundations for offshore wind turbines. *Renew Energy*. 2014;63:125-132. https://doi.org/10.1016/j.renene.2013.08.041
16. Luengo J, Negro V, García-Barba J, López-Gutiérrez J-S, Esteban MD. New detected uncertainties in the design of foundations for offshore wind turbines. *Renew Energy*. 2019;131:667-677. https://doi.org/10.1016/j.renene.2018.07.103
17. Kim S-H, Shin H-K, Joo Y-C, Kim K-H. A study of the wake effects on the wind characteristics and fatigue loads for the turbines in a wind farm. *Renew Energy*. 2015;74:536-543. https://doi.org/10.1016/j.renene.2014.08.054
18. Nybø A, Nielsen FG, Godvik M. Quasi-static response of a bottom-fixed wind turbine subject to various incident wind fields. *Wind Energy*. 2021;24(12):1482-500. https://doi.org/10.1002/we.2642
19. Horn J-TH, Krokstad JR, Amdahl J. Hydro-elastic contributions to fatigue damage on a large monopile. *Energy Procedia*. 2016;94:102-114. https://doi.org/10.1016/j.egypro.2016.09.203
20. Schloer S, Bredmose H, Bingham HB, Larsen TJ. Effects from fully nonlinear irregular wave forcing on the fatigue life of an offshore wind turbine and its monopile foundation. In: Proceedings of the ASME 2012 31st International Conference on Ocean, Offshore and Arctic Engineering American Society of Mechanical Engineers; 2012; Rio de Janeiro, Brazil.

21. Horn J-T, Krokstad JR, Amdahl J. Long-term fatigue damage sensitivity to wave directionality in extra-large monopile foundations. *Proc Inst Mech Eng Part M: J Eng Marit Environ*. 2018;232(1):37-49. https://doi.org/10.1177/1475090217727136

22. Sørum SH, Krokstad JR, Amdahl J. Wind-wave directional effects on fatigue of bottom-fixed offshore wind turbine. *J Phys Conf Ser*. 2019;1356: 012011. https://doi.org/10.1088/1742-6596/1356/1/012011

23. Bachynski EE, Ormberg H. Hydrodynamic modeling of large-diameter bottom-fixed offshore wind turbines. In: Proceedings of the ASME 2015 34th International Conference on Ocean, Offshore and Arctic Engineering American Society of Mechanical Engineers; 2015; St. John's, Newfoundland, Canada.

24. Aasen S, Page AM, Skjolden Skau K, Nygaard TA. Effect of foundation modelling on the fatigue lifetime of a monopile-based offshore wind turbine. *Wind Energ Sci*. 2017;2(2):361-376.

25. Katsikogiannis G, Bachynski EE, Page AM. Fatigue sensitivity to foundation modelling in different operational states for the DTU 10mw monopile-based offshore wind turbine. *J Phys Conf Ser*. 2019;1356:012019. https://doi.org/10.1088/1742-6596/1356/1/012019

26. Campolongo F, Saltelli A, Cariboni J. From screening to quantitative sensitivity analysis. a unified approach. *Comput Phys Commun*. 2011;182:978-988.

27. Jansen MJW. Analysis of variance designs for model output. *Comput Phys Commun*. 1999;117(1):35-43.

28. Kucherenko S, Albrecht D, Saltelli A. Exploring multi-dimensional spaces: A comparison of latin hypercube and quasi monte carlo sampling techniques. arXiv preprint arXiv:1505.02350; 2015.

29. Wang R, Diwekar U, Grégoire Padró CE. Efficient sampling techniques for uncertainties in risk analysis. *Environ Prog*. 2004;23(2):141-157.

30. Jonkman J, Butterfield S, Musial W, Scott G. Definition of a 5MW reference wind turbine for offshore system development. *Report*, Denver, CO, US, National Renewable Energy Laboratory (NREL); 2009.

31. Bak C, Zahle F, Bitsche R, et al. Description of the DTU 10 MW reference wind turbine. *Report*, Kgs. Lyngby, DK, DTU Wind Energy; 2013.

32. Gaertner E, Rinker J, Sethuraman L, et al. Definition of the IEA 15-megawatt offshore reference wind turbine, Denver, CO, US, International Energy Agency; 2020.

33. Jonkman J, Musial W. Offshore code comparison collaboration (OC3) for IEA task 23 offshore wind technology and deployment. *Report*, Golden, Colorado, USA, NREL; 2010.

34. Velarde J, Bachynski EE. Design and fatigue analysis of monopile foundations to support the DTU 10 MW offshore wind turbine. *Energy Procedia*. 2017;137:3-13. https://doi.org/10.1016/j.egypro.2017.10.330

35. Katsikogiannis G, Sørum SH, Bachynski EE, Amdahl J. Environmental lumping for efficient fatigue assessment of large-diameter monopile wind turbines. *Mar Struct*. 2021;77:102939.

36. Hansen MH, Henriksen LC. Basic DTU wind energy controller. *Report*, Roskilde, Denmark, DTU Wind Energy; 2013.

37. NREL. ROSCO. Version 2.2.0. https://github.com/NREL/rosco; 2020.

38. Reistad M, Breivik O, Haakenstad H, Aarnes OJ, Furevik BR, Bidlot JR. A high-resolution hindcast of wind and waves for the North Sea, the Norwegian Sea, and the Barents Sea. *J Geophys Res Oceans*. 2011;116(C5):C05019.

39. Bundesamt für Seeschifffahrt und Hydrographie. Fino - datenbankinformationen. https://www.bsh.de/DE/THEMEN/Beobachtungssysteme/Messnetz-MARNET/FINO/fino_node.html; 2020.

40. Jusoh I, Wolfram J. Effects of marine growth and hydrodynamic loading on offshore structures. *Jurnal Mekanikal*. 1996;1(1).

41. Lacasse S, Nadim F. Uncertainties in characterising soil properties. In: Uncertainty in the geologic environment: from theory to practice American Society of Civil Engineers; 1996; Madison, Wisconsin.

42. Zaaijer MB. Foundation modelling to assess dynamic behaviour of offshore wind turbines. *Appl Ocean Res*. 2006;28(1):45-57. https://doi.org/10.1016/j.apor.2006.03.004

43. DNV-GL (Det Norske Veritas - Germanischer Lloyd). Fatigue design of offshore steel structures (DNVGL-RP-C203).

44. Folsø R, Otto S, Parmentier G. Reliability-based calibration of fatigue design guidelines for ship structures. *Mar Struct*. 2002;15(6):627-651. https://doi.org/10.1016/S0951-8339(01)00031-4

45. DNV-GL (Det Norske Veritas - Germanischer Lloyd). Loads and site conditions for wind turbines (DNVGL-ST-0437); 2016.

46. Pfaffel S, Faulstich S, Rohrig K. Performance and reliability of wind turbines: a review. *Energies*. 2017;10(11):1904.

47. Larsen J, Soerensen H, Christiansen E, Naef S. Experiences from Middelgrunden 40 MW offshore wind farm Copenhagen Offshore Wind; 2005; Copenhagen.

48. Horn J-TH, Krokstad JR, Amdahl J. Joint probability distribution of environmental conditions for design of offshore wind turbines Proceedings of the ASME 2017 36th International Conference on Ocean, Offshore and Arctic Engineering; 2017; Trondheim, Norway.

49. SINTEF Ocean. Simo 4.10.3 user guide, Trondheim, Norway, SINTEF Ocean; 2017.

50. SINTEF Ocean. Riflex 4.10.3 user guide, Trondheim, Norway, SINTEF Ocean; 2017.

51. Jonkman BJ. TurbSim user's guide: Version 1.50, Technical Report, Denver, CO, US, National Renewable Energy Lab (NREL); 2009.

52. Larsen HMA. How 2 HAWC2, the user's manual. edited by the DTU wind energy HAWC2 development team, Roskilde, DK, Risø National Laboratory, Technical University of Denmark; 2020.

53. Correia A. A Pile-head Macro-element Approach to Seismic Design of Monoshaft Supported Bridges. *Ph.D. Thesis*. Pavia, Italy: European School for Advanced Studies in Reduction of Seismic Risk, ROSE School; 2011.

54. Page AM, Skau KS, Jostad HP, Eiksund GR. A new foundation model for integrated analyses of monopile-based offshore wind turbines. *Energy Procedia*. 2017;137:100-107. https://doi.org/10.1016/j.egypro.2017.10.337

55. Page A, Grimstad G, Eiksund G, Jostad HP. A macro-element pile foundation model for integrated analyses of monopile based offshore wind turbines. *Ocean Engineering*. 2018; Vol. 167:23-35.

56. Page A, Grimstad G, Eiksund G, Jostad HP. A macro-element model for multidirectional cyclic lateral loading of monopiles in clay. *Comput Geotech*. 2019;106:314-326.

57. Klinkvort RT, Sturm H, Page AM, Zhang Y, Jostad HP. A consistent, rigorous and super-fast monopile design approach Proceedings of the 4th International Symposium on Frontiers in Offshore Geotechnics; 2022; Austin, Texas, US.

58. Burton T, Jenkins N, Sharpe D, Bossanyi E. *Wind Energy Handbook*: John Wiley & Sons, Ltd; 2011.

59. MacCamy R.C., FRA. Wave Forces on Piles: A Diffraction Theory, Washington, D.C., US, Office of Naval Research, U. S. Department of the Navy; 1954.

60. Brodtkorb PA, Johannesson P, Lindgren G, Rychlik I, Rydén J, Sjö E. WAFO—a Matlab toolbox for the analysis of random waves and loads The 10th International Offshore and Polar Engineering Conference; 2000; Seattle, Washington.

61. Masseran N, Razali AM, Ibrahim K, Latif MT. Fitting a mixture of von Mises distributions in order to model data on wind direction in Peninsular Malaysia. *Energy Convers Manag*. 2013;72:94-102.

62. Larsen GC. Offshore fatigue design turbulence. *Wind Energy*. 2001;4(3):107-120. https://doi.org/10.1002/we.49

63. Ernst B, Seume JR. Investigation of site-specific wind field parameters and their effect on loads of offshore wind turbines. *Energies*. 2012;5(10):3835-3855.

64. Türk M, Emeis S. The dependence of offshore turbulence intensity on wind speed. *J Wind Eng Ind Aerodyn*. 2010;98(8):466-471. https://doi.org/10.1016/j.jweia.2010.02.005

65. Germanishcer Lloyd Industrial Services GmbH. Rules and guidelines, IV industrial services, 2 guideline for the certification of offshore wind turbines; 2012.

66. Wolfram J, Theophanatos A. The effects of marine fouling on fluid loading of cylinders: some experimental results 17th Annual Offshore Technology Conference; 1985; Houston, Texas.

67. Feng Y, Tavner PJ, Long H. Early experiences with uk round 1 offshore wind farms. *Energy*. 2010;163. https://doi.org/10.1680/ener.2010.163.4.167

68. IEC. International Electrotechnical Commission, Wind turbine generator systems-Part 1: Safety requirements. 4th edition (IEC 61400-1); 2019.

69. Wise AS, Bachynski EE. Wake meandering effects on floating wind turbines. *Wind Energy*. 2020;23(5):1266-1285. https://doi.org/10.1002/we.2485

70. DNV-GL. Det Norske Veritas - Germanischer Lloyd, Environmental conditions and environmental loads (DNVGL-RP-C205); 2017.

71. Torsethaugen K, Haver S. Simplified double peak spectral model for ocean waves The Fourteenth International Offshore and Polar Engineering Conference; 2004; Toulon, France.

72. Smilden E, Bachynski EE, Sørensen AJ. Key contributors to lifetime accumulated fatigue damage in an offshore wind turbine support structure Proceedings of the ASME 2017 36th International Conference on Ocean, Offshore and Arctic Engineering; 2017; Trondheim, Norway.

73. Faltinsen OM. *Sea Loads on Ships and Offshore Structures*. Cambridge: Cambridge University Press; 1990.

74. Wirsching PH. Fatigue reliability for offshore structures. *J Struct Eng*. 1984;110(10):2340-2356.

75. Trumars JMV, Jonsson JO, Bergdahl L. The effect of wind and wave misalignment on the response of a wind turbine at Bockstigen Proceedings of the ASME 2006 25th International Conference on Offshore Mechanics and Arctic Engineering; 2010; Shanghai, China.
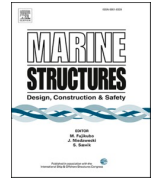
Paper 2:

Environmental lumping for efficient fatigue assessment of large-diameter monopile wind turbines

George Katsikogiannis, Stian H. Sørum, Erin E. Bachynski, Jørgen Amdahl

Environmental lumping for efficient fatigue assessment of large-diameter monopile wind turbines

George Katsikogiannis [*], Stian Høegh Sørum, Erin E. Bachynski, Jørgen Amdahl

Centre for Autonomous Marine Operations and Systems, Department of Marine Technology, Norwegian University of Science and Technology, Trondheim, NO-7491, Norway

ABSTRACT

Fatigue damage is one of the governing factors for the design of offshore wind turbines. However, the full fatigue assessment is a time-consuming task. During the design process, the site-specific environmental parameters are usually condensed by a lumping process to reduce the computational effort. Preservation of fatigue damage during lumping requires an accurate consideration of the met-ocean climate and the dynamic response of the structure. Two lumping methods (time-domain and frequency-domain) have been evaluated for a monopile-based 10 MW offshore wind turbine, both based on damage-equivalent contour lines. Fatigue damage from lumped load cases was compared to full long-term fatigue assessment. The lumping methods had an accuracy of 94–98% for the total long-term fatigue damage and 90% for individual wind speed classes, for aligned wind and waves. Fatigue damage was preserved with the same accuracy levels for the whole support structure. A significant reduction of computational time (93%) was achieved compared to a full long-term fatigue assessment. For the cases with 30° and 60° wind-wave misalignment, there was a mean underestimation of approximately 10%. Variations in penetration depth did not affect the selection of the lumped sea-state parameters. This work presents a straightforward method for the selection of damage-equivalent lumped load cases, which can adequately preserve long-term fatigue damage throughout the support structure, providing considerable reduction of computational effort.

1. Introduction

Approximately 82% of all installed substructures for offshore wind farms in Europe employ monopile foundations [1]. It is expected that the monopile will remain the preferred choice due to manufacturing and fabrication experience [2]. Even with the introduction of higher capacity (8–12 MW) offshore wind turbines (OWTs), large-diameter monopiles are considered one of the most promising concepts for the future.

The design of monopile OWTs relies on dynamic analyses, coupling aerodynamics, hydrodynamics, soil-structure interaction and the wind turbine control system. Fatigue is one of the governing factors for the final design. Various methods can be applied for estimating the dynamic response and fatigue damage of offshore structures [3]. The results are sensitive to factors such as environmental load models, soil-structure interaction and statistical uncertainties. Time-domain simulations are considered the most accurate

approach for fatigue damage estimation [4], because non-linear effects and coupling between environmental loads and structural responses are taken into account. However, fatigue assessment based on fully-integrated time-domain analyses is a time-consuming process, as all relevant combinations of environmental parameters should be considered. This includes joint occurrence of wind speed (U_w), significant wave height (H_s), wave peak period (T_p) and wind-wave directionality. Therefore, it is highly beneficial to reduce the number of environmental conditions considered for fatigue limit state (FLS) design. The challenge is to select a reduced set of load cases which accurately predicts the fatigue damage at all locations along the tower and monopile over the lifetime of the structure.

Lumping approaches from oil & gas industry, such as block lumping methods [5,6], cannot be applied for OWTs because they do not account for wind-wave correlation. Different lumping methods have been developed and applied for fatigue design of OWTs, such as Kühn's iterative damage-equivalent method [7], and Seidel's spectral energy-equivalent approach [8,9]. Still, design guidelines [10, 11] lack recommendations for how this should be performed.

Passon & Branner [12] showed that environmental lumping methods need to capture the OWTs' dynamics. The same study [12] introduced a new damage-equivalent lumping method for waves. This method preserves the wave-induced damage better than the probability-based averaging of sea-state parameters [13], Kühn's [7], and Seidel's [8,9] approaches. Passon & Branner also demonstrated the accuracy of the different lumping methods and their sensitivity to variation of different input parameters. Passon [14] extended the damage-equivalent wave lumping method to include wind-wave correlations. Lumped sea-state parameters are determined for each wind speed, wind direction and wave direction using damage-equivalent contour lines at selected positions within the OWT. The method was applied to a generic OWT configuration for a large-diameter (>8 m) monopile foundation. It was shown that the resulting lumped sea-states can accurately reproduce the long-term fatigue damage. However, several simplifications were introduced: the rotor-nacelle-assembly was modelled by a simplified mass-equivalent representation of the NREL 5 MW turbine [15] and only hydrodynamically induced fatigue damage was considered. Wind loads and aerodynamic damping were disregarded. This non-operational condition resembles design load case 7.2 [10], which typically only corresponds to 5% of a turbine's operational life [16].

To the authors' knowledge, the performance of Passon's method under simultaneous wind-wave loading has not been documented. Assessing this is important for a coupled system like OWTs. The present study develops and investigates the suitability of the damage-equivalent contour line lumping method for a 10 MW monopile-based OWT in operational conditions. Wind- and wave-induced responses are considered in an integrated manner. A frequency-domain lumping method for establishing the damage-equivalent contour lines and lumped load cases is developed. This is based on wave-induced dynamic responses. The resultant contour lines and load cases are compared to those obtained from a time-domain lumping method, which accounts for simultaneous dynamic wind and wave loads. The frequency-domain scheme is also evaluated for misaligned wind and waves.

To evaluate the accuracy of the lumping methods, the fatigue damage from the lumped load cases is calculated for combined wind and wave loads. The damage along the support structure compares well with results from full long-term fatigue damage assessment. Finally, the sensitivity of the selected lumped load cases to sea-state parameter variations and design changes, such as foundation characteristics, is examined. These topics have not been addressed before, and some of them were recommended by Passon [14] for further investigation. The proposed method predicts the long-term fatigue damage with high accuracy throughout the support structure while reducing the computation effort significantly compared to a full long-term analysis. This can be of great importance in the early design phase or for evaluating various types of modelling uncertainties, e.g. for different OWT design positions within a wind farm.

The paper is organized as follows: in section 2 a detailed description of the damage-equivalent lumping process and the lumping methods considered in the study is given, section 3 describes the environmental conditions, simulation and environmental load models, and section 4 gives all relevant information about fatigue damage calculations in the study. Finally, section 5 summarizes the results and section 6 concludes the paper with recommendations for future work.

2. Fatigue damage-equivalent lumping process

The full wind-wave climate used for OWT design is typically represented by wind speed-dependent scatter diagrams. Each wind speed class $k = 1, ..., N_{U_w}$ is usually associated with the mean wind speed at hub height, $U_{w,k}$, and a wind speed-dependent scatter diagram, SD_k. Each scatter diagram consists of N_{H_s} classes for significant wave height (H_s) and N_{T_p} classes for spectral peak period (T_p). The scatter diagrams contain the probability of occurrence, $p_{i,j,k}$ for wind speed class k, wave height class i and peak period class j. This results in a large number of load cases to be analysed for fatigue damage assessment. The computational effort required for fully-integrated time-domain analysis of so many load cases is significant. The lumping process aims to determine a reduced set of load cases, which represents the full wind-wave climate and predicts the correct fatigue damage.

2.1. Establishment of damage-equivalent contour lines

The selection of lumped sea-states is based on the damage-equivalent contour line method, as described by Passon [14]. Damage-equivalent contour lines (also referred as contour lines) refer to combinations of H_s and T_p that result in the same damage level at a given location along the structure. The basis of the method is to find $H_s - T_p$ combinations along these contour lines that can reproduce the total fatigue damage for a given wind speed class scatter diagram (SD_k). By finding the intersection of damage-equivalent contour lines from different locations along the support structure, a single $H_s - T_p$ combination for the lumped

sea-state can be found.

The first step to determine the contour lines is to calculate the unit damage $d_{i,j,k}^*$ for each sea-state in SD_k. This represents the fatigue damage for a specified time period with stationary environmental conditions, typically 1 h. The unit damages $d_{i,j,k}^*$ for selected locations along the OWT support structure are obtained either from fully-integrated time-domain analyses (subsection 2.2) or from a frequency-domain approach (subsection 2.3). The actual fatigue damage $d_{i,j,k}$ for each $H_s - T_p$ combination in SD_k is calculated by scaling the unit damage $d_{i,j,k}^*$ with the probability of occurrence $p_{i,j,k}$, according to Eq. (1). This follows from Palmgren-Miner's linear damage accumulation hypothesis [3,11].

$$d_{i,j,k} = p_{i,j,k} \cdot d_{i,j,k}^* \tag{1}$$

To establish the damage contour line, the target damage level d_{t_k} and target probability p_{t_k} are introduced. As shown in Eq. (2), d_{t_k} represents the total fatigue damage of all sea-states in SD_k, while p_{t_k} is the total probability of occurrence of SD_k.

$$d_{t_k} = \sum_{i=1}^{N_{H_k}} \sum_{j=1}^{N_{T_p}} d_{i,j,k} \quad \text{and} \quad p_{t_k} = \sum_{i=1}^{N_{H_k}} \sum_{j=1}^{N_{T_p}} p_{i,j,k} \tag{2}$$

The unit damages $d_{i,j,k}^*$ are now scaled by the probability p_{t_k} to obtain the scaled damages $d_{Si,j,k}^*$, according to Eq. (3). $d_{Si,j,k}^*$ represents the fatigue damage that will be predicted if $H_{s,i}, T_{p,j}$ is selected as the lumped load case for wind speed class k.

$$d_{Si,j,k}^* = p_{t_k} \cdot d_{i,j,k}^* \tag{3}$$

The intersection between $d_{Si,j,k}^*$ and d_{t_k} forms the damage contour line of the $H_s - T_p$ combinations that result in the target damage d_{t_k}. An example is shown in Fig. 1 for wind class 16–18 m/s. The multi-coloured surfaces represent the scaled damages $d_{Si,j,k}^*$ and the pink plane is the target damage level d_{t_k}. Each location along the OWT support structure has different response characteristics, resulting in different damage-equivalent contour lines. Therefore, damage equivalency throughout the whole support structure can only be maintained for sea-states that lie on the damage-equivalent contours for all locations. This will be discussed in detail in Secs. 2.2 and 2.3.

In the present study, two methods for establishing the damage-equivalent contour lines have been considered, based on time-domain and frequency-domain calculations. The steps described above are followed for both methods, with the difference being how the unit damage $d_{i,j,k}^*$ is calculated. The time-domain lumping method, described in subsection 2.2, serves as a validation of the frequency-domain lumping method. It uses fully-integrated analyses to account for simultaneous wind and wave excitation. Because $d_{i,j,k}^*$ shall be calculated for all possible sea-states in each wind speed class (including those with zero probability of occurrence), the computational effort is actually larger than that of a full long-term fatigue analysis. The frequency-domain lumping method (subsection 2.3) reduces the computational effort. Here, the unit damage $d_{i,j,k}^*$ is calculated based on a transfer function relating stress range to wave elevation.

After selecting the lumped sea-states, fully-integrated time-domain analyses are conducted for the reduced load set and the fatigue damage is compared to full scatter analysis results. Fig. 2 shows an overview of the methods used in the study for the fatigue damage calculation.
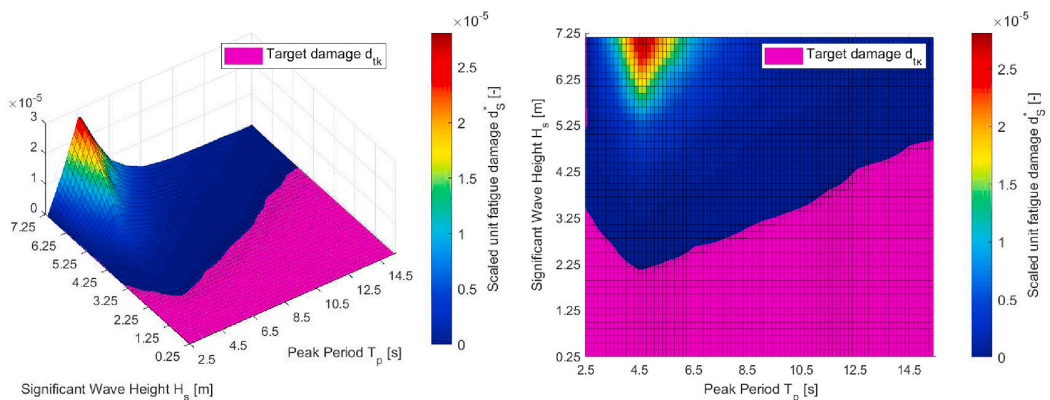

Fig. 1. Scaled damage $d_{S_k}^*$ (multi-coloured surface) and target damage level d_{t_k} (pink plane) for determining damage contour lines at mudline for wind speed class 16–18 m/s. (For interpretation of the references to colour in this figure legend, the reader is referred to the Web version of this article.)
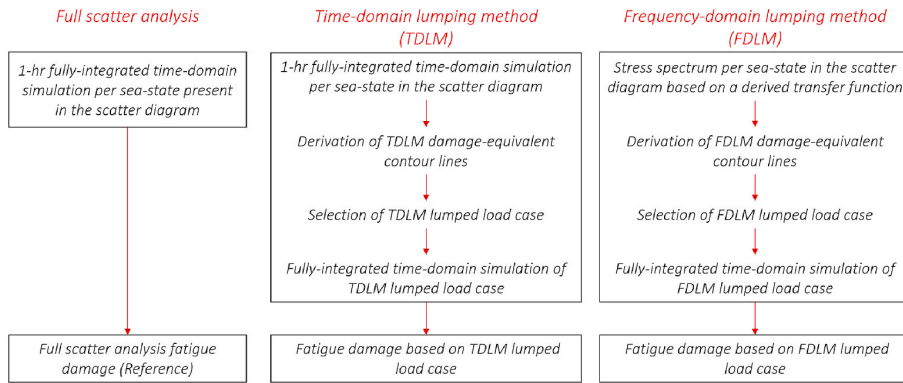
Fig. 2. Overview of lumping methods and full scatter analysis procedure for fatigue damage calculation in a single wind speed class.

2.2. The time-domain lumping method

The time-domain lumping method uses fully-integrated dynamic analyses to determine the damage-equivalent contour lines. The OWT is subjected to simultaneous turbulent wind and irregular wave excitation, and one analysis is conducted for each $U_w - H_s - T_p$ combination. The duration of each stochastic realisation is 1 h, following the recommendations of design standards [10,11]. The responses from the dynamic analyses are extracted at selected locations along the OWT and the fatigue damage is estimated using the rainflow cycle counting method, as shown in Fig. 3.

From the simulations, the unit ($d^*_{i,j,k}$) and actual ($d_{i,j,k}$) fatigue damage for each sea-state are established. The target fatigue damage d_{t_k} (Eq. (2)) varies along the support structure, resulting in different damage-equivalent contour lines for each location. Therefore, different $H_s - T_p$ combinations are required to achieve the target fatigue damage d_{t_k} for each location, and damage equivalency throughout the whole support structure can only be maintained for certain $H_s - T_p$ combinations. Having established the damage contour lines for several locations, a lumped load case can be determined by their intersection and used to represent the whole SD_k. This is illustrated in Fig. 4, where the contour lines for various locations along the monopile (red lines) and tower (blue lines) are shown for two wind speed classes. The lines vary, as each line represents a target fatigue damage that is usually different for different locations. However, they approximately intersect at one point. This $H_s - T_p$ combination (represented by the green circle) is considered the lumped sea-state for which long-term damage equivalency can be maintained along the support structure.

2.3. The frequency-domain lumping method

The frequency-domain approach seeks to extract the damage-equivalent contours in a simplified manner, based solely on wave loads. This is done using stress transfer functions, $H_{\zeta\sigma}$, relating wave elevation to stress range. Each wind speed class has its own transfer function because the soil stiffness and damping are influenced by the mean aerodynamic thrust, while the aerodynamic damping depends on the operating point of the turbine.

In this study, the transfer functions are extracted by subjecting the non-linear time-domain model of the OWT to frequency-limited 3-hr white noise wave excitation. A linear relationship is then assumed between the wave excitation and stress response of the OWT, yielding the transfer function as

$$H_{\zeta\sigma}(f) = \sqrt{\frac{S_{\sigma\sigma}(f)}{S_{\zeta\zeta}(f)}} \tag{4}$$

Here, $S_{\sigma\sigma}(f)$ is the power spectral density of the stress response, and $S_{\zeta\zeta}(f)$ is the incident wave spectrum. This is repeated for all wind classes.

Frequencies between 0 Hz and 0.7 Hz are included in the white noise wave spectrum, to include all relevant response frequencies. The significant wave height of white noise excitation is chosen as the mid value of the most probable H_s class in the scatter diagram for each wind speed. MacCamy & Fuchs' load model [18] is used in the simulations, as the transfer functions should represent the whole range of T_p values in the scatter diagram. Aerodynamic damping and mean thrust are captured by subjecting the operational turbine to a constant, uniform wind field. Tower shadow effects are neglected to avoid aerodynamic excitation interfering with the transfer functions.

The stress spectra for each sea-state in a wind speed class are found by combining the stress transfer function, $H_{\zeta\sigma}$, with the design wave spectra. From this, the unit fatigue damages $d^*_{i,j,k}$ are calculated. Assuming the stress to be Gaussian distributed and narrow-banded, the closed-form formulation [19] based on a Rayleigh distribution for stress cycles is used to estimate unit fatigue damage. For broad-banded spectra, Dirlik's empirical equation is used [20]. The bandwidth of the spectrum is evaluated based on the
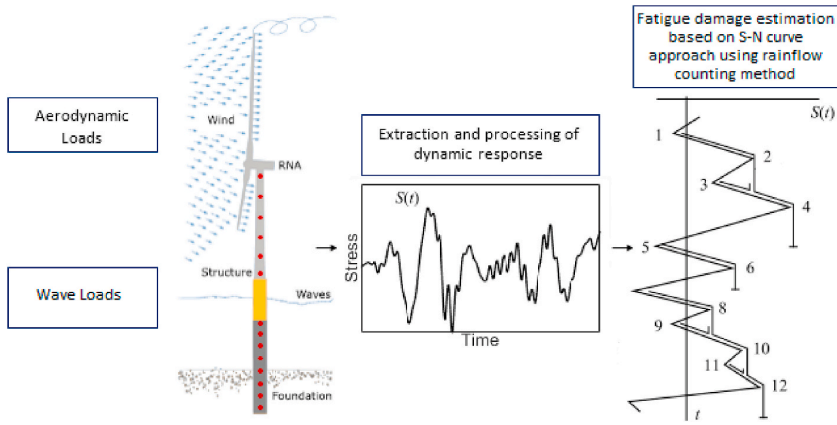
Fig. 3. Unit fatigue damage $d^*_{i,j,k}$ calculation per sea-state in time-domain lumping method for several locations (red dots) along a monopile-based OWT (monopile illustration [17], rainflow counting illustration [3]). (For interpretation of the references to colour in this figure legend, the reader is referred to the Web version of this article.)

(a) Wind class 14-16 m/s **(b)** Wind class 18-20 m/s
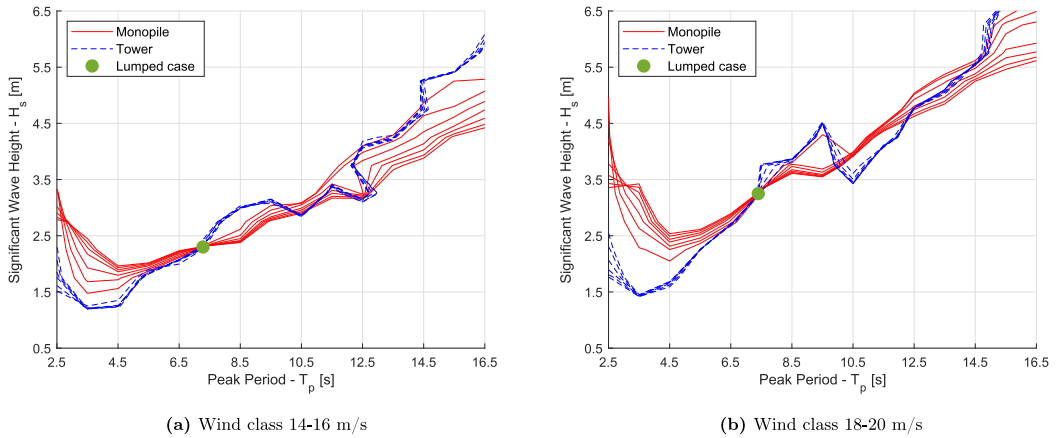
Fig. 4. Damage-equivalent contour lines for various locations along the monopile and tower and the resultant lumped load case determined from time-domain lumping method.

Fig. 5. Procedure for calculating wave-induced stress spectrum for each sea-state in a scatter diagram SD_k associated with wind speed class k for frequency-domain lumping method.

(a) Wind class 14-16 m/s   (b) Wind class 18-20 m/s

Fig. 6. Damage-equivalent contour lines for various locations along the monopile and tower and the resultant lumped load case determined from frequency-domain lumping method.

bandwidth parameter $\beta = T_c/T_z$, where T_c is the mean period between peaks and T_z is the mean zero up-crossing period. Values of $\beta \geq 0.96$ indicate a narrow-b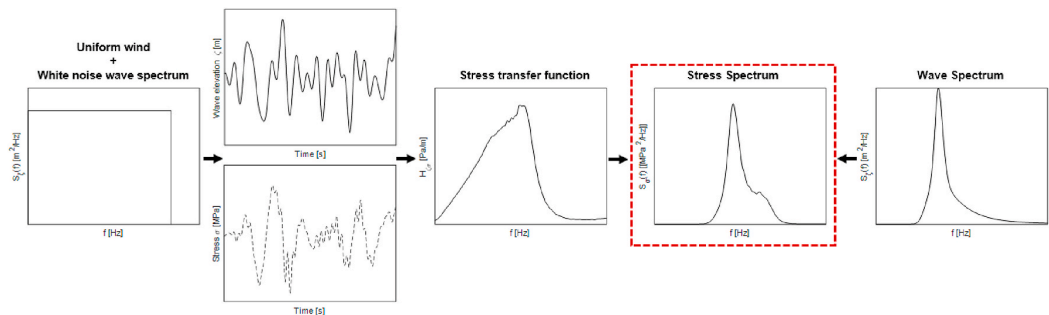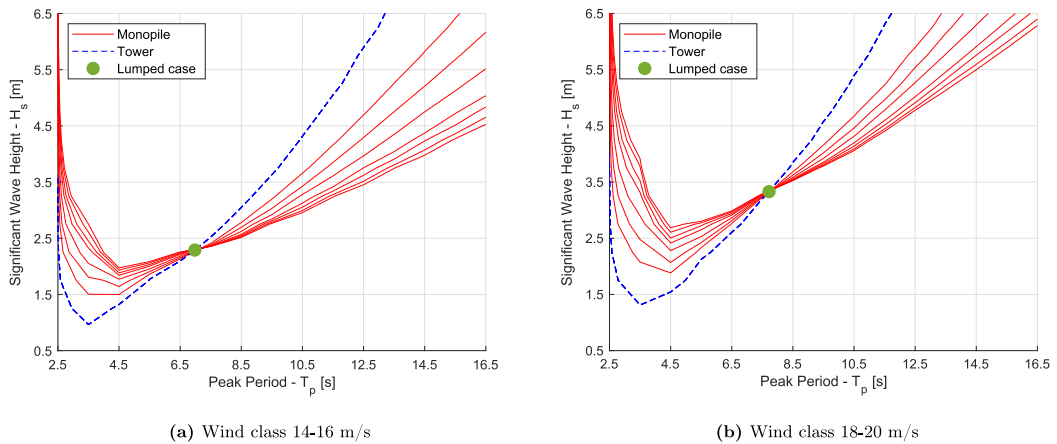anded spectrum [19]. Fig. 5 illustrates the steps for frequency-domain analysis. Once the unit fatigue damages are calculated, the lumping procedure proceeds as described in subsection 2.1.

Having determined the contour lines, the lumped load case can be found from their intersection, as illustrated in Fig. 6. It should be noted that the contour lines are for the same locations as in Fig. 4, but the contours are identical for all locations in the tower. This is further discussed in subsection 5.2, where the contour lines between the two lumping methods are compared.

The frequency-domain lumping method was also used for the wind-wave misalignment cases. In misaligned cases, the 3-hr white noise wave excitation is applied with the required misalignment angle, and the stress transfer function is extracted at the location on the cross section with the highest unit fatigue damage. Due to the low aerodynamic damping in the cross-wind direction, this position is in general not aligned with the wave direction (see subsection 5.4).

3. Environmental conditions and simulation models

This section will describe the model used in the case study, including environmental conditions, turbine properties and numerical modelling approaches.

3.1. Environment conditions - organization of environmental parameters

A numerical hindcast model from the National Kapodistrian University of Athens (NKUA) was used to generate 10-yr statistics for several locations in the North Sea, Atlantic Ocean and Mediterranean Sea for the Marina Platform project [21]. The hindcast data have a resolution of 1 h for the period 2001 to 2010 for a site located at the Norwegian Continental Shelf with geographic coordinates (55.11°N, 3.47°E) and 30 m water depth. The dataset provides information about met-ocean parameters such as mean wind speed (U_w) 10 m above sea level, significant wave height (H_s), wave peak period (T_p) and wind-wave directionality. The wind and wave roses of the site are shown in Fig. 7.

The wind speed U_{119} used in the study has been estimated at the hub height (119 m) of the wind turbine. Wind shear is accounted for by the power law with exponent $\alpha = 0.14$ [10]. A Kaimal wind spectrum with turbulence according to the normal turbulence model (NTM) for Class C turbines is used [10]. Current is not taken into account, as recommended by design standards [10].

The met-ocean data are expressed as 3D scatter diagrams of U_{119}, H_s and T_p. Wind speed classes in the operational range (4–25 m/s) have been considered, with classes of 2 m/s. For each wind speed, the corresponding sea-states are gathered in H_s classes of 0.5 m between 0.25 m and 9.25 m and T_p classes of 1 s in the range 2.5–16.5 s.

3.2. Simulation models

The simulation model is based on the DTU 10 MW reference wind turbine (DTU 10 MW RWT) [22], supported by a monopile foundation. The wind turbine has a hub height of 119 m relative to the MSL and a rotor diameter of 178.3 m. The rotor-nacelle as-sembly, tower and monopile above seabed were modelled in SIMO-RIFLEX, an aero-hydro-servo-elastic software developed by SINTEF Ocean. All wind inflow simulations were performed using TurbSim from NREL [23].

3.2.1. Wind turbine and support structure model
The wind turbine blades were modelled using the structural and aerodynamic coefficients from Ref. [22] and the controller adopted
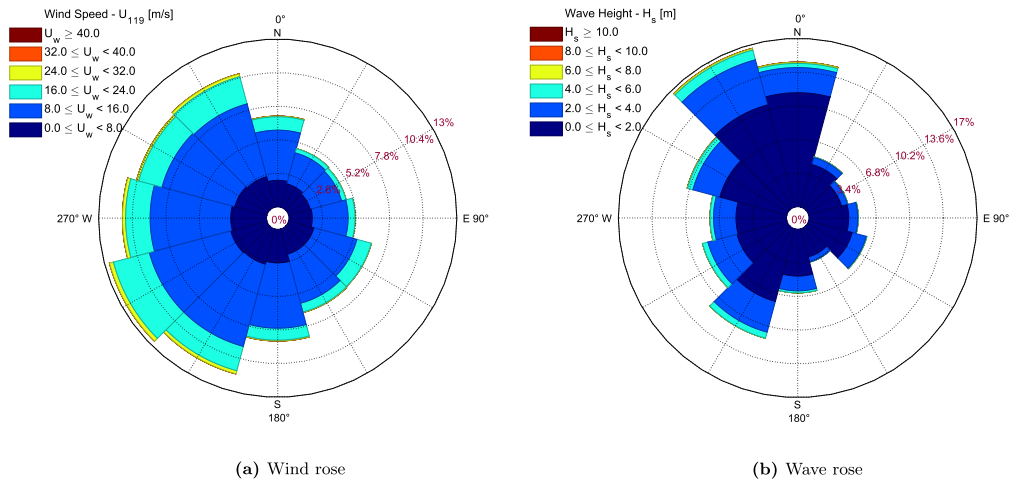
(a) Wind rose   **(b)** Wave rose

Fig. 7. Site wind and wave roses based on the hindcast data.

was the basic DTU Wind Energy Controller [22]. Aerodynamic loads were calculated using the blade element momentum theory with engineering corrections such as the Glauert correction, Prandtl corrections for tip loss and hub loss [24], and dynamic stall and dynamic wake [25]. The tower was modelled with axisymmetric beam elements having 10 sections of constant diameter each, decreasing from a specified diameter at the bottom to the top of the tower. Similarly, the monopile was modelled with axisymmetric beam elements above seabed. The monopile part below seabed (foundation model) is described in detail in subsection 3.2.2.

3.2.2. Foundation model

A non-linear elasto-plastic model including hysteretic behaviour, based on the macro-element concept, was used for the foundation model. This type of model condenses the foundation and surrounding soil response to a force-displacement relation at one point, commonly located at mudline, separating the foundation and the rest of the structure [26].

This applied model predicts the load-displacement response and the hysteretic damping of monopile-based OWTs in integrated time-domain analyses [27]. The macro-element formulation is based on results from finite element analysis (FEA) of the soil and the foundation. The performance of the macro-element model was compared against field test measurements and FEA results for three piled foundations [17]. The model can reproduce the non-linear load-displacement response and the hysteretic behaviour observed in monopiles with different length-over-diameter ratios. Good agreement between the macro-element predictions and the FEA results confirms that the model can reproduce the soil-structure interaction with the same level of accuracy as the FEA, but with a considerable reduction in computational effort.

The macro-element model used in this study is calibrated to FEA results of full 3D continuum modelling of the soil volume and the foundation. The FE analysis considers a 3 m layer of sand and clay layers below. Tables 1 and 2 summarise the sand and clay layer properties respectively, used for the macro-element model calibration. The behaviour of the clay layers is represented by the NGI-ADP soil model [28], which describes the elasto-plastic, non-linear stress behaviour of saturated clays under undrained monotonic loading conditions. The model accounts for the effect of multi-directional loading, which has been found to affect the foundation stiffness and

Table 1
FEA soil parameters for sand layer (0–3 m), modelled with the hardening soil model.

Parameter	Value	Unit
Drainage type	Drained	–
Submerged weight, γ'	10	kN/m³
Secant stiffness in standard drained triaxial test E_{50}^{ref}	3.0E+04	kPa
Tangent stiffness for primary oedometer loading, E_{oed}^{ref}	3.0E+04	kPa
Unloading and reloading stiffness, E_{ur}^{ref}	9.1E+04	kPa
Power for stress-level dependency of stiffness, m	0.54	–
Effective cohesion, C_{ref}'	1	kPa
Effective angle of internal friction, φ_{ref}'	34.25	deg
Angle of dilatancy, ψ	4.25	deg
Reference shear modulus at very small strains, G_0^{ref}	9.4E+04	kPa
Threshold shear strain at which $G_s = 0.722 \cdot G_0$, $\gamma_{0.7}$	0.015	%

Table 2

FEA soil parameters for clay layers (3–100 m), modelled with the NGI-ADP model.

Parameter	Unit	Depth [m]				
		3–9	9–18	18–36	36–72	72–100
γ'	kN/m³	10	10	10	10	10
$G_{ur}/S_{u,A}$	–	1252	782.2	553.1	391.1	299.5
$\gamma_{f,C}$	%	10	10	10	10	10
$\gamma_{f,E}$	%	15	15	15	15	15
$\gamma_{f,DSS}$	%	15	15	15	15	15
$S_{u,ref}$	kPa	30	90	180	360	720
$S_{u,inc}$	kPa/m	10	10	10	10	10
$S_{u,P}/S_{u,A}$	–	0.48	0.48	0.48	0.48	0.48
$S_{u,DSS}/S_{u,A}$	–	0.67	0.67	0.67	0.67	0.67

- $G_{ur}/S_{u,A}$: Ratio of unloading/reloading shear modulus over active shear strength $\gamma_{f,C}$.

- $\gamma_{f,E}$, $\gamma_{f,DSS}$: Shear strain at failure in compression, extension, and direct simple shear (DSS) respectively.

- $S_{u,ref}$, $S_{u,inc}$: Active undrained shear strength at the top of each clay layer, and increase per meter.

- $S_{u,P}/S_{u,A}$: Ratio of passive shear strength over active shear strength.

- $S_{u,DSS}/S_{u,A}$: Ratio of DSS shear strength over active shear strength.

hysteretic damping [27]. The model communicates with SIMO-RIFLEX through a dynamic link library (DLL). The macro-element model does not directly compute the forces along the part of the pile embedded in the soil. A separate post-processing numerical tool has been employed to compute the moment distribution along the pile, developed by Norwegian Geotechnical Institute (NGI). A simplified illustration of the OWT model is shown in Fig. 8.

Five different monopile foundation designs have been used in this study. All models have a diameter (D) of 9 m and wall thickness (t) of 0.11 m. The base-case model has a penetration depth (L) of 36 m [29]. This is the model that is used to compare the fatigue damage from the derived lumped load cases to the full scatter results. The rest of the models, which vary in terms of penetration depth, are used to evaluate the sensitivity of the lumped load cases selection to foundation design. Table 3 summarizes the design properties of the models.

To quantify the natural frequency and damping of each foundation model, a free vibration analysis with no wind and no waves was conducted. The analysis was performed by gradually applying a force of 1.5 MN at the tower top and then releasing the force to allow the OWT to vibrate. Global damping was then quantified from the time history of the fore-aft bending moment at the mudline using the logarithmic decrement method, expressed in Eq. (5).

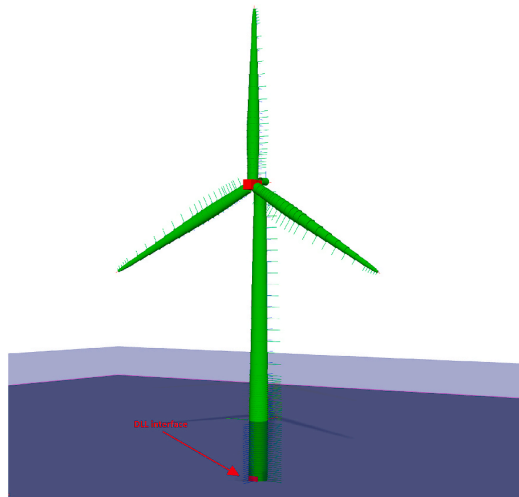$$\delta = \ln\left(\frac{A_i}{A_{i+1}}\right) = 2\pi \frac{\xi}{\sqrt{1-\xi^2}} \approx 2\pi\xi \tag{5}$$

Fig. 8. Illustration of DTU 10 MW model in SIMO-RIFLEX.

Table 3
Foundation designs used in the study.

Foundation Model	Penetration Depth	L/D ratio	Monopile Diameter	Wall Thickness
[−]	[m]	[−]	[m]	[m]
1	22.5	2.5		
2	24.75	2.75		
3	27.0	3.0	9.0	0.11
(Base-case) 4	36.0	4.0		
5	45.0	5.0		

δ is the logarthmic decrement, A_i and A_{i+1} are two successive amplitudes and ξ is the global damping ratio estimate for that load cycle. Fig. 9 shows the first fore-aft natural frequencies of the support structure and the global damping ratios of the models, evaluated during the free decay tests. Higher load levels result in lower foundation stiffness and consequently in lower natural frequencies. In addition, the nonlinear damping is evident in the non-zero slope of the damping ratio with respect to response amplitude. This is clear for all the foundation models, which follow a steady behaviour from lower to higher response amplitudes.

3.2.3. Wave load and wave kinematics models

Two wave load models have been considered for the full scatter analysis, Morison's equation and MacCamy & Fuchs formulation [18] with Morison-type drag loads. Morison's equation cannot capture the diffraction effects important for low wave periods, but can be combined with wave kinematics of arbitrary order.

An estimate of the difference between the two models is found by considering the inertia loads on a rigid pile and calculating the wave load spectrum for several sea-states. Assuming a JONSWAP wave spectrum, the variance (σ^2) of the wave loads is determined for both models. The ratio $\sigma^2_{M\&F}/\sigma^2_{Mor}$ is used as a measure to identify the validity range of Morison's equation. Morison's equation is applied for sea-states where the difference between the two models is less than 5%. This corresponds to analyses with T_p higher than 10 s. The drag (C_D) and inertia (C_M) coefficients are assumed to be 0.9 and 2.0, respectively [30]. MacCamy & Fuchs formulation with Morison type drag is used for analyses with T_p lower than 10 s. The added mass coefficient related to the structural response is assumed to be constant and equal to 1.0 for the MacCamy & Fuchs hydrodynamic model.

Two wave kinematic theories have been considered for the full scatter analysis, Airy linear wave theory and Stokes' 2nd order waves. Recommendations for wave models can be found in design guidelines when considering regular waves, but not for irregular waves [30]. To find the regions where 2nd order wave theory is needed, the wave loads on a rigid monopile fixed at sea bed were compared. Linear wave theory with constant extrapolation of the wave potential up the instantaneous free surface was found sufficient for $H_s \leq 4.5$ m. Second-order wave theory is used for higher sea-states. However, MacCamy & Fuchs load model is only valid for linear wave theory. Consequently, MacCamy & Fuchs with linear waves is used for analyses with H_s higher than 4.5 m and T_p lower than 10 s.

3.2.4. Verification of frequency-domain modelling approach

To verify the validity of the frequency-domain model, the stress spectra from the derived transfer functions were compared to stress spectra estimated from time-domain simulations. The three environmental conditions shown in Table 4 were used for the comparisons. Ten 1-hr simulations were conducted for each load case and the resultant stress spectra were averaged. Good agreement between the resulting stress spectra for the tower base and mudline is observed. This is shown in Fig. 10 for load case 2, while Table 5 compares the standard deviation for the load cases.
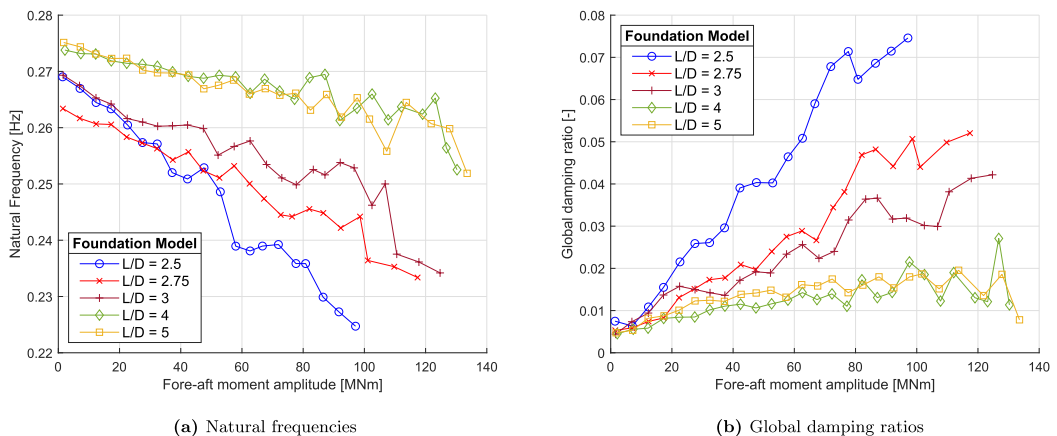

(a) Natural frequencies

(b) Global damping ratios

Fig. 9. Dynamic properties of the foundation models from free-vibration test.

Table 4

Load cases for verification of frequency-domain approach.

Load Case	Wind Class	Mean Wind Speed	Significant Wave Height	Peak Period	Wave Spectrum
[−]	[m/s]	[m/s]	[m]	[s]	[−]
1	8–10	9.07	0.75	4.5	Pierson-Moskowitz
2	14–16	14.95	2.25	6.5	JONSWAP
3	18–20	20.91	3.25	7.5	JONSWAP

Further, it is desirable that no aerodynamic loads besides the mean thrust force and aerodynamic damping are present when establishing the transfer functions. By evaluating the variation in rotor speed and blade pitch, it was verified that the white-noise wave excitation does not significantly affect the operation of the turbine. For all wind speeds, the coefficient of variation was less than 0.5% for the rotor speed and the standard deviation of blade pitch angle was less than $0.07°$.

4. Fatigue damage estimation

The time-domain simulations give the time history of loads at various cross sections along the monopile. These loads are denoted N_x (axial force), M_y and M_z (bending moments). Based on the coordinate system in Fig. 11, the axial stress σ_x at a given point (r, θ) on the outer surface of the tubular cross section with outer radius r is estimated as:

$$\sigma_x = \frac{N_x}{A} - \frac{M_y}{I_y} r \sin(\theta) + \frac{M_z}{I_z} r \cos(\theta) \tag{6}$$

Here, A is the cross-sectional area, I_y and I_z are the second moment of area for the cross section computed about the y and z axes, respectively. The shear stress and its resultant fatigue damage was not taken into account due to its negligible effect relative to the axial stress. The number of load cycles for different stress levels is computed based on rainflow counting technique [31] using the WAFO Toolbox [32], modified to allow for bi-linear S-N curves [33]. Representative S-N curves were selected based on DNV GL's recommended practice [4]. Curve "D" for steel in seawater with cathodic protection (Table 2.2 in Ref. [4]) was selected for the monopile, and curve "D" for steel in air (Table 2.1 in Ref. [4]) was selected for the tower. Since the fatigue damage is more pronounced in welds, S-N curves for girth welds were used [33]. A reference thickness equal to 25 mm and a thickness exponent on fatigue strength of 0.2 were used based on [4]. No stress concentration factor (SCF) is taken into account.

4.1. Long-term fatigue damage estimation

Three environmental models of increasing complexity have been utilised for comparing the long-term fatigue damage from the lumped load cases and the full scatter results. The first two models consider aligned wind and waves, while the third model accounts for wind-wave misalignment. It is assumed that the joint probability of all parameters can be expressed as the product of marginal and conditional probabilities [34]. The first model (model N°1) assumes aligned wind and waves without considering any directional variability. The probability of occurrence of an environmental condition is given by Eq. (7).

$$P_1\{U_{119}, H_s, T_p\} = P\{U_{119}\} P\{H_s, T_p | U_{119}\} \tag{7}$$

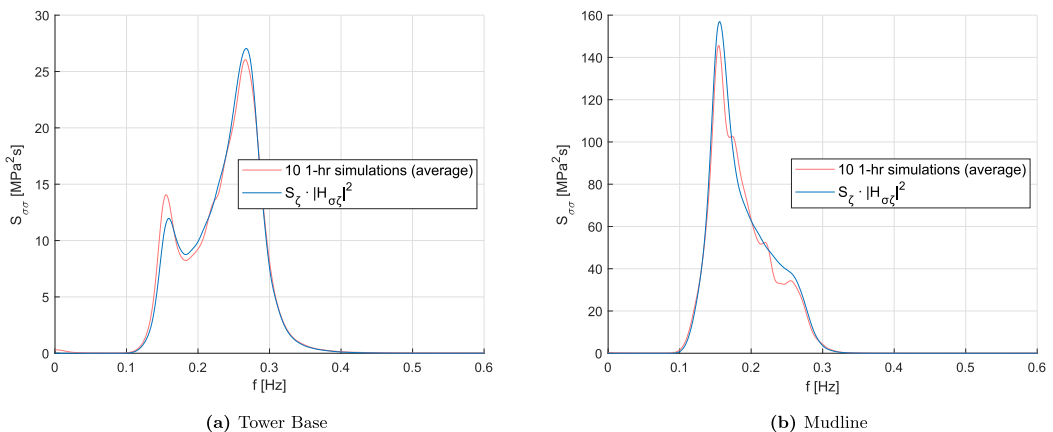(a) Tower Base   (b) Mudline

Fig. 10. Stress spectra comparison between the transfer function ($H_{\zeta\sigma}$) from the 3-hr white noise excitation and the actual wave spectrum (S_ζ) (basis of frequency-domain lumping method) and the averaged spectra of 10 1-hr time-domain simulations for load case 2.

Table 5

Standard deviation comparison from stress spectra of the sea-states used for the verification frequency-domain lumping method (FDLM).

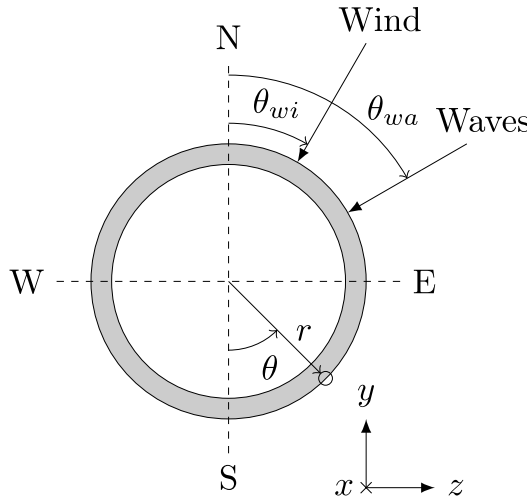| Load Case	Mudline		Tower Base	
	$S_\zeta \cdot \|H_{\zeta\sigma}\|^2$ (Basis of FDLM)	1-hr simulations (Average)	$S_\zeta \cdot \|H_{\zeta\sigma}\|^2$ (Basis of FDLM)	1-hr simulations (Average)
[−]		Standard deviation [MPa]		
1	1.16	1.18	0.87	0.82
2	3.31	3.30	1.59	1.60
3	5.36	5.31	2.37	2.33

Fig. 11. Tubular cross-section local coordinate system and environmental parameters.

Long-term fatigue damage is calculated as the sum of the short-term (1 h) damage of each condition scaled by the probability of occurrence, by Eq. (8).

$$D_{LT_1} = 24 \cdot 365 \cdot N \cdot \sum_{k=1}^{N_{U_w}} \sum_{i=1}^{N_{H_s}} \sum_{j=1}^{N_{T_p}} d^*_{i,j,k} \cdot P_1\{U_{119}, H_s, T_p\} \tag{8}$$

Here, N is the design lifetime in years, $d^*_{i,j,k}$ is the 1-h fatigue damage, N_{U_w} is the number of wind speed classes, and N_{H_s}, N_{T_p} the number of H_s and T_p classes for a scatter diagram SD_k, associated with wind speed class k.

In the second model (model N°2), long-term directional variability of wind is taken into account. Each wind speed class is divided into twelve sectors ($N_{\theta_{wi}}$), each covering an angle of 30°. The probability of occurrence of a sea-state and fatigue damage for this model are formulated by Eqs. (9) and (10)

$$P_2\{U_{119}, \theta_{wi}, H_s, T_p\} = P\{U_{119}\}P\{\theta_{wi}|U_{119}\}P\{H_s, T_p|U_{119}, \theta_{wi}\} \tag{9}$$

$$D_{LT_2} = 24 \cdot 365 \cdot N \cdot \sum_{k=1}^{N_{U_w}} \sum_{l=1}^{N_{\theta_{wi}}} \sum_{i=1}^{N_{H_s}} \sum_{j=1}^{N_{T_p}} d^*_{i,j,k,l} \cdot P_2\{U_{119}, \theta_{wi}, H_s, T_p\} \tag{10}$$

where θ_{wi} is the wind direction with respect to North.

Model N°3 is an extension of the second model, taking into account wind-wave misalignment per wind speed class. When considering misaligned wind and waves, the hindcast does not contain enough data to accurately model the full joint probability distribution. Eqs. (11) and (12) are used for Model N°3.

$$P_3\left\{U_{119}, \theta_{wi}, \theta_{rel}, H_s, T_p\right\} = P\{U_{119}\}P\{\theta_{wi}|U_{119}\}P\{\theta_{rel}|U_{119}\}P\{H_s, T_p|U_{wi}, \theta_{rel}\} \tag{11}$$

$$D_{LT_3} = 24 \cdot 365 \cdot N \cdot \sum_{k=1}^{N_{U_w}}\sum_{l=1}^{N_{\theta_{wi}}}\sum_{m=1}^{N_{\theta_{rel}}}\sum_{i=1}^{N_{H_s}}\sum_{j=1}^{N_{T_p}} d_{i,j,k,l,m} \cdot P_3\left\{U_{119}, \theta_{wi}, \theta_{rel}, H_s, T_p\right\} \tag{12}$$

Here, θ_{rel} is the absolute wind-wave misalignment angle in the interval $\theta_{rel} \in [0°, 180°]$. For all three models described, the wave climate $P\{H_s, T_p\}$ is represented as a conditional scatter diagram. By utilizing the symmetry of the monopile, the same simulation results can be used for all wind directions.

5. Results and discussion

The results section is ordered as follows. In subsection 5.1, the lumped load cases from the time-domain and frequency-domain methods are compared to the most probable and most damage contributing H_s, T_p classes from the full long-term analysis. In subsection 5.2, selected contour lines from the two lumping methods are compared for two different wind speed classes and their differences are discussed. In subsection 5.3.1, the uncertainty of fatigue damage prediction for the lumped load cases is evaluated. In subsection 5.3.2, the fatigue damage from the lumped load cases is compared to full scatter results for aligned wind and waves, and subsection 5.3.3 focuses on damage preservation along the support structure through the lumping process. In subsection 5.5, the damage sensitivity to variations in H_s and T_p values of the lumped load cases is discussed. In subsection 5.4, the frequency-domain lumping method is evaluated and compared to full scatter results for wind-wave misalignment conditions. Finally, subsection 5.6 focuses on the sensitivity of the resulting load cases from frequency-domain lumping method to different foundation designs, with varying penetration depth.

5.1. Lumped load cases compared to wind speed scatter diagrams

First, the sea-state parameters of the lumped load cases from time-domain (subsection 2.2) and frequency-domain (subsection 2.3) methods are compared. The lumped $H_s - T_p$ combinations, which represent the wind speed class scatter diagrams (SD_k), are also compared to the most probable H_s, T_p classes within each SD_k and to the H_s, T_p classes that resulted in the largest fatigue damage based on the full scatter analysis. The results are shown in Fig. 12 and Table 6.

Both methods result in similar H_s values (~0.1 m difference for most wind speed classes), following a gradual increase from low to high wind speeds, as expected. The slightly higher H_s values (~0.15–0.3 m) obtained by the frequency-domain lumping method close to the rated speed can be explained by the fact that in this wind speed range, the slowly-varying wind component dominates the dynamic response and consequently the fatigue damage [35]. This physical process is not taken into account during the frequency-domain lumping method, which then leads to higher values for the required H_s. Finally, the derived H_s values are similar to the most probable and most damage contributing H_s classes from the full scatter analysis results.

The two methods show a larger scatter regarding the T_p values of the lumped load cases. In most wind speed classes the differences in T_p are between 0.1 s and 0.5 s, without a specific trend above the rated speed. Below the rated speed, lower T_p values are obtained from the time-domain lumping method. Lower T_p counteracts the lower H_s values in that range as the decreased peak period leads to an larger number of load cycles per time, increasing the fatigue damage. Additionally, considering that the natural period of the structure

(a) Significant wave height per wind class

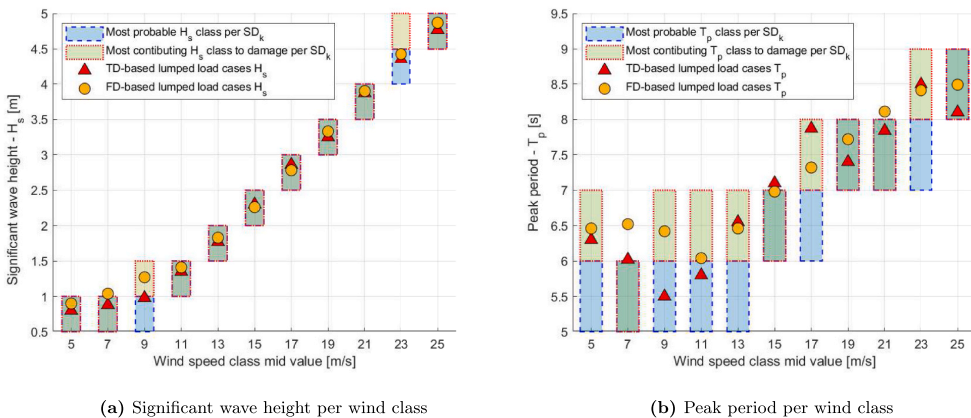(b) Peak period per wind class

Fig. 12. Derived sea-state parameters $H_s - T_p$ of the lumped load cases compared to the most probable and most contributing sea-state parameters derived from the full scatter analysis (SD_k: Scatter diagram of wind class k, *TD*: Time-domain, *FD*: Frequency-domain).

Table 6

Summary of lumped load cases and sea-state parameters for each wind class.

Wind Class	H_s [m]				T_p [s]			
[m/s]	TDLC[a]	FDLC[b]	MPSD[c]	MCSD[d]	TDLC	FDLC	MPSD	MCSD
4–6	0.80	0.90	[0.5,1.0]	[0.5,1.0]	6.30	6.46	[5,6]	[6,7]
6–8	0.88	1.04	[0.5,1.0]	[0.5,1.0]	6.02	6.52	[5,6]	[5,6]
8–10	0.98	1.27	[0.5,1.0]	[1.0,1.5]	5.50	6.42	[5,6]	[6,7]
10–12	1.35	1.41	[1.0,1.5]	[1.0,1.5]	5.80	6.04	[5,6]	[6,7]
12–14	1.77	1.83	[1.5,2.0]	[1.5,2.0]	6.55	6.46	[5,6]	[6,7]
14–16	2.30	2.26	[2.0,2.5]	[2.0,2.5]	7.10	6.98	[6,7]	[6,7]
16–18	2.86	2.78	[2.5,3.0]	[2.5,3.0]	7.87	7.32	[6,7]	[7,8]
18–20	3.25	3.33	[3.0,3.5]	[3.0,3.5]	7.40	7.72	[7,8]	[7,8]
20–22	3.87	3.9	[3.5,4.0]	[3.5,4.0]	7.84	8.11	[7,8]	[7,8]
22–24	4.36	4.43	[4.0,4.5]	[4.5,5.0]	8.50	8.41	[7,8]	[8,9]
24–26	4.77	4.87	[4.5,5.0]	[4.5,5.0]	8.10	8.49	[8,9]	[8,9]

[a] TDLC: Lumped load case based on time-domain method.
[b] FDLC: Lumped load case based on frequency-domain method.
[c] MPSD: Most probable sea-state parameter class.
[d] MCSD: Most damage contributing sea-state parameter class (from full scatter analysis).

is approximately 3.85 s (Fig. 9a), a decreased peak period approaches the range of the support structure natural period. This leads to pronounced dynamic responses, increasing the fatigue damage.

5.2. Contour lines comparison between the lumping methods

The overall shape of the contour lines from the two lumping methods highlights the dynamic response of the support structure. This is indicated in Fig. 13 for two wind speed classes. For peak periods in the vicinity of the first natural period (3.7–4.0 s), resonance increases the fatigue damage. Low H_s values are then required to obtain the target damage value d_{t_k} for each location. For long wave periods, the response can be considered as quasi-static, and the increased peak period further decreases the number of load cycles per time. Therefore, a considerably higher H_s is required to obtain the target fatigue damage. A similar trend is observed for short wave periods; although the number of load cycles increases as a result of the decreased mean wave period, the dynamic amplification factor is low.

The contour lines from the time-domain lumping method show more irregular behaviour compared to those from frequency-domain and those found by Passon [14]. This is a consequence of how the unit damage $d_{i,j,k}^*$ is estimated for each sea-state in SD_k. In the time-domain method, $d_{i,j,k}^*$ is estimated using a single 1-hr realisation for each sea-state. The aleatory uncertainty in fatigue damage from a single 1-h realisation can be up to 25% depending on the location (as shown in subsection 5.3.1), leading to the irregular shape of the contour lines. The irregularities are pronounced for the contour lines that correspond to the tower, especially for wind classes below and close to the rated wind speed. This is because fatigue damage estimation for the tower is strongly affected by both the random wind and
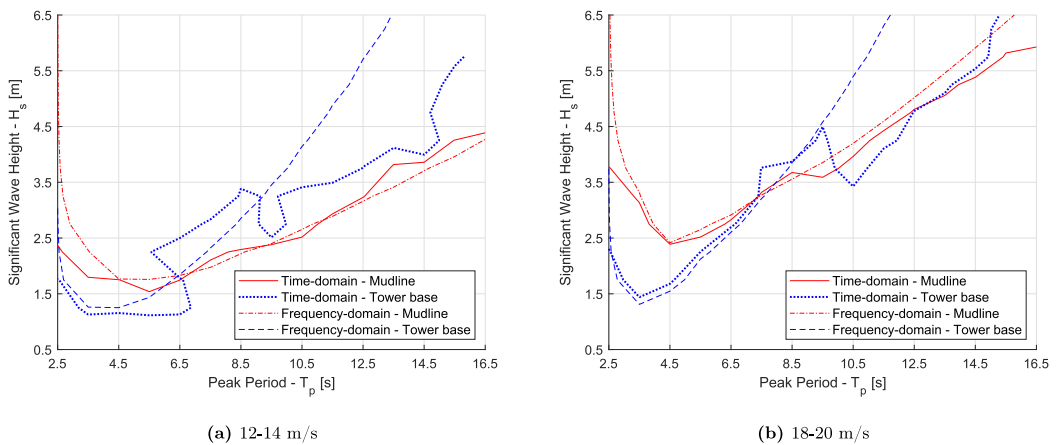

(a) 12-14 m/s

(b) 18-20 m/s

Fig. 13. Contour lines from frequency-domain and time-domain lumping methods. The contours are shown for the monopile at mudline and tower base (11 m above sea-surface).

wave field of each realisation, while the monopile's dynamic response and resultant damage is dominated by the wave loading.

The monopile contour lines from the two methods align well for the whole range of $H_s - T_p$ combinations. As shown in Figs. 4 and 6, different locations in the monopile have different contour lines. This is caused by the total response being a combination of quasi-static and dynamic response. For the tower, the frequency-domain contours require larger H_s than the time-domain method for high T_p values. This is due to the lack of wind-induced responses in the frequency-domain lumping process. Further, the contour lines in Fig. 6 are identical for the tower, since the loads are only caused by the acceleration of the rotor-nacelle assembly. This is not the case for the time-domain lumping, where aerodynamic loads also contribute to the response. Nonetheless, the contours from the two methods align well for moderate sea-states, where the fatigue damage is dominated by the wave excitation and the pronounced dynamic responses close to the support structure first natural period.

Fig. 14 shows a comparison between the stress spectra obtained using the transfer functions of frequency-domain lumping method and the stress spectra of the same load cases subjected to combined fluctuating wind and irregular wave loading. At mudline, the main difference between the spectra is the low-frequency wind-induced response ($f < 0.1$ Hz) and the 3P rotor response, which are not present in the frequency-domain model. However, wave excitation is the main contributor to the fatigue damage. Therefore, the monopile contour lines of the two methods are in good agreement because wave loading is included in both lumping methods.

The tower base response is dominated by the slowly-varying wind components. Inertia loads from the RNA acceleration at the natural frequency (f_n) and the 3P rotor loads also contribute to the response. To compensate for the lack of the slowly-varying response due to wind excitation, the frequency-domain lumping method leads to higher H_s values than the time-domain method for large T_p. This effect is enhanced for wind classes close to the rated speed, where the contribution of wind-induced response to fatigue damage is relatively high.
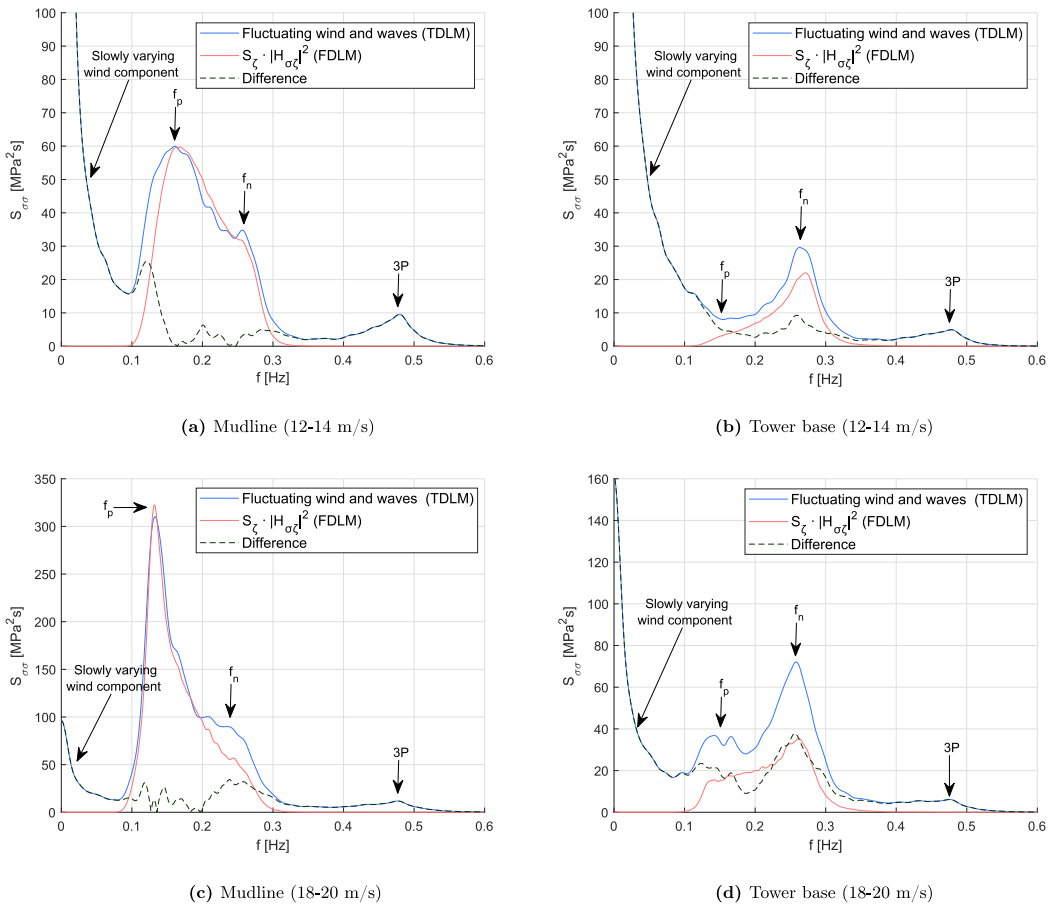

(a) Mudline (12-14 m/s)

(b) Tower base (12-14 m/s)

(c) Mudline (18-20 m/s)

(d) Tower base (18-20 m/s)

Fig. 14. Stress spectra from the frequency-domain lumping method (FDLM) using the transfer function $H_{\zeta\sigma}$ obtained based on uniform wind and 3-hr white noise wave loading, and from time-domain lumping method (TDLM) for combined wind-wave loading for the lumped load cases in wind class 12–14 m/s (top) and 18–20 m/s (bottom). f_p denotes the wave peak frequency, f_n is the support structure natural frequency and 3P is the blade passing frequency.

5.3. Fatigue damage comparison for aligned wind-waves

The assessment of a lumping method is based on the accuracy of the predicted damage from the lumped cases when compared to a full scatter analysis. To estimate the fatigue damage of the reduced load set, the OWT is subjected fully-integrated time-domain analyses with simultaneous turbulent wind and irregular wave excitation for the frequency-domain lumped load cases (Table 6 - FDLC). The time-domain lumped load cases (Table 6 - TDLC) have not been compared to full scatter results for two reasons. Firstly, because the lumped load cases from time- and frequency-domain methods are similar. Secondly, the time-domain lumping method is only used for comparison to frequency-domain method and not as an alternative to full scatter analysis because of its high computational effort.

5.3.1. Evaluation of damage estimation uncertainty by the lumped cases

The statistical uncertainty is expected to increase when a single environmental condition is used to represent all sea-states in a wind speed class. Therefore, several realisations of the same condition may be required to obtain accurate estimates of the fatigue damage. This is investigated by conducting 20 1-hr analyses for each lumped load case, with random wind and wave seed. The uncertainty is expressed by the coefficient of variation (C.o.V.) for a given number of seeds per sea-state. Fatigue damage is evaluated at the upwind position at mudline and at tower base. Fig. 15 shows the results for five selected wind speed classes. C.o.V. varies between approximately 4.5% and 24% for a single realisation, with a gradual reduction as the number of seeds increases.

For locations along the support structure where the wind contribution to fatigue damage is considerable, the estimated damage varies more. For example, in Fig. 15, the C.o.V. is larger at the tower base than at the mudline. Therefore, more analyses are required to achieve same level of C.o.V. For both locations, the C.o.V. is higher for wind classes close to the OWT rated speed (11 m/s), showing a maximum for class 8–10 m/s, while the lowest C.o.V. values are found for the highest wind speed class (24–26 m/s). By requiring a C.o. V. limit of 10% for the evaluation of the lumping method, five 1-hr time-domain analyses for each lumped load case are used for the comparisons with the full scatter results. This is considered a reasonable compromise between accuracy and computational effort.

5.3.2. Lumped load cases damage compared to full scatter results

This section will compare the long-term fatigue damage estimates obtained from the lumped load cases with the results from the full scatter analysis. This is first done assuming aligned wind and waves, corresponding to environmental models N°1 and N°2 in subsection 4.1. To evaluate the uncertainty caused by using five 1-h realisations of the lumped load cases, 4 "sets" of results are generated. Each set consists five 1-hr realisations of the 11 lumped load cases (Table 6 - FDLC) associated with the different wind speed classes. The average damage is used for the comparisons. A negative (positive) difference implies an underestimation (overestimation) of the damage calculated by the lumped set with respect to the full scatter result. The results are compared at the location along the monopile with the highest long-term fatigue damage, 8.25 m below the mudline. Fig. 16 shows the total and per wind class damage comparisons.

Although the four sets consist of identical lumped load cases in terms of environmental parameters, stochastic variation in the estimated fatigue damage is significant. The relative differences for individual wind speed classes for both models show a variation between approximately ±13% with respect to full scatter results as a consequence of seed variability. As an example, focusing on wind class 20–22 m/s in Fig. 16b, the damage difference ranges between 11% (Set N°1) to −6.7% (Set N°4) compared to the full scatter results. The total fatigue damage relative differences are however relatively stable, with the largest underestimation being
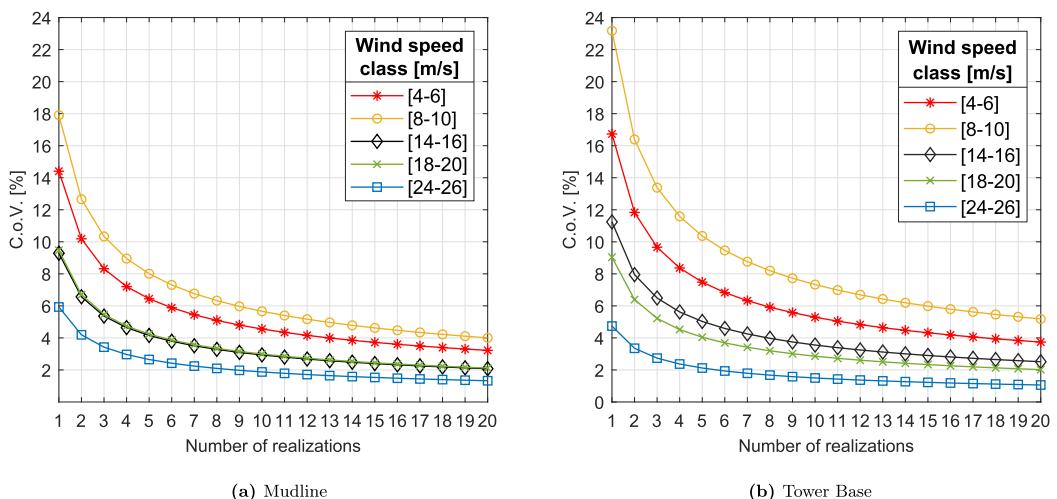

(a) Mudline

(b) Tower Base

Fig. 15. Statistical uncertainty of fatigue damage estimation as a function of number of seed realisations for two locations along the support structure.
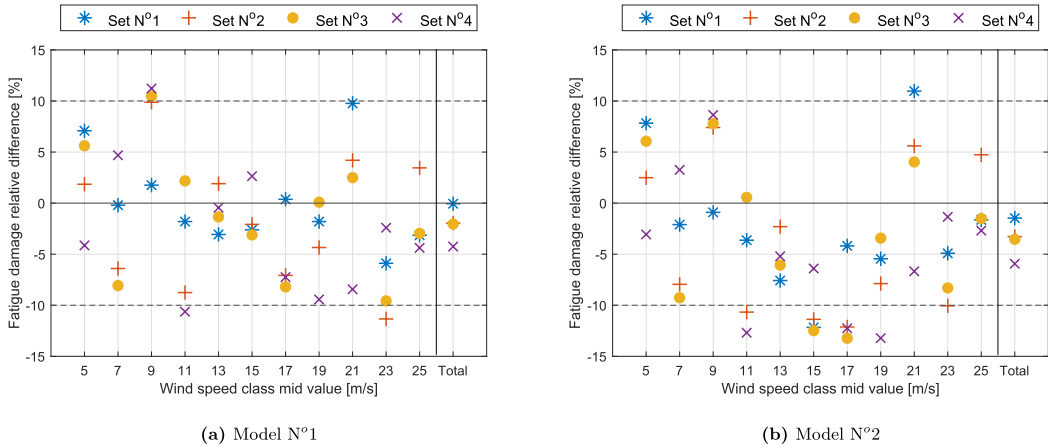
(a) Model N°1

(b) Model N°2

Fig. 16. Total and per wind class fatigue damage relative difference between lumped load cases per set and full scatter results for aligned wind and waves, without (Model N°1) and with (Model N°2) considering long-term wind direction variability. Comparison at the monopile location (vertical and around the circumference) with the highest long-term fatigue damage.

approximately 6%. The fatigue damage relative differences of models N°1 and N°2 compared to full scatter results show negligible variations, implying that the damage equivalency of the lumping method holds without and with considering long-term wind directional variability. Based on the above, using five realisations for each lumped load case results in acceptable variations in fatigue damage estimation per wind class. Finally, comparing Model N°1 and Model N°2, a significant reduction (~64%) of the total and per wind class fatigue damage was observed, due to the long-term wind directional variability, explained by the wind-wave roses in Fig. 7.

5.3.3. Fatigue damage equivalency along the OWT support structure

Several damage-equivalent contour lines along the monopile and tower were used, as described in section 2. The objective is to select a lumped load case for which the fatigue damage could be potentially preserved for the whole support structure. Fig. 17 confirms that this is achieved, using three wind speed classes for illustration. The lumped load cases can result in either underestimation or overestimation of the fatigue damage compared to full scatter results as shown in Fig. 16. Overall, the deviations are small, especially for the total fatigue damage, considering all the relevant uncertainties related to lumping process, fatigue calculation, and non-linearities.

The total fatigue damage preservation through the lumping process is also illustrated for three different cross sections along the support structure in Fig. 18, for environmental Model N°2. In addition, Fig. 19 shows the individual contribution to the total fatigue damage from each wind speed class for each cross section in Fig. 18. As noted in subsection 5.2, the fatigue damage in the tower is dominated by the responses due to wind loading close to the rated speed. This is indicated by the relatively high contribution of wind classes 6–8 m/s 10–12 m/s and 12–14 m/s in Fig. 19a. For locations in lower positions along the monopile, the wave loads gradually become more important for the fatigue damage.

5.4. Misaligned wind-wave conditions

The frequency-domain lumping method was also applied for wind-wave misalignment conditions. The same procedure is followed as described in subsection 2.3, except that the 3-hr white noise wave excitation is now applied with the required misalignment angle with respect to the uniform wind field, which is applied in the fore-aft direction. The stress transfer function is extracted at the location on the cross section with the highest unit fatigue damage.

With misaligned wind and wave conditions comes a difference in the direction of the primary excitation sources of an OWT. As a result, the maximum response will neither be aligned with the wind nor the wave direction. Further, the lack of aerodynamic damping in the cross-wind direction will increase the cross-wind response for the wave-only analyses [36]. This is illustrated in Fig. 20, where the lumped load case for wind class 18–20 m/s was simulated with fluctuating wind and waves and with uniform wind and waves. In both cases, wind is arriving from 0° (fore-aft direction) and waves are arriving from 30°. The difference between the locations with largest fatigue damage when considering and neglecting the turbulent wind excitation is approximately 35° in the tower base, i.e. larger than the wind-wave misalignment. This differs from the case with aligned wind and waves, and it is of interest to investigate the accuracy of the lumping method when considering wind-wave misalignment.

Three wind speed classes have been analysed to limit the computational effort. These are the wind speed classes 6–8, 12–14 and 18–20 m/s, which have been analysed for 30° and 60° wind-wave misalignment. Only the 30° results are presented here, as the results for the two misalignment angles are similar. Fig. 21 shows the maximum fatigue damage along the monopile and tower. The lumped load cases underpredicts the fatigue damage for all wind speeds. For the wind class 12–14 m/s, the error is 7% for the most critical
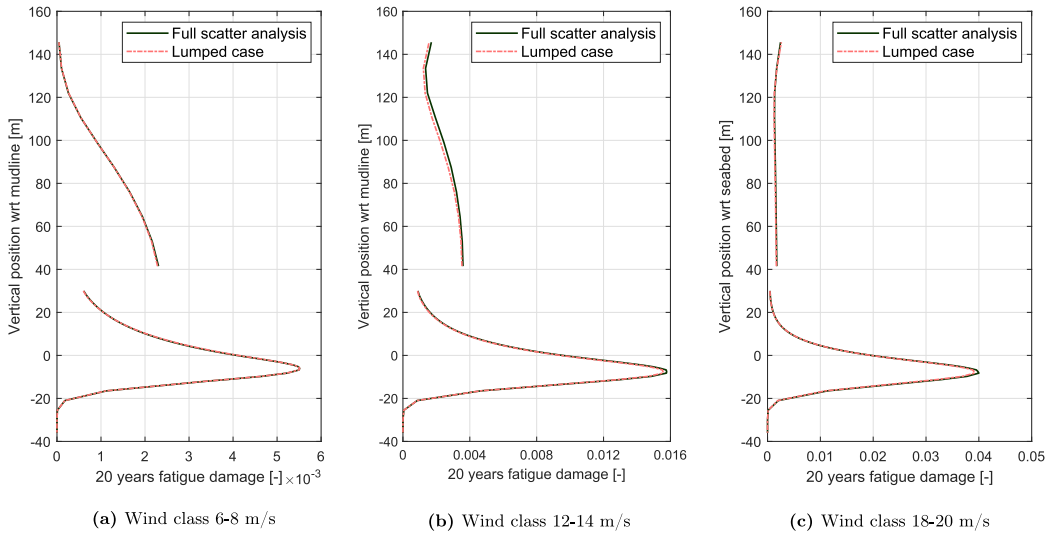
Fig. 17. Lifetime fatigue damage from full scatter diagram analyses and lumped load cases for aligned wind-waves (Model N°1).
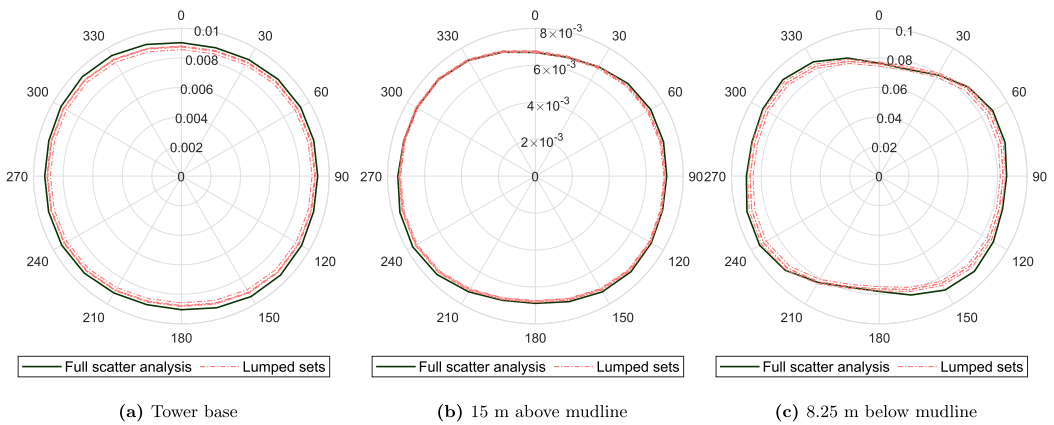

Fig. 18. Total fatigue damage for three different cross-sections along the support structure obtained from full scatter analysis and the 4 lumped load sets (Model N°2).
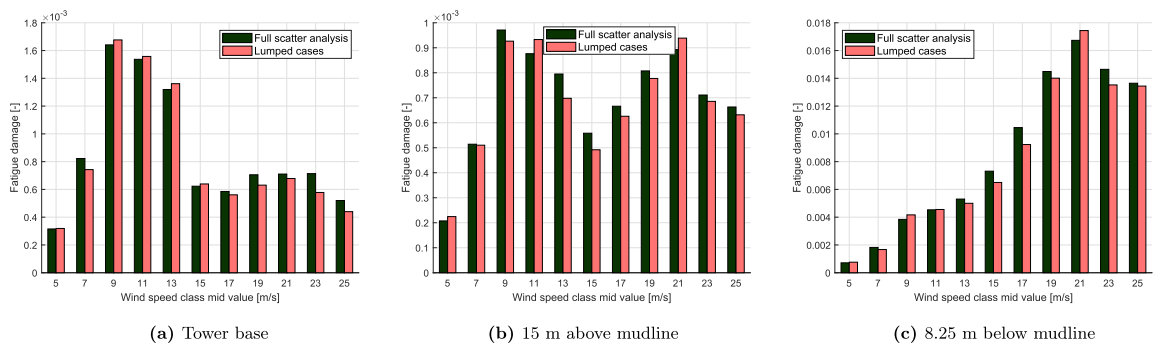

Fig. 19. Contribution of individual wind speed classes to total fatigue damage for the three cross-sections of Fig. 18 from full scatter analysis and a lumped load set (Model N°2).
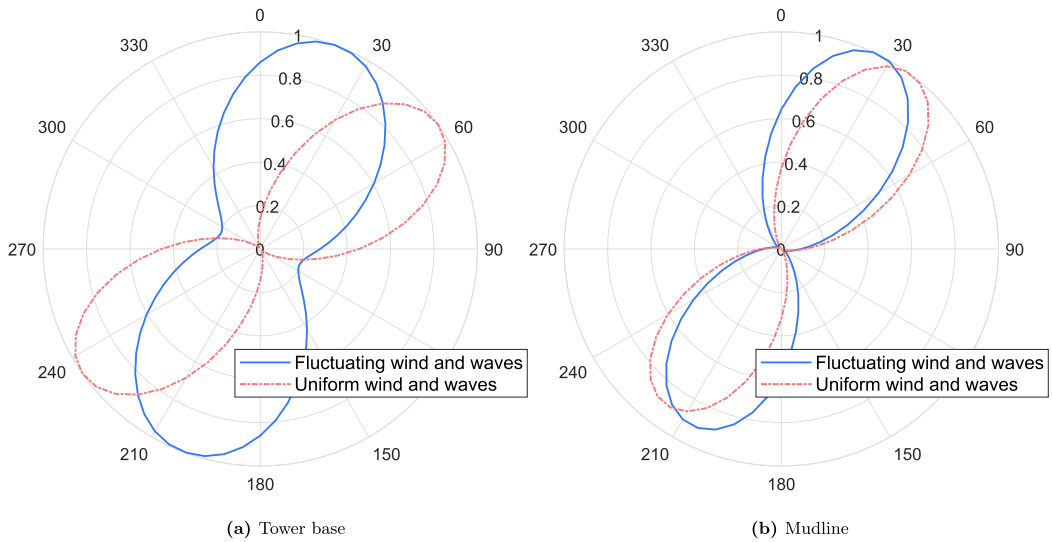
(a) Tower base

(b) Mudline

Fig. 20. Normalised fatigue damage at tower base and mudline for lumped load case in wind class 18–20 m/s with 30° wind-wave misalignment. The mean wind direction is from 0°.
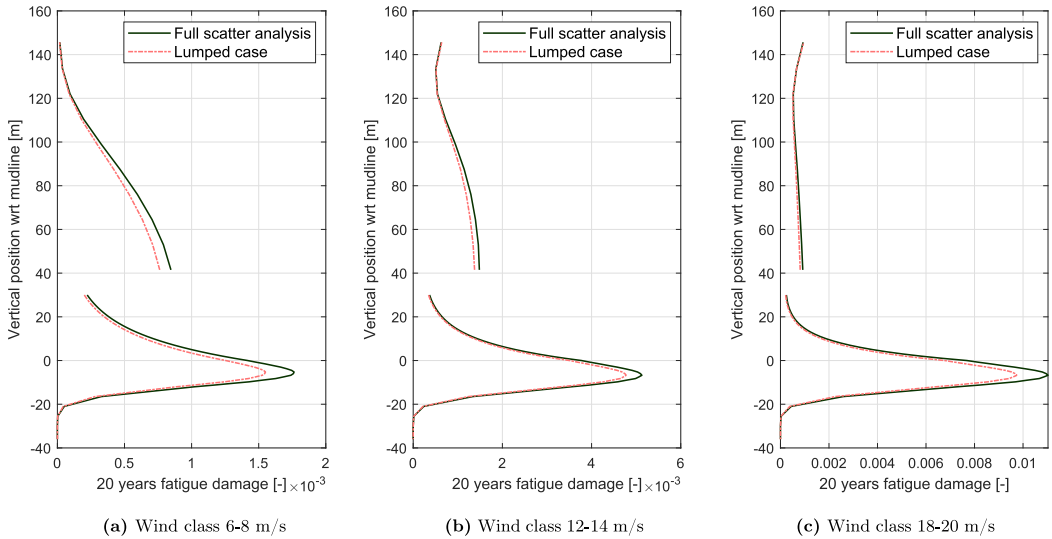

(a) Wind class 6-8 m/s

(b) Wind class 12-14 m/s

(c) Wind class 18-20 m/s

Fig. 21. Lifetime fatigue damage from full scatter diagram and lumped load cases with 30° wind-wave misalignment.

position on both the tower and monopile. In the two other wind speed classes, the error is 10–12% at the most critical positions.

These errors are larger than those seen for aligned wind and waves. However, the corresponding error in damage equivalent stress is 2.3% or lower for all cases. This is similar to the uncertainty introduced by the thickness tolerance for tower and monopile walls, as reported in Ref. [37].

5.5. Fatigue damage sensitivity to lumped load cases

The sensitivity of the fatigue damage to variation in H_s and T_p is evaluated for three wind speed classes; 8–10 m/s, 12–14 m/s, and 18–20 m/s. Each parameter is varied around its nominal value (i.e. the FLDC value from Table 6) with a factor between 0.6 and 1.4, while the other parameter is kept constant. All the $H_s - T_p$ combinations of the modified load cases are within the wave steepness limits suggested by the design codes [30]. The average 1-hr fatigue damage from 10 realisations is compared. The sensitivity is expressed as

the ratio between the damage of the modified load cases to the damage from the nominal lumped load case. An example of damage sensitivity to $H_s - T_p$ is shown in Fig. 22 for two wind speed classes, and for different locations along the support structure. The bottom and top x-axis show the normalised and actual parameter values, respectively. The results are similar for all three wind classes.

Fig. 22a clearly indicates that for locations on the tower and close to the sea surface, there is an approximately linear variation of the fatigue damage with respect to H_s. As the moment arm increases for locations deeper along the monopile and closer to mudline, the relation between H_s and fatigue damage variation gradually approaches to follow H_s^4. This is lower than the theoretical limit for wave-only loads, where the fatigue damage would follow H_s^5 [7,29]. The lower exponent reflects that wind-induced loads also contribute to the fatigue damage, which decreases the sensitivity to wave loads.

Fig. 22b indicates that the influence of T_p variation to fatigue damage is similar along the support structure, given that T_p is sufficiently far from the natural period of the structure. For longer wave periods, the response becomes more quasi-static, reducing the number of load cycles. As a result, fatigue damage is steadily decreased, with slight variations along the support structure. The opposite effect is observed by decreasing the T_p. However, when approaching the natural period range (i.e. 3.7–4.0 s), the effect of T_p variation is pronounced due to the high dynamic amplification. The effect is more significant for the tower and monopile locations close to sea surface as the relative deflections in the first mode shape are larger there than i.e. at mudline. The sensitivity seen for variations in T_p corresponds well with T_p^{-1}. This is the theoretical curve obtained for wave-only loads if it is assumed that changes in T_p only affect the number of load cycles [7]. A steeper curve is obtained if changes in wave kinematics are taken into account, with the limit T_p^{-11} for a narrow-banded wave spectrum [29]. As for H_s, the true curve approaches T_p^{-1} since the wind loads reduce the sensitivity to wave loads.

If it is desirable to modify the sea-state parameters of the lumped load cases (i.e. to get less or more conservative fatigue damage values), it is recommended to change the T_p value, ensuring that it has sufficient distance from the natural period. This is due to the fact that T_p variations affect the different locations in tower and monopile more similarly. In contrast, H_s variations affect the locations with large moment arm (i.e. close to mudline) more significantly than locations close to sea surface and the tower.

5.6. Lumped load cases selection sensitivity in foundation design changes

The penetration depth is one of the most important design parameters for monopile foundations from safety and economical perspective. The frequency-domain lumping method for aligned wind and waves, was applied to the other four foundation models (subsection 3.2.2), which vary in penetration depth. The purpose was to evaluate the lumped load case selection sensitivity on foundation design variations. Fig. 23 shows the contour lines for wind speed class 18–20 m/s for two foundation models at mudline and tower base.

Contour lines are similar also for the rest of the models. Slight differences of the dynamic properties of the models (Fig. 9) affected the contour lines only in the natural period range of the structure, while for T_p larger than 4.5 s the contour lines are identical. The same is observed for all wind speed classes. This resulted in identical lumped load cases for all wind speed classes, as illustrated in Fig. 23 where the selected $H_s - T_p$ combinations for each class are shown. As a result, the same lumped load cases can be used for different designs with good accuracy as long as T_p of the lumped load case is far enough away from the OWT natural period.

6. Conclusion

In this paper two environmental lumping methods were investigated based on the damage-equivalent contour lines approach. The DTU 10 MW reference wind turbine supported on a monopile foundation is used for the study. The aim of both methods is to condense
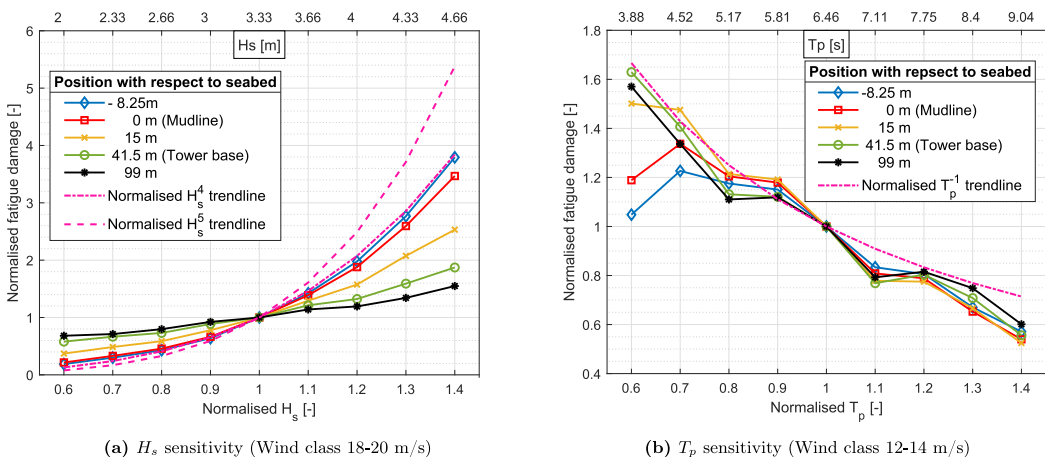

(a) H_s sensitivity (Wind class 18-20 m/s) (b) T_p sensitivity (Wind class 12-14 m/s)

Fig. 22. Normalised fatigue damage sensitivity for various locations along the support structure as function of H_s, T_p variation.

(a) Contour lines
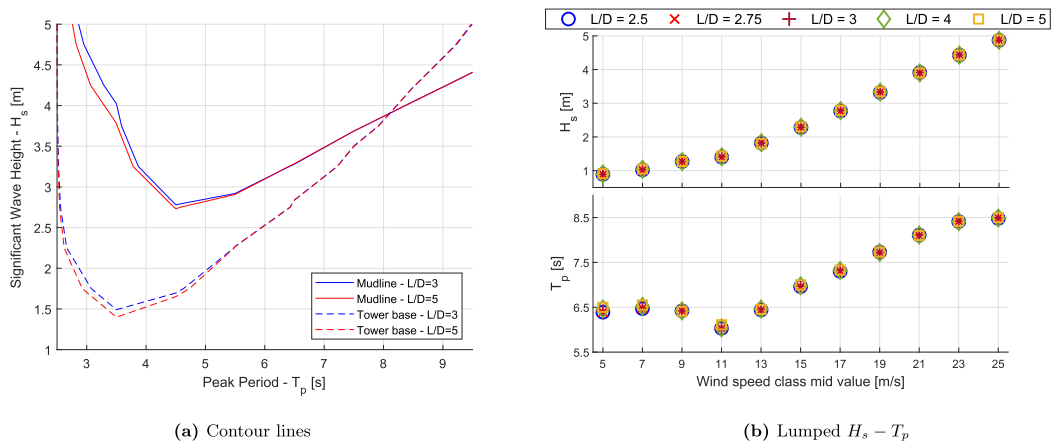
(b) Lumped $H_s - T_p$

Fig. 23. (a) Contour lines of two foundation models from frequency-domain lumping method for wind speed class 18–20 m/s (b) Lumped sea-state parameters of each foundation model per wind speed class.

each scatter diagram associated with a wind speed class to a single sea-state load case. The frequency-domain method uses a transfer function from wave elevation to stress, to determine the contour lines and resultant lumped load cases. Stress transfer functions are extracted from a 3-hr white-noise wave excitation and uniform wind for a given scatter diagram. The time-domain approach is based on time-domain simulations, it is only used for comparison to frequency-domain method and not as an alternative to full scatter analysis.

The wind turbine operational range was considered, including 11 wind speed classes, each one associated with a sea-state scatter diagram. Selected lumped load cases are subjected to simultaneous wind-wave loads to predict long-term fatigue damage. The accuracy of the damage estimate varied between $\pm 13\%$ for individual wind speed classes with a maximum difference of $\sim 6\%$ for the total fatigue damage compared to full scatter fatigue assessment. These differences are considered to be acceptable notably in view of the significant improvement in computational efficiency ($\sim 93\%$); 55 1-hr time-domain simulations (5 for each lumped load case to reduce statistical uncertainty) have been conducted for a reduced load set instead of 800 (full scatter analysis). Furthermore, these differences are tolerable considering the inherent uncertainty of condensing a scatter diagram in one load case, the uncertainty in fatigue damage estimation per 1-hr simulation and the nonlinearities in the environmental models. Similar accuracy is found for aligned wind-waves with and without considering long-term wind direction variability. It is recommended to validate this in sites with different environmental databases.

Using several contour lines for the selection of lumped load cases ensured preservation of fatigue damage with the same level of accuracy in the whole support structure, compared to the full scatter results. The fatigue damage sensitivity to H_s and T_p variations was also evaluated. As long as the nominal T_p value is far from the natural period, variations of $\sim 10\%$ result in fairly uniform change in the damage along the support structure. However, similar changes in H_s lead to significant damage differences ($\sim 40\%$) for locations with large moment arm (i.e. close to mudline), while locations close to sea-surface and the tower are much less affected ($\sim 10\%$). For wind-wave misalignment cases, an underestimation of approximately 10% was observed in fatigue damage for the evaluated wind speed classes. Taking into account the considerable reduction in computational effort, this error might be acceptable in an early design stage.

Lumped load cases from frequency-domain lumping method were compared for five monopile designs of different penetration depth, with L/D ratio varying from 2.5 to 5. For the system being considered, the dynamic properties were insensitive to the penetration length, such that the resulting lumped cases did not change significantly. This is useful, as design changes are expected during the design optimisation process, but this should be examined for other structural parameters, such as monopile diameter or thickness, where larger changes in the natural period may be expected.

Declaration of competing interest

The authors declare that they have no known competing financial interests or personal relationships that could have appeared to influence the work reported in this paper.

Acknowledgements

References

[1] Selot F, Fraile D, Brindley G. Offshore wind in Europe - key trends and statistics, Published in February 2020, WindEurope. Tech. rep; 2020.
[2] Hermans JM, Peeringa KW. Future XL monopile foundation design for a 10MW wind turbine in deep water. Tech. rep; December, 2016. ECN-E–16-069.
[3] ABS (American Bureau of Shipping). Guide for the fatigue assessment of offshore structures. 2014.
[4] DNV-GL (Det Norske Veritas - Germanischer Lloyd), Fatigue design of offshore steel structures (DNVGL-RP-C203).
[5] Du J, Chang A, Wang S, Li H. A novel lumping block method for fatigue damage assessment of mooring chain. 2014.
[6] DNV-GL (Det Norske Veritas - Germanischer Lloyd). Riser fatigue. 2017 (DNVGL-RP-F204).
[7] Kühn M. Dynamics and design optimisation of offshore wind energy Conversion systems. Ph.D. Thesis. Delft, The Netherlands: Technische Universiteit Delft; 2001. ISBN 90-76468-07-9.
[8] M. Seidel, Wave induced fatigue loads - insights from frequency domain calculations, Stahlbau 83. doi:10.1002/stab.201410184.
[9] Seidel M. Wave induced fatigue loads on monopiles - new approaches for lumping of scatter tables and site specific interpolation of fatigue loads. In: International wind engineering conference. IWEC; 2014.
[10] IEC (International Electrotechnical Commission). Design Requirements of offshore wind turbines. 2009 (IEC 61400-3).
[11] DNV-GL (Det Norske Veritas - Germanischer Lloyd). Support structures for wind turbines. 2016 (DNVGL-ST-0126).
[12] Passon P, Branner K. Condensation of long-term wave climates for the fatigue design of hydrodynamically sensitive offshore wind turbine support structures. Ships Offshore Struct 2014;11:142–66.
[13] Jenkins N, Burton A, Sharpe D, Bossanyi E. Wind energy handbook. John Wiley and Sons Ltd; 2001.
[14] Passon P. Damage equivalent wind-wave correlations on basis of damage contour lines for the fatigue design of offshore wind turbines. Renew Energy 2015;81: 723–36.
[15] Jonkman J, Butterfield S, Musial W, Scott G. Definition of a 5-mw reference wind turbine for offshore system development. Report NREL/TP-500-38060; TRN: US200906US200906CO (United States) (2009). URL, https://www.osti.gov/servlets/purl/947422.
[16] Carroll J, McDonald A, Dinwoodie I, McMillan D, Revie M, Lazakis I. Availability, operation and maintenance costs of offshore wind turbines with different drive train configurations. Wind Energy 2017;20(2):361–78. https://doi.org/10.1002/we.2011.
[17] Page A, Grimstad G, Eiksund G, Jostad HP. A macro-element pile foundation model for integrated analyses of monopile based offshore wind turbines. Ocean Eng 2018;167:23–35.
[18] MacCamy RC, Fuchs RA. Wave forces on piles: a diffraction theory. Tech. Memo No. 69, U.S. Army Corps of Engrs; 1954.
[19] Barltrop NDP, Adams AJ. Dynamics of fixed marine structures. third ed. Oxford: Butterworth-Heinemann; 1991.
[20] Dirlik T. Application of computers in fatigue analysis, Phd thesis. 1985. http://wrap.warwick.ac.uk/2949/.
[21] Li L, Gao Z, Moan T. Joint environmental data at five European offshore sites for design of combined wind and wave energy devices. In: International conference on ocean, offshore and arctic engineering. OMAE; 2013.
[22] Bak C, Zahle F, Bitsche R, Kim T, Yde A, Henriksen LC, et al. Description of the DTU 10 MW reference wind turbine. Tech. rep., Technical University of Denmark, Department of Wind Energy; 2013.
[23] Jonkman BJ. TurbSim user's guide: version 1.50, technical report. Tech. rep; 2009. NREL/TP-500-39797, National Renewable Energy Laboratory.
[24] Burton T, Jenkins N, Sharpe D, Bossanyi E. Wind energy handbook. John Wiley & Sons, Ltd; 2011.
[25] Bachynski E, Ormberg H. Comparison of engineering models for the aerodynamic load distribution along a wind turbine blade 2015. 2015. p. 561–7.
[26] Correia A. A pile-head macro-element approach to seismic design of monoshaft supported bridges. 2011. Ph.D. thesis, Pavia, Italy.
[27] Page A, Grimstad G, Eiksund G, Jostad HP. A macro-element model for multidirectional cyclic lateral loading of monopiles in clay. Comput Geotech 2019;106: 314–26.
[28] Grimstad G, Andresen L, Jostad HP. Ngi-adp: anisotropic shear strength model for clay. Int J Numer Anal Methods GeoMech 2012;36(4):483–97. https://doi.org/10.1002/nag.1016.
[29] Velarde J, Bachynski EE. In: Design and fatigue analysis of monopile foundations to support the DTU 10 MW offshore wind turbine, vol. 137. Energy Procedia; 2017. p. 3–13.
[30] DNV-GL (Det Norske Veritas - Germanischer Lloyd). Environmental conditions and environmental loads. 2017 (DNVGL-RP-C205).
[31] Matsuishi M, Endo T. Fatigue of metals subjected to varying stress. In: Kyushu branch of jpan society of mechanics engineering; 1968. p. 37–40.
[32] Brodtkorb P, Johannesson P, Lindgren G, Rychlik I, Ryden J, Sjo E. WAFO—a MATLAB Toolbox for the analysis of random waves and loads. In: 10th international offshore and polar engineering conference (ISOPE), vol. 3; 2000. p. 343–50.
[33] Bachynski EE, Kvittem MI, Luan C, Moan T. Wind-wave misalignment effects on floating wind turbines: motions and tower load effects. J Offshore Mech Arctic Eng 2014;136.
[34] Horn JT, Bitner-Gregersen EM, Krokstad J, Leira B, Amdahl J. A new combination of conditional environmental distributions. Appl Ocean Res 2018;73:17–26.
[35] Katsikogiannis G, Bachynski EE, Page AM. Fatigue sensitivity to foundation modelling in different operational states for the DTU 10 MW monopile-based offshore wind turbine. J Phys Conf 2019;1356:012019.
[36] Damgaard M, Ibsen LB, Andersen LV, Andersen J. Cross-wind modal properties of offshore wind turbines identified by full scale testing. Wind Engineering & Industrial Aerodynamics 2013;116:94–108.
[37] Velarde J, Kramhøft C, Sørensen JD. Global sensitivity analysis of offshore wind turbine foundation fatigue loads. Renew Energy 2019;140:177–89. https://doi.org/10.1016/j.renene.2019.03.055.

Paper 3:

Comparison of numerical response predictions for a bottom-fixed offshore wind turbine

Stian H. Sørum, Jan-Tore H. Horn, Jørgen Amdahl

14th Deep Sea Offshore Wind R&D Conference, EERA DeepWind'2017, 18-20 January 2017, Trondheim, Norway

Comparison of numerical response predictions for a bottom-fixed offshore wind turbine

Stian Høegh Sørum[a,*], Jan-Tore H. Horn[a], Jørgen Amdahl[a]

[a]Centre of Autonomous Marine Operations and Systems (AMOS), Department of Marine Technology, Norwegian University of Science and Technology (NTNU), NO-7491 Trondheim, Norway

Abstract

Numerical simulations are widely used for response calculations on offshore wind turbines. Code-to-code comparisons are frequently used for verification of the codes, as full-scale measurements can be difficult to obtain. However, most code comparisons performed focus on documenting the responses predicted by the different codes, or on the effect of specific differences between the codes. Little insight is provided to how these differences would affect design calculations, such as the fatigue utilization. In this paper, the response predictions of the programs SIMA, vpOne and FAST are compared using the DTU 10 MW reference wind turbine on a monopile foundation. While differences in the models are first highlighted through a number of simplified load cases, a lifetime fatigue evaluation of the model is then performed for the monopile at mudline. In the deterministic load cases the response of all models are quite similar, while some differences become apparent in the stochastic analysis. For the fatigue calculations, a difference of 14 % is found in the damage equivalent bending moment at mudline. This demonstrates how sensitive the fatigue utilization is to small differences is code capabilities and modelling.

Keywords: Bottom-fixed wind turbine; code comparison; stochastic wind and waves; fatigue

1. Introduction

The most widely-used method for analysis of offshore wind turbines (OWTs) is numerical time-domain simulations. However, limited access to full-scale measurements makes it difficult to validate the computer codes against real-life measurements. Software-to-software comparisons have therefore been used extensively in verification of developed codes. Here, the OC3, OC4 and OC5 projects [1–4] stand as the greatest efforts, with a large number of institutions and codes contributing to large-scale comparisons. Other code comparisons have also been performed; either with the introduction of new code features or as more ad-hoc investigations to explain differences between the codes [5–10].

---

* Corresponding author. Tel.: +47 932 45 097.
  E-mail address: stian.h.sorum@ntnu.no

In addition to verifying the theory implementations, code-to-code comparisons are suitable for investigating how different solution methods affect the calculation results. A large number of different calculation and solution methods are available and implemented in the different codes. Aerodynamic loads are typically calculated using the blade element momentum theory (BEM), while CFD analyses and generalized dynamic wake are examples of alternative calculation methods[11]. The BEM theory can also include a number of engineering corrections. Wave kinematics can be calculated using linear or higher order wave theory, and integrated to the mean or instantaneous free surface. Furthermore, a number of options are available for modelling of soil-structure interactions. Kühn [12] presents three options for a monopile structure: the use of nonlinear springs along the length of the pile, implementation of a translational and rotational spring at the mudline, or the use of an equivalent cantilever beam. Finally, the structural dynamics can be analysed using either the finite element method, modal analysis, multibody dynamics or a combination of these.

This paper aims at investigating how the calculated fatigue utilization will vary between different computer codes. To do this, the DTU 10 MW reference wind turbine [13] is modelled in SIMA v3.3.2 from SINTEF Ocean, FAST v8 from NREL and vpOne from Virtual Prototyping. The paper will first present the model, before an overview of the theory implementations and modelling capabilities of the codes will be given. Following this, the response to deterministic load cases are presented to easier identify the differences between the codes. Finally, a number of stochastic load cases are analysed before a simplified fatigue analysis is performed.
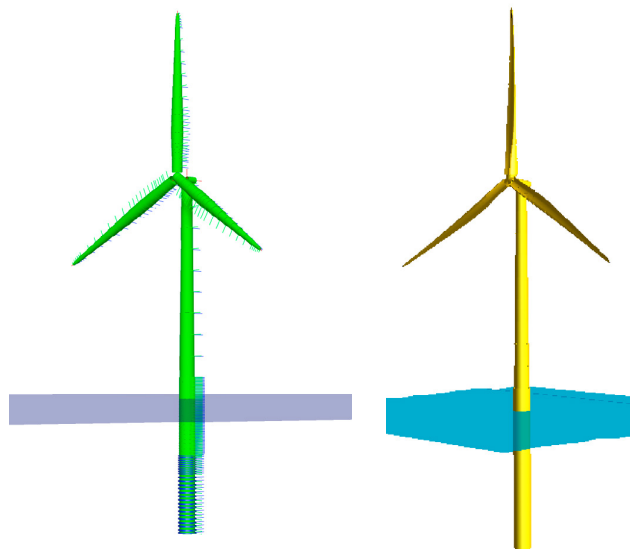
2. Model Description

Fig. 1. Model in SIMA (left) and vpOne (right)

The turbine used in the analyses is the DTU 10 MW reference turbine, as described in [13], with the basic DTU 10 MW controller [14]. In order to reduce the natural period, the wall thickness of the tower has been increased by 20 %. Furthermore, the inner foils of the turbine have been modified, both following [15]. The turbine is placed on a monopile foundation in 30 m water depth, which extends to 42 m below the mudline. The transition piece is modelled from 10 m below the mean water level (MWL) to 11.5 m above MWL. Both the transition piece and monopile have an outer diameter of 9 m, while the thickness is set to an equivalent thickness of 0.15 m for the transition piece and 0.11 m for the monopile. Soil properties are taken from Dogger Bank, and the soil is modelled as non-linear springs using the p-y curves in accordance with [16] in SIMA and vpOne. In FAST, an equivalent cantilever beam is used to represent the soil stiffness. Structural damping was modelled as mass and stiffness proportional damping in SIMA

and vpOne, while modal damping was applied in FAST. This was set to be 0.70 % of critical damping at the first and second tower modes. The turbine as modelled in SIMA and vpOne is shown in Figure 1.

3. Program Capabilities

This section briefly presents the capabilities of the three codes, and will furthermore specify which options that have been used in the analyses. For more detailed theory, or description of other capabilities, the reader is referred to the relevant theory manuals [17–22]. A summary of the differences can be found in Table 1, with the exception of the aerodynamics, which is given in Table 2.

Table 1. Differences in code capabilities

	SIMA	VpOne	FAST
Wave Kinematics	Airy or Stokes 5th order (Airy used)	Airy, Stokes 5th order or Stream function (Airy used)	Airy or 2nd order waves (Airy used)
Hydrodynamic stretching	None, Wheeler, constant extrapolation, moving of potential (Wheeler used)	Wheeler or constant extrapolation (Wheeler used)	None
Hydrodynamic load model	Morison, MacCamy & Fuchs (Morison used)	Morison, MacCamy & Fuchs (Morison used)	Morison, potential flow (Morison used)
Soil stiffness model	Non-linear springs	Non-linear springs	Equivalent beam
Structural model	FEM, Beam elements	FEM, Beam elements	Modal model, FEM (modal model used)
Controller type	Java	DLL	DLL

3.1. Aerodynamic Loads

While all three codes utilize BEM theory, there are different corrections implemented in the three codes [17,20], as given in Table 2. Furthermore, the distribution of aerodynamic properties varies between the programs. In SIMA, the aerodynamic properties are specified for each structural element, while FAST defines the properties at given cross sections and interpolates the values. VpOne allows both options to be used, and the SIMA method has been used in the analyses. As an alternative to BEM, FAST can also calculate aerodynamic loads using Generalized Dynamic Wake (GDW), but this is currently not available in the latest version of AeroDyn (v15)[20]. All codes can include tower drag, but this has not been utilized in this paper.

Table 2. Aerodynamic corrections

	SIMA	VpOne	FAST (AeroDyn v15)
Prandtl's correction	Tip loss	Tip loss	Hub & tip loss
Glauert correction	Burton formulation	Two options, as given in [23]	Buhl formulation
Dynamic Wake	Øye model	Øye model	No
Dynamic stall (not used)	Øye model	Øye model	Beddoes-Leishman model
Upwind tower influence	Potential flow	Potential flow	Potential flow
Skewed inflow	Yes	Yes	Yes

3.2. Hydrodynamic Loads

All codes calculate the hydrodynamic loads using Morison's equation, while diffraction can be taken into account using MacCamy & Fuchs correction is SIMA and vpOne [17,18,21]. Furthermore, SIMA and vpOne include the option to extrapolate the wave kinematics to the instantaneous free surface, either by constant extrapolation or Wheeler stretching. As vpOne requires extrapolation of some kind, Wheeler stretching has been used in both the SIMA and vpOne simulations. Stretching is not yet available in FAST v8.

Airy wave theory has been used in all analyses, and the Morison coefficients have been specified to 1.0 and 0.9 for the added mass and drag terms.

3.3. Soil Modelling

SIMA and vpOne both utilize distributed non-linear springs in the soil modelling. In FAST, the soil is modelled using an equivalent cantilever beam. This requires the cantilever to be tuned in order to provide the correct natural period and response, which has been done using the steady state tower top displacement and mudline bending moment as the tuning parameters.

3.4. Structural Model

Both SIMA and vpOne are non-linear finite element analysis programs developed for the offshore industry. While the element formulations differ between the two codes, they both allow for large rotations and displacements, as well as non-linear material behaviour [17,19].

In FAST, the tower and blades are modal models in ElastoDyn, while the equivalent monopile is modelled as a FEM structure and reduced to a modal model using the Craig-Bampton method [22]. The two first tower modes in fore-aft and side-side direction are included together with the two first flapwise modes and first edgewise mode of the blades. It is also possible to model the full structure as finite element models in BeamDyn, but this has not been utilized here.

3.5. RNA Model

How the components in the rotor nacelle assembly (RNA) are modelled also varies between the codes. In both SIMA and FAST, the blade pitch is applied as a prescribed rotation of the blades. This is done differently in vpOne, where the pitch actuators are modelled as torsional springs and a torque is applied to pitch the blades.

Furthermore, both SIMA and vpOne applies the generator torque directly on the shaft, as given by the control system. The drivetrain dynamics are therefore embedded in the shaft properties. In FAST, these dynamics are calculated by a mathematical model of the drivetrain, before the resulting torque is applied to the structural model.

Finally, vpOne and FAST can both use the DTU controller as it is provided. A JAVA version of the controller is required in SIMA, and this may therefore not be as updated as in the other programs. All controllers have been tuned with the same coefficients.

4. Load Cases

In order to compare the predicted response of the turbine, a number of simulations have been run. These are presented in Table 3, where the first three load cases represent deterministic load cases that aim at highlighting the differences among the codes and models. The remaining load cases are stochastic, and aim at illustrating how the code differences influence the predicted response to stochastic loading.

Table 3. Load Cases

Load Case	Simulation type	Wind	Waves	Turbine operational	Tower top
1	Decay test	None	None	No	Free
2	Steady state	Constant uniform	None	Yes	Free
3	Stepped wind	Stepped, uniform	None	Yes	Fixed
4	Turbulent wind	Stochastic, w/shear	None	Yes	Free
5	Irregular waves	None	Irregular	No	Free
6	Combined wind and waves	Stochastic, w/shear	Irregular	Yes	Free

5. Decay Test and Modal Analysis

As a first comparison between the codes, a decay test on a non-operational turbine was performed. The FAST model was subjected to steady, uniform wind speed for 150 s, before the wind speed was abruptly changed to 0.01

m/s. An equivalent force was applied to the tower top of the SIMA and vpOne models, which were released at the same time as the change in wind speed in FAST. Figure 2 shows the decay of the tower base bending moment, and verifies similar damping properties for the models as well as confirming the first natural period of the fore-aft tower motion to be similar. By calculating the logarithmic decrement, the damping level of all models was confirmed.
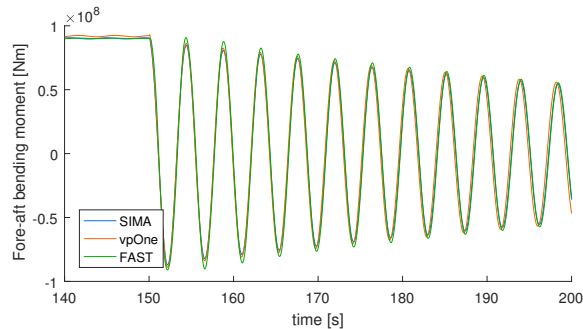
Fig. 2. Decay test

An eigenvalue analysis was also performed in SIMA and vpOne. The natural frequencies of the first modes are given in Table 4 and show reasonable similarities between the models. In FAST, the modes have been identified in the response spectra, and show good agreement with the those obtained with SIMA and vpOne.

Table 4. Eigenfrequencies in [Hz]

	SIMA	vpOne	Difference
1st tower side-to-side	0.227	0.226	0.4 %
1st tower fore-aft	0.228	0.228	0 %
1st blade asymmetric flapwise (yaw)	0.564	0.563	0.2 %
1st blade asymmetric flapwise (pitch)	0.594	0.592	0.3 %
1st blade collective flap	0.624	0.624	0 %
1st blade asymmetric edgewise 1	0.951	0.946	0.5 %
1st blade asymmetric edgewise 2	0.957	0.951	0.6 %
2nd tower side-to-side	1.303	1.241	4.8 %
2nd tower fore-aft	1.189	1.183	0.5 %
2nd blade asymmetric flapwise (yaw)	1.460	1.466	0.5 %
2nd blade asymmetric flapwise (tilt)	1.682	1.715	2 %

6. Wind Only Analysis

6.1. Steady State

To determine the basic aerodynamic and structural properties of the model in each code, the steady state responses were found. The turbines were subjected to constant, uniform wind varying from cut-in to cut-out, and the response after the initial start-up phase was found. For all quantities and wind speeds, the average value over the last 50 s of the analysis was taken as the steady-state solution.

The steady-state solutions are given in Figures 3 and 4. While there in general is good agreement between the three codes, some differences can be noted. For the aerodynamic quantities, FAST returns a lower rotational speed, torque and thereby also power production in the region where the blade pitch is zero. Also, SIMA returns a slightly higher rotational speed than vpOne at 10.5 and 11 m/s, which results in earlier pitching of the blades and a reduction of the thrust force in SIMA. While this can be related to the aerodynamic theories as well as structural and aerodynamic models of the blades, there are also some differences in blade pitch and thereby thrust force at wind speeds above rated.

This may be the result of differences in both the aerodynamics and the way the controller system is implemented in the different codes.

There are also some notable differences in the structural response predicted by the codes. Both the blade tip deflection and tower top displacement show a trend of being larger in vpOne for high wind speeds. This may partially be explained by differences in the predicted thrust, but the tower and foundation also seem to be slightly softer in vpOne. Up to rated wind speed, FAST predicts a lower tower top deflection than the other programs. This can partially be explained by the reduced thrust force in FAST, but also indicates a slightly stiffer structure.
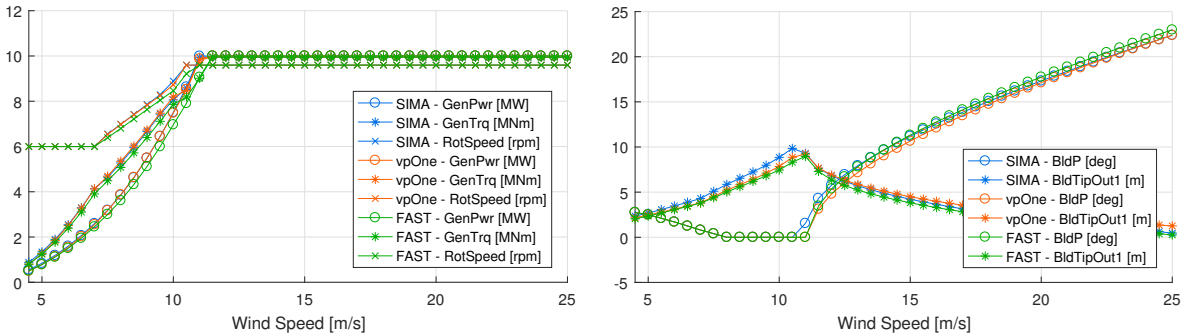

Fig. 3. Steady state responses as function of wind speed. GenPwr = Generator power, GenTrq = Generator torque, RotSpeed = Rotor speed, BldP = Pitch angle of blade 1, BldTipOut1 = Out-of-plane deflection of blade tip, blade 1
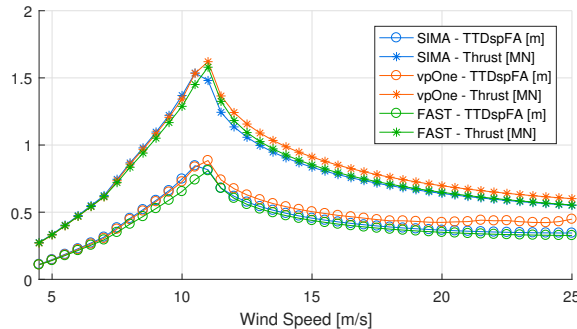

Fig. 4. Steady state responses as function of wind speed. TTDspFA = Fore-aft displacement of tower top, Thrust = Thrust force

6.2. Stepped Wind

The stepped wind analysis was performed to investigate how the control system and aerodynamics work together. With the tower top fixed to eliminate structural motions, the turbine was subjected to steady, uniform wind which was increased in steps of 1 m/s every 50 s, as shown in Figure 5. Some differences between the models become apparent: while FAST converges faster to the steady-state values for wind speeds below rated, SIMA and vpOne converge faster for wind speeds just above rated. For high wind speeds the three models reveal very similar behaviour, with the exception of blade pitch. The blade pitch is however consistent with the steady-state solutions, while the other observed differences indicate that there are some discrepancies in the controller dynamics in the three codes.

6.3. Stochastic Wind

While the above load cases have revealed some difference between the response predicted in the different codes, this does not represent realistic wind loading. The response was therefore analysed in two load cases with turbulent
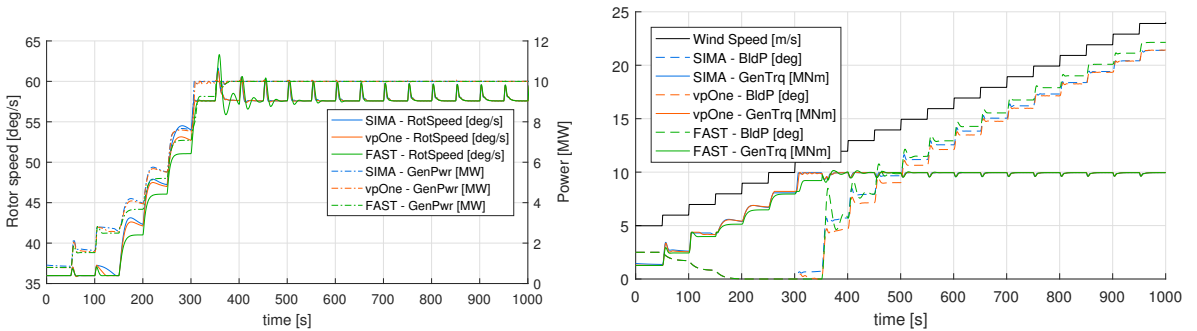
Fig. 5. Response to stepped wind

wind; one with wind speed below rated and one with wind speed above rated. LC 4.1 has a wind speed of 8 m/s measured 100 m above mean sea level, while LC 4.2 has a wind speed of 16 m/s. Both load cases have assumed turbulence class B and a power law exponent of 0.14. Turbsim from NREL has been used to generate 10 minute wind files for each load case, and the calculated spectra are the average of five seeds.
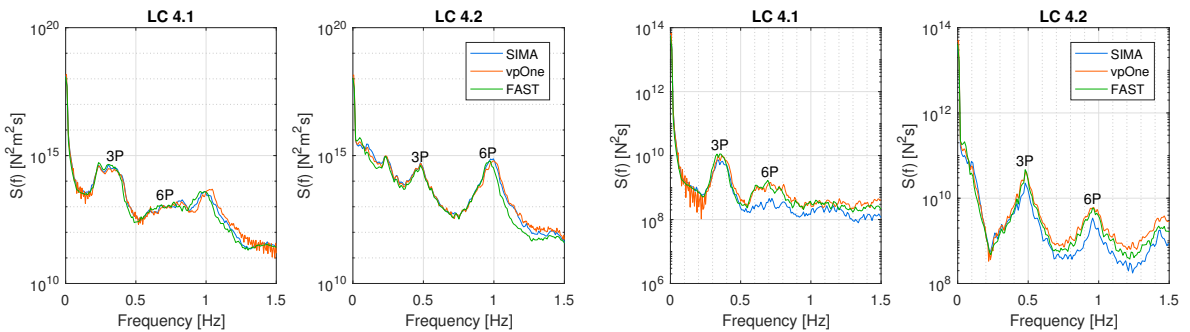

Fig. 6. Response power spectra for mudline moment (left) and thrust force (right) under turbulent wind

Figure 6 shows the response spectra for thrust and mudline bending moment. The spectra for mudline moment shows very similar response characteristics, while SIMA tends to give a lower estimate of thrust force spectrum, especially for the blade passing frequencies.

7. Stochastic Waves

To investigate the hydrodynamic models, two load conditions with irregular waves were analysed; one with a significant wave height of 1 m and peak period of 5 s and one with H_s of 2.5 m and T_p of 7 s. These are denoted respectively LC 5.1 and 5.2. In both conditions, the wave train and resulting wave kinematics are created from a JONSWAP spectrum by the codes. To minimize the aerodynamic damping, the blades were pitched to 82° and the wind speed set to 0.01 m/s.

The response spectra in Figure 7 shows that the base shear reaction is similar in the entire wave frequency range for all three codes, while the response at the first tower bending mode is of different amplitude. The same is seen for the moment at mudline, but this response is completely dominated by resonance.
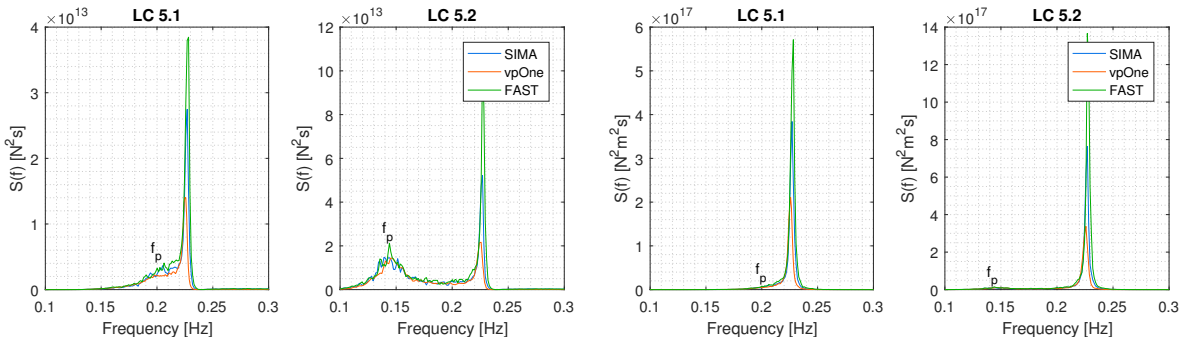
Fig. 7. Response power spectra for base shear (left) and mudline moment (right) under irregular wave loading

8. Combined Wind and Waves

The final analysis was performed for combined wind and wave loading, and were used in both a fatigue analysis and a spectral analysis. First, the results of the fatigue analysis are presented, then a selection of the response spectra are reported for some of the load cases.

The turbine is subjected to turbulent wind, created with TurbSim, and irregular waves generated by the simulation codes. For each condition, five one-hour simulations are carried out in SIMA and FAST, while the results in vpOne are based on 20 ten-minute simulations due to memory limitations in the used version of the program. The environmental data for the simulation parameters are taken from hindcast data provided by the Norwegian Meteorological Institute [24] for the location 54.8 °N, 1.92 °E, which is in the Dogger Bank area. The wind speed is divided into bins of 2 m/s from 4 to 20 m/s, and the most probable sea state for each wind speed is found using bins of 0.5 m for significant wave height and 1 s for the peak period. The resulting environmental conditions are shown in Figure 8, where the condition with the lowest wind speed is denoted LC 6.1 and the condition with the highest wind speed is denoted LC 6.9.
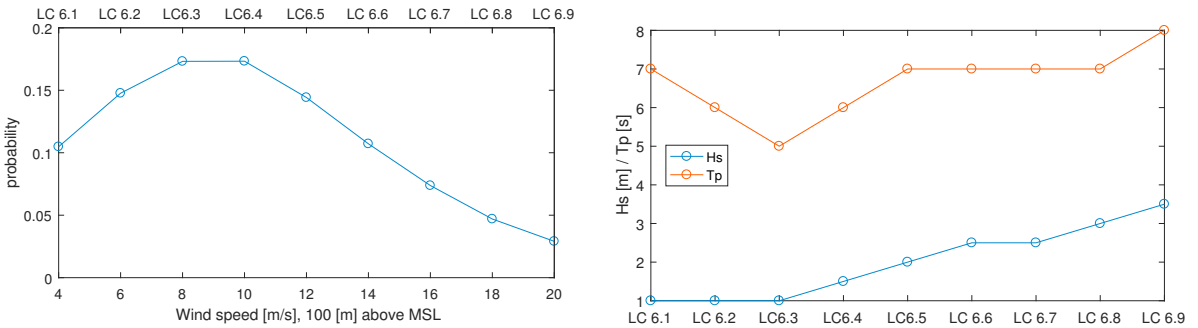

Fig. 8. Wind speed with probability of occurrence (left) and corresponding wave parameters

8.1. Fatigue Analysis

The fatigue utilization at mudline is calculated using the rainflow counting module in the WAFO toolbox for MATLAB [25], S-N curve D for steel in sea water with cathodic protection [26] and an assumed stress concentration factor of 1. For SIMA and FAST, the average utilization during one hour is calculated directly from the simulations, while the 10 minute average utilization from vpOne is scaled up to an equivalent one-hour value. To get the lifetime contribution to fatigue damage over 30 years, each environmental condition is scaled with the probability of occurrence as given in Figure 8.

Some general trends can be observed from the resulting fatigue damage, plotted in Figure 9. FAST does in general calculate higher fatigue damage than the other programs, with the largest difference being at wind speeds in the region
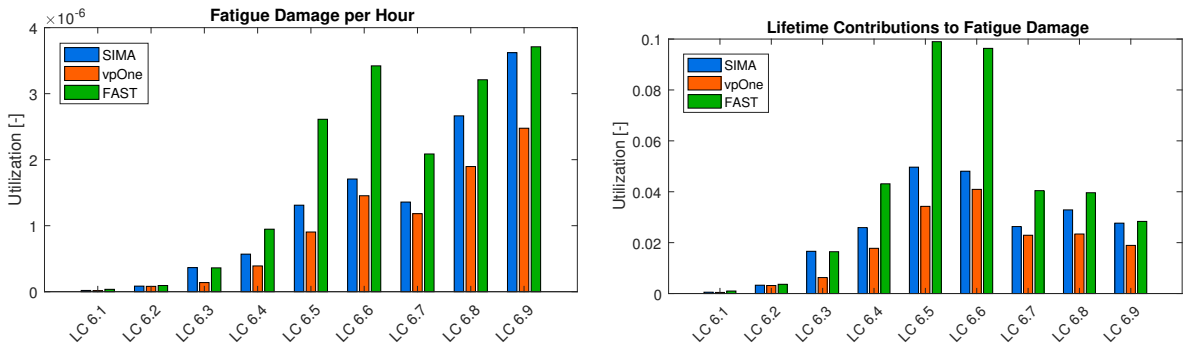
Fig. 9. Utilization in one hour (left) and over 30 years (right)

of 12-14 s, i.e. just above rated wind speed. This is the same region where the controller shows the largest difference in behaviour in the stepped wind analysis, as seen in Figure 5. Another trend is that vpOne returns significantly lower fatigue damage than both FAST and SIMA for high wind speeds and large waves. This indicates that vpOne has a lower response to waves than both SIMA and FAST. A more detailed discussion of this will be given in the next section.

The right plot in Figure 9 shows the fatigue damage contribution for each environmental condition over a lifetime of 30 years. This highlights that the load cases with the highest differences between the predicted results are also those with the largest overall contributions to the fatigue damage. This causes a rather large difference in the predicted total utilization over 30 years, as shown in Table 5. The total damage equivalent load for the mudline bending moment is given in the same table, and shows a 15 % difference between the upper and lower estimates when high-cycle fatigue is assumed.

Table 5. Total fatigue damage

	SIMA	vpOne	FAST
Utilization over 30 years [-]	0.23	0.17	0.37
Damage equivalent load [kNm] (1 [Hz] loading)	1.71	1.60	1.87

8.2. Stochastic Wind and Waves

Using the same simulations as in the fatigue analysis, the power spectra of mudline moment and thrust force are plotted in Figure 10 for LC 6.6 and 6.9 in order to investigate the reason for the differences in fatigue damage in these load cases. For both environments, vpOne seems to have a larger aerodynamic damping of the 1st fore-aft mode of the tower while FAST has the lowest damping. This is consistent with what is seen in the wave-only analysis in Figure 7, and may be explained by the apparently softer tower in vpOne. For both the thrust force and mudline moment, FAST has a peak at approximately 0.05 Hz in LC 6.6. The same peak is less distinct for both SIMA and vpOne, and cannot be identified in LC 6.9. None of the natural frequencies in Table 4 corresponds to 0.05 Hz, but the frequency of the oscillations of blade pitch and rotor speed in Figure 5 is in this frequency range.

9. Discussion

While the models behave similar in the simplified load cases, there is a large difference between the predicted fatigue damage. This is especially caused by differences at wind speeds just above rated, where the fatigue damage can be expected to be dominated by aerodynamic loads. As FAST predicts a larger damage than the other codes, this is likely to be caused by how the aerodynamic properties are defined along the blades.
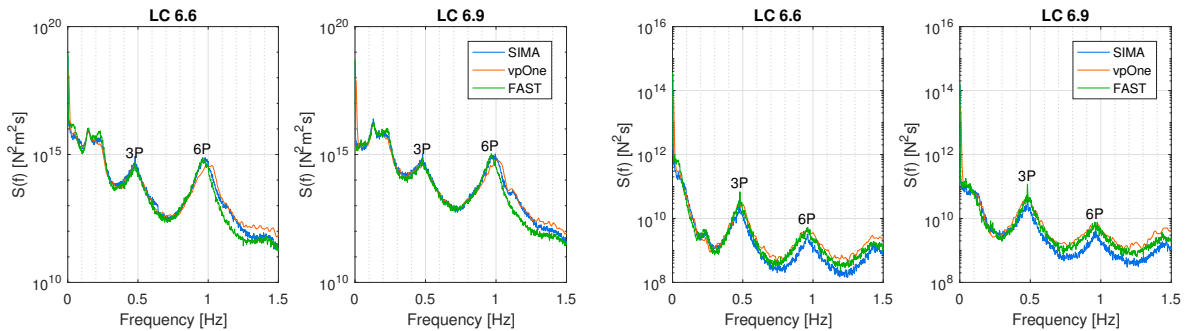
Fig. 10. Response power spectra for mudline moment (left) and thrust force (right) under combined wind and wave loading

Furthermore, the response spectra in FAST shows an increased response at a frequency outside the natural frequencies and load frequencies. This is attributed how the control system and drivetrain interact with the aerodynamic loads. While this could possibly have been achieved by different tuning of the controllers, this shows how the differences between the programs result in discrepancies in the predicted responses if the same system is modelled in each code.

10. Conclusion

The response of the DTU 10 MW reference turbine on a monopile foundation was analysed for a number of deterministic and stochastic load cases using the computer codes SIMA, vpOne and FAST. A number of differences in the predicted responses have been identified. In the final fatigue analysis, the damage equivalent bending moment at mudline was found to vary between 1.60 and 1.87 kNm. The resulting fatigue damage is significantly larger, and the estimated utilization varies between 0.17 and 0.37. This variation is found to be caused by small differences in the predicted tower top displacement, leading to unequal aerodynamic damping, and deviations in the the controller dynamics.

From this, the sensitivity of the calculated response to discrepancies in modelling and code capabilities is highlighted. While the response of the structure to the deterministic load cases are quite similar, the differences result in the large differences in the final fatigue utilization.

Acknowledgements

References

[1] Jonkman, J., Musial, W.. Offshore code comparison collaboration (OC3) for IEA task 23 offshore wind technology and deployment. Report; NREL; 2010.

[2] Popko, W., Vorpahl, F., Zuga, A., Kohlmeier, M., Jonkman, J., Robertson, A., et al. Offshore code comparison collaboration continuation (OC4), Phase I - results of coupled simulations of an offshore wind turbine with jacket support structure: Preprint. Report; 2012.

[3] Robertson, A., Jonkman, J., Vorpahl, F., Popko, W., Qvist, J., Frøyd, L., et al. Offshore code comparison collaboration continuation within IEA wind task 30: Phase II results regarding a floating semisubmersible wind system. In: ASME 2014 33rd International Conference on Ocean, Offshore and Arctic Engineering; vol. 9B: Ocean Renewable Energy. 2014,.

[4] Robertson, A.N., Wendt, F.F., Jonkman, J.M., Popko, W., Vorpahl, F., Stansberg, C.T., et al. OC5 Project Phase I: Validation of Hydrodynamic Loading on a Fixed Cylinder. Report; NREL; 2015.

[5] Karimirad, M., Meissonnier, Q., Gao, Z., Moan, T.. Hydroelastic code-to-code comparison for a tension leg spar-type floating wind turbine. Marine Structures 2011;24(4):412–435.

[6] Barahona, B., Jonkman, J.M., Damiani, R., Robertson, A., Hayman, G.. Verification of the new FAST v8 Capabilities for the Modeling of Fixed-Bottom Offshore Wind Turbines. AIAA SciTech Forum; American Institute of Aeronautics and Astronautics; 2015,.

[7] Ormberg, H., Bachynski, E.E.. Global analysis of floating wind turbines: Code development, model sensitivity and benchmark study. In: The Twenty-second International Offshore and Polar Engineering Conference. International Society of Offshore and Polar Engineers; 2012,.

[8] Ormberg, H., Passano, E., Luxcey, N.. Global analysis of a floating wind turbine using an aero-hydro-elastic model: Part 1—code development and case study. In: ASME 2011 30th International Conference on Ocean, Offshore and Arctic Engineering. American Society of Mechanical Engineers; 2011, p. 837–847.

[9] Luxcey, N., Ormberg, H., Passano, E.. Global analysis of a floating wind turbine using an aero-hydro-elastic numerical model: Part 2—benchmark study. In: ASME 2011 30th International Conference on Ocean, Offshore and Arctic Engineering. American Society of Mechanical Engineers; 2011, p. 819–827.

[10] Hansen, M.O.L., Aas Jakobsen, K., Holmas, T., Amdahl, J.. VPONE – a new FEM based servo hydro- and aeroelastic code for wind turbines. Proceedings European Offshore Wind 2009 Conference and Exhibition 2009;.

[11] Hansen, M.O.L., Sørensen, J.N., Voutsinas, S., Sørensen, N., Madsen, H.A.. State of the art in wind turbine aerodynamics and aeroelasticity. Progress in Aerospace Sciences 2006;42(4):285–330.

[12] Kühn, M.J.. Dynamics and design optimisation of offshore wind energy conversion systems. Phd thesis; 2001.

[13] Bak, C., Zahle, F., Bitsche, R., Kim, T., Yde, A., Henriksen, L.C., et al. Design and performance of a 10 MW wind turbine. J Wind Energy To be accepted;.

[14] Hansen, M.H., Henriksen, L.C.. Basic DTU wind energy controller. Report; DTU Wind Energy; 2013.

[15] Bachynski, E.E., Ormberg, H.. Hydrodynamic modeling of large-diameter bottom-fixed offshore wind turbines. In: ASME 2015 34th International Conference on Ocean, Offshore and Arctic Engineering. American Society of Mechanical Engineers; 2015,.

[16] The International Organization for Standardization, . ISO 19901-4 Geotechnical and foundation design considerations. 2016.

[17] MARINTEK, . RIFLEX theory manual. Report; MARINTEK; 2015.

[18] USFOS Reality Engineering, . USFOS hydrodynamics. Report; 2010.

[19] SINTEF, . USFOS - a computer program for progressive collapse analysis of steel offshore structures. Theory manual. Report; 1993.

[20] Jonkman, J., Hayman, G.J., J., J.B.. AeroDyn v15 User's Guide and Theory Manual - DRAFT. Report; NREL; 2016.

[21] Jonkman, J., Robertson, A., Hayman, G.J.. HydroDyn User's Guide and Theory Manual. Report; NREL; Undated.

[22] Damiani, J., Jonkman, J., G., H.. SubDynUser's Guide and Theory Manual. Report; NREL; 2015.

[23] Hansen, M.O.L.. Aerodynamics of Wind Turbines. 2nd edition ed.; Earthscan; 2008. ISBN 9781849770408.

[24] Reistad, M., Breivik, O., Haakenstad, H., Aarnes, O.J., Furevik, B.R., Bidlot, J.. A high-resolution hindcast of wind and waves for the North Sea, the Norwegian Sea, and the Barents Sea. Journal of Geophysical Research: Oceans 2011;116(C5).

[25] WAFO-group, . WAFO - A Matlab Toolbox for Analysis of Random Waves and Loads - A Tutorial. Math. Stat., Center for Math. Sci., Lund Univ.; Lund, Sweden; 2011.

[26] DNV GL AS, . DNV-RP-C203 - Fatigue design of offshore steel structures. 2016.

Paper 4:

Wind-wave directional effects on fatigue of bottom-fixed offshore wind turbine

Stian H. Sørum, Jørgen R. Krokstad, Jørgen Amdahl

Wind-wave directional effects on fatigue of bottom-fixed offshore wind turbine

S H Sørum[1]**, J R Krokstad**[2]**, J Amdahl**[1]

[1] Centre for Autonomous Marine Operations and Systems, Department of Marine Technology, Norwegian University of Science and Technology, NO-7491 Trondheim
[2] Department of Marine Technology, Norwegian University of Science and Technology, NO-7491 Trondheim

E-mail: `stian.h.sorum@ntnu.no`

Abstract.
   The current trend for offshore wind energy is that larger turbines are placed on monopile foundations at increasing water depth. This requires larger foundations, increasing the importance of hydrodynamic loading. It is well established that wave loads perpendicular to the wind direction are important for the fatigue damage in monopile foundations. However, this is normally only taken into account considering wind-wave misalignment. In this paper, the effect of assuming short-crested waves in design calculations is considered. The lifetime fatigue damage may increase significantly for hydrodynamically sensitive support structures when modelling the waves as short-crested rather than long-crested. For the turbines in this paper, the fatigue damage increased with up to 80 %. At the same time, the changes in fatigue damage were small for support structures that are less hydrodynamically sensitive. The work performed in this paper shows that the typical design assumption of long-crested waves may be both conservative and non-conservative. This fact is important to be aware of when designing support structures for offshore wind turbines.

1. Introduction

Offshore wind turbines (OWTs) are subject to several sources of dynamic loading, including wind and wave loads. With increasingly large turbines being installed[1], the aerodynamic loads increase. Larger loads, in turn, lead to increased capacity requirements for the support structure. In Europe, monopiles are the dominating foundation type, making up 66 % of all installations in 2018[1]. Increasing the structural capacity of these foundations often leads to larger dimensions, which in turn increases the wave loading. Further, new turbines are typically installed in deeper water, with 27 m being the average for 2018[1]. This serves to increase the importance of wave loads relative to wind loads.

   Fatigue damage is typically determining the final dimensions of monopile foundations[2]. Wave-induced responses contribute to this fatigue damage, especially when wind and waves are misaligned[3]. For wind-wave misalignment, the lack of aerodynamic damping in the crosswind direction gives large responses even for moderate excitation. Fischer et al.[3] have previously shown the importance of including misalignment in design calculations for a 5 MW turbine, and the sensitivity of the transverse response to damping levels was demonstrated by Koukoura et al.[4]. Kim and Natarajan[5] showed the importance of deeper water, demonstrating increased

importance of misalignment conditions when the water depth was raised from 25 to 35 meters. The influence of soil modelling was also shown, giving increased fatigue damage for softer soil. Smilden et al.[6] showed that misalignment angles up to $45°$ contribute significantly to the fatigue damage of a large diameter monopile. Design standards such as [7] also require that wind-wave misalignment is included in design calculations.

Common for the papers [3]-[6] is that the misalignment between wind and *long-crested* waves is considered. However, wind-wave misalignment may also occur from *short-crested* waves. For a structure with uniform properties, Vugts[8] showed that it is conservative to assume long-crested waves. This conclusion cannot be generalized for OWTs, due to the presence of aerodynamic damping only in-line with the wind. In a short-term perspective, the fatigue damage from short-crested waves can be both larger or smaller than the fatigue damage from long-crested waves. This will, amongst others, depend on the misalignment between the wind and the mean wave direction, the level of wave spreading and which position on the structure that is considered most critical for fatigue. Few studies exist on the effect of short-crested waves on OWTs, but Trumars, Jonsson and Bergdal[9] investigated this using measurement data from a 500 kW turbine at 6.5 m water depth. Horn, Krokstad and Amdahl[10] investigated several aspects of wave modelling by considering wave excitation and aerodynamic damping. Kim and Natarajan[5] showed that the soil stiffness is important for how wind-wave misalignment influences fatigue damage. As short-crested waves introduce further wind-wave misalignment, it is expected that the soil stiffness will influence also the effect of wave spreading.

This paper contributes to increasing the knowledge about the response of monopile supported OWTs to short-crested waves, and how this differs from the response to long-crested waves. The primary goal is to assess whether the assumption of long-crested waves in design calculations yields conservative estimates of the lifetime fatigue damage in the support structure. Further, the influence of varying sensitivity to wave loading is assessed by using models with different mode shapes. Both the natural period of the first global tower modes and the corresponding mode shapes influence the importance of wave loads. Only changes in the mode shapes are considered here, as OWTs are typically designed with a target natural frequency[11]. The analyses consider three similar monopile foundations in varying soil conditions. The towers are tuned to give the desired natural frequencies. A long-term fatigue analysis is performed for each design, to demonstrate how the different mode shapes affect the fatigue damage in long-crested or short-crested waves.

The paper is organised as follows: Section 2 presents the wave directionality effects considered. In Section 3 the OWT and simulation set-up used in this study is described. Following this, the simulation results are given in Section 4; first for aligned wind and waves to determine the relative importance of wind and wave loads, then for long-crested and short-crested waves including wind-wave misalignment. Finally, the results are discussed in Section 5, and a conclusion is drawn.

2. Wave directionality
Wind-wave misalignment may occur from misalignment between the wind direction and the mean wave direction, as well as from wave spreading. Further, wind driven waves and swell waves may behave differently with regards to misalignment. Wind generated waves will typically travel in a direction close to the wind direction, but can have significant wave spreading. Swell waves are generated independent of the local wind conditions, and may have more pronounced misalignment. This will depend on the dominating wind directions and swell directions at each individual site. At the same time, swell waves are mainly long-crested, meaning that all waves travel in the same direction.

The difference between wind waves and swell in terms of misalignment in shown in Figure 1 for the site described in Section 3.3. The figures shows the absolute value of misalignment

for swell waves to the left and for wind waves to the right. It is clear that the misalignment is limited for wind-generated waves, while all misalignment angles occur for the swell waves.
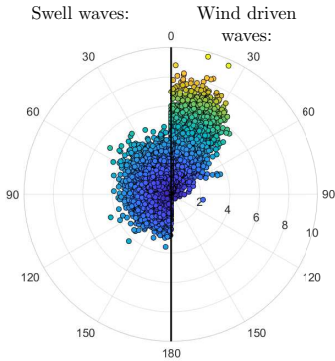

Figure 1. Scatter of absolute value of wind-wave misalignment for swell (left) and wind driven waves (right). The radial axis shows H_s in metres.
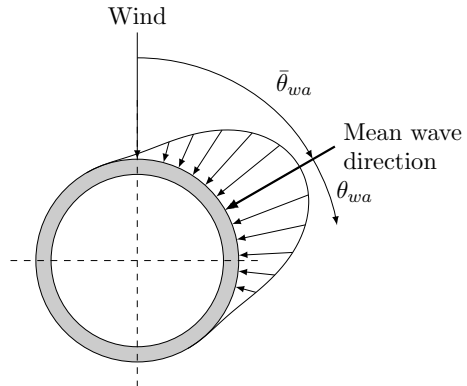

Figure 2. Mean wave direction, $\bar{\theta}_{wa}$, and direction of wave components, θ_{wa}, relative to wind direction
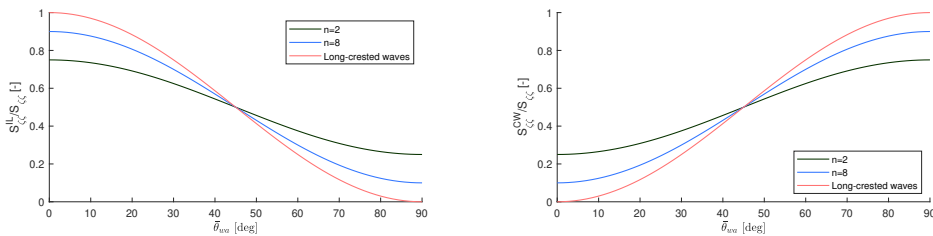

Figure 3. Ratio of in-line (left) and crosswind (rigth) wave spectrum as function of mean misalignment angle.

Several engineering models for wave spreading can be used in the analyses. These include both frequency independent and frequency dependent models. DNV GL[12] recommends modelling short-crested waves by multiplying the unidirectional wave spectrum, $S_{\zeta\zeta}(\omega)$, with a directional spreading function $D(\theta_{wa})$. The wave spectrum for short-crested waves is then given as

$$S_{\zeta\zeta}(\omega, \theta_{wa}) = S_{\zeta\zeta}(\omega)D(\theta_{wa}) \tag{1}$$

Here, θ_{wa} is the angle of each directional component relative to the mean wave direction $\bar{\theta}_{wa}$ as shown in Figure 2. The formulation for $D(\theta_{wa})$ used in this paper is

$$D(\theta_{wa}) = \frac{\Gamma(1 + n/2)}{\sqrt{\pi}\Gamma(1/2 + n/2)} cos^n(\theta_{wa} - \bar{\theta}_{wa}) \tag{2}$$

with $|\theta_{wa} - \bar{\theta}_{wa}| \leq \pi/2$[12]. The spreading exponent n is typically in the range 2-4 for wind waves, while $n > 7$ is recommended for swell waves.

For OWTs, it is interesting to consider the wave energy travelling in the same direction as the wind and that travelling perpendicular to the wind. The energy distribution will vary with both the mean wave direction and wave spreading. Figure 3 shows the ratio of total wave energy travelling in-line with the wind and in the crosswind direction for different misalignment angles. The figure shows that short-crested waves will increase the crosswind wave energy for misalignment angles up to 45°. For wind driven waves, conditions with less than 45° misalignment can be expected to dominate, and a significant increase in the crosswind response will be seen. At the same time, the aerodynamic loads will contribute to the response in-line with the wind. The reduction in response in the in-line direction will, therefore, be less than the reduction in wave loading.

3. Methodology
This paper investigates the effect of wave directionality by performing time-domain simulations. In this section, the simulation models and methodology is presented.

3.1. Model description
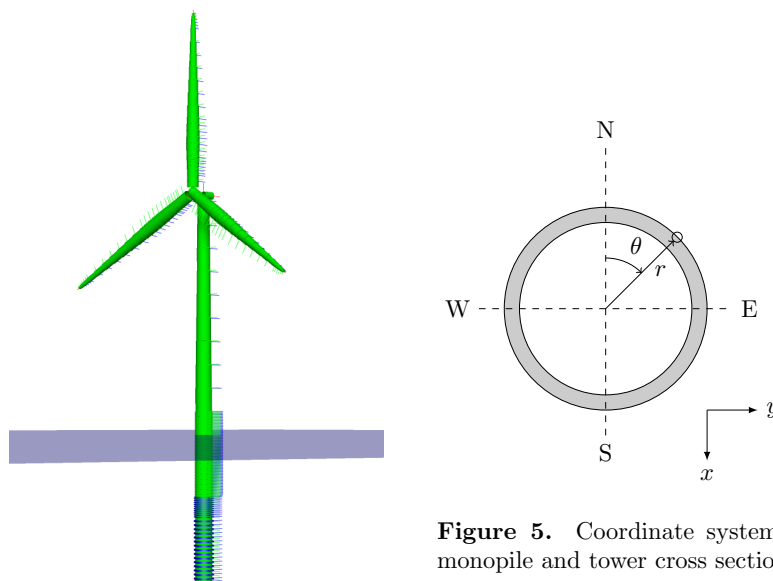
Figure 5. Coordinate system of monopile and tower cross section.

Figure 4. Wind turbine model in SIMA

The turbine model is based on the DTU 10 MW reference wind turbine [13], and is shown in Figure 4. Compared to the reference turbine, the inner blade foils have been altered and the tower has been stiffened by increasing the wall thickness by 20 %, both as described in [14]. The tower is placed on a monopile foundation with a diameter of 8 m and wall thickness of 0.11 m, standing in 30 m water depth. Below the mudline, the monopile extends for another 42 m. The characteristics of the soil springs are based on the $p - y$ curves computed in accordance with ISO 19901-4[15] for a location at Dogger Bank.

Table 1. Variation in parameters between models, given as fraction of the value for the base model

Parameter	Base model	Soft model	Stiff model
Relative soil stiffness	1	0.65	8
Relative tower wall thickness	1	1.65	0.725

Table 2. Natural frequencies of models, in [Hz]

Mode	Base model	Stiff soil	Soft soil
1st fore-aft	0.2069	0.2072	0.2063
2nd fore-aft	1.0522	1.3014	0.9708
1st side-side	0.2063	0.2061	0.2060
2nd side-side	1.0100	1.3665	1.0022

Structural and soil damping is modelled as stiffness proportional Rayleigh damping. To account for soil damping, the damping coefficient is doubled below the mudline. In [16], a review of measured damping levels of monopile OWTs is given, and the damping is found to vary between 1.1 % and 2.8 % of critical damping. A damping level of 1.1 % at the first tower mode was therefore selected to ensure conservative results.

The simulations are carried out in the aero-hydro-servo-elastic computer program SIMA v. 3.2.2, developed by SINTEF Ocean. All structural members are modelled as non-linear beam elements, while soil-structure interaction is modelled by non-linear springs. Hydrodynamic loads are calculated using Morison's equation based on linear wave kinematics evaluated to the mean water level, while aerodynamic loads are calculated with the blade element momentum theory including dynamic inflow, dynamic wake, tip loss and tower shadow effects[17].

3.2. Variations to model

In order to analyse the effect of varying sensitivity to wave loads, two additional models were created. The model described in Section 3.1 will hereafter be referred to as the base model. Further, one model with stiffer soil and one model with softer soil were analysed by linear scaling of the p-y curves. These will be referred to as the stiff model and soft model, respectively.

In order to get comparable results and similar environmental loads, the natural period of the 1st global tower mode and the outer diameter of the structures were kept unchanged. Together with the soil stiffness, this left the tower wall thickness as the parameter that could be changed in the models. For the soft model this set a limit to how much the soil stiffness could be reduced while still keeping the natural frequencies at the target values. The stiff model was then altered to give a similar change in the mode shape of the first global modes. The model variations are summarized in Table 1.

In Table 2, the natural frequencies of the first tower modes are given for all three models. This shows similar natural frequencies for the first tower modes, while the 2nd modes have a variation of about 30 % in the natural frequencies. As the second modes are outside the wave frequency range, this difference is assumed negligible.

Given equal natural periods, the mode shape will determine the sensitivity of each model to wave loads. In Figure 6 the mode shapes of the first and second fore-aft tower modes are shown,

all scaled to give a maximal displacement of 1. As can be seen from the figures, increasing the soil stiffness reduces the displacement in the lower part of the substructure, while the opposite is seen for the model with reduced soil stiffness. It is also worth noticing that the second tower modes show almost no displacement in the tower top for the stiffest soil, which indicates that this mode will not be significantly excited by the thrust force. The excitation due to the rotor tilt moment may still be as significant for this model as for the softer models, as the slope of the modal displacement is approximately equal in all models.
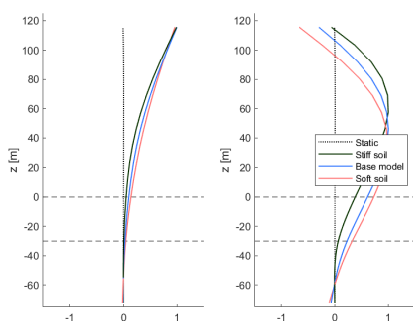
3.3. Environmental parameters

Figure 6. 1st (left) and 2nd (right) tower mode in fore-aft direction. The dashed lines show the mean water level and mudline.

Figure 7. Location of metocean data[18].

The environmental conditions are based on 60 years of hindcast data [19], for the location 54.8 °N, 1.92 °E in Dogger Bank as shown in Figure 7. The joint distribution of wind and waves are described in [18]. In [6], the misalignment between wind and total waves was investigated. Misalignment angles above 60° were found to be rare for significant wave heights above 3 m, while misalignment above 30° is rare for significant wave heights above 5 m. The misalignment bins of 0° and 30° make up more than 75 % of the registered environmental conditions.

Each environmental condition has been simulated as five 1-hour realizations, and the results are based on the average of these realizations. The wind files are generated in TurbSim using the Kaimal wind spectrum and turbulence class B, while the waves are realizations of the JONSWAP spectrum, as defined in [12]. When short-crested waves are simulated, the wave spectrum is modelled as the product of the directional spectrum in Eq. 2 and a JONSWAP spectrum. The spreading parameter n was set to 2, and the individual wave components are assumed uncoupled. Frequency dependency of the spreading function is not considered.

3.3.1. Simulation load cases To reduce the computational effort, the sea states have been lumped to one equivalent sea state per wind speed, as described in [20]. The resulting environmental parameters for aligned wind and waves are shown in Figure 8. Further, it is assumed that the same approach is valid for misaligned wind and waves. The misaligned load cases are found by grouping the absolute value of misalignment to bins of 30°, as shown in Figure 9. One equivalent sea state is found for each wind speed and misalignment bin. A total of 129 load cases are simulated for the misalignment conditions.
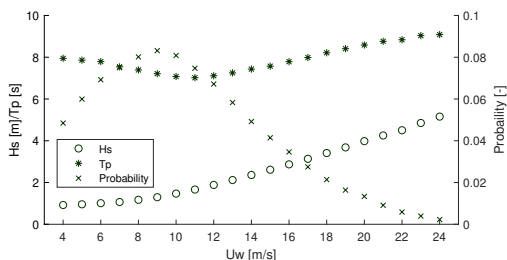
Figure 8. Load cases with corresponding probability for aligned wind and waves.
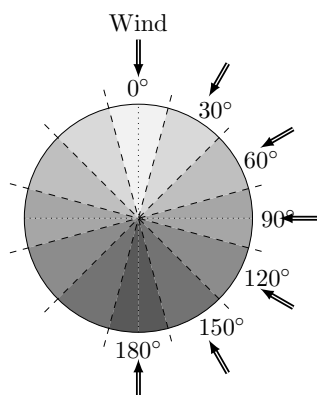

Figure 9. Bins for wind/wave misalignment. The wind is always from 0°, while the arrows represent the direction of waves for each bin. Bins with the same absolute value of misalignment, illustrated by the same color, are merged. [6, 21].

3.4. Fatigue calculations

The fatigue calculations are performed based on the time series of the axial stress in the monopile and tower, for locations distributed along the length of the support structure. The stress is calculated as

$$\sigma_a(r,\theta) = \frac{N}{A} + \frac{M_y}{I_y} r cos(\theta) - \frac{M_z}{I_z} r sin(\theta) \tag{3}$$

where N is the axial force and A the crossection area, while r is the radius at the calculation point. The bending moments, M_y and M_z, second area moments, I_y and I_z, and angular position are defined in accordance with the axis system showed in Figure 5.

Knowing the time series of stress, the fatigue damage is calculated using the S-N curve approach and rainflow counting, as implemented in the WAFO package[22] with a correction for a 2-slope S-N curve as given in [23]. The S-N curve for the monopile is assumed to be curve D for steel in sea water with cathodic protection, given in Table 2-2 in [24]. Curve D for steel in air is used for the tower, confer Table 2-1 in [24]. Stress concentration factors due to the presence of e.g. welds should in principle also be considered, but these have been set to 1 for simplicity.

4. Results

4.1. Aligned wind and waves

The relative importance of the wind and wave loading to the fatigue damage can be found by assuming long-crested waves and aligned wind and waves over the lifetime of the structure. In Figure 10, the relative lifetime contribution to the fatigue damage for each wind speed is shown. The values are normalized by the total fatigue damage for each of the models, so that the figure shows the amount of the total fatigue damage caused by each wind speed.
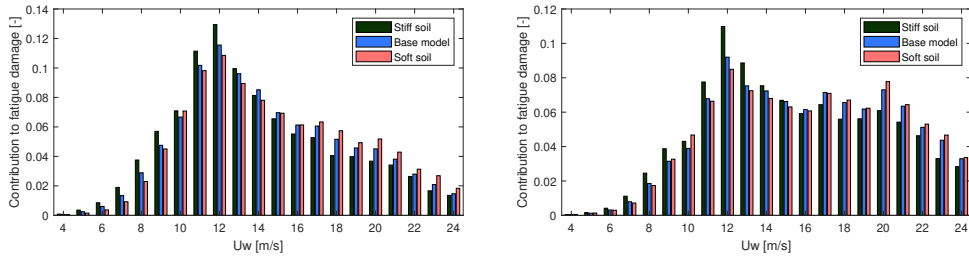
16th Deep Sea Offshore Wind R&D conference

IOP Conf. Series: Journal of Physics: Conf. Series **1356** (2019) 012011

IOP Publishing

doi:10.1088/1742-6596/1356/1/012011

Figure 10. Contribution to lifetime fatigue damage per wind speed for the most critical position on tower (left) and monopile (right). The values are normalized by the total fatigue damage for each model.

In the tower, the largest contribution to the fatigue damage is from wind speeds close to rated. These conditions have a high probability of occurrence and are associated with large aerodynamic thrust. In the monopile, the same conditions give the largest contributions to the lifetime fatigue. Still, conditions associated with high wind speeds, corresponding to high waves, show a larger influence on the fatigue damage in the monopile.

The trend is that the model with stiff soil has a larger contribution to the lifetime fatigue damage from conditions where the wind loads are dominating. For the model with soft soil, environmental conditions associated with large wave loads show a larger contribution to the fatigue damage. This indicates that the model with soft soil is more sensitive to wave loads. The effect of modelling the waves as short-crested is expected to be largest for this model, and smallest for the model with stiff soil.

4.2. Wave directionality

When assessing the effect of wave directionality, the wind-wave misalignment and long-term distribution of wind direction is taken into account. The fatigue damage is calculated for various positions around the cross section, and the maximum fatigue damage found for each elevation at the monopile and tower. The ratio R_D is used to express the effect of short-crested waves:

$$R_D = \frac{D_{SC}(z)}{D_{LC}(z)} \tag{4}$$

where $D_{SC}(z)$ is the maximum fatigue damage at height z with short-crested waves. $D_{LC}(z)$ is the corresponding value with long-crested waves.

Figure 11 shows the distribution of R_D over the length of the monopile and tower. From the figure, it is seen that the effect on the fatigue damage with short-crested waves is highest on the model with soft soil. This model was also found to be most sensitive to wave loading with aligned wind and waves.

In the monopile, the largest effect of varying the wave directionality model is seen in the upper part of the pile. All models show an increase in fatigue damage for short-crested waves ($R_D > 1$) in the upper part of the pile. The effect is largest for the model with soft soil. This is further explained in Section 4.3.

For the tower, the effect of wave loading is primarily in the tower base, where the response is driven by the aerodynamic thrust and the inertia forces from the rotor-nacelle assembly (RNA). The latter is mainly influenced by the wave loading. Close to the RNA, the response is primarily dominated by the tilting moment of the rotor. The fatigue damage in the tower top is therefore insensitive to the choice of wave model.
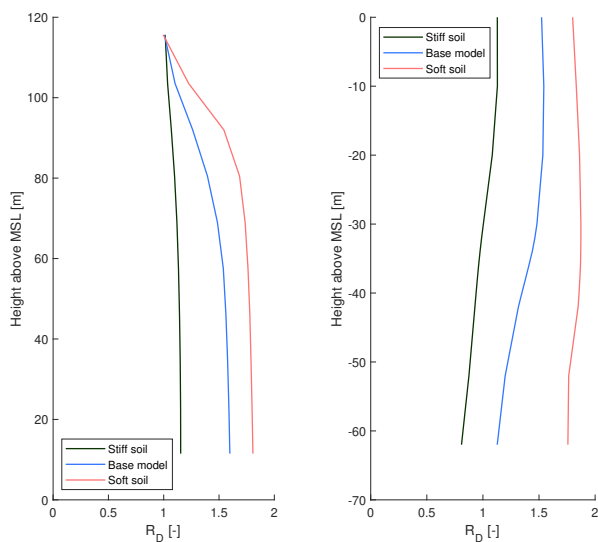
Figure 11. Ratio of fatigue damage predicted with short-crested waves to fatigue damage with long-crested waves. Results are shown for the tower (left) and monopile (right).

From a design perspective, it is the highest fatigue damage that is of the most interest. The ratio R_D^{max} is introduced to describe the influence of wave directionality model on the largest fatigue damage:

$$R_D^{max} = \frac{\max\{D_{SC}(z)\}}{\max\{D_{LC}(z)\}} \tag{5}$$

The values are shown in Figure 12 for both the tower and the pile. For the tower, the values are consistent with the maximum values in Figure 11. This is not the case for the monopile, as the maximum fatigue damage in general occurs for a different depth than the maximum value of R_D.

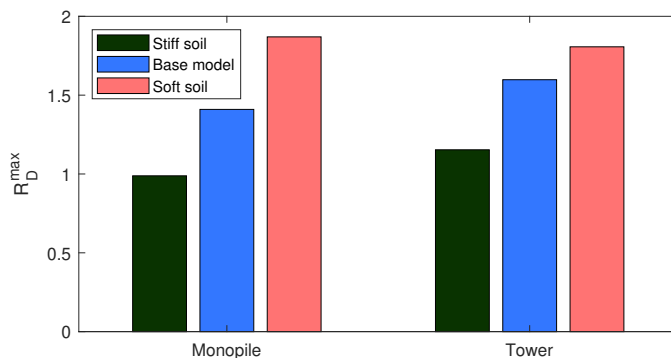**Figure 12.** Ratio R_D^{max} for monopile (left) and tower (right)

In summary, long-crested waves only gives a conservative prediction of fatigue damage for the tower with the stiff soil properties. In all other cases, the fatigue damage in the tower and monopile is higher for short-crested waves. This implies that short-crested waves should be considered for fatigue calculations of large monopile foundations.

4.3. Selected load cases

While the lifetime fatigue damage at different locations in the support structure is of interest from a design perspective, the long-term distribution of environmental parameters obscures the response under different load conditions. The results from two selected load cases will be given here, for a better understanding of how the response differs when long-crested or short-crested waves is assumed. The key parameters are given in Table 3, and correspond to two of the load cases for wind speed 11 m/s.

Table 3. Selected load cases for detailed analysis.

Wind speed [m/s]	H_s [m]	T_p [s]	Misalignment [deg]	Probability of occurrence [-]
11	1.8	5.6	0	4.0 %
11	2	7	60	0.4 %

For the load case with aligned wind and waves, the wave modelling gives small differences in the fore-aft response. This is caused by the high aerodynamic loads and relatively small waves associated with the selected load cases. The response is shown at the left in Figure 13, where the power spectral density (psd) of the fore-aft bending moment at mudline is plotted. The fore-aft response is here defined as the response in the mean wind direction. The difference between the wave models is more significant in the side-side direction. As expected, the side-side response is negligible when long-crested waves is assumed. If short-crested waves is assumed, the peak spectral density is higher than in the fore-aft direction, although the response is very narrow-banded.
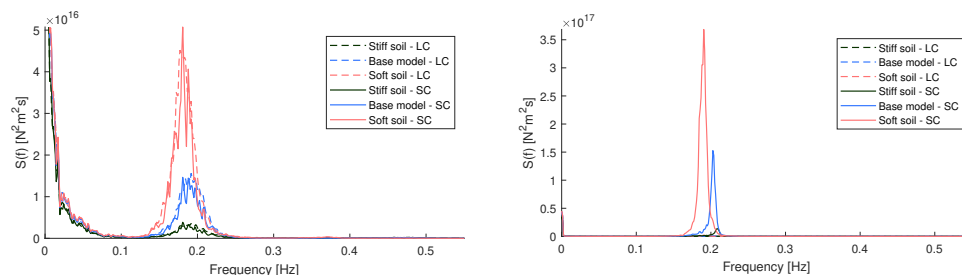
Figure 13. Fore-aft (left) and side-side (right) moment spectrum for wind speed 11 m/s and aligned wind and waves

For the misaligned case, the opposite trend is seen. As shown in Figure 14, there is an increase in the fore-aft moment when short-crested waves is assumed. This is as expected from Figure 3, where it is shown that short-crested waves will increase the wave energy in the fore-aft direction for large misalignment angles. The change is most significant for the model with soft soil, and decreases with increasing soil stiffness. In the side-side direction, the change in the response spectrum is now less sensitive to the assumption of long-crested or short-crested waves.

5. Discussion

The results show that it can be both conservative and non-conservative to assume long-crested waves in fatigue calculations. While the soil stiffness and tower wall thickness have been altered
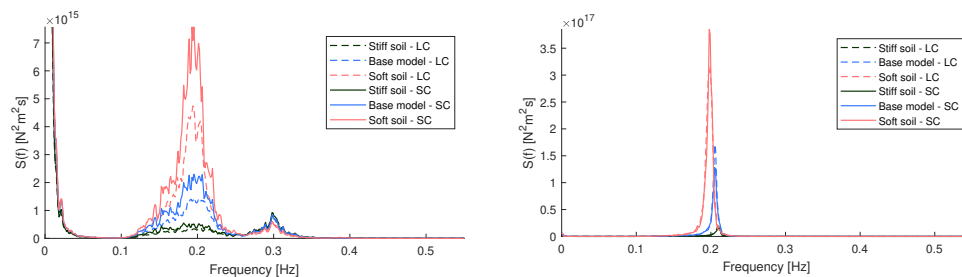
Figure 14. Fore-aft (left) and side-side (right) moment spectrum for wind speed 11 m/s and 60° misalignment between wind and waves

here, other parameters may also influence the effect of wave spreading. In general, it can be expected that short-crested waves will yield increased fatigue damage as wave loads become more important. From a design perspective, the mode shape and 1st natural period will influence the structure's sensitivity to waves. A large modal displacement near the mean water level or a natural period close to the wave period will make wave loads more important. This will again make it more important to consider short-crested waves.

The designer can also influence the crosswind damping level, e.g. by fitting tuned mass dampers[25] or applying active load mitigation[2]. Increasing the crosswind damping will reduce the response from waves travelling in the crosswind direction, which can be beneficial when considering both wind-wave misalignment and short-crested waves. Increasing the damping will also make an OWT more similar to the structures analysed by Vugts[8], which will increase the conservatism from assuming long-crested waves.

Several factors that are outside the designer's control will also influence whether it is conservative or not to assume long-crested waves. The effect of short-crested waves depends on the wind-wave misalignment, as shown in Figure 3 and in the selected load cases. If a site evaluated for installation of wind turbines mainly have aligned wind and wave conditions, short-crested waves will increase the fatigue damage. Similarly, short-crested waves at a site with pronounced wind-wave misalignment will reduce the crosswind excitation, potentially reducing the lifetime fatigue damage.

The wave characteristics will also be important in this sense. For the site analysed in this paper, wind-wave misalignment mainly occurs for swell waves. These waves normally have little wave spreading. Thus the fatigue calculations with short-crested swell waves may yield reduced fatigue damage, but the results may be non-conservative since swell waves are mainly long-crested with significant misalignment.

The above discussion shows how complex it is to evaluate whether it is conservative or non-conservative to assume long-crested waves in design calculations. A designer must, therefore, take care to ensure conservative, but not overly conservative, fatigue estimations. Different modelling approaches may be applicable for wave spreading. This will depend on the properties of the support structure, the short-term environmental conditions analysed and the long-term distribution of environmental parameters.

6. Conclusion
This paper has investigated the effect of modelling waves as long-crested or short-crested for monopile supported wind turbines in varying soil conditions. Previous studies have concluded that it is conservative to assume long-crested waves in the fatigue calculations of monopile supported OWTs. In this paper, it is shown that this conclusion is not valid for all monopile

designs. As monopile foundations become more sensitive to wave loads, it may be non-conservative to assume long-crested waves. Consequently, short-crested waves should be taken into account when designing monopile foundations for deep water, for soft soil, for harsh wave conditions or with large dimensions.

Acknowledgments

References

[1] WindEurope 2019 Offshore wind in Europe. Key trends and statistics 2018 Tech. rep.
[2] Fischer T, de Vries W, Rainey P, Schmidt B, Argyriadis K and Kühn M 2012 **15** 99–117 ISSN 1095-4244
[3] Fischer T, Rainey P, Bossanyi E and Kühn M 2011 *Wind Engineering* **35** 561–73
[4] Koukoura C, Brown C, Natarajan A and Vesth A 2016 *Engineering Structures* **120** 147–57
[5] Kim T and Natarajan A *51st AIAA Aerospace Sciences Meeting including the New Horizons Forum and Aerospace Exposition 2013* (American Institute of Aeronautics and Astronautics Inc.)
[6] Smilden E, Bachynski E E and Sørensen A J 2017 *ASME 2017 36th International Conference on Ocean, Offshore and Arctic Engineering* (American Society of Mechanical Engineers)
[7] DNV GL AS 2016 DNVGL-ST-0437 Loads and site conditions for wind turbines
[8] Vugts J H 2005 *Applied Ocean Research* **27** 173–185 ISSN 0141-1187
[9] Trumars J M V, Jonsson J O and Bergdahl L 2006 *ASME 2006 25th International Conference on Offshore Mechanics and Arctic Engineering* (ASME)
[10] Horn J T, Krokstad J R and Amdahl J 2018 *Proceedings of the Institution of Mechanical Engineers, Part M: Journal of Engineering for the Maritime Environment* **232** 37–49
[11] Arany L, Bhattacharya S, Macdonald J and Hogan S J 2017 *Soil Dynamics and Earthquake Engineering* **92** 126–152 ISSN 0267-7261
[12] Det Norske Veritas AS 2014 DNV-RP-C205 - Environmental conditions and environmental loads
[13] Bak C, Zahle F, Bitsche R, Kim T, Yde A, Henriksen L C, Andersen P B, Natarajan A and Hansen M To be accepted *J. Wind Energy*
[14] Bachynski E E and Ormberg H 2015 *ASME 2015 34th International Conference on Ocean, Offshore and Arctic Engineering* (American Society of Mechanical Engineers)
[15] The International Organization for Standardization 2016 ISO 19901-4 Geotechnical and foundation design considerations
[16] Suja-Thauvin L, Krokstad J R and Frimann-Dahl J F 2016 *Energy Procedia* **94** 329–38
[17] MARINTEK 2015 RIFLEX theory manual
[18] Horn J T H, Krokstad J R and Amdahl J 2017 Joint probability distribution of environmental conditions for design of offshore wind turbines *ASME 2017 36th International Conference on Ocean, Offshore and Arctic Engineering* (American Society of Mechanical Engineers)
[19] Reistad M, Breivik O, Haakenstad H, Aarnes O J, Furevik B R and Bidlot J R 2011 *Journal of Geophysical Research: Oceans* **116** 1–18
[20] Kühn M J 2001 *Dynamics and design optimisation of offshore wind energy conversion systems* Ph.D. thesis TU Delft, Delft University of Technology
[21] Shrestha B and Kühn M 2016 *Journal of Physics: Conference Series* **753** 1–10
[22] WAFO-group 2011 *WAFO - A Matlab Toolbox for Analysis of Random Waves and Loads - A Tutorial*
[23] Bachynski E E, Kvittem M I, Luan C and Moan T 2014 *Journal of Offshore Mechanics and Arctic Engineering* **136** 041902–1–12
[24] DNV GL AS 2016 DNV-RP-C203 - Fatigue design of offshore steel structures
[25] Damgaard M, Ibsen L B, Andersen L V and Andersen J K F 2013 *Journal of Wind Engineering and Industrial Aerodynamics* **116** 94–108

Paper 5:

Wind and soil model influences on the uncertainty in fatigue of monopile supported wind turbines

Stian H. Sørum, Erin E. Bachynski-Polić, Jørgen Amdahl

Wind and soil model influences on the uncertainty in fatigue of monopile supported wind turbines

SH Sørum, EE Bachynski-Polić and J Amdahl

Centre for Autonomous Marine Operations and Systems, Department of Marine Technology, NTNU, 7491 Trondheim, Norway

E-mail: `stian.h.sorum@ntnu.no`

Abstract. Several alternative engineering models are available for the use in analysis of offshore wind turbines. However, it is not always clear which of the models will yield the most accurate or sufficiently conservative results. This paper investigates the effect of using two alternative soil-structure interaction models and two wind coherence models. The focus is on assessing how these modelling choices influence the predicted long-term fatigue damage in the support structure. The two soil models are a macro-element model and a p-y-curve model with Rayleigh damping. This gives differences in both the damping and stiffness properties of the turbine model. The differences between the two soil models tend to decrease as the turbine size increases. The wind coherence models considered are the Kaimal spectrum with exponential coherence and the Mann uniform shear turbulence model. The Kaimal model predicts the highest response at low frequencies, while the Mann model gives the highest response predictions at higher frequencies. Which turbulence model predicts the highest long-term fatigue damage is then determined by the natural frequencies, rotor and blade passing frequencies of the different turbines.

1. Introduction

Several engineering models may be selected for analysis of offshore wind turbines (OWTs). Different models may yield different results and thereby give different designs. Further, it is often unclear which of the available models are most accurate. They may be based on different assumptions, incorporate different physical effects, or be developed for different applications.

This paper will investigate the influence of using different models for two aspects of the fatigue analysis of monopile supported OWTs. Both the soil-structure interaction (SSI) and wind coherence models influence the response prediction, and thereby the design fatigue lifetime, of OWTs. While previous studies have looked into both the model development and short-term response, this paper will focus on the long-term effects of using the different models. As the difference between the models vary with turbine size, three turbines in the size range 5 to 15 MW are considered. Finally, the influence of uncertainty in the site parameters (e.g. turbulence intensity and soil stiffness) is investigated.

1.1. Soil Modelling

Traditionally, SSI was modelled with p-y curves, based on experience from the offshore oil and gas industry[1]. These represent the soil resistance as non-linear elastic springs distributed along the length of the pile. While still used, the PISA project showed the need for modifying

the curves for the offshore wind industry[2]. Other methods have been developed, such as the apparent fixity method, and the use of linear stiffness and damping matrices[3, 4, 5]. Aasen et al.[5] also used a 1D rotational element fixed below seafloor, with many properties similar to the macro element developed by Page et al.[6, 7] The study showed a difference of up to 4 years in predicted lifetime when using the different soil models[5]. Katsikogiannis et al.[8] found differences of up to 180% in the short-term fatigue damage between the macro-element and p-y-curve approach in cases with negligible aerodynamic damping. In this paper, the difference between the macro-element model and p-y-curve approach will be further investigated.

1.2. Wind Coherence Modelling

The IEC standard[9] recommends two models for the wind field when analysing OWTs: The Kaimal spectral model with exponential coherence (denoted "Kaimal model" hereafter) and the Mann uniform shear turbulence model (hereafter denoted the "Mann model"). It is expected that the two models show larger deviations as turbine size increases. Several studies have investigated the difference between these two models. Myrtvedt, Nybø & Nielsen[10] and Nybø, Nielsen & Godvik[11] both investigated the response of a bottom-fixed 10-MW turbine, showing the largest difference at stable conditions[11] and at close to rated wind speeds[10]. Bachynski & Eliassen[12] investigated the response of a 5-MW turbine on several floating support structures, and found differences of up to 40% in the standard deviation of the floater motions. Wise & Bachynski[13] showed that the Kaimal model yields a higher response at low frequencies and a lower response at high frequencies, also this for floating turbines. The same was observed at 3P frequencies by Bachynski & Eliassen[12].

2. Model Description

This study considers three turbine models; the NREL 5-MW[14], DTU 10-MW[15] and IEA 15-MW[16] reference wind turbines. The turbines are assumed located on the Norwegian Continental Shelf, at a water depth of 30 m. The soil conditions at the site are assumed to be an idealized clay profile with quadratic variation of the shear modulus with depth and linearly increasing undrained shear strength. The 5-MW monopile is from the OC3 project[17], while the 10-MW foundation is based on Velarde and Bachynski[18]. The 15-MW tower is the IEA design, and the monopile is designed for a natural period below 5.5 s. The fatigue capacity of the latter was checked using equivalent sea states[19]. Table 1 summarizes the properties of the turbines.

Table 1. Key parameters of the turbines in the study.

Parameter	Unit	NREL	DTU	IEA
Rated power	MW	5	10	15
Rated wind speed	m/s	11.4	11.4	10.59
Rated rotor speed	rpm	12.1	9.6	7.56
Rotor diameter	m	126	178.3	240
Hub height	m	90	119	150
Monopile diameter	m	7	9	11
Monopile wall thickness	m	0.07	0.11	0.11
1st fore-aft natural period	s	3.9	3.6	5.3

2.1. Environmental Model

The environmental model assumes the distribution of the wave parameters are conditional on the wind speed, with the wind direction as an independent variable. For each wind speed, a single sea state is used to represent the sea state distribution[19]. This gives the probability of occurrence for an environmental condition as

$$P(U_i, \theta_{wi,j}, \theta_{rel,k}) = P_n(U_i) \cdot P(\theta_{wi,j}) \cdot P_n(\theta_{rel,k}|U_i). \tag{1}$$

$P_n(U_i)$ is the probability of occurrence for wind speed U_i, $P(\theta_{wi,j})$ is the probability of occurrence of wind direction $\theta_{wi,j}$ and $P_n(\theta_{rel,k}|U_k)$ is the probability of occurrence for wind-wave misalignment bin $\theta_{rel,k}$. Three wind speed bins are considered: close to rated (8-10 m/s), intermediate (14-16 m/s) and high (20-22 m/s), while two misalignment angles (0° and 30°) are included. The distribution of the environmental parameters are based on 60 years of data from the NORA10 hindcast data base[20]. $P_n(U_i)$ and $P_n(\theta_{rel,k}|U_k)$ are normalized to give a total probability of 1 for the environmental conditions considered. Further details are given by Sørum et al.[21] The wave elevation is modelled using a Pierson-Moskowitz spectrum for the lowest wind speed and a JONSWAP spectrum for the two higher wind speeds.

2.2. Load Models

Hydrodynamic loads are calculated using linear wave kinematics, and MacCamy & Fuchs load model[22] combined with Morison-type drag loads. The hydrodynamic added mass is assumed to correspond to an added mass coefficient of 1.0.

Aerodynamic loads on the blades are calculated using unsteady blade element momentum theory with Glauert induction and Prandtl tip loss corrections for the operational turbine. Dynamic stall and dynamic wake correction is also included. For the parked turbine, aerodynamic loads are calculated based on the undisturbed wind field. The Kaimal turbulence model with exponential coherence and the Mann turbulence model are both used in this study, although only the Kaimal model is utilized when investigating the effect of the different soil models. Wind shear is modelled using the power law formulation.

2.3. Simulation Models

The wind turbine, tower and monopile above seafloor are modelled in SIMO-Riflex, an aero-hydro-servo-elastic simulation tool from SINTEF Ocean[23, 24]. Linear-elastic beam elements are used to model the structural components above seafloor.

2.4. Foundation Models

The two foundation models used in this study are a macro-element formulation and a p-y-curve model. In the part of the study investigating the effect of wind coherence models, only the macro element has been used.

A macro element reduces the soil-structure interaction to a load-displacement relationship at the seafloor, which reduces the simulation time. The macro element used here accounts for the non-linear load-displacement relationship of monopile OWTs at the seafloor and takes into account the different loading and offloading characteristics of the soil. This introduces hysteretic damping into the model. A more detailed description of the model is given by Page et al.[7]. The macro element is connected to the structural model at seafloor. A post-processing tool based on beam elements with springs is applied for determining the monopile loads below this[25].

The p-y curves are modelled as non-linear elastic springs attached to the beam model of the monopile below seafloor. Soil damping is accounted for by increasing the structural damping, which is tuned to give the same average damping coefficient as the macro element in a decay test starting from rated thrust.

Both the macro element, the post-processing tool and the p-y curves are calibrated to the soil-structure interaction found by a 3D continuum finite element analysis performed in Plaxis.

2.5. Fatigue Damage Calculation

Fatigue damage is calculated based on the axial stress variations in the tower and monopile. The individual stress cycles are extracted using the rainflow counting technique in WAFO[26], modified to allow for bi-linear SN curves. Miner's sum with thickness correction[27] is used to calculate the fatigue damage. The fatigue utilization is found as the ratio between the calculated fatigue damage and the fatigue capacity, Δ_C. DNV's SN-curve "D" for steel in sea water is used for the monopile, while the curve for steel in air is used for the tower.

2.6. Parameter Variations

To investigate if there is a coupling between the model variations and site parameters, the turbines were analysed using random realizations of 16 parameters. These parameters represent the uncertainty in a fixed design, and include uncertainty in the environmental description, soil uncertainty, fatigue parameter uncertainties and more. A list of the parameters is given in Appendix A, with the data source or reference for the distributions. 30 samples were used, with details on distributions and sampling strategy given by Sørum et al.[21]. Results from the individual realizations are used only when investigating the coupling (Sections 4.4 and 5.5) and when extracting response spectra. The remaining results are mean values across all realizations.

3. Fatigue Damage Utilization

The maximum long-term fatigue damage utilization along the support structure is shown in Figure 1, with $z = 0$ representing the sea floor. The lines represent the mean value of the 30 samples of the design parameters described in Section 2.6. Three locations of interest are identified in the support structures. The fatigue damage in the tower top is mainly caused by the rotor pitching moment. In the tower base, the loads are primarily caused by the aerodynamic thrust force and the wave-induced inertia loads. Finally, the loading at seafloor is caused by both aerodynamic loads and wave loads. The latter is also representative for the location with the highest fatigue utilization in the monopile, approximately one pile diameter below seafloor.
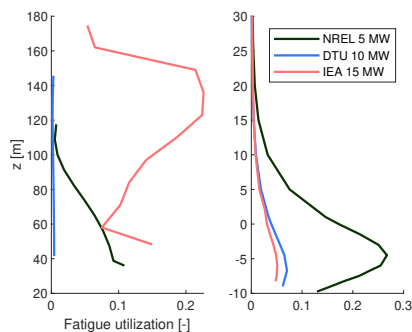

Figure 1. Maximum lifetime fatigue utilization in the tower (left) and monopile (right). Note that the transition pieces and lower parts of the monopiles are excluded.

4. Effects of Soil Model

The following sections will demonstrate how the differences between the two soil models influence the basic properties of the turbine models, followed by an assessment of the effect on the long-term fatigue damage.

4.1. Effect on Natural Frequency and Damping

The differences between the SSI models introduce differences in both the natural frequency and damping properties of the models. This is illustrated by decay tests, measuring the natural frequency and damping ratio in percent of critical damping for the different turbines.
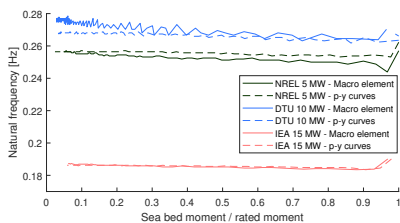

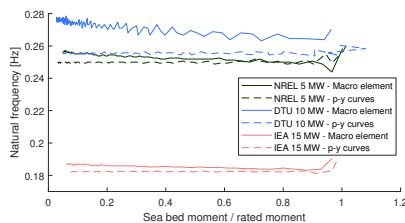**Figure 2.** Natural frequencies, with no thrust force.

Figure 3. Natural frequencies, at rated thrust.

Figure 2 shows the fore-aft natural frequencies as function of the measured bending moment at the seafloor with zero mean load. The p-y model shows little variation in natural frequency with amplitude, while the macro-element model has a clear trend of the natural frequency decreasing with increasing response amplitude. The amplitude-dependency of the natural frequency is largest for the 5-MW turbine and smallest for the 15-MW turbine. Including the rated thrust as a mean load, the natural frequency is reduced when using the p-y curves as shown in Figure 3. The change is most significant for the smallest turbine. Depending on the mean load and response amplitude, the two soil models may then yield both lower and higher natural frequencies than the other.
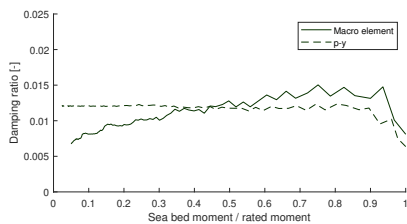
Figure 4. Damping ratio NREL 5-MW turbine.
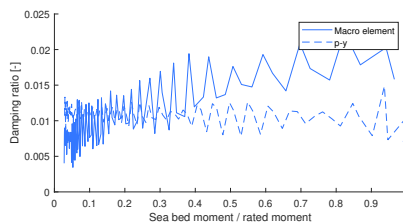
Figure 5. Damping ratio DTU 10-MW turbine.

The soil models also show a difference in how damping is included. The amplitude-dependent damping of the macro element is shown in Figures 4 to 6. This shows how the damping in the macro-element models increase with amplitude. The opposite is seen for the p-y curves, where the damping is amplitude-independent. Due to the tuning of the damping for the latter model, the amplitude for which the two SSI models predict the same damping also varies.
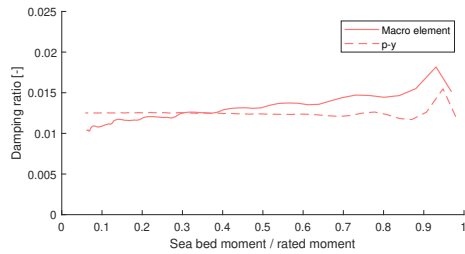
Figure 6. Damping ratio IEA 15-MW turbine.
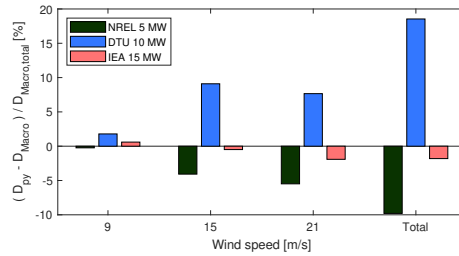
Figure 7. Difference in fatigue damage predictions at seafloor using the macro-element and p-y-curve models.

4.2. Response Above Seafloor

The effect of changing the soil model is similar across the support structure above seafloor, but with diminishing differences close to the tower top. However, as shown in Figure 7 there is a significant difference between the turbines. This figure shows the difference in the lifetime fatigue damage predicted per wind speed, and is normalized by the total fatigue damage predicted using the macro-element model. For both the 5-MW and 15-MW turbines, the macro element yields the highest fatigue damage. The opposite is the case for the 10-MW turbine, which also shows the highest difference between the models.

The 5-MW turbine shows a lower fatigue damage estimate when using the p-y curves for all wind speeds. Figures 8 and 9 illustrate the reason: Both the stiffness and damping are higher when using the p-y curves, leading to a reduced response and a lower fatigue damage. This trend is not universally true, amongst other it depends on the whether the response is in line with the wind or in the cross-wind direction. Still, the majority of the load cases show this trend, resulting in a higher fatigue damage prediction when using the macro-element model.
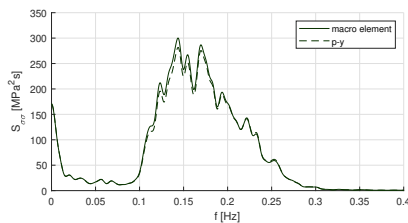
Figure 8. Upwind stress spectra at seafloor for the 5-MW turbine when operating at wind speed 15 m/s.
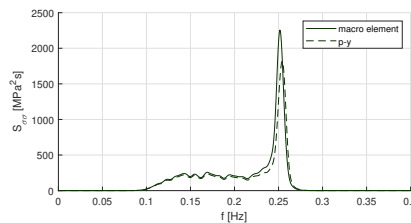
Figure 9. Upwind stress spectra at seafloor for the 5-MW turbine when parked at wind speed 15 m/s.

For the 10-MW turbine the opposite is the case: In a majority of the load cases the highest stiffness and damping is seen for the macro element, and a higher prediction of fatigue damage above seafloor is seen when using the p-y-curve model. Finally, the difference between the two models is smaller for the 15-MW turbine. This is also seen in Figures 2, 3 and 6, where there is a close match between the natural frequency and damping of the two soil models.

4.3. Response Below Seafloor

A different picture is seen below seafloor, illustrated in Figure 10 for the location in the monopile with highest fatigue damage. The first trend is that the difference between the models is more positive/less negative than above seafloor, indicating that the p-y model predicts higher responses when moving down into the soil. The reason is illustrated in Figure 11 for the 15-MW turbine. In the stiffness-dominated low frequencies, there is a good agreement between the macro-element (solid line) and p-y-curve (dashed line) response both at the sea floor (pink lines) and at the location with highest fatigue damage (black lines). However, there is a difference around the natural frequency (∼0.18 Hz). Here, the damping provided by the macro element is higher when moving down into the soil. This leads to larger response amplitudes, and increased fatigue damage predictions below sea floor when using the p-y-curve model.
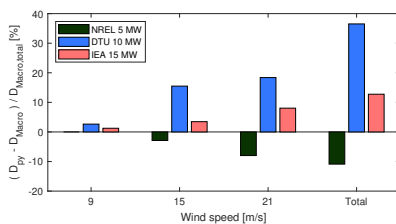
Figure 10. Difference in fatigue damage predictions below seafloor using the macro-element and p-y-curve models.
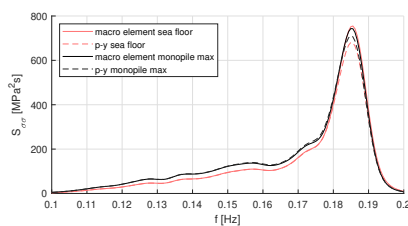
Figure 11. Upwind stress spectra at seafloor and below seafloor for the parked 15-MW turbine.

4.4. Interaction with Uncertain Design Parameters

Figure 12 shows the difference in fatigue prediction when using the two soil models versus the undrained shear strength. The latter is varied as described in Section 2.6. Increased shear strength reduces the fatigue damage predictions of the p-y-curve model, compared to the macro element. No other interactions were seen between the design parameters and the soil model.
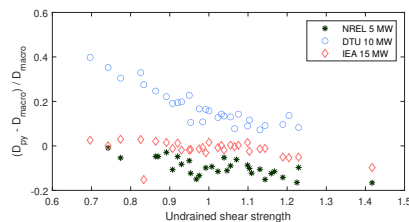
Figure 12. Difference in fatigue prediction for the soil models versus undrained shear strength.

5. Effects of Wind Model

This section presents the effect of varying the wind coherence models, starting with a description of the coherence properties before the turbine response is analysed.

5.1. Differences Between Wind Fields

When looking at the characteristics of the wind field simulated by the Kaimal and Mann models, two properties are of primary interest. The first is the spectral coherence, describing the relationship between the the wind speed at two different spatial locations. In the Kaimal model, this is described by an exponential coherence function, while the Mann model uses a velocity tensor model. To evaluate influence on coherence, the coherence of the wind speed at the hub and at the outer edge of the rotor disk at hub height is calculated. This is defined as

$$\gamma_{xy}(f) = \frac{S_{xy}(f)}{\sqrt{S_{xx}(f)S_{yy}(f)}} = C_{xy}(f) + iQ_{xy}(f) \qquad (2)$$

where γ_{xy} is the coherence between two points x and y, S_{xy} is the cross-spectrum, and S_{xx} and S_{yy} are the auto spectra. C_{xy} and Q_{xy} are the real and imaginary part of the coherence.
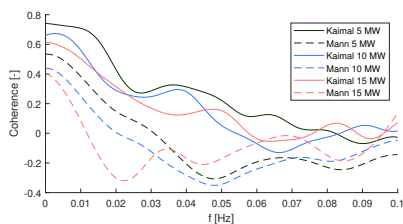
Figure 13. Spectral coherence between hub and outer rotor disk. Wind speed is 21 m/s.
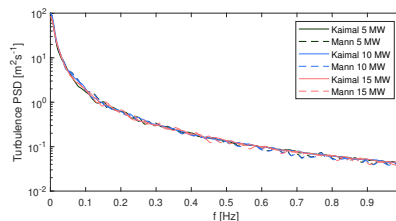
Figure 14. Hub-height wind turbulence spectrum at 15 m/s.

The coherence for wind speed 21 m/s is shown in Figure 13. Two effects are seen: The coherence decreases with increasing rotor disk area, and the coherence is higher for the Kaimal model than the Mann model. The effect of the former is that the 5-MW turbine will see more consistent variations in the wind speed across the rotor disk and higher variations in the effective wind speed. Similarly, the higher coherence with the Kaimal model will introduce higher variations in the effective wind speed than the Mann model. The expected consequence of this is higher variations in thrust force higher fatigue damage when the coherence is high.

The second property of interest the power spectral density (PSD) of the wind speed. As the Mann model has been adapted to give the same spectral properties as Kaimal, the spectra are expected to be similar. This is confirmed in Figure 14 for mean wind speed 15 m/s. The same is seen for the other wind speeds in the study.

5.2. Tower Top Response

The wind field is translated to structural response through the aerodynamic loads. While these loads are in turn influenced by the structural response, the loads from the rotor with a nacelle prevented from moving can provide a clearer picture of the difference between the wind models. This is particularly true for the tower top fore-aft bending moment, as shown in Figure 15. At low frequencies, the spectral value of the aerodynamic moment is higher when applying the Kaimal model. This corresponds well with the lower correlation of the Mann model. At higher frequencies the aerodynamic moment predicted by the Mann model is higher than the Kaimal moment, particularly visible at the 3P frequencies. This has been observed also by e.g. Bachynski & Eliassen[12] and Wise & Bachynski[13], and occurs despite the spectral density of the wind speed being equal. Note that the spectra in Figure 15 are normalized by the moment caused by the rated thrust force, M_{thrust}.
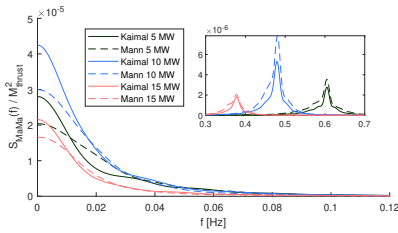
Figure 15. Aerodynamic moment at tower top for wind speed 15 m/s with a fixed rotor position.
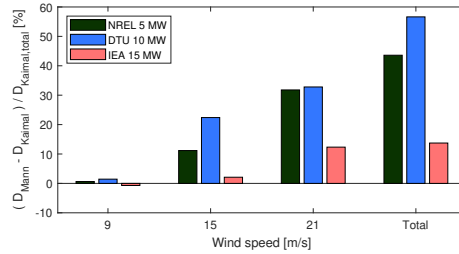
Figure 16. Differences in fatigue damage at tower top when using Kaimal and Mann turbulence models.

The total response and the effect on the fatigue damage is a combination of the higher response from the Kaimal model at low frequencies and the Mann model at higher frequencies. As the response at higher frequencies has more load cycles than the response at low frequencies, the influence on the fatigue damage will be higher than what is apparent from the PSDs.

Figure 16 shows how these effects add up at the tower top. The height of each bar is the difference between the fatigue damage predicted by the Kaimal and Mann models at each wind speed, normalized by the total fatigue damage predicted by the Kaimal model. The first observation is that the difference between the models increases with the wind speed. Secondly, the Mann model consistently predicts a higher fatigue damage, with the exception of the 15-MW turbine at wind speed 9 m/s. The difference between the fatigue damage predictions from the Kaimal and Mann models at the tower top are therefore dominated by the higher 3P response.

5.3. Tower Base Response

While the response at tower top can be understood from the aerodynamic loads, the structural dynamics become more important at the tower base. For the 5-MW turbine, the response is dominated by the low frequencies, as shown in Figure 17. At these frequencies the Kaimal model yields the highest response, including at the 1st natural frequency of the turbine.
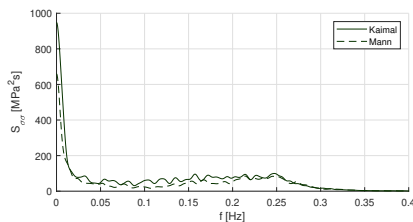
Figure 17. Upwind stress spectra at tower base for the 5-MW turbine in operational conditions, wind speed 15 m/s
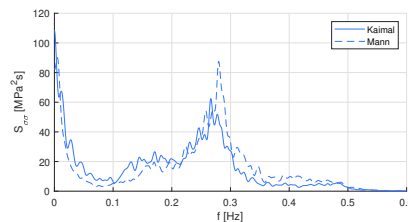
Figure 18. Upwind stress spectra at tower base for the 10-MW turbine in operational conditions, wind speed 15 m/s

The higher natural frequency of the 10-MW turbine reduces the difference between the two models at the natural frequency, as shown in Figure 18. As high-frequency (3P) loads become less important at low wind speeds, the Kaimal model predicts the highest fatigue damage at the two lowest wind speeds. The Mann model gives the highest fatigue damage at 21 m/s and in total, as shown in Figure 19.
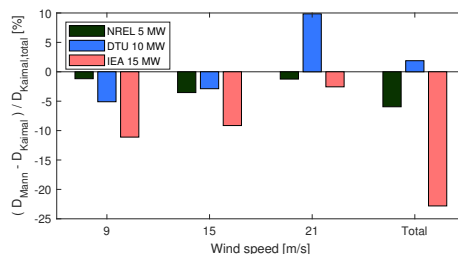
Figure 19. Differences in fatigue damage at tower base when using Kaimal and Mann turbulence models.

The 15-MW turbine has its natural frequency between the 5-MW and 10-MW turbines. This means that the Kaimal model predicts the highest fatigue damage for all wind speeds, but with the difference between the models decreasing as the wind speed increases.

5.4. Seafloor Response

The response at seafloor is primarily dominated by the wave loads. Still, the wind model influences the response also here. The differences in response are governed by the same mechanisms as at the tower base, but the majority of the response at seafloor is found at the wave frequencies. This means that the overall response is less influenced by the wind loads, giving less sensitivity to the choice of turbulence model.

5.5. Interaction with Uncertain Design Parameters

The interaction between the coherence model and the uncertain site parameters described in Section 2.6 was investigated. This was done in a similar manner to the soil model investigation in Section 4.4. However, no significant correlations were found between the wind coherence model and any single site parameter.

6. Discussion and Conclusion

The study has looked into the effect of modelling the soil-structure interaction by the use of p-y curves and a macro element, as well as the effect of modelling wind coherence using the Kaimal and Mann models. All model variations had effects that both increased and decreased the fatigue predictions compared to the alternative models. As an analyst it is important to be aware of how these models influence a specific turbine model to ensure conservative results.

For the soil model variations there, is a difference in both the predicted stiffness and damping. While the smallest turbine was most sensitive to the hysteretic effects, the largest uncertainty seems to be introduced by the calibration of the models. Although the macro element in general is expected to capture the response more accurately[6], the results from this paper highlight the importance of considering the calibration uncertainty. This may vary between the models, and a model with low calibration uncertainty should if possible be used in the analyses.

When considering the wind coherence models, the Kaimal model yields a higher response at low frequencies. The Mann model predicts a higher response at higher frequencies. This is particularly important for the 3P response. Additionally, the frequency where the change between which of the two coherence models that predicts the highest response is close to the 1st natural frequency of the foundations. A support structure with a low natural frequency tends to have highest response prediction from the Kaimal model, while a high natural frequency will give more conservative results using the Mann model.

Appendix A

Table 2. Design parameters varied throughout the study and the associated data sources/references. For details, se Sørum et al.[21].

Parameter	Reference/Data source
Wind speed distribution	NORA10[20]
Wind direction	NORA10[20]
Turbulence intensity	FINO1[28]
Wind shear	FINO1[28]
Yaw error	Veldkamp[29]
Significant wave height	NORA10[20]
Wave peak period	NORA10[20]
Wind-wave misalignment	NORA10[20]
Marine growth thickness	Jusoh & Wolfram[30]
Monopile drag coefficient	Peering & Bedon[31], Veldkamp[29]
Soil undrained shear strength	Lacasse & Nadim[32]
Soil void ratio	Lacasse & Nadim[32]
Monopile diameter	Zaaijer[3], Hübler et al.[33]
SN curve parameters	DNV GL[27]
Fatigue capacity	Folsø et al.[34], Peering & Bedon[31]
Turbine availability	DNV GL[35], Pfaffel et al.[36], Larsen et al.[37]

References

[1] Wu X, Hu Y, Li Y, Yang J, Duan L, Wang T, Adcock T, Jiang Z, Gao Z, Lin Z, Borthwick A and Liao S 2019 Renewable and Sustainable Energy Reviews **104** 379–393

[2] Byrne B W, McAdam R, Burd H J, Houlsby G T, Martin C M, Zdravkovi L, Taborda D M G, Potts D M, Jardine R J, Sideri M, Schroeder F C, Gavin K, Doherty P, Igoe D, Muirwood A, Kallehave D and Skov Gretlund J New design methods for large diameter piles under lateral loading for offshore wind applications 3rd International Symposium on Frontiers in Offshore Geotechnics, ISFOG 2015, June 10, 2015 - June 12, 2015 Frontiers in Offshore Geotechnics III - Proceedings of the 3rd International Symposium on Frontiers in Offshore Geotechnics, ISFOG 2015 (CRC Press/Balkema) pp 705–710

[3] Zaaijer M B 2006 Applied Ocean Research **28** 45–57

[4] Page A M, Schafhirt S, Eiksund G R, Skau K S, Jostad H P and Sturm H June 26-July 1, 2016 Alternative numerical pile foundation models for integrated analyses of monopile-based offshore wind turbines Proceedings of the Twenty-sixth (2016) International Ocean and Polar Engineering Conference (Rhodos, Greece: International Society of Offshore and Polar Engineers) pp 111–119

[5] Aasen S, Page A M, Skjolden Skau K and Nygaard T A 2017 Wind Energ. Sci. **2** 361–376

[6] Page A M, Grimstad G, Eiksund G R and Jostad H P 2018 Ocean Engineering **167** 23–35

[7] Page A, Grimstad G, Eiksund G and Jostad H P 2019 Computers and Geotechnics **Vol. 106** 314–326

[8] Katsikogiannis G, Bachynski E E and Page A M 2019 Journal of Physics: Conference Series **1356** 012019

[9] IEC 2019 International Electrotechnical Commission, Design Requirements for fixed offshore wind turbines (IEC 61400-3)

[10] Myrtvedt M H, Nybø A and Nielsen F G 2020 Journal of Physics: Conference Series **1669** 012013

[11] Nybø A, Nielsen F G and Godvik M 2021 Wind Energy **24** 1482–1500

[12] Bachynski E E and Eliassen L 2019 Wind Energy **22** 219–238

[13] Wise A S and Bachynski E E 2020 Wind Energy **23** 1266–1285

[14] Jonkman J, Butterfield S, Musial W and Scott G 2009 Definition of a 5MW reference wind turbine for offshore system development Report National Renewable Energy Laboratory (NREL) Denver, CO, US

[15] Bak C, Zahle F, Bitsche R, Kim T, Yde A, Henriksen L C, Andersen P B, Natarajan A and Hansen M To be accepted J. Wind Energy

[16] Gaertner E, Rinker J, Sethuraman L, Zahle F, Anderson B, Barter G, Abbas N, Meng F, Bortolotti P, Skrzypinski W, Scott G, Feil R, Bredmose H, Dykes K, Sheilds M, Allen C and Viselli A 2020 Definition of the IEA 15-megawatt offshore reference wind turbine Tech. rep. International Energy Agency Denver, CO, US URL `https://www.nrel.gov/docs/fy20osti/75698.pdf`

[17] Jonkman J and Musial W 2010 Offshore code comparison collaboration (OC3) for IEA task 23 offshore wind technology and deployment Report NREL Golden, Colorado, USA

[18] Velarde J and Bachynski E E 2017 Energy Procedia **137** 3–13

[19] Katsikogiannis G, Sørum S H, Bachynski E E and Amdahl J 2021 Marine Structures **77** 102939

[20] Reistad M, Breivik O, Haakenstad H, Aarnes O J, Furevik B R and Bidlot J R 2011 Journal of Geophysical Research: Oceans **116** 1–18

[21] Sørum S H, Katsikogiannis G, Bachynski-Polić E E, Amdahl J, Page A M and Klinkvort R T Accepted to Wind Energy

[22] MacCamy RC, Fuchs R A 1954 Wave Forces on Piles: A Diffraction Theory Tech. rep. Office of Naval Research, U. S. Department of the Navy Washington, D.C., US

[23] SINTEF Ocean 2017 SIMO 4.10.3 user guide Tech. rep. SINTEF Ocean Trondheim, Norway

[24] SINTEF Ocean 2017 RIFLEX 4.10.3 user guide Tech. rep. SINTEF Ocean Trondheim, Norway

[25] Klinkvort R T, Sturm H, Page A M, Zhang Y and Jostad H P August 28–31, 2022 A consistent, rigorous and super-fast monopile design approach Proceedings of the 4th International Symposium on Frontiers in Offshore Geotechnics (Austin, Texas, US: American Society of Civil Engineers)

[26] WAFO-group 2011 WAFO - A Matlab Toolbox for Analysis of Random Waves and Loads - A Tutorial

[27] DNV-GL (Det Norske Veritas - Germanischer Lloyd) Fatigue design of offshore steel structures (DNVGL-RP-C203)

[28] Bundesamt für Seeschifffahrt und Hydrographie FINO - datenbankinformationen

[29] Veldkamp H F 2006 Chances in wind energy: a probalistic approach to wind turbine fatigue design Thesis Delft University Delft, NL

[30] Jusoh I and Wolfram J 1996 Jurnal Mekanikal **1**

[31] Peeringa J and Bedon G 2017 Energy Procedia **137** 255–260

[32] Lacasse S and Nadim F 1996 Uncertainties in characterising soil properties Uncertainty in the geologic environment: from theory to practice (Madison, Wisconsin: American Society of Civil Engineers)

[33] Hübler C, Gebhardt C G and Rolfes R 2017 Renewable Energy **111** 878–891

[34] Folsø R, Otto S and Parmentier G 2002 Marine Structures **15** 627–651

[35] DNV-GL (Det Norske Veritas - Germanischer Lloyd) 2016 Loads and site conditions for wind turbines (DNVGL-ST-0437)

[36] Pfaffel S, Faulstich S and Rohrig K 2017 energies **10** 1904

[37] Larsen J, Soerensen H, Christiansen E and Naef S October 26-28, 2005 Experiences from Middelgrunden 40 MW offshore wind farm Copenhagen Offshore Wind (Copenhagen: Danish Wind Industry Association)

PhD Theses Published at the Department of Marine Technology

Previous PhD theses published at the Department of Marine Technology
(earlier: Faculty of Marine Technology)
NORWEGIAN UNIVERSITY OF SCIENCE AND TECHNOLOGY

Report No.	Author	Title
	Kavlie, Dag	Optimization of Plane Elastic Grillages, 1967
	Hansen, Hans R.	Man-Machine Communication and Data-Storage Methods in Ship Structural Design, 1971
	Gisvold, Kaare M.	A Method for non-linear mixed -integer programming and its Application to Design Problems, 1971
	Lund, Sverre	Tanker Frame Optimalization by means of SUMT-Transformation and Behaviour Models, 1971
	Vinje, Tor	On Vibration of Spherical Shells Interacting with Fluid, 1972
	Lorentz, Jan D.	Tank Arrangement for Crude Oil Carriers in Accordance with the new Anti-Pollution Regulations, 1975
	Carlsen, Carl A.	Computer-Aided Design of Tanker Structures, 1975
	Larsen, Carl M.	Static and Dynamic Analysis of Offshore Pipelines during Installation, 1976
UR-79-01	Brigt Hatlestad, MK	The finite element method used in a fatigue evaluation of fixed offshore platforms. (Dr.Ing. Thesis)
UR-79-02	Erik Pettersen, MK	Analysis and design of cellular structures. (Dr.Ing. Thesis)
UR-79-03	Sverre Valsgård, MK	Finite difference and finite element methods applied to nonlinear analysis of plated structures. (Dr.Ing. Thesis)
UR-79-04	Nils T. Nordsve, MK	Finite element collapse analysis of structural members considering imperfections and stresses due to fabrication. (Dr.Ing. Thesis)
UR-79-05	Ivar J. Fylling, MK	Analysis of towline forces in ocean towing systems. (Dr.Ing. Thesis)
UR-79- x	Finn Gunnar Nielsen, MH	Hydrodynamic problems related to oil barriers for offshore application
UR-80-06	Nils Sandsmark, MM	Analysis of Stationary and Transient Heat Conduction by the Use of the Finite Element Method. (Dr.Ing. Thesis)
UR-80-09	Sverre Haver, MK	Analysis of uncertainties related to the stochastic modeling of ocean waves. (Dr.Ing. Thesis)

UR-81-15	Odland, Jonas	On the Strength of welded Ring stiffened cylindrical Shells primarily subjected to axial Compression
UR-82-17	Engesvik, Knut	Analysis of Uncertainties in the fatigue Capacity of Welded Joints
UR-82-18	Rye, Henrik	Ocean wave groups
UR-83-30	Eide, Oddvar Inge	On Cumulative Fatigue Damage in Steel Welded Joints
UR-83-33	Mo, Olav	Stochastic Time Domain Analysis of Slender Offshore Structures
UR-83-34	Amdahl, Jørgen	Energy absorption in Ship-platform impacts
UR-84-37	Mørch, Morten	Motions and mooring forces of semi submersibles as determined by full-scale measurements and theoretical analysis
UR-84-38	Soares, C. Guedes	Probabilistic models for load effects in ship structures
UR-84-39	Aarsnes, Jan V.	Current forces on ships
UR-84-40	Czujko, Jerzy	Collapse Analysis of Plates subjected to Biaxial Compression and Lateral Load
UR-85-46	Alf G. Engseth, MK	Finite element collapse analysis of tubular steel offshore structures. (Dr.Ing. Thesis)
UR-86-47	Dengody Sheshappa, MP	A Computer Design Model for Optimizing Fishing Vessel Designs Based on Techno-Economic Analysis. (Dr.Ing. Thesis)
UR-86-48	Vidar Aanesland, MH	A Theoretical and Numerical Study of Ship Wave Resistance. (Dr.Ing. Thesis)
UR-86-49	Heinz-Joachim Wessel, MK	Fracture Mechanics Analysis of Crack Growth in Plate Girders. (Dr.Ing. Thesis)
UR-86-50	Jon Taby, MK	Ultimate and Post-ultimate Strength of Dented Tubular Members. (Dr.Ing. Thesis)
UR-86-51	Walter Lian, MH	A Numerical Study of Two-Dimensional Separated Flow Past Bluff Bodies at Moderate KC-Numbers. (Dr.Ing. Thesis)
UR-86-52	Bjørn Sortland, MH	Force Measurements in Oscillating Flow on Ship Sections and Circular Cylinders in a U-Tube Water Tank. (Dr.Ing. Thesis)
UR-86-53	Kurt Strand, MM	A System Dynamic Approach to One-dimensional Fluid Flow. (Dr.Ing. Thesis)
UR-86-54	Arne Edvin Løken, MH	Three Dimensional Second Order Hydrodynamic Effects on Ocean Structures in Waves. (Dr.Ing. Thesis)
UR-86-55	Sigurd Falch, MH	A Numerical Study of Slamming of Two-

Dimensional Bodies. (Dr.Ing. Thesis)

UR-87-56	Arne Braathen, MH	Application of a Vortex Tracking Method to the Prediction of Roll Damping of a Two-Dimension Floating Body. (Dr.Ing. Thesis)
UR-87-57	Bernt Leira, MK	Gaussian Vector Processes for Reliability Analysis involving Wave-Induced Load Effects. (Dr.Ing. Thesis)
UR-87-58	Magnus Småvik, MM	Thermal Load and Process Characteristics in a Two-Stroke Diesel Engine with Thermal Barriers (in Norwegian). (Dr.Ing. Thesis)
MTA-88-59	Bernt Arild Bremdal, MP	An Investigation of Marine Installation Processes – A Knowledge - Based Planning Approach. (Dr.Ing. Thesis)
MTA-88-60	Xu Jun, MK	Non-linear Dynamic Analysis of Space-framed Offshore Structures. (Dr.Ing. Thesis)
MTA-89-61	Gang Miao, MH	Hydrodynamic Forces and Dynamic Responses of Circular Cylinders in Wave Zones. (Dr.Ing. Thesis)
MTA-89-62	Martin Greenhow, MH	Linear and Non-Linear Studies of Waves and Floating Bodies. Part I and Part II. (Dr.Techn. Thesis)
MTA-89-63	Chang Li, MH	Force Coefficients of Spheres and Cubes in Oscillatory Flow with and without Current. (Dr.Ing. Thesis
MTA-89-64	Hu Ying, MP	A Study of Marketing and Design in Development of Marine Transport Systems. (Dr.Ing. Thesis)
MTA-89-65	Arild Jæger, MH	Seakeeping, Dynamic Stability and Performance of a Wedge Shaped Planing Hull. (Dr.Ing. Thesis)
MTA-89-66	Chan Siu Hung, MM	The dynamic characteristics of tilting-pad bearings
MTA-89-67	Kim Wikstrøm, MP	Analysis av projekteringen for ett offshore projekt. (Licenciat-avhandling)
MTA-89-68	Jiao Guoyang, MK	Reliability Analysis of Crack Growth under Random Loading, considering Model Updating. (Dr.Ing. Thesis)
MTA-89-69	Arnt Olufsen, MK	Uncertainty and Reliability Analysis of Fixed Offshore Structures. (Dr.Ing. Thesis)
MTA-89-70	Wu Yu-Lin, MR	System Reliability Analyses of Offshore Structures using improved Truss and Beam Models. (Dr.Ing. Thesis)
MTA-90-71	Jan Roger Hoff, MH	Three-dimensional Green function of a vessel with forward speed in waves. (Dr.Ing. Thesis)
MTA-90-72	Rong Zhao, MH	Slow-Drift Motions of a Moored Two-Dimensional Body in Irregular Waves. (Dr.Ing. Thesis)
MTA-90-73	Atle Minsaas, MP	Economical Risk Analysis. (Dr.Ing. Thesis)

MTA-90-74	Knut-Aril Farnes, MK	Long-term Statistics of Response in Non-linear Marine Structures. (Dr.Ing. Thesis)
MTA-90-75	Torbjørn Sotberg, MK	Application of Reliability Methods for Safety Assessment of Submarine Pipelines. (Dr.Ing. Thesis)
MTA-90-76	Zeuthen, Steffen, MP	SEAMAID. A computational model of the design process in a constraint-based logic programming environment. An example from the offshore domain. (Dr.Ing. Thesis)
MTA-91-77	Haagensen, Sven, MM	Fuel Dependant Cyclic Variability in a Spark Ignition Engine - An Optical Approach. (Dr.Ing. Thesis)
MTA-91-78	Løland, Geir, MH	Current forces on and flow through fish farms. (Dr.Ing. Thesis)
MTA-91-79	Hoen, Christopher, MK	System Identification of Structures Excited by Stochastic Load Processes. (Dr.Ing. Thesis)
MTA-91-80	Haugen, Stein, MK	Probabilistic Evaluation of Frequency of Collision between Ships and Offshore Platforms. (Dr.Ing. Thesis)
MTA-91-81	Sødahl, Nils, MK	Methods for Design and Analysis of Flexible Risers. (Dr.Ing. Thesis)
MTA-91-82	Ormberg, Harald, MK	Non-linear Response Analysis of Floating Fish Farm Systems. (Dr.Ing. Thesis)
MTA-91-83	Marley, Mark J., MK	Time Variant Reliability under Fatigue Degradation. (Dr.Ing. Thesis)
MTA-91-84	Krokstad, Jørgen R., MH	Second-order Loads in Multidirectional Seas. (Dr.Ing. Thesis)
MTA-91-85	Molteberg, Gunnar A., MM	The Application of System Identification Techniques to Performance Monitoring of Four Stroke Turbocharged Diesel Engines. (Dr.Ing. Thesis)
MTA-92-86	Mørch, Hans Jørgen Bjelke, MH	Aspects of Hydrofoil Design: with Emphasis on Hydrofoil Interaction in Calm Water. (Dr.Ing. Thesis)
MTA-92-87	Chan Siu Hung, MM	Nonlinear Analysis of Rotordynamic Instabilities in Highspeed Turbomachinery. (Dr.Ing. Thesis)
MTA-92-88	Bessason, Bjarni, MK	Assessment of Earthquake Loading and Response of Seismically Isolated Bridges. (Dr.Ing. Thesis)
MTA-92-89	Langli, Geir, MP	Improving Operational Safety through exploitation of Design Knowledge - an investigation of offshore platform safety. (Dr.Ing. Thesis)
MTA-92-90	Sævik, Svein, MK	On Stresses and Fatigue in Flexible Pipes. (Dr.Ing. Thesis)
MTA-92-91	Ask, Tor Ø., MM	Ignition and Flame Growth in Lean Gas-Air Mixtures. An Experimental Study with a Schlieren

System. (Dr.Ing. Thesis)

MTA-86-92	Hessen, Gunnar, MK	Fracture Mechanics Analysis of Stiffened Tubular Members. (Dr.Ing. Thesis)
MTA-93-93	Steinebach, Christian, MM	Knowledge Based Systems for Diagnosis of Rotating Machinery. (Dr.Ing. Thesis)
MTA-93-94	Dalane, Jan Inge, MK	System Reliability in Design and Maintenance of Fixed Offshore Structures. (Dr.Ing. Thesis)
MTA-93-95	Steen, Sverre, MH	Cobblestone Effect on SES. (Dr.Ing. Thesis)
MTA-93-96	Karunakaran, Daniel, MK	Nonlinear Dynamic Response and Reliability Analysis of Drag-dominated Offshore Platforms. (Dr.Ing. Thesis)
MTA-93-97	Hagen, Arnulf, MP	The Framework of a Design Process Language. (Dr.Ing. Thesis)
MTA-93-98	Nordrik, Rune, MM	Investigation of Spark Ignition and Autoignition in Methane and Air Using Computational Fluid Dynamics and Chemical Reaction Kinetics. A Numerical Study of Ignition Processes in Internal Combustion Engines. (Dr.Ing. Thesis)
MTA-94-99	Passano, Elizabeth, MK	Efficient Analysis of Nonlinear Slender Marine Structures. (Dr.Ing. Thesis)
MTA-94-100	Kvålsvold, Jan, MH	Hydroelastic Modelling of Wetdeck Slamming on Multihull Vessels. (Dr.Ing. Thesis)
MTA-94-102	Bech, Sidsel M., MK	Experimental and Numerical Determination of Stiffness and Strength of GRP/PVC Sandwich Structures. (Dr.Ing. Thesis)
MTA-95-103	Paulsen, Hallvard, MM	A Study of Transient Jet and Spray using a Schlieren Method and Digital Image Processing. (Dr.Ing. Thesis)
MTA-95-104	Hovde, Geir Olav, MK	Fatigue and Overload Reliability of Offshore Structural Systems, Considering the Effect of Inspection and Repair. (Dr.Ing. Thesis)
MTA-95-105	Wang, Xiaozhi, MK	Reliability Analysis of Production Ships with Emphasis on Load Combination and Ultimate Strength. (Dr.Ing. Thesis)
MTA-95-106	Ulstein, Tore, MH	Nonlinear Effects of a Flexible Stern Seal Bag on Cobblestone Oscillations of an SES. (Dr.Ing. Thesis)
MTA-95-107	Solaas, Frøydis, MH	Analytical and Numerical Studies of Sloshing in Tanks. (Dr.Ing. Thesis)
MTA-95-108	Hellan, Øyvind, MK	Nonlinear Pushover and Cyclic Analyses in Ultimate Limit State Design and Reassessment of Tubular Steel Offshore Structures. (Dr.Ing. Thesis)
MTA-95-109	Hermundstad, Ole A., MK	Theoretical and Experimental Hydroelastic Analysis of High Speed Vessels. (Dr.Ing. Thesis)

MTA-96-110	Bratland, Anne K., MH	Wave-Current Interaction Effects on Large-Volume Bodies in Water of Finite Depth. (Dr.Ing. Thesis)
MTA-96-111	Herfjord, Kjell, MH	A Study of Two-dimensional Separated Flow by a Combination of the Finite Element Method and Navier-Stokes Equations. (Dr.Ing. Thesis)
MTA-96-112	Æsøy, Vilmar, MM	Hot Surface Assisted Compression Ignition in a Direct Injection Natural Gas Engine. (Dr.Ing. Thesis)
MTA-96-113	Eknes, Monika L., MK	Escalation Scenarios Initiated by Gas Explosions on Offshore Installations. (Dr.Ing. Thesis)
MTA-96-114	Erikstad, Stein O., MP	A Decision Support Model for Preliminary Ship Design. (Dr.Ing. Thesis)
MTA-96-115	Pedersen, Egil, MH	A Nautical Study of Towed Marine Seismic Streamer Cable Configurations. (Dr.Ing. Thesis)
MTA-97-116	Moksnes, Paul O., MM	Modelling Two-Phase Thermo-Fluid Systems Using Bond Graphs. (Dr.Ing. Thesis)
MTA-97-117	Halse, Karl H., MK	On Vortex Shedding and Prediction of Vortex-Induced Vibrations of Circular Cylinders. (Dr.Ing. Thesis)
MTA-97-118	Igland, Ragnar T., MK	Reliability Analysis of Pipelines during Laying, considering Ultimate Strength under Combined Loads. (Dr.Ing. Thesis)
MTA-97-119	Pedersen, Hans-P., MP	Levendefiskteknologi for fiskefartøy. (Dr.Ing. Thesis)
MTA-98-120	Vikestad, Kyrre, MK	Multi-Frequency Response of a Cylinder Subjected to Vortex Shedding and Support Motions. (Dr.Ing. Thesis)
MTA-98-121	Azadi, Mohammad R. E., MK	Analysis of Static and Dynamic Pile-Soil-Jacket Behaviour. (Dr.Ing. Thesis)
MTA-98-122	Ulltang, Terje, MP	A Communication Model for Product Information. (Dr.Ing. Thesis)
MTA-98-123	Torbergsen, Erik, MM	Impeller/Diffuser Interaction Forces in Centrifugal Pumps. (Dr.Ing. Thesis)
MTA-98-124	Hansen, Edmond, MH	A Discrete Element Model to Study Marginal Ice Zone Dynamics and the Behaviour of Vessels Moored in Broken Ice. (Dr.Ing. Thesis)
MTA-98-125	Videiro, Paulo M., MK	Reliability Based Design of Marine Structures. (Dr.Ing. Thesis)
MTA-99-126	Mainçon, Philippe, MK	Fatigue Reliability of Long Welds Application to Titanium Risers. (Dr.Ing. Thesis)
MTA-99-127	Haugen, Elin M., MH	Hydroelastic Analysis of Slamming on Stiffened Plates with Application to Catamaran Wetdecks. (Dr.Ing. Thesis)
MTA-99-	Langhelle, Nina K., MK	Experimental Validation and Calibration of

128		Nonlinear Finite Element Models for Use in Design of Aluminium Structures Exposed to Fire. (Dr.Ing. Thesis)
MTA-99-129	Berstad, Are J., MK	Calculation of Fatigue Damage in Ship Structures. (Dr.Ing. Thesis)
MTA-99-130	Andersen, Trond M., MM	Short Term Maintenance Planning. (Dr.Ing. Thesis)
MTA-99-131	Tveiten, Bård Wathne, MK	Fatigue Assessment of Welded Aluminium Ship Details. (Dr.Ing. Thesis)
MTA-99-132	Søreide, Fredrik, MP	Applications of underwater technology in deep water archaeology. Principles and practice. (Dr.Ing. Thesis)
MTA-99-133	Tønnessen, Rune, MH	A Finite Element Method Applied to Unsteady Viscous Flow Around 2D Blunt Bodies With Sharp Corners. (Dr.Ing. Thesis)
MTA-99-134	Elvekrok, Dag R., MP	Engineering Integration in Field Development Projects in the Norwegian Oil and Gas Industry. The Supplier Management of Norne. (Dr.Ing. Thesis)
MTA-99-135	Fagerholt, Kjetil, MP	Optimeringsbaserte Metoder for Ruteplanlegging innen skipsfart. (Dr.Ing. Thesis)
MTA-99-136	Bysveen, Marie, MM	Visualization in Two Directions on a Dynamic Combustion Rig for Studies of Fuel Quality. (Dr.Ing. Thesis)
MTA-2000-137	Storteig, Eskild, MM	Dynamic characteristics and leakage performance of liquid annular seals in centrifugal pumps. (Dr.Ing. Thesis)
MTA-2000-138	Sagli, Gro, MK	Model uncertainty and simplified estimates of long term extremes of hull girder loads in ships. (Dr.Ing. Thesis)
MTA-2000-139	Tronstad, Harald, MK	Nonlinear analysis and design of cable net structures like fishing gear based on the finite element method. (Dr.Ing. Thesis)
MTA-2000-140	Kroneberg, André, MP	Innovation in shipping by using scenarios. (Dr.Ing. Thesis)
MTA-2000-141	Haslum, Herbjørn Alf, MH	Simplified methods applied to nonlinear motion of spar platforms. (Dr.Ing. Thesis)
MTA-2001-142	Samdal, Ole Johan, MM	Modelling of Degradation Mechanisms and Stressor Interaction on Static Mechanical Equipment Residual Lifetime. (Dr.Ing. Thesis)
MTA-2001-143	Baarholm, Rolf Jarle, MH	Theoretical and experimental studies of wave impact underneath decks of offshore platforms. (Dr.Ing. Thesis)
MTA-2001-144	Wang, Lihua, MK	Probabilistic Analysis of Nonlinear Wave-induced Loads on Ships. (Dr.Ing. Thesis)
MTA-2001-145	Kristensen, Odd H. Holt, MK	Ultimate Capacity of Aluminium Plates under Multiple Loads, Considering HAZ Properties.

(Dr.Ing. Thesis)

MTA-2001-146	Greco, Marilena, MH	A Two-Dimensional Study of Green-Water Loading. (Dr.Ing. Thesis)
MTA-2001-147	Heggelund, Svein E., MK	Calculation of Global Design Loads and Load Effects in Large High Speed Catamarans. (Dr.Ing. Thesis)
MTA-2001-148	Babalola, Olusegun T., MK	Fatigue Strength of Titanium Risers – Defect Sensitivity. (Dr.Ing. Thesis)
MTA-2001-149	Mohammed, Abuu K., MK	Nonlinear Shell Finite Elements for Ultimate Strength and Collapse Analysis of Ship Structures. (Dr.Ing. Thesis)
MTA-2002-150	Holmedal, Lars E., MH	Wave-current interactions in the vicinity of the sea bed. (Dr.Ing. Thesis)
MTA-2002-151	Rognebakke, Olav F., MH	Sloshing in rectangular tanks and interaction with ship motions. (Dr.Ing. Thesis)
MTA-2002-152	Lader, Pål Furset, MH	Geometry and Kinematics of Breaking Waves. (Dr.Ing. Thesis)
MTA-2002-153	Yang, Qinzheng, MH	Wash and wave resistance of ships in finite water depth. (Dr.Ing. Thesis)
MTA-2002-154	Melhus, Øyvin, MM	Utilization of VOC in Diesel Engines. Ignition and combustion of VOC released by crude oil tankers. (Dr.Ing. Thesis)
MTA-2002-155	Ronæss, Marit, MH	Wave Induced Motions of Two Ships Advancing on Parallel Course. (Dr.Ing. Thesis)
MTA-2002-156	Økland, Ole D., MK	Numerical and experimental investigation of whipping in twin hull vessels exposed to severe wet deck slamming. (Dr.Ing. Thesis)
MTA-2002-157	Ge, Chunhua, MK	Global Hydroelastic Response of Catamarans due to Wet Deck Slamming. (Dr.Ing. Thesis)
MTA-2002-158	Byklum, Eirik, MK	Nonlinear Shell Finite Elements for Ultimate Strength and Collapse Analysis of Ship Structures. (Dr.Ing. Thesis)
IMT-2003-1	Chen, Haibo, MK	Probabilistic Evaluation of FPSO-Tanker Collision in Tandem Offloading Operation. (Dr.Ing. Thesis)
IMT-2003-2	Skaugset, Kjetil Bjørn, MK	On the Suppression of Vortex Induced Vibrations of Circular Cylinders by Radial Water Jets. (Dr.Ing. Thesis)
IMT-2003-3	Chezhian, Muthu	Three-Dimensional Analysis of Slamming. (Dr.Ing. Thesis)
IMT-2003-4	Buhaug, Øyvind	Deposit Formation on Cylinder Liner Surfaces in Medium Speed Engines. (Dr.Ing. Thesis)
IMT-2003-5	Tregde, Vidar	Aspects of Ship Design: Optimization of Aft Hull with Inverse Geometry Design. (Dr.Ing. Thesis)

IMT-2003-6	Wist, Hanne Therese	Statistical Properties of Successive Ocean Wave Parameters. (Dr.Ing. Thesis)
IMT-2004-7	Ransau, Samuel	Numerical Methods for Flows with Evolving Interfaces. (Dr.Ing. Thesis)
IMT-2004-8	Soma, Torkel	Blue-Chip or Sub-Standard. A data interrogation approach of identity safety characteristics of shipping organization. (Dr.Ing. Thesis)
IMT-2004-9	Ersdal, Svein	An experimental study of hydrodynamic forces on cylinders and cables in near axial flow. (Dr.Ing. Thesis)
IMT-2005-10	Brodtkorb, Per Andreas	The Probability of Occurrence of Dangerous Wave Situations at Sea. (Dr.Ing. Thesis)
IMT-2005-11	Yttervik, Rune	Ocean current variability in relation to offshore engineering. (Dr.Ing. Thesis)
IMT-2005-12	Fredheim, Arne	Current Forces on Net-Structures. (Dr.Ing. Thesis)
IMT-2005-13	Heggernes, Kjetil	Flow around marine structures. (Dr.Ing. Thesis
IMT-2005-14	Fouques, Sebastien	Lagrangian Modelling of Ocean Surface Waves and Synthetic Aperture Radar Wave Measurements. (Dr.Ing. Thesis)
IMT-2006-15	Holm, Håvard	Numerical calculation of viscous free surface flow around marine structures. (Dr.Ing. Thesis)
IMT-2006-16	Bjørheim, Lars G.	Failure Assessment of Long Through Thickness Fatigue Cracks in Ship Hulls. (Dr.Ing. Thesis)
IMT-2006-17	Hansson, Lisbeth	Safety Management for Prevention of Occupational Accidents. (Dr.Ing. Thesis)
IMT-2006-18	Zhu, Xinying	Application of the CIP Method to Strongly Nonlinear Wave-Body Interaction Problems. (Dr.Ing. Thesis)
IMT-2006-19	Reite, Karl Johan	Modelling and Control of Trawl Systems. (Dr.Ing. Thesis)
IMT-2006-20	Smogeli, Øyvind Notland	Control of Marine Propellers. From Normal to Extreme Conditions. (Dr.Ing. Thesis)
IMT-2007-21	Storhaug, Gaute	Experimental Investigation of Wave Induced Vibrations and Their Effect on the Fatigue Loading of Ships. (Dr.Ing. Thesis)
IMT-2007-22	Sun, Hui	A Boundary Element Method Applied to Strongly Nonlinear Wave-Body Interaction Problems. (PhD Thesis, CeSOS)
IMT-2007-23	Rustad, Anne Marthine	Modelling and Control of Top Tensioned Risers. (PhD Thesis, CeSOS)
IMT-2007-24	Johansen, Vegar	Modelling flexible slender system for real-time

simulations and control applications

IMT-2007-25	Wroldsen, Anders Sunde	Modelling and control of tensegrity structures. (PhD Thesis, CeSOS)
IMT-2007-26	Aronsen, Kristoffer Høye	An experimental investigation of in-line and combined inline and cross flow vortex induced vibrations. (Dr. avhandling, IMT)
IMT-2007-27	Gao, Zhen	Stochastic Response Analysis of Mooring Systems with Emphasis on Frequency-domain Analysis of Fatigue due to Wide-band Response Processes (PhD Thesis, CeSOS)
IMT-2007-28	Thorstensen, Tom Anders	Lifetime Profit Modelling of Ageing Systems Utilizing Information about Technical Condition. (Dr.ing. thesis, IMT)
IMT-2008-29	Refsnes, Jon Erling Gorset	Nonlinear Model-Based Control of Slender Body AUVs (PhD Thesis, IMT)
IMT-2008-30	Berntsen, Per Ivar B.	Structural Reliability Based Position Mooring. (PhD-Thesis, IMT)
IMT-2008-31	Ye, Naiquan	Fatigue Assessment of Aluminium Welded Box-stiffener Joints in Ships (Dr.ing. thesis, IMT)
IMT-2008-32	Radan, Damir	Integrated Control of Marine Electrical Power Systems. (PhD-Thesis, IMT)
IMT-2008-33	Thomassen, Paul	Methods for Dynamic Response Analysis and Fatigue Life Estimation of Floating Fish Cages. (Dr.ing. thesis, IMT)
IMT-2008-34	Pákozdi, Csaba	A Smoothed Particle Hydrodynamics Study of Two-dimensional Nonlinear Sloshing in Rectangular Tanks. (Dr.ing.thesis, IMT/ CeSOS)
IMT-2007-35	Grytøyr, Guttorm	A Higher-Order Boundary Element Method and Applications to Marine Hydrodynamics. (Dr.ing.thesis, IMT)
IMT-2008-36	Drummen, Ingo	Experimental and Numerical Investigation of Nonlinear Wave-Induced Load Effects in Containerships considering Hydroelasticity. (PhD thesis, CeSOS)
IMT-2008-37	Skejic, Renato	Maneuvering and Seakeeping of a Singel Ship and of Two Ships in Interaction. (PhD-Thesis, CeSOS)
IMT-2008-38	Harlem, Alf	An Age-Based Replacement Model for Repairable Systems with Attention to High-Speed Marine Diesel Engines. (PhD-Thesis, IMT)
IMT-2008-39	Alsos, Hagbart S.	Ship Grounding. Analysis of Ductile Fracture, Bottom Damage and Hull Girder Response. (PhD-thesis, IMT)
IMT-2008-40	Graczyk, Mateusz	Experimental Investigation of Sloshing Loading and Load Effects in Membrane LNG Tanks Subjected to Random Excitation. (PhD-thesis, CeSOS)

IMT-2008-41	Taghipour, Reza	Efficient Prediction of Dynamic Response for Flexible amd Multi-body Marine Structures. (PhD-thesis, CeSOS)
IMT-2008-42	Ruth, Eivind	Propulsion control and thrust allocation on marine vessels. (PhD thesis, CeSOS)
IMT-2008-43	Nystad, Bent Helge	Technical Condition Indexes and Remaining Useful Life of Aggregated Systems. PhD thesis, IMT
IMT-2008-44	Soni, Prashant Kumar	Hydrodynamic Coefficients for Vortex Induced Vibrations of Flexible Beams, PhD thesis, CeSOS
IMT-2009-45	Amlashi, Hadi K.K.	Ultimate Strength and Reliability-based Design of Ship Hulls with Emphasis on Combined Global and Local Loads. PhD Thesis, IMT
IMT-2009-46	Pedersen, Tom Arne	Bond Graph Modelling of Marine Power Systems. PhD Thesis, IMT
IMT-2009-47	Kristiansen, Trygve	Two-Dimensional Numerical and Experimental Studies of Piston-Mode Resonance. PhD-Thesis, CeSOS
IMT-2009-48	Ong, Muk Chen	Applications of a Standard High Reynolds Number Model and a Stochastic Scour Prediction Model for Marine Structures. PhD-thesis, IMT
IMT-2009-49	Hong, Lin	Simplified Analysis and Design of Ships subjected to Collision and Grounding. PhD-thesis, IMT
IMT-2009-50	Koushan, Kamran	Vortex Induced Vibrations of Free Span Pipelines, PhD thesis, IMT
IMT-2009-51	Korsvik, Jarl Eirik	Heuristic Methods for Ship Routing and Scheduling. PhD-thesis, IMT
IMT-2009-52	Lee, Jihoon	Experimental Investigation and Numerical in Analyzing the Ocean Current Displacement of Longlines. Ph.d.-Thesis, IMT.
IMT-2009-53	Vestbøstad, Tone Gran	A Numerical Study of Wave-in-Deck Impact usin a Two-Dimensional Constrained Interpolation Profile Method, Ph.d.thesis, CeSOS.
IMT-2009-54	Bruun, Kristine	Bond Graph Modelling of Fuel Cells for Marine Power Plants. Ph.d.-thesis, IMT
IMT 2009-55	Holstad, Anders	Numerical Investigation of Turbulence in a Sekwed Three-Dimensional Channel Flow, Ph.d.-thesis, IMT.
IMT 2009-56	Ayala-Uraga, Efren	Reliability-Based Assessment of Deteriorating Ship-shaped Offshore Structures, Ph.d.-thesis, IMT
IMT 2009-57	Kong, Xiangjun	A Numerical Study of a Damaged Ship in Beam Sea Waves. Ph.d.-thesis, IMT/CeSOS.
IMT 2010-58	Kristiansen, David	Wave Induced Effects on Floaters of Aquaculture Plants, Ph.d.-thesis, CeSOS.

IMT 2010-59	Ludvigsen, Martin	An ROV-Toolbox for Optical and Acoustic Scientific Seabed Investigation. Ph.d.-thesis IMT.
IMT 2010-60	Hals, Jørgen	Modelling and Phase Control of Wave-Energy Converters. Ph.d.thesis, CeSOS.
IMT 2010- 61	Shu, Zhi	Uncertainty Assessment of Wave Loads and Ultimate Strength of Tankers and Bulk Carriers in a Reliability Framework. Ph.d. Thesis, IMT/ CeSOS
IMT 2010-62	Shao, Yanlin	Numerical Potential-Flow Studies on Weakly-Nonlinear Wave-Body Interactions with/without Small Forward Speed, Ph.d.thesis,CeSOS.
IMT 2010-63	Califano, Andrea	Dynamic Loads on Marine Propellers due to Intermittent Ventilation. Ph.d.thesis, IMT.
IMT 2010-64	El Khoury, George	Numerical Simulations of Massively Separated Turbulent Flows, Ph.d.-thesis, IMT
IMT 2010-65	Seim, Knut Sponheim	Mixing Process in Dense Overflows with Emphasis on the Faroe Bank Channel Overflow. Ph.d.thesis, IMT
IMT 2010-66	Jia, Huirong	Structural Analysis of Intect and Damaged Ships in a Collission Risk Analysis Perspective. Ph.d.thesis CeSoS.
IMT 2010-67	Jiao, Linlin	Wave-Induced Effects on a Pontoon-type Very Large Floating Structures (VLFS). Ph.D.-thesis, CeSOS.
IMT 2010-68	Abrahamsen, Bjørn Christian	Sloshing Induced Tank Roof with Entrapped Air Pocket. Ph.d.thesis, CeSOS.
IMT 2011-69	Karimirad, Madjid	Stochastic Dynamic Response Analysis of Spar-Type Wind Turbines with Catenary or Taut Mooring Systems. Ph.d.-thesis, CeSOS.
IMT - 2011-70	Erlend Meland	Condition Monitoring of Safety Critical Valves. Ph.d.-thesis, IMT.
IMT – 2011-71	Yang, Limin	Stochastic Dynamic System Analysis of Wave Energy Converter with Hydraulic Power Take-Off, with Particular Reference to Wear Damage Analysis, Ph.d. Thesis, CeSOS.
IMT – 2011-72	Visscher, Jan	Application of Particla Image Velocimetry on Turbulent Marine Flows, Ph.d.Thesis, IMT.
IMT – 2011-73	Su, Biao	Numerical Predictions of Global and Local Ice Loads on Ships. Ph.d.Thesis, CeSOS.
IMT – 2011-74	Liu, Zhenhui	Analytical and Numerical Analysis of Iceberg Collision with Ship Structures. Ph.d.Thesis, IMT.
IMT – 2011-75	Aarsæther, Karl Gunnar	Modeling and Analysis of Ship Traffic by Observation and Numerical Simulation. Ph.d.Thesis, IMT.

Imt – 2011-76	Wu, Jie	Hydrodynamic Force Identification from Stochastic Vortex Induced Vibration Experiments with Slender Beams. Ph.d.Thesis, IMT.
Imt – 2011-77	Amini, Hamid	Azimuth Propulsors in Off-design Conditions. Ph.d.Thesis, IMT.
IMT – 2011-78	Nguyen, Tan-Hoi	Toward a System of Real-Time Prediction and Monitoring of Bottom Damage Conditions During Ship Grounding. Ph.d.thesis, IMT.
IMT- 2011-79	Tavakoli, Mohammad T.	Assessment of Oil Spill in Ship Collision and Grounding, Ph.d.thesis, IMT.
IMT- 2011-80	Guo, Bingjie	Numerical and Experimental Investigation of Added Resistance in Waves. Ph.d.Thesis, IMT.
IMT- 2011-81	Chen, Qiaofeng	Ultimate Strength of Aluminium Panels, considering HAZ Effects, IMT
IMT- 2012-82	Kota, Ravikiran S.	Wave Loads on Decks of Offshore Structures in Random Seas, CeSOS.
IMT- 2012-83	Sten, Ronny	Dynamic Simulation of Deep Water Drilling Risers with Heave Compensating System, IMT.
IMT- 2012-84	Berle, Øyvind	Risk and resilience in global maritime supply chains, IMT.
IMT- 2012-85	Fang, Shaoji	Fault Tolerant Position Mooring Control Based on Structural Reliability, CeSOS.
IMT- 2012-86	You, Jikun	Numerical studies on wave forces and moored ship motions in intermediate and shallow water, CeSOS.
IMT- 2012-87	Xiang ,Xu	Maneuvering of two interacting ships in waves, CeSOS
IMT- 2012-88	Dong, Wenbin	Time-domain fatigue response and reliability analysis of offshore wind turbines with emphasis on welded tubular joints and gear components, CeSOS
IMT- 2012-89	Zhu, Suji	Investigation of Wave-Induced Nonlinear Load Effects in Open Ships considering Hull Girder Vibrations in Bending and Torsion, CeSOS
IMT- 2012-90	Zhou, Li	Numerical and Experimental Investigation of Station-keeping in Level Ice, CeSOS
IMT- 2012-91	Ushakov, Sergey	Particulate matter emission characteristics from diesel enignes operating on conventional and alternative marine fuels, IMT
IMT- 2013-1	Yin, Decao	Experimental and Numerical Analysis of Combined In-line and Cross-flow Vortex Induced Vibrations, CeSOS

IMT-2013-2	Kurniawan, Adi	Modelling and geometry optimisation of wave energy converters, CeSOS
IMT-2013-3	Al Ryati, Nabil	Technical condition indexes doe auxiliary marine diesel engines, IMT
IMT-2013-4	Firoozkoohi, Reza	Experimental, numerical and analytical investigation of the effect of screens on sloshing, CeSOS
IMT-2013-5	Ommani, Babak	Potential-Flow Predictions of a Semi-Displacement Vessel Including Applications to Calm Water Broaching, CeSOS
IMT-2013-6	Xing, Yihan	Modelling and analysis of the gearbox in a floating spar-type wind turbine, CeSOS
IMT-7-2013	Balland, Océane	Optimization models for reducing air emissions from ships, IMT
IMT-8-2013	Yang, Dan	Transitional wake flow behind an inclined flat plate-----Computation and analysis, IMT
IMT-9-2013	Abdillah, Suyuthi	Prediction of Extreme Loads and Fatigue Damage for a Ship Hull due to Ice Action, IMT
IMT-10-2013	Ramìrez, Pedro Agustìn Pèrez	Ageing management and life extension of technical systems- Concepts and methods applied to oil and gas facilities, IMT
IMT-11-2013	Chuang, Zhenju	Experimental and Numerical Investigation of Speed Loss due to Seakeeping and Maneuvering. IMT
IMT-12-2013	Etemaddar, Mahmoud	Load and Response Analysis of Wind Turbines under Atmospheric Icing and Controller System Faults with Emphasis on Spar Type Floating Wind Turbines, IMT
IMT-13-2013	Lindstad, Haakon	Strategies and measures for reducing maritime CO2 emissons, IMT
IMT-14-2013	Haris, Sabril	Damage interaction analysis of ship collisions, IMT
IMT-15-2013	Shainee, Mohamed	Conceptual Design, Numerical and Experimental Investigation of a SPM Cage Concept for Offshore Mariculture, IMT
IMT-16-2013	Gansel, Lars	Flow past porous cylinders and effects of biofouling and fish behavior on the flow in and around Atlantic salmon net cages, IMT
IMT-17-2013	Gaspar, Henrique	Handling Aspects of Complexity in Conceptual Ship Design, IMT
IMT-18-2013	Thys, Maxime	Theoretical and Experimental Investigation of a Free Running Fishing Vessel at Small Frequency of Encounter, CeSOS
IMT-19-2013	Aglen, Ida	VIV in Free Spanning Pipelines, CeSOS

IMT-1-2014	Song, An	Theoretical and experimental studies of wave diffraction and radiation loads on a horizontally submerged perforated plate, CeSOS
IMT-2-2014	Rogne, Øyvind Ygre	Numerical and Experimental Investigation of a Hinged 5-body Wave Energy Converter, CeSOS
IMT-3-2014	Dai, Lijuan	Safe and efficient operation and maintenance of offshore wind farms ,IMT
IMT-4-2014	Bachynski, Erin Elizabeth	Design and Dynamic Analysis of Tension Leg Platform Wind Turbines, CeSOS
IMT-5-2014	Wang, Jingbo	Water Entry of Freefall Wedged – Wedge motions and Cavity Dynamics, CeSOS
IMT-6-2014	Kim, Ekaterina	Experimental and numerical studies related to the coupled behavior of ice mass and steel structures during accidental collisions, IMT
IMT-7-2014	Tan, Xiang	Numerical investigation of ship's continuous- mode icebreaking in leverl ice, CeSOS
IMT-8-2014	Muliawan, Made Jaya	Design and Analysis of Combined Floating Wave and Wind Power Facilities, with Emphasis on Extreme Load Effects of the Mooring System, CeSOS
IMT-9-2014	Jiang, Zhiyu	Long-term response analysis of wind turbines with an emphasis on fault and shutdown conditions, IMT
IMT-10-2014	Dukan, Fredrik	ROV Motion Control Systems, IMT
IMT-11-2014	Grimsmo, Nils I.	Dynamic simulations of hydraulic cylinder for heave compensation of deep water drilling risers, IMT
IMT-12-2014	Kvittem, Marit I.	Modelling and response analysis for fatigue design of a semisubmersible wind turbine, CeSOS
IMT-13-2014	Akhtar, Juned	The Effects of Human Fatigue on Risk at Sea, IMT
IMT-14-2014	Syahroni, Nur	Fatigue Assessment of Welded Joints Taking into Account Effects of Residual Stress, IMT
IMT-1-2015	Bøckmann, Eirik	Wave Propulsion of ships, IMT
IMT-2-2015	Wang, Kai	Modelling and dynamic analysis of a semi-submersible floating vertical axis wind turbine, CeSOS
IMT-3-2015	Fredriksen, Arnt Gunvald	A numerical and experimental study of a two-dimensional body with moonpool in waves and current, CeSOS
IMT-4-2015	Jose Patricio Gallardo Canabes	Numerical studies of viscous flow around bluff bodies, IMT

IMT-5-2015	Vegard Longva	Formulation and application of finite element techniques for slender marine structures subjected to contact interactions, IMT
IMT-6-2015	Jacobus De Vaal	Aerodynamic modelling of floating wind turbines, CeSOS
IMT-7-2015	Fachri Nasution	Fatigue Performance of Copper Power Conductors, IMT
IMT-8-2015	Oleh I Karpa	Development of bivariate extreme value distributions for applications in marine technology,CeSOS
IMT-9-2015	Daniel de Almeida Fernandes	An output feedback motion control system for ROVs, AMOS
IMT-10-2015	Bo Zhao	Particle Filter for Fault Diagnosis: Application to Dynamic Positioning Vessel and Underwater Robotics, CeSOS
IMT-11-2015	Wenting Zhu	Impact of emission allocation in maritime transportation, IMT
IMT-12-2015	Amir Rasekhi Nejad	Dynamic Analysis and Design of Gearboxes in Offshore Wind Turbines in a Structural Reliability Perspective, CeSOS
IMT-13-2015	Arturo Jesùs Ortega Malca	Dynamic Response of Flexibles Risers due to Unsteady Slug Flow, CeSOS
IMT-14-2015	Dagfinn Husjord	Guidance and decision-support system for safe navigation of ships operating in close proximity, IMT
IMT-15-2015	Anirban Bhattacharyya	Ducted Propellers: Behaviour in Waves and Scale Effects, IMT
IMT-16-2015	Qin Zhang	Image Processing for Ice Parameter Identification in Ice Management, IMT
IMT-1-2016	Vincentius Rumawas	Human Factors in Ship Design and Operation: An Experiential Learning, IMT
IMT-2-2016	Martin Storheim	Structural response in ship-platform and ship-ice collisions, IMT
IMT-3-2016	Mia Abrahamsen Prsic	Numerical Simulations of the Flow around single and Tandem Circular Cylinders Close to a Plane Wall, IMT
IMT-4-2016	Tufan Arslan	Large-eddy simulations of cross-flow around ship sections, IMT

IMT-5-2016	Pierre Yves-Henry	Parametrisation of aquatic vegetation in hydraulic and coastal research,IMT
IMT-6-2016	Lin Li	Dynamic Analysis of the Instalation of Monopiles for Offshore Wind Turbines, CeSOS
IMT-7-2016	Øivind Kåre Kjerstad	Dynamic Positioning of Marine Vessels in Ice, IMT
IMT-8-2016	Xiaopeng Wu	Numerical Analysis of Anchor Handling and Fish Trawling Operations in a Safety Perspective, CeSOS
IMT-9-2016	Zhengshun Cheng	Integrated Dynamic Analysis of Floating Vertical Axis Wind Turbines, CeSOS
IMT-10-2016	Ling Wan	Experimental and Numerical Study of a Combined Offshore Wind and Wave Energy Converter Concept
IMT-11-2016	Wei Chai	Stochastic dynamic analysis and reliability evaluation of the roll motion for ships in random seas, CeSOS
IMT-12-2016	Øyvind Selnes Patricksson	Decision support for conceptual ship design with focus on a changing life cycle and future uncertainty, IMT
IMT-13-2016	Mats Jørgen Thorsen	Time domain analysis of vortex-induced vibrations, IMT
IMT-14-2016	Edgar McGuinness	Safety in the Norwegian Fishing Fleet – Analysis and measures for improvement, IMT
IMT-15-2016	Sepideh Jafarzadeh	Energy effiency and emission abatement in the fishing fleet, IMT
IMT-16-2016	Wilson Ivan Guachamin Acero	Assessment of marine operations for offshore wind turbine installation with emphasis on response-based operational limits, IMT
IMT-17-2016	Mauro Candeloro	Tools and Methods for Autonomous Operations on Seabed and Water Coumn using Underwater Vehicles, IMT
IMT-18-2016	Valentin Chabaud	Real-Time Hybrid Model Testing of Floating Wind Tubines, IMT
IMT-1-2017	Mohammad Saud Afzal	Three-dimensional streaming in a sea bed boundary layer
IMT-2-2017	Peng Li	A Theoretical and Experimental Study of Wave-induced Hydroelastic Response of a Circular Floating Collar
IMT-3-2017	Martin Bergström	A simulation-based design method for arctic maritime transport systems

IMT-6-2018	Bård Stovner	Aided Intertial Navigation of Underwater Vehicles
IMT-7-2018	Erlend Liavåg Grotle	Thermodynamic Response Enhanced by Sloshing in Marine LNG Fuel Tanks
IMT-8-2018	Børge Rokseth	Safety and Verification of Advanced Maritime Vessels
IMT-9-2018	Jan Vidar Ulveseter	Advances in Semi-Empirical Time Domain Modelling of Vortex-Induced Vibrations
IMT-10-2018	Chenyu Luan	Design and analysis for a steel braceless semi-submersible hull for supporting a 5-MW horizontal axis wind turbine
IMT-11-2018	Carl Fredrik Rehn	Ship Design under Uncertainty
IMT-12-2018	Øyvind Ødegård	Towards Autonomous Operations and Systems in Marine Archaeology
IMT-13-2018	Stein Melvær Nornes	Guidance and Control of Marine Robotics for Ocean Mapping and Monitoring
IMT-14-2018	Petter Norgren	Autonomous Underwater Vehicles in Arctic Marine Operations: Arctic marine research and ice monitoring
IMT-15-2018	Minjoo Choi	Modular Adaptable Ship Design for Handling Uncertainty in the Future Operating Context
MT-16-2018	Ole Alexander Eidsvik	Dynamics of Remotely Operated Underwater Vehicle Systems
IMT-17-2018	Mahdi Ghane	Fault Diagnosis of Floating Wind Turbine Drivetrain- Methodologies and Applications
IMT-18-2018	Christoph Alexander Thieme	Risk Analysis and Modelling of Autonomous Marine Systems
IMT-19-2018	Yugao Shen	Operational limits for floating-collar fish farms in waves and current, without and with well-boat presence
IMT-20-2018	Tianjiao Dai	Investigations of Shear Interaction and Stresses in Flexible Pipes and Umbilicals
IMT-21-2018	Sigurd Solheim Pettersen	Resilience by Latent Capabilities in Marine Systems
IMT-22-2018	Thomas Sauder	Fidelity of Cyber-physical Empirical Methods. Application to the Active Truncation of Slender Marine Structures
IMT-23-2018	Jan-Tore Horn	Statistical and Modelling Uncertainties in the Design of Offshore Wind Turbines

IMT-24-2018	Anna Swider	Data Mining Methods for the Analysis of Power Systems of Vessels
IMT-1-2019	Zhao He	Hydrodynamic study of a moored fish farming cage with fish influence
IMT-2-2019	Isar Ghamari	Numerical and Experimental Study on the Ship Parametric Roll Resonance and the Effect of Anti-Roll Tank
IMT-3-2019	Håkon Strandenes	Turbulent Flow Simulations at Higher Reynolds Numbers
IMT-4-2019	Siri Mariane Holen	Safety in Norwegian Fish Farming – Concepts and Methods for Improvement
IMT-5-2019	Ping Fu	Reliability Analysis of Wake-Induced Riser Collision
IMT-6-2019	Vladimir Krivopolianskii	Experimental Investigation of Injection and Combustion Processes in Marine Gas Engines using Constant Volume Rig
IMT-7-2019	Anna Maria Kozlowska	Hydrodynamic Loads on Marine Propellers Subject to Ventilation and out of Water Condition.
IMT-8-2019	Hans-Martin Heyn	Motion Sensing on Vessels Operating in Sea Ice: A Local Ice Monitoring System for Transit and Stationkeeping Operations under the Influence of Sea Ice
IMT-9-2019|	Stefan Vilsen	Method for Real-Time Hybrid Model Testing of Ocean Structures – Case on Slender Marine Systems
IMT-10-2019	Finn-Christian W. Hanssen	Non-Linear Wave-Body Interaction in Severe Waves
IMT-11-2019	Trygve Olav Fossum	Adaptive Sampling for Marine Robotics
IMT-12-2019	Jørgen Bremnes Nielsen	Modeling and Simulation for Design Evaluation
IMT-13-2019	Yuna Zhao	Numerical modelling and dyncamic analysis of offshore wind turbine blade installation
IMT-14-2019	Daniela Myland	Experimental and Theoretical Investigations on the Ship Resistance in Level Ice
IMT-15-2019	Zhengru Ren	Advanced control algorithms to support automated offshore wind turbine installation
IMT-16-2019	Drazen Polic	Ice-propeller impact analysis using an inverse propulsion machinery simulation approach
IMT-17-2019	Endre Sandvik	Sea passage scenario simulation for ship system performance evaluation

IMT-18-2019	Loup Suja-Thauvin	Response of Monopile Wind Turbines to Higher Order Wave Loads
IMT-19-2019	Emil Smilden	Structural control of offshore wind turbines – Increasing the role of control design in offshore wind farm development
IMT-20-2019	Aleksandar-Sasa Milakovic	On equivalent ice thickness and machine learning in ship ice transit simulations
IMT-1-2020	Amrit Shankar Verma	Modelling, Analysis and Response-based Operability Assessment of Offshore Wind Turbine Blade Installation with Emphasis on Impact Damages
IMT-2-2020	Bent Oddvar Arnesen Haugaløkken	Autonomous Technology for Inspection, Maintenance and Repair Operations in the Norwegian Aquaculture
IMT-3-2020	Seongpil Cho	Model-based fault detection and diagnosis of a blade pitch system in floating wind turbines
IMT-4-2020	Jose Jorge Garcia Agis	Effectiveness in Decision-Making in Ship Design under Uncertainty
IMT-5-2020	Thomas H. Viuff	Uncertainty Assessment of Wave-and Current-induced Global Response of Floating Bridges
IMT-6-2020	Fredrik Mentzoni	Hydrodynamic Loads on Complex Structures in the Wave Zone
IMT-7-2020	Senthuran Ravinthrakumar	Numerical and Experimental Studies of Resonant Flow in Moonpools in Operational Conditions
IMT-8-2020	Stian Skaalvik Sandøy	Acoustic-based Probabilistic Localization and Mapping using Unmanned Underwater Vehicles for Aquaculture Operations
IMT-9-2020	Kun Xu	Design and Analysis of Mooring System for Semi-submersible Floating Wind Turbine in Shallow Water
IMT-10-2020	Jianxun Zhu	Cavity Flows and Wake Behind an Elliptic Cylinder Translating Above the Wall
IMT-11-2020	Sandra Hogenboom	Decision-making within Dynamic Positioning Operations in the Offshore Industry – A Human Factors based Approach
IMT-12-2020	Woongshik Nam	Structural Resistance of Ship and Offshore Structures Exposed to the Risk of Brittle Failure
IMT-13-2020	Svenn Are Tutturen Værnø	Transient Performance in Dynamic Positioning of Ships: Investigation of Residual Load Models and Control Methods for Effective Compensation
IMT-14-2020	Mohd Atif Siddiqui	Experimental and Numerical Hydrodynamic Analysis of a Damaged Ship in Waves
IMT-15-2020	John Marius Hegseth	Efficient Modelling and Design Optimization of Large Floating Wind Turbines

IMT-16-2020	Asle Natskår	Reliability-based Assessment of Marine Operations with Emphasis on Sea Transport on Barges
IMT-17-2020	Shi Deng	Experimental and Numerical Study of Hydrodynamic Responses of a Twin-Tube Submerged Floating Tunnel Considering Vortex-Induced Vibration
IMT-18-2020	Jone Torsvik	Dynamic Analysis in Design and Operation of Large Floating Offshore Wind Turbine Drivetrains
IMT-1-2021	Ali Ebrahimi	Handling Complexity to Improve Ship Design Competitiveness
IMT-2-2021	Davide Proserpio	Isogeometric Phase-Field Methods for Modeling Fracture in Shell Structures
IMT-3-2021	Cai Tian	Numerical Studies of Viscous Flow Around Step Cylinders
IMT-4-2021	Farid Khazaeli Moghadam	Vibration-based Condition Monitoring of Large Offshore Wind Turbines in a Digital Twin Perspective
IMT-5-2021	Shuaishuai Wang	Design and Dynamic Analysis of a 10-MW Medium-Speed Drivetrain in Offshore Wind Turbines
IMT-6-2021	Sadi Tavakoli	Ship Propulsion Dynamics and Emissions
IMT-7-2021	Haoran Li	Nonlinear wave loads, and resulting global response statistics of a semi-submersible wind turbine platform with heave plates
IMT-8-2021	Einar Skiftestad Ueland	Load Control for Real-Time Hybrid Model Testing using Cable-Driven Parallel Robots
IMT-9-2021	Mengning Wu	Uncertainty of machine learning-based methods for wave forecast and its effect on installation of offshore wind turbines
IMT-10-2021	Xu Han	Onboard Tuning and Uncertainty Estimation of Vessel Seakeeping Model Parameters
IMT-01-2022	Ingunn Marie Holmen	Safety in Exposed Aquacultrue Operations
IMT-02-2022	Prateek Gupta	Ship Performance Monitoring using In-service Measurements and Big Data Analysis Methods
IMT-03-2022	Sangwoo Kim	Non-linear time domain analysis of deepwater riser vortex-induced vibrations
IMT-04-2022	Jarle Vinje Kramer	Hydrodynamic Aspects of Sail-Assisted Merchant Vessels
IMT-05-2022	Øyvind Rabliås	Numerical and Expermental Studies of Maneuvering in Regular and Irregular Waves

IMT-06-2022	Pramod Ghimire	Simulation-Based Ship Hybrid Power System Conspet Studies and Performance Analyses
IMT-07-2022	Carlos Eduardo Silva de Souza	Structural modelling, coupled dynamics, and design of large floating wind turbines
IMT-08-2022	Lorenzo Balestra	Design of hybrid fuel cell & battery systems for maritime vessels
IMT-09-2022	Sharmin Sultana	Process safety and risk management using system perspectives – A contribution to the chemical process and petroleum industry
IMT-10-2022	Øystein Sture	Autonomous Exploration for Marine Minerals
IMT-11-2022	Tiantian Zhu	Information and Decision-making for Major Accident Prevention – A concept of information-based strategies for accident prevention
IMT-12-2022	Siamak Karimi	Shore-to-Ship Charging Systems for Battery-Electric Ships
IMT-01-2023	Huili Xu	Fish-inspired Propulsion Study: Numerical Hydrodynamics of Rigid/Flexible/Morphing Foils and Observations on Real Fish
IMT-02-2023	Chana Sinsabvarodom	Probabilistic Modelling of Ice-drift and Ice Loading on Fixed and Floating Offshore Structures
IMT-03-2023	Martin Skaldebø	Intelligent low-cost solutions for underwater intervention using computer vision and machine learning
IMT-04-2023	Hans Tobias Slette	Vessel operations in exposed aquaculture – Achieving safe and efficient operation of vessel fleets in fish farm systems experiencing challenging metocean conditions
IMT-05-2023	Ruochen Yang	Methods and models for analyzing and controlling the safety in operations of autonomous marine systems
IMT-06-2023	Tobias Rye Torben	Formal Approaches to Design and Verification of Safe Control Systems for Autonomous Vessels
IMT-07-2023	YoungRong Kim	Modeling Operational Performance for the Global Fleet & Application of an Energy Saving Measure
IMT-08-2023	Henrik Schmidt-Didlaukies	Modeling and Hybrid Feedback Control of Underwater Vehicles
IMT-09-2023	Ehsan Esmailian	Optimal Ship Design for Operating in Real Sea States
IMT-10-2023	Astrid Vamråk Solheim	Exploring the performance of conceptual offshore production systems for deep-sea mining
IMT-11-2023	Benjamin Lagemann	Conceptual design of low-emission ships